

A THEORETICAL AND EXPERIMENTAL INVESTIGATION OF
PARAMETRICALLY EXCITED NONLINEAR MECHANICAL SYSTEMS

by

Lawrence D. Zavodney

Dissertation submitted to the Faculty of the
Virginia Polytechnic Institute and State University
in partial fulfillment of the requirements for the degree of

DOCTOR OF PHILOSOPHY

in

Engineering Mechanics

APPROVED:

Ali H. Nayfeh, Chairman

Dean T. Mook

Daniel Frederick

Scott L. Hendricks

Michael Williams

December 1987

Blacksburg, Virginia

ACKNOWLEDGEMENTS

It is difficult, if not impossible, to trace the development of one's own thinking about a specific discipline, and then acknowledge those responsible, but I am keenly aware of how much I have been influenced by my advisor Professor Ali H. Nayfeh. Perhaps the greatest compliment occurs when another's ideas are adopted as one's own. This has happened to some degree during my tenure at VPI & SU and also at Yarmouk University, Jordan, where, at Dr. Nayfeh's invitation, I accompanied him for two years and served on the faculty of the Department of Mechanical Engineering. I am also grateful to have had the opportunity to study under Professor Dean T. Mook, who also served as co-chairman during Professor Nayfeh's leave of absence. I thank my other committee members, Professors Daniel Frederick, Scott L. Hendricks, and Michael Williams for reading the manuscript and providing helpful comments. Professors Larry D. Mitchell and William Hallauer were originally on my committee and assisted me with the experimental aspects of my research, but could not attend my defense; I thank them also.

There are a number of other people who have helped me in various ways. Mr. Nestor Sanchez ran the analogue computer cases, generated the data, and prepared the bifurcation maps in Chapter III. Mr. B. Balachandran assisted me in conducting the experiments in Chapter V, sometimes past 4:00 in the morning. Mr. Tariq Nayfeh ran some of the analogue computer cases in Chapter II and some of the digital computer

cases in Chapters II and II, including the fractal basin maps. Mr. Harold Neal developed a comprehensive menu-driven computer program to control the signal generator for general purpose multi-frequency waveform generation. Mr. Mike Colbert adapted a portion of that code and developed a menu-driven feedback controller that was used for the experiments. Mr. Rick O'Donnel of GenRad assisted me with the real-time three-dimensional plotting program used in Chapter V, and Mr. Mahir Nayfeh assisted me with modifications. Mr. Cliff Martin prepared most of the ink drawings in the first four chapters and Mr. Peter Ifju prepared some of the ink drawings in Chapter II.

Developing a lab requires the serves of a machine shop and electronics shop; I thank our machinists Mr. Bob Davis, Mr. Archie Montgomery, Mr. Bill Shaver, and Mr. David Hughes for fabricating the components for the shaker system, support equipment, and the test specimens and fixture. I also thank Mr. Kulkarni Upendra for assisting me with the design of the servo accelerometer conditioner/amplifier, and Mr. Mike Colbert and Mr. Stefan Kim for their assistance in fabricating the instrument. Mr. George Lough assisted me with instrument repairs and maintenance. I am certainly indebted to Mrs. Sally G. Shrader for her proficient and expert assistance in the seemingly endless task of typing and retyping successive drafts of the manuscript, and I appreciated her pleasant and cheerful attitude.

This work was supported by the Air Force Office of Scientific Research under Grants AFOSR-86-0090 and F49620-87-C-0088, and the Office of Naval Research under Grant N00014-83-K-0184, NR 4322753. Several

companies supported this work with donations to the laboratory: Structural Dynamics Research Corporation (SDRC) donated Modal-Plus software through the University Program, PCB donated a model 308 accelerometer, and Sundstrand Data Control, Inc. donated a QA-1400 servo accelerometer.

This work would not have been possible if I did not have the support and encouragement of my beloved wife Deborah, for whom I am extremely grateful. During this time, we watched our first daughter Sara grow up and become a little girl, and we witnessed the birth of our second daughter Kristin. I cannot say that I sacrificed very many hours from them that was rightfully theirs because I did not. Although the preparation of this dissertation has required many hours of diligent work, it has been an enjoyable experience, and I move on with many pleasant memories.

TABLE OF CONTENTS

	Page
ACKNOWLEDGEMENTS	ii
TABLE OF CONTENTS	v
LIST OF FIGURES	x
LIST OF TABLES	xxiv
CHAPTER I INTRODUCTION	1
1.1 Historical Review	1
1.2 Parametric Vibration	3
1.2.1 Resonance	6
1.2.2 Examples and Causes of Parametric Vibration	12
1.2.3 Paradoxical Phenomena	15
1.2.4 Parametric Instability - The Nature of a Parametric Resonance	17
1.2.5 Internal (Autoparametric) Resonance	22
1.2.6 Combination Resonance	24
1.3 Problem Formulation and Solution	25
1.3.1 Mathematical Formulation	28
1.3.2 Solution of the Equations	29

1.4	Literature Review	33
1.4.1	Single-Degree-of-Freedom Systems	35
1.4.2	Multi-Degree-of-Freedom Systems . . .	40
1.4.3	Lumped Mass Systems	44
1.4.4	Pendulum Systems	46
1.4.5	Beams, Bars, Rods, and Strings	49
1.4.6	Rotating Shafts	53
1.4.7	Plates and Shells	54
1.4.8	Flow-Induced Parametric Vibration . .	56
1.4.9	Structures Containing Liquid	58
1.4.10	Parametric Instability	62
1.5	Summary and Purpose	63
CHAPTER II	FUNDAMENTAL PARAMETRIC RESONANCE IN A SINGLE- DEGREE-OF-FREEDOM SYSTEM WITH QUADRATIC AND CUBIC NONLINEARITIES	79
2.1	Multiple Scales Analysis	79
2.2	Numerical Results of Approximate Solution	87
2.3	Analogue Computer Simulation	93
2.4	Digital Computer Simulation	102
2.5	Chapter Summary	106

CHAPTER III	PRINCIPAL PARAMETRIC RESONANCE IN A SINGLE- DEGREE-OF-FREEDOM SYSTEM WITH QUADRATIC AND CUBIC NONLINEARITIES	144
3.1	Multiple Scales Analysis	144
3.2	Numerical Results	150
3.3	Analogue Computer Simulation	156
3.4	Bifurcation Diagram	160
3.5	Digital Computer Simulation	164
3.5	Chapter Summary	165
CHAPTER IV	FORMULATION AND VARIATIONAL SOLUTION OF A SLENDER BEAM CARRYING A LUMPED MASS SUBJECT TO A PARAMETRIC EXCITATION	200
4.1	Formulation of the Nonlinear Problem	200
4.2	Solution of the Free Vibration Linear Problem	207
4.3	One-Mode Approximation of the Nonlinear Problem	213
4.4	Scaling of the Time Modulation Equation	217
4.5	Chapter Summary	220

CHAPTER V	PERTURBATION SOLUTION AND EXPERIMENTAL RESULTS OF A SLENDER BEAM CARRYING A LUMPED MASS SUBJECT TO A PARAMETRIC EXCITATION	226
5.1	Multiple Scales Analysis	226
5.2	Numerical Results of Approximate Solution . . .	232
5.3	Results of Preliminary Experiments on Test Models	234
5.4	Results and Discussion of the Composite Beam Experiments	237
5.5	Results and Discussion of the Metallic Beam Experiments	241
5.6	Concluding Remarks and Chapter Summary	243
CHAPTER VI	COMBINATION RESONANCES IN A TWO-DEGREE-OF- FREEDOM SYSTEM WITH INTERNAL RESONANCES AND QUADRATIC NONLINEARITIES	263
6.1	Multiple Scales Analysis	264
6.2	Stability of Steady-State Solutions	269
6.3	Numerical Results and Discussion	272
6.3.1	Effects of Detuning Parameters σ_1 and σ_2	273
6.3.2	Effects of Phase τ	275

	Page
6.3.3 Effects of Amplitude of Second Excitation f_{21}	277
6.4 Chapter Summary	281
REFERENCES	313
APPENDIX A. DESCRIPTION OF LABORATORY FACILITY	337
B. PROCEDURE TO MEASURE THE NATURAL FREQUENCY	346
C. PROCEDURE TO MEASURE THE DAMPING COEFFICIENT	349
D. PROCEDURE TO CALIBRATE THE STRAIN GAGE	350
E. PROCEDURE TO MEASURE THE FREQUENCY RESPONSE	352
F. PROCEDURE TO MEASURE THE AMPLITUDE RESPONSE	354
G. DIMENSIONS AND PROPERTIES OF BEAM SPECIMENS	355
VITA	357
ABSTRACT	

LIST OF FIGURES

Figure	Page	
1.1	Frequency response function of a spring-mass-damper to an (a) external sinusoidal force and (b) external sinusoidal base displacement for different values of the damping coefficient ξ	67
1.2	Examples of dynamic systems subjected to parametric excitation.	68
1.3	Free-body diagram of a string element in a displaced position.	71
1.4	Response amplitude to a parametric excitation for (a) a linear system, (b) a nonlinear system, and (c) a nonlinear system that possesses a subcritical instability.	72
1.5	Stability diagram of the undamped Mathieu oscillator, also known as the Strutt diagram.	73
1.6	Effect of damping on the instability regions of Figure 1.5.	74
1.7	Examples of dynamic systems with autoparametric interaction caused by internal resonance.	75
1.8	Examples of dynamic systems susceptible to combination resonances caused by parametric excitation	77

Figure	Page
1.9 Stability diagrams of a multi-degree-of-freedom system showing the combination resonances that exist in a particular system.	78
2.1 Potential wells and corresponding phase-plane portraits for three distinct cases: (a) $\delta = 3.0$, (b) $\delta = 4.0$, and (c) $\delta = 5.0$	108
2.2 Variation of the steady-state response amplitude a with the excitation g	109
2.3 Time history of u showing the response decaying to the stable trivial response, as predicted by the perturbation solution.	110
2.4 Long-time history of the amplitude and phase, obtained by numerically integrating the amplitude- and phase-modulation equations (2.18)-(2.20).	111
2.5 Phase-plane portraits of the three steady-state solutions predicted by the perturbation solution shown in Figures 2.2 and 2.4.	112
2.6 Phase-plane portraits of the three steady-state solutions obtained by numerical integration of (2.1) for the system parameters used in Figure 2.5.	113

Figure	Page
2.7 Comparison of the time history of the response obtained using the perturbation solution with that obtained by numerically integrating the original equation for the three distinct solutions shown in Figures 2.2, 2.4, 2.5, and 2.6.	114
2.8 Variation of the steady-state amplitude a with the frequency detuning σ	115
2.9 Variation of the steady-state amplitude a with the perturbation parameter ϵ	116
2.10 Variation of the steady-state amplitude a with the damping coefficient μ	117
2.11 Variation of the steady-state amplitude a with the coefficient α of the cubic nonlinearity.	118
2.12 Variation of the steady-state amplitude a with the coefficient δ of the quadratic nonlinearity.	119
2.13 Laboratory setup showing the analogue computers and instrumentation.	120
2.14 Analogue computer program used to simulate the nonlinear Mathieu oscillator using the nonlinear van der Pol oscillator as the excitation.	121
2.15 Phase-plane portraits and accompanying frequency spectra of the system response, obtained by analogue computer simulation.	122

Figure	Page
2.16 Long-time history for selected cases shown in Figure 2.15, obtained by analogue computer simulation.	132
2.17 Phase-plane portraits of stable steady-state solutions of (2.1) for case (c) shown in Figure 2.1.	134
2.18 Transient responses for each of the three different steady-state responses shown in Figure 2.15.	135
2.19 Fractal basin boundary showing domains of attraction for the three attractors shown in Figure 2.18: black-large outer attractor, red limit-cycle attractor about the focus at -10.0 , white-trivial attractor; $-20 \leq u \leq 10$, $-20 \leq \dot{u} \leq 20$	136
2.20 (a) Phase-plane portrait and (b) Poincaré map of the system obtained by numerical integration of (2.1) showing what appears to be chaotic response: $g = 6.80$	137
2.21 (a) Phase-plane portrait and (b) Poincaré map of the system obtained by numerical integration of (2.1) showing chaotic response: $g = 22.0$	138
2.22 Poincaré maps of the chaotic response shown in Figure 2.21 at different phases of the excitation.	139
2.23 Phase-plane portraits of the attractor at the origin showing its first period doubling bifurcation encircling the focus at the origin (a) $g = 29.8$ and (b) $g = 30.5$. . .	140

Figure	Page
2.24 Phase-plane portraits of an attractor that coexists with those found earlier for (a) $g = 24.0$, (b) $g = 45.0$, and (c) $g = 50.0$	141
2.25 (a) Phase-plane portrait and (b) Poincaré map of the system obtained by numerical integration of (2.1) showing a 5x response.	142
2.26 (a) Phase-plane portrait and (b) Poincaré map of the system obtained by numerical integration of (2.1) showing a 7x response.	143
3.1 Potential wells and corresponding phase-plane portraits for three distinct cases: (a) $\delta = 3.0$, (b) $\delta = 4.0$, (c) $\delta = 5.0$	167
3.2 Variation of the steady-state response amplitude a with the excitation amplitude g : (a) $\sigma = 0.0$, (b) $\sigma = -15.0$	168
3.3 Variation of the steady-state response amplitude a with the excitation frequency detuning σ	169
3.4 Long-time history of the amplitude showing only two stable steady states obtained by numerically integrating the amplitude- and phase-modulation equations (3.12)-(3.14).	170

Figure	Page
3.5 Time history of the response as it decays to the trivial solution, which is one of the two stable responses predicted by the perturbation solution.	171
3.6 Phase-plane plot of the steady-state nontrivial response for the case shown in Figures 3.2-3.4.	172
3.7 Time history of the steady-state response obtained by numerical integration and by the perturbation solution.	173
3.8 Variation of the steady-state response amplitude a with the damping coefficient μ	174
3.9 Variation of the steady-state response amplitude a with the coefficient α of the cubic nonlinearity.	175
3.10 Variation of the steady-state response amplitude a with the coefficient δ of the quadratic nonlinearity.	176
3.11 Phase-plane portraits and accompanying frequency spectra of the system response, obtained by analogue computer simulation.	177
3.12 Long-time history for selected cases shown in Figure 3.11, obtained by analogue computer simulation.	186
3.13 Bifurcation map in the g - Ω plane for four of the steady-state attractors shown in Figure 3.11.	190
3.14 Bifurcation map in the g - Ω plane for both superharmonic and subharmonic resonances.	191

Figure	Page
3.15 Additional attractors and their bifurcation boundaries in the g - ω plane.	192
3.16 (a) Phase portrait, (b) Poincaré map, and (c) representative time history of a chaotic response.	193
3.17 Basin of attraction for the system shown in Figure 3.11(a) obtained by numerical integration.	194
3.18 Basin of attraction for the system shown in Figure 3.17 for $g = 1.5$ and $\phi = 2.000$	195
3.19 Fractal basin of attraction for the system shown in Figure 3.18 for $g = 2.0$	196
3.20 Fractal basin of attraction for the system shown in Figure 3.18 for $g = 2.5$	197
3.21 Fractal basin of attraction for the system shown in Figure 3.18 for $g = 3.0$	198
3.22 Fractal basin of attraction for the system shown in Figure 3.18 for $g = 4.2$; red denotes the new large outer attractor.	199a
3.23 Enlarged region of Figure 3.22 showing structure is preserved at the boundaries.	199b
4.1 Cantilevered beam with a concentrated mass subjected to vertical base motion.	221

Figure	Page
4.2 Free-body diagram of the concentrated mass showing shearing forces and bending moments which cause the resultant accelerations.	222
4.3 Shape function and derivatives for the first mode of the cantilevered beam shown in Figure 4.1.	223
4.4 Shape function and derivatives for the second mode of the cantilevered beam shown in Figure 4.1.	224
4.5 Stroboscopic photograph of a beam in the maximum deflected position when excited by a principal parametric resonance to the first mode.	225
5.1 Variation of the steady-state amplitude a with the frequency of excitation ϕ	247
5.2 Variation of the steady-state amplitude a with the amplitude of excitation f in region II of Figure 5.1: $\phi = 2.000$	248
5.3 Variation of the steady-state amplitude a with the amplitude of excitation f in region III of Figure 5.1.	249
5.4 Comparison of the frequency response curves predicted by the perturbation theory when the frequency detuning is introduced (a) into the natural frequency as done in this analysis, and (b) into the excitation frequency.	250

Figure	Page
5.5 Variation of the steady-state amplitude a^* with the frequency of excitation Ω of a metallic beam that later had developed a fatigue crack (shown in Figure 5.6).	251
5.6 Photograph of the first metallic beam that failed by fatigue.	252
5.7 Metallic beam specimen made from alloy steel and ground to the dimensions shown.	253
5.8 Time traces of (a) table acceleration, (b) table displacement, and (c) strain gage (beam displacement) showing the subharmonic distortion to the table motion caused by the large bending moment reaction from the beam.	254
5.9 Photograph of the composite beam.	255
5.10 Variation of the response amplitude a^* with the frequency of excitation ϕ for three levels of excitation amplitude f of the composite beam. Note that chaotic behavior occurs at the largest amplitude of excitation.	256

Figure	Page
5.11 Spectral time history of the composite beam to a principal parametric excitation: (a) $\phi = 2.000$, (b) $\phi = 2.013$. Both responses start with the trivial solution. When $\phi = 2.013$ two solutions are possible.	257
5.12 Variation of the steady-state amplitude a^* with the amplitude of excitation f of the composite beam for three frequencies of excitation.	258
5.13 Power spectra of the table acceleration and strain gage signals for large amplitude motion of the composite beam.	259
5.14 Photograph of the precision ground and polished beam after a fatigue crack rendered it useless for further research.	260
5.15 Variation of the steady-state amplitude a^* with the frequency of excitation ϕ of the metallic beam shown in Figure 5.13 for two acceleration levels.	261
5.16 Variation of the amplitude a^* with the amplitude of excitation f of the beam shown in Figure 5.14.. . . .	262
6.1 Variation of the steady-state response amplitudes a_1 and a_2 with the internal resonance detuning parameter σ_1	285

Figure	Page	
6.2	Steady-state response curves a_1 and a_2 vs. the detuning parameter σ_2 due to parametric resonance: $\tau = 0.785$ radians.	286
6.3	Steady-state response curves a_1 and a_2 vs. the detuning parameter σ_2 due to parametric resonance: $\tau = 1.309$ radians.	287
6.4	Variation of the steady-state response curves with the phase angle τ	288
6.5	Variation of the steady-state response curves with the phase angle τ	289
6.6	Time history of a_1 , $f_{12} = 7.00$, $f_{21} = 7.86$	290
6.7	Time history of the response of the system corresponding to the parameters in Figures 6.4 and 6.6b as calculated by numerically integrating the governing differential equations (6.1) and (6.2).	291
6.8	Variation of the u_n with time obtained by numerically integrating the governing differential equations.	292
6.9	Modulation of the amplitudes of the modes of the system corresponding to the parameters in Figure 6.6a.	293
6.10	Separatrix dividing the $a_1(0)$ and $a_2(0)$ domain into the fixed-point attractor basin and the limit-cycle attractor basin.	294

Figure	Page
6.11 Initial values of a_1 and a_2 in the basin of the limit-cycle attractor of Figure 6.10.	295
6.12 Response of the system corresponding to the parameters in Figure 6.9.	296
6.13 Projection of the trajectory in the $a_1 - a_2$ plane with initial values of a_1 and a_2 in the basin of the fixed-point attractor of Figure 6.10.	297
6.14 Projection of the trajectory onto the $a_1 - a_2$ plane for the case of a quenched response.	298
6.15 Variation of the steady-state response curves with the amplitude of the second excitation f_{21}	299
6.16 Variation of the steady-state response curves with f_{21}	300
6.17 Variation of the steady-state response curves with f_{21}	301
6.18 Variation of the steady-state response amplitudes a_1 and a_2 with f_{21} showing three regions of stable non- trivial solutions.	302
6.19 Time histories of a_1 for various points on the response curve in Figure 6.18 as predicted by the perturbation analysis.	303

Figure	Page
6.20 Time histories of the responses of u_1 and u_2 as numerically integrated from the governing differential equations.	304
6.21 Periodic limit cycle corresponding to the parameters of Figures 6.18 and 6.19, point c.	305
6.22 Time histories of a_1 showing the limit cycle bifurcating in the region between points x and y in Figure 6.18.	306
6.23 Projection of the limit cycle trajectory on the plane $a_1 - a_2$ corresponding to the parameters of Figures 6.18 and 6.22 between points x and y.	307
6.24 Variations of the amplitudes of the steady-state response with the amplitude f_{21} of the second mode in the presence of a strong excitation of the first mode.	308
6.25 Variations of the amplitudes of the steady-state response with the second excitation amplitude f_{21} in the presence of a weak excitation of the first mode.	309
6.26 Variations of the amplitudes of the steady-state response with the second excitation amplitude f_{21} without first-mode excitation.	310

Figure	Page
6.27 Transition curves separating regions of steady-state solutions from regions of nonsteady-state solutions.	311
A.1 Photograph of the vibration laboratory at VPI & SU.	343
A.2 Close-up photograph of the shaker showing head, bearings, displacement transducer, accelerometer, and flexible beam with lumped mass.	344
A.3 Typical instrumentation schematic.	345
D.1 Photograph of micrometer used to calibrate the strain gage that measured the beam displacement.	351

LIST OF TABLES

Table	Page
6.1 Perturbation results for the steady-state non-trivial solution compared with the numerically obtained results: $f_{12} = 7.00$, $f_{21} = 5.04$, $\tau = 0.2618$, $\sigma_1 = \sigma_2 = 0$. The percent error decreases for decreasing f_{21}	312

CHAPTER I

INTRODUCTION

1.1 Historical Review

The study of the relationship between the motion of physical systems and the forces causing the motion is a subject that has fascinated the human mind since ancient times. The study of statics goes back to the time of the Greek philosophers when Archimedes of Syracuse (287-212 BC) demonstrated the principle of the lever. Previously Aristotle (384-322 BC) had tried in vain to formulate the relationship between the motion of a body and the forces causing the motion. He erroneously postulated that the velocity was proportional to the applied force. It was not until Galileo Galilei (1564-1642) correctly described the motion of a simple pendulum that the first significant contribution to dynamics was made. His experiments on uniformly accelerated bodies led Sir Isaac Newton (1642-1727) to formulate his fundamental law of motion which stated that the rate of change of a body's velocity was proportional to the applied force. Except for certain limitations where velocities approach the speed of light, Newton's law of motion is the foundation of classical dynamics today.

An important branch of modern engineering is the analysis and prediction of the dynamic behavior of physical systems. An omnipresent type of dynamic behavior is vibratory or oscillatory motion, or simply

vibration, in which the system oscillates about one or more equilibrium positions. Bridges and buildings vibrate, engines and machinery vibrate, aircraft and ground vehicles and watercraft vibrate, eardrums and vocal chords vibrate, and piano strings and air in pipe organs vibrate.

The most important aspect of vibration is the phenomenon of resonance. Resonant oscillations are forced oscillations (except for internal resonance) occurring for some specific relationship between the frequency of excitation and the natural frequencies of the system. Physically, resonances are manifested by large amplitudes of oscillation of the system when only a relatively small excitation force is applied to the system. With large amplitudes of vibration that occur in a structure at resonance, two major problems are immediately apparent. The first is that large strains can occur in the structure which in turn cause large stresses, possibly exceeding the yield stress, the ultimate stress, or even the rupture stress. The second problem is that of fatigue. Both can lead to catastrophic failure.

Today, structural vibration problems present a major hazard and design limitation for a wide range of engineering products. First, there are a number of structures, from turbine blades and suspension bridges to proposed large flexible spacecraft and space stations, for which structural integrity is of paramount concern, and for which a thorough and precise knowledge of the dynamic characteristics is essential. Then, there is an even wider set of components or assemblies for which vibration is directly related to performance, either by

causing temporary or permanent malfunction during excessive motion, or by creating disturbance or discomfort, including that of noise. For all of these examples, it is important that the vibration levels encountered in service or operation be anticipated and brought under satisfactory control. But to anticipate and bring vibration under control requires knowledge of the mechanisms that produce the resonance (i.e., large amplitude vibration), and it is to the acquisition of this knowledge that this dissertation is directed.

1.2 Parametric Vibration

Forces that can cause vibration in mechanical systems are often classified as either external or parametric, or in cases where both act simultaneously, as combined external and parametric. Parametric vibration is oscillatory motion that occurs in a system that is caused by time-dependent variation of system parameters such as inertia, damping, or stiffness. The time dependence is usually periodic and explicit, which implies an external energy source and hence the possibility of unstable behavior. These systems are typically modeled by homogeneous differential equations with rapidly varying coefficients. This is in contrast to externally excited systems which are modeled by inhomogeneous differential equations with constant coefficients.

In one sense, a single-degree-of-freedom system with a nonlinear restoring force appears to have a time-dependent stiffness because the stiffness is a function of the displacement and the displacement is a

function of time. However, this relationship is implicit and therefore is not classified as parametric.

A uniform rod can exhibit three basic types of free vibration: axial (longitudinal), transverse (lateral), and torsional. Our present discussion will focus on the axial and transverse vibrations. If pulsating transverse forces are applied to the rod, they will induce transverse vibrations in the rod. Likewise, if pulsating axial forces are applied to the rod, they will induce axial vibrations in the rod. These two examples are classified as external vibration because the governing partial differential equation has a time modulation which, when discretized, takes the form of

$$[m]\{\ddot{q}\} + [c]\{\dot{q}\} + [k]\{q\} = \{F(t)\}, \quad (1.1)$$

where the coefficient matrices are constant. In both of these cases, if the frequency of excitation is near a natural frequency of the rod (in their respective directions), a very large response will occur, and it will be in the direction of the excitation force (i.e., collinear).

Now consider the case of an axial pulsating force applied to the rod, and suppose a disturbance in the transverse direction is given to the rod. The mathematical model of a beam that includes a transverse displacement (e.g., Bolotin [1964]) is described by an equation that can be reduced to a Mathieu type

$$\ddot{u}_n(t) + \omega_n^2[1 - 2\epsilon\cos(\Omega t)]u_n(t) = 0, \quad (1.2)$$

when the pulsating axial force is described by

$$p(t) = p_0 + p_1 \cos \Omega t .$$

Because this equation has an explicit time-dependent coefficient in the displacement term, it falls into the class of parametrically excited systems governed by

$$[m(t)]\{\ddot{q}\} + [c(t)]\{\dot{q}\} + [k(t)]\{q\} = 0 . \quad (1.3)$$

If certain instability criteria are satisfied, a small disturbance in the transverse direction will grow, even though the excitation force is in the axial direction. Since the resulting motion is quite large compared to the excitation, it is indeed a resonance, but not in the conventional sense because the motion is orthogonal to the excitation, and it occurs at an excitation frequency that is typically twice a system resonance. Such a state is called a parametric resonance, a parametric instability, or a parametric vibration. The terms are synonymous because typically a parametric vibration is either (a) excited and produces a significant response, or (b) is not excited at all. This is in sharp contrast to a conventional external resonance in which the Frequency Response Function (FRF) gradually increases prior to the resonant frequency and then decreases after it. This contrast with externally excited systems arises because a parametric vibration (i.e., a sustained transverse vibration caused solely by an axial force in our example) can be excited only for certain combinations of the system parameters. In general, if a pulsating force causes a parametric

vibration, it will be a large amplitude response for reasons that will be seen later. Consequently, in this dissertation, the term parametric resonance will be used to denote a state of parametric vibration. The term resonance here is used in a broader sense than the conventional one for a linear externally excited system in which case a system resonant frequency and the excitation frequency coincide. We therefore begin with a formal definition of resonance.

1.2.1 Resonance

The term resonance is typically used to describe the state of a system that exhibits a large response when excited by a relatively small force. This happens in a linear system when the excitation frequency is near a natural frequency of the system. In linear externally excited systems, only damping can reduce the amplitude of vibration at resonance. In the limiting case of zero damping, the response amplitude is infinite. This behavior is seen in the Frequency Response Function (FRF) shown in Figure 1.1, which characterizes linear equations of the form given by (1.1) for selected values of the damping coefficient. Actually, linear mathematical models are only idealizations because all real structures have some degree of nonlinear behavior. In the following discussion, we define primary and secondary resonances in both external and parametric systems.

Consider the undamped Duffing oscillator subject to an external harmonic excitation given by

$$\ddot{u} + \omega^2 u + \epsilon \alpha u^3 = f \cos \Omega t, \quad (1.4)$$

where ω , α , and f are constants, and ϵ is a small dimensionless parameter. This is an inhomogeneous equation with constant coefficients. If we perform a straightforward expansion (SFE) of the response by assuming a form of the solution as

$$u(t;\epsilon) = u_0(t) + \epsilon u_1(t) + \epsilon^2 u_2(t) + \dots \quad (1.5)$$

and substitute into (1.4), we find at order ϵ^0

$$\ddot{u}_0 + \omega^2 u_0 = f \cos \Omega t, \quad (1.6)$$

and at order ϵ^1

$$\ddot{u}_1 + \omega^2 u_1 = -\alpha u_0^3. \quad (1.7)$$

The solution to (1.6) is

$$u_0 = a \cos(\omega t + \beta) + \Lambda \cos \Omega t, \quad (1.8)$$

where

$$\Lambda = \frac{f}{(\omega - \Omega)(\omega + \Omega)},$$

and a and β are constants. Here we see that a small divisor exists when $\Omega \approx \omega$, and causes an infinite response when $\Omega = \omega$. Since this is the first (and most common) resonance that occurs, it is called a primary resonance. It is also the most dangerous resonance associated

with externally excited systems because it has the largest response for a given excitation level.

At the next order, we solve for u_1 and require that $\Omega \neq \omega$. Any particular solution for u_1 will have the form

$$\begin{aligned}
 u_1 = & -\frac{3\alpha a t}{4} \left(\frac{a^2}{2} + \Lambda^2 \right) \sin(\omega t + \beta) \\
 & + \frac{\alpha \Lambda^3}{4(3\Omega - \omega)(3\Omega + \omega)} \cos(3\Omega t) + \frac{3\alpha a^2 \Lambda}{4(\Omega - 3\omega)(\Omega - \omega)} \cos[(\Omega - 2\omega)t + 2\beta] \\
 & + \text{other terms that are not secular or do not contain} \quad (1.9) \\
 & \text{small divisors.}
 \end{aligned}$$

We see at this order that new small divisor terms appear when $\Omega \approx \omega/3$ or $\Omega \approx 3\omega$. Since these small divisor terms produce resonances at the next order, they are called secondary resonances. If $\Omega \approx \omega/3$, a resonant response occurs at frequency ω , and since the resonance is at a higher frequency than the excitation, it is called a superharmonic resonance. Likewise, if $\Omega \approx 3\omega$, a resonant response occurs at frequency ω , and since it is at a lower frequency, it is called a subharmonic resonance. If the nonlinear cubic term $\epsilon \alpha u^3$ were replaced by a quadratic term $\epsilon \delta u^2$, these secondary resonances would occur at frequencies $\Omega \approx \omega/2$ and $\Omega \approx 2\omega$.

In addition to these, there are subsuperharmonic and supersubharmonic resonances when appropriate nonlinear terms are present.

Next we consider a parametrically excited system governed by the linear Mathieu equation

$$\ddot{u} + \omega^2 u + \epsilon g u \cos \Omega t = 0. \quad (1.10)$$

Again, assuming a SFE, we obtain the reduced equations

$$\varepsilon^0: \ddot{u}_0 + \omega^2 u_0 = 0, \quad (1.11)$$

$$\varepsilon^1: \ddot{u}_1 + \omega^2 u_1 = -g u_0 \cos \Omega t, \quad (1.12)$$

$$\varepsilon^2: \ddot{u}_2 + \omega^2 u_2 = -g u_1 \cos \Omega t. \quad (1.13)$$

The solutions for the first two equations are

$$u_0 = a \cos(\omega t + \beta), \quad (1.14)$$

$$u_1 = \frac{g a}{2\Omega(\Omega+2\omega)} \cos[(\Omega + \omega)t + \beta] \\ + \frac{g a}{2\Omega(\Omega-2\omega)} \cos[(\Omega - \omega)t + \beta]. \quad (1.15)$$

When $\Omega \approx 2\omega$, one of the particular solutions for u_1 has a small divisor, and hence produces a large response. Since this is the first resonance, it is called a primary or a first-order parametric resonance; in this dissertation we will call it a principal parametric resonance. We also have a small divisor when $\Omega \approx 0$, but this corresponds to a static load that would alter the natural frequency of the system.

If Ω is far away from 0 or 2ω , we can proceed with the SFE to the next order, and obtain the particular solution for u_2 which has the form

$$u_2 = \frac{-g^2 a t}{4\omega(\Omega+2\omega)(\Omega-2\omega)} \sin(\omega t + \beta) \\ + \frac{g^2 a}{16\Omega^2(\Omega+\omega)(\Omega+2\omega)} \cos[(2\Omega + \omega)t + \beta] \\ + \frac{g^2 a}{16\Omega^2(\Omega-\omega)(\Omega-2\omega)} \cos[(2\Omega - \omega)t + \beta]. \quad (1.16)$$

We note that when $\Omega \approx \omega$, a new resonance (small divisor coefficient) appears. Since this resonance occurs at the next order, it is called a secondary or a second-order resonance; in this dissertation we will call it a fundamental parametric resonance. If this analysis were continued, we would conclude that parametric resonances occur when $\Omega \approx 0, \omega, 2\omega, 3\omega, \dots$.

In the preceding discussion, we used the terms natural frequency and resonant frequency. Although these terms are often used in the literature interchangeably, they are not exactly the same. The terms natural frequency and linear natural frequency are synonymous; they arise by definition from normalizing the equation of motion

$$m\ddot{x} + c\dot{x} + kx = F \cos\Omega t \quad (1.17)$$

to the mass. The resulting coefficient of the displacement is the square of the natural frequency

$$\omega_0^2 = \frac{k}{m} . \quad (1.18)$$

Since it depends only on coefficients of linear terms, it is by definition the linear natural frequency. A nonzero subscript is used to indicate the natural frequency of a higher mode. The natural frequency is a defined quantity and corresponds to a unique point on the FRF-- where the phase of the excitation force leads the displacement response by 90° (e.g., see Figure 1.1(a)). If the phase could be measured, then we could measure the natural frequency, but this is not customarily done.

The resonant frequency ω_r corresponds to the peak of the FRF and is related to the natural frequency by

$$\omega_r = \sqrt{1 - 2\zeta^2} \omega_0, \quad (1.19)$$

where

$$\zeta = \frac{c}{2m}. \quad (1.20)$$

In the absence of damping, ω_r reduces to the natural frequency.

Whenever a forced response is used to determine the "natural frequencies", it is the resonant frequencies that are estimated--not the natural frequencies. If there are any nonlinearities they may also affect the measurement.

The damped natural frequency ω_d corresponds to the frequency of the homogeneous solution of the differential equation and is related to the natural frequency by

$$\omega_d = \sqrt{1 - \zeta^2} \omega_0. \quad (1.21)$$

Whenever a free response is used to determine the "natural frequencies", it is the damped natural frequencies that are estimated. Again, if there are any nonlinearities present, they may also affect the measurement.

In practice, however, the three frequencies are close to each other when the damping factor ζ is small, which is usually the case in metallic structures. Often the difference is less than the frequency resolution of the analyzer, and other problems associated with measuring

accurately the natural frequencies of a system--such as nonlinearity--are always present.

1.2.2 Examples and Causes of Parametric Vibration

Equations of the Mathieu type

$$\ddot{u} + 2\mu\dot{u} + (\omega_0^2 + g \cos\omega t)u = 0 \quad (1.22)$$

model many physical systems, the most common are probably beams or rods with dynamic axial loads and the pendulum with a moving support. There are many structures that are modeled by beams and cables with time varying end loads. Some typical dynamic systems subject to parametric excitations are shown in Figure 1.2.

To grasp the physical significance of a parametric excitation in non-pendulum type systems and how the parametric excitation is distinguished from an external excitation, consider the center section of a string undergoing transverse vibration and simultaneously subjected to a pulsating tension, as shown in Figure 1.2(h). A free body diagram is shown in Figure 1.3. If the time dependent part of the tension has a frequency twice the natural frequency of the first mode, the transverse component of the tension will act like an external force on the system driving it at resonance.

Another way to visualize parametric vibration is to observe the motion of the roller support at the end of a simply-supported beam undergoing large amplitude fundamental mode vibration (see Figure 1.2(d)). When the midpoint of the beam is in the upper-most position,

the roller support has moved in. As the beam moves down through the static equilibrium position to its lowest position, the end moves out and then back in to occupy its original position, thus completing one cycle of motion. As the beam completes the other half of its cycle, the roller support at the end of the beam completes another full cycle. The roller supported end is observed to complete two full cycles of motion axially while the beam executes one full cycle transversely.

Consequently, a periodic force applied to the beam in the axial direction at the roller supported end of the beam tends to excite transverse vibration in the beam at one-half the frequency of excitation. If the excitation frequency happens to be twice a natural frequency of the beam, then a principal parametric resonance will occur if the critical value is exceeded.

Parametric vibrations frequently occur because of pulsations to existing static loads. These loads can be axial forces, torques applied to shafts, inplane forces and moments applied to plates and shells, or the pressure in fluid flow in and around tubes. Fluid flowing past a body exerts forces in the form of dynamic pressure. When the fluid is moving along a body, as in internal and external pipe flow, parametric resonances can be excited if the average pressure acting on the body has pulsating components at the right frequency. An axial force acting on a beam can be applied indirectly through oscillating magnetic fields or oscillating friction forces from structure supports. Rocket tanks and their liquid propellant and flexible missiles under pulsating axial thrusts can experience parametric resonances, causing severe sloshing in

the former and transverse bending in the latter. Helicopters are particularly susceptible to parametric resonances; helicopter blades in forward flight can experience a free stream that varies periodically with time and the longitudinal component of flow alternates once during one rotation. Torque transmitted through the long shafts connecting the tail rotor to the power plant often operate at hypercritical angular velocities, and any pulsations in the torque can excite parametric resonances. Related to the rotor dynamics of helicopters are the vibration problems of large wind turbines, which have some unique problems. The rotor blades are subjected to a periodic gravity force which appears as a parametric excitation in the governing equations, and the combined aerodynamic loads can cause coupled flap-lag-torsional vibrations. Slender rods in structures that carry tensile and compressive loads can have a time varying component caused by a variety of sources such as a rotating machine or an elastic fluctuation (geometrical variation) of the structure. An airplane wing is an example of this type of behavior. The flapping motion of the wing puts time varying compressive and tensile loads on the internal substructure which can induce subharmonic or parametric resonances. In-plane forces and moments applied to panels are similar to axial loads on bars and can have both static and dynamic components, possibly leading to parametric resonances. The resulting panel motion is transverse (out of plane) to the plane of the applied moment. Girder plates on bridges have experienced fatigue cracks as a result of parametrically induced vibration.

Thus we see that parametric vibration is possible in a wide variety of structural components, and hence the engineer needs to be aware of when it may present a problem.

1.2.3 Paradoxical Phenomena

There are many interesting and unique phenomena associated with parametric resonances, a very interesting one being the inverted pendulum (e.g., Ness [1967]). If the hinge support of the pendulum is given a harmonic motion in the vertical direction with certain values of amplitude and frequency of oscillation, the pendulum's inverted equilibrium position can be rendered stable. The ensuing motion consists of small amplitude pendulum type oscillations about the "upside-down" position. This type of behavior--where a statically unstable equilibrium position is rendered dynamically stable--is not uncommon; we are all familiar with the spinning top (gyroscope). The inverted pendulum is of interest here because it derives its dynamic stability specifically from a parametric excitation.

There is an interesting paradox associated with the inverted pendulum. Consider a bar type pendulum undergoing base motion such that the pendulum is inverted and undergoing small amplitude pendulum type oscillation. If a washer (with a central hole that is slightly larger than the diameter of the bar) is placed on the bar, it will not fall; it will remain on the bar almost at rest, as if it were weightless! The nonlinearly coupled differential equations describing this system have

been solved (e.g., see Chelomey [1985]) by the method of averaging, and they predict the stable equilibrium washer points on the bar.

There is another stabilizing effect caused by parametric excitations. Consider a simply supported beam subjected to a static compressive axial load that exceeds the Euler buckling load. If a periodic load with the appropriate frequency and amplitude is added to the static load (i.e., $p(t) = p_0 + p_1 \cos \omega t$), the beam that was previously buckled will straighten; thus a statically unstable equilibrium position is again rendered stable by a parametric excitation. The critical load of a beam can be doubled by the addition of a parametric excitation, as pointed out by Stephenson (1908).

Another paradox is that of a heavy ball in a vibrating fluid. Consider a cylindrical fluid-filled tube that is attached to a shaker table. When a solid ball (made of a material whose specific gravity exceeds the specific gravity of the fluid) is placed into the cylinder, the ball will fall and sink to the bottom. If the cylinder is subjected to vertical sinusoidal vibration, the ball will rise in the cylinder. By increasing the amplitude of vibration, an air cavity containing a small quantity of fluid is formed under the ball with the remaining fluid above the ball. One can also observe the opposite phenomenon: a ball which is lighter than the fluid can sink under vibration. Chelomey [1985] has provided photographs of these paradoxes.

1.2.4 Parametric Instability--The Nature of a Parametric Resonance

The nature of a parametric resonance is so distinctive that it is often called a parametric instability. Therefore, as part of an introduction to parametric resonance, we will discuss stability in dynamic systems. The term unstable, as applied to dynamic systems, conveys two meanings: (a) when a response is unstable we imply that it cannot be realized in real time either in numerical or analogue simulation, or in a physical model such as in a laboratory experiment, or (b) when a response is unstable we say that it is divergent and grows without bound. Both are associated with exponentially growing terms and are related to a solution that is not realizable after a long time.

Any trivial or periodic nontrivial solution of an equation that models a dynamic system is classified as either asymptotically stable, marginally stable, or unstable. Often, the stability is determined by examining its behavior in the phase plane. Unforced systems will decay to stable foci and appear as spirals winding into the attracting focus. Nonlinear systems may have more than one focus, in which case the initial conditions determine which stable focus will attract the response. A saddle point is another type of equilibrium point that can attract the response--but only if the system is exactly on one of the two inbound trajectories. In this case it would take an infinite amount of time to reach the equilibrium point, and hence is only an idealization. Since it also possesses two outbound separatrices (trajectories), any system response that approaches a saddle point will eventually be repelled. A cusp is a rare type of equilibrium position

that can also attract the response with its only inbound separatrix, but like the saddle point it cannot keep the response because it possesses an outbound trajectory.

When a system is forced harmonically, steady-state vibration (i.e., constant amplitude) may develop, depending on the type of excitation and on the initial conditions. In some cases, the foci give rise to limit cycles that initially encircle the foci, but as the excitation is increased, the response may bifurcate in such a way that it may encircle two or more equilibrium positions. Encircling only two equilibrium positions occurs when one of the two points is actually a repeated root, and can occur when a focus and saddle point merge.

Limit cycles appear to be unstable because small amplitude motion is observed to grow by spiraling outward from a focus, but large amplitude motion is observed to decay by spiraling inward. They are therefore stable. Some systems may possess more than one limit cycle. Hence basing a stability analysis on only the local behavior may give erroneous information about the global behavior.

Systems that neither grow without bound nor decay to zero are considered marginally stable. An undamped linear oscillator is an example of this.

We now consider stability in a linear parametric oscillator of the Mathieu type given by (1.22). For small levels of excitation, a parametric resonance is not excited. Disturbances to the system decay to the trivial solution; consequently it is asymptotically stable. As we increase the excitation, we approach the critical value and the decay

rate diminishes. If we perform an experiment and slowly increase the excitation level, the effective decay rate will decrease; disturbances would still decay, but they would require more cycles to do so. As we increase g further, we reach a level of excitation where the effective decay rate is zero; the steady-state response to a disturbance is a periodic vibration that neither grows nor decays. This is the critical value and represents a boundary between decaying responses and exponentially growing responses. Hence, the system is marginally stable. Any increase in the excitation will cause the amplitude to grow exponentially. This boundary is shown in Figure 1.4(a). If we plot the value of the critical amplitude versus the frequency of excitation, the results would appear as shown in Figure 1.5, which is often called the Strutt diagram. When damping is present, it increases the critical value and hence diminishes the unstable regions, lifting the transition curves off the frequency axis, as shown in Figure 1.6.

Herein lies a distinctive feature of a parametric resonance--the presence of damping alone may not affect the unbounded response. For excitation levels below the critical value, the system response to disturbances decays; for excitation levels above the critical value, the system response to disturbances grows. The response is either trivial or infinite, depending on the damping, amplitude, and frequency of excitation. This behavior is in sharp contrast to a resonance in an externally excited system where damping transforms an infinite response into a finite response and always reduces the response amplitude (e.g., see Figure 1.1).

However, we always observe parametric resonances with finite amplitudes--not infinite amplitudes as predicted by the Mathieu equation (1.22). Since damping alone cannot account for this behavior, we must call upon the discarded nonlinear terms in the original equation. Just as nonlinearity bends the backbone curve in an external resonance, it bends the parametric stability boundary curve, which in turn limits the unbounded growth. This is illustrated in Figure 1.4(b) which shows the response amplitude versus the amplitude of excitation at a given frequency. If the frequency is changed slightly, the critical point will shift as before, but more importantly, the upper portion of the curve may shift left relative to the critical point causing an overhang to occur, as shown in Figure 1.4(c). With this multi-valued response curve, we now have the possibility of exciting a parametric resonance at a level of excitation that is below the linear critical value. This behavior is called a sub-critical instability and typically occurs when the excitation frequency is detuned in the direction of the effective nonlinearity, e.g., a lower frequency for a softening nonlinearity.

There are other distinctive features of a parametric resonance that should be noted. We saw in Figure 1.4 that increasing the level of excitation does not (a) permit a resonance until a subcritical value is reached, or (b) cause a resonance until the critical value is reached. Once the critical value is reached, very small increases in the amplitude of the excitation will cause very large changes in the response because (a) the gradient is very large as shown in Figure 1.4(b) just past the critical value, or (b) the system will jump up to

the steady-state value as shown in Figure 1.4(c). The jump is not instantaneous or sudden in time--it grows with each cycle of motion.

We have summarized the essential nature of a parametric resonance by comparing it to an external resonance. Because the linear Mathieu oscillator has behavior similar to an unstable focus (i.e., a repeller), once the critical value of excitation has been exceeded, the parametric resonance is often called a parametric instability. Stability information, such as that presented in a Strutt diagram, is determined by examining the behavior of the linearized equation, and hence represents the boundary at which the trivial solution loses its asymptotic stability. When nonlinear terms are present, a subcritical instability may exist. This phenomenon actually enlarges the unstable regions by the amount of overhang. The nonlinear terms also limit the infinite response to a finite amplitude response. Damping, on the other hand, diminishes the unstable regions, but does little to affect the steady-state amplitude. Damping may enlarge the unstable regions in multiple-degree-of-freedom (MDOF) systems where combination resonances occur.

Determining these regions of instability is a major engineering problem, but equally important is determining the amplitude of vibration for the nonlinear system. If these regions cannot be avoided (e.g., in rotating machines and rotating shafts that operate at hypercritical angular velocities and hence have critical regions that the system must pass through) then the next engineering problem is to determine the transient response for a "pass through".

Although the basic theory of parametric resonance is applied in this dissertation to elastic structural systems, the theory can be applied to other real systems in which periodic variation of parameters occurs. Examples include parametric amplifiers, electromechanical systems, cyclotrons, and propagation of waves in a periodic continuous medium.

1.2.5 Internal (Autoparametric) Resonance

Internal resonance is a phenomenon that is unique to nonlinear MDOF systems and can exist between two or more modes depending on the strength of the nonlinear coupling. A system is said to possess internal resonance if $\sum c_i \omega_i = 0$, where the c_i are positive or negative integers. For example, if a system possesses quadratic nonlinear coupling, then two modes having natural frequencies ω_i and ω_j are said to be internally resonant if $\omega_i \approx 2\omega_j$. Three modes can be internally resonant if $\omega_i \approx \omega_j + \omega_k$. When higher-order nonlinearities (e.g., cubic and quartic) are present, the possible combinations of resonant frequencies increase, thus broadening the possibility of internal resonance. The significant feature of internal resonance is that it funnels energy from an excited mode through the nonlinear coupling terms into another mode that is not directly excited, causing multi-frequency oscillations in multi-degree-of-freedom systems. These subharmonic or superharmonic tones can be more than 10 times higher in amplitude than the directly excited mode, and hence cannot be ignored.

Some examples of systems that can be internally resonant are shown in Figure 1.7. The elastic pendulum with a 2:1 internal resonance is quite popular and easily demonstrates this phenomenon. A long flexible beam that is horizontally positioned and parametrically excited (e.g., see Figure 1.7(i)) can have two modes with a frequency ratio of 2:1. If, for example, the fourth mode has a frequency $\omega_4 \approx 2\omega_3$ and is parametrically excited with a frequency $\Omega \approx 2\omega_4$, the fourth mode will initially respond. If the amplitude of excitation is increased above a critical threshold level, the third mode will be excited and respond with a larger amplitude than the fourth mode, and at a frequency $\omega_3 \approx \omega_4/2 \approx \Omega/4$.

The term autoparametric resonance appears in the literature, and although it is synonymous with internal resonance, it is actually the consequence of an internal resonance. If we examine a two-degree-of-freedom system that is internally resonant and simultaneously possesses quadratic nonlinearities, we may find coupled equations of the form

$$\begin{aligned} \ddot{u}_1 + \omega_1^2 u_1 + \delta_1 u_1 u_2 + g u_1 \cos(\Omega t) &= 0, \\ \ddot{u}_2 + \omega_2^2 u_2 + \delta_2 u_2^2 + h u_2 \cos(\Omega t + \tau) &= 0, \end{aligned} \tag{1.23}$$

that describe the motion. The system is made internally resonant by adjusting ω_2 to be approximately $2\omega_1$. If we excite the second mode parametrically by setting $g = 0$ and $\Omega \approx 2\omega_2$, the second mode will respond and achieve a steady-state amplitude. However, the sinusoidal response of the second mode, given by

$$u_2 = a_2 \cos(\omega_2 t + \beta_2), \quad (1.24)$$

is a fast-varying function and appears as a coefficient to u_1 in (1.23). It therefore becomes a "parametric" coefficient for the first mode, and once the critical amplitude of u_2 is exceeded, it will parametrically excite u_1 . In this case, the parametric excitation to the first mode comes not from an external oscillator, but from the structure itself-- specifically another resonating mode. Because this happens, the parametric resonance of the first mode is called an autoparametric resonance. This interaction can occur in externally excited systems also. In both parametrically and externally excited systems, internal or autoparametric resonance is only possible because of the presence of the nonlinear coupling term.

1.2.6 Combination Resonance

Combination resonance is another example of a unique phenomenon that can occur only in a nonlinear MDOF structure; it has no counterpart in linear theory. A combination resonance can occur if two or more modes are appropriately coupled and the excitation frequency is nearly equal to

$$\Omega = a_i \omega_i + b_j \omega_j + c_k \omega_k + \dots, \quad (1.25)$$

where the a_i , b_j , and c_k are positive or negative rational numbers. For example, an excitation frequency that is the sum of the first bending mode and the first torsional mode of a slender beam would be given by

$$\Omega \approx \omega_b + \omega_t , \quad (1.26)$$

and the ensuing motion to a parametric excitation would consist of a combined response of both modes--even though neither was directly excited. When a flexible beam is clamped in an upright position to a shaker head oscillating in a vertical direction, transverse (horizontal) resonant vibrations are parametrically excited when the frequency is nearly twice any of the linear natural frequencies. When the frequency of excitation is close to the sum or difference of two modes, a combination resonance occurs, and the resulting motion consists of a superposition of the two modes, as if each was individually excited. This and other models in which combination resonances can occur are shown in Figure 1.8.

Another principal engineering problem directly related to parametrically excited systems is (a) to predict which combination resonances are possible, and (b) to determine the boundaries of those unstable regions. A typical combination instability diagram for a particular system is shown in Figure 1.9. Some of the methods used to determine these instability regions are discussed in the literature review.

1.3 Problem Formulation and Solution

Mathematical formulations of many physical problems usually consist of differential equations that are nonlinear. Because the governing differential equations are nonlinear, the structure is often referred to

as being nonlinear. Strictly speaking, structures are neither linear nor nonlinear. The adjectives linear and nonlinear apply to the behavior governed by the differential equations which are used to model the physical behavior of the structure. The nonlinearity may be due to material properties, deflection amplitude, asymmetrical geometry of the structure, the boundary conditions, or any combination of these and other sources. In some cases a nonlinear differential equation can be replaced by a related linear differential equation that approximates the actual nonlinear equation closely enough to give useful results. However, such linearization is not always possible or desirable; when it is not, the original nonlinear equation must be used.

A linear equation used to model a structure is in general the least precise model because it can always be improved by including nonlinear terms to do three things: (a) to increase the accuracy of the predicted response, (b) to extend the range of useable solutions (e.g., for larger displacements), and (c) to explain or predict new phenomena that have no counterparts in linear theory. So, the question of whether we can use a linear model depends on the nature of the information being sought. The engineer is thus faced with the question of how to anticipate those cases when a linear model -- and for the purposes of this dissertation, a linear model with constant coefficients -- is inadequate in its predictions. For example, by neglecting a parametric term in the mathematical model of a parametrically excited system, a parametric resonance cannot be predicted, and consequently is not considered in the design. In this case, the analysis would predict a stable trivial

response when the system is excited parametrically at twice the natural frequency of the system, even if the excitation amplitude were quite large. If the parametric term were included, then the analysis could predict exponential growth of a parametric resonance. The first case predicts a trivial response, and the second case predicts an unbounded response. Both are in error, but at least the latter predicts the parametric resonance.

By including both the parametric terms and appropriate nonlinear terms in the mathematical model, finite amplitudes of the resonance are predicted, and this behavior is consistent with observations. This happens because, as amplitudes get large, nonlinearities (that were ignored to linearize the mathematical model) come into play and essentially "put the clamps on" the system response, causing it to attain a finite steady-state value. Consequently, the nonlinear terms are most significant at resonance and should not be ignored!

In summary, we have seen compelling reasons why nonlinear terms should be retained. Some phenomena are unique to nonlinear systems, and have no counterpart in linear theory. Hence, we cannot account for the effect of nonlinearity simply as a deviation from linear behavior. It is precisely the nonlinear coupling between modes that allows for the presence of internal and combination resonances because these resonances cannot exist in linear systems. Also, there is the problem of subcritical instability which also owes its unique existence to nonlinear terms. If the nonlinear terms were neglected, then we could not account for this phenomenon either.

1.3.1 Mathematical Formulation

Precisely deriving the equations of motion to a desired level of accuracy is a matter of considerable complexity and difficulty. Symbolic codes such as FORMAC and MACSYMA have been developed to assist in such formidable tasks. For example, to use Lagrange's method, we express the kinetic and potential energies and then obtain the governing equations of motion with the aid of the computer. It is not the purpose of this dissertation to investigate the "art" of mathematical modeling of elastic structures.

When flexible structures are modeled as continuous systems, the results are nonlinear partial differential equations in one to three spatial dimensions and time. Typically, these are reduced to a finite set of nonlinear ordinary differential equations in time by making an expansion of the spatial variable and truncating the series at some point. Galerkin's procedure is a popular choice for doing this. When a continuous structure is discretized from the start (e.g., as a lumped mass system), the results are a finite set of ordinary differential equations. At this point, the analyst determines which terms are significant to his analysis and discards the "insignificant" terms, starting typically with the highest order nonlinear ones. In many cases all of the nonlinear terms are eliminated so a closed-form solution can be sought. Thus, the final mathematical model is usually an idealized representation that, as Barr [1980] points out, may be "usually rather far removed from being in any way a precise representation of the

structure, so much so that it is perhaps a pleasant surprise when theoretical predictions show any reasonable agreement with tests conducted on laboratory models. It is much easier to be content with qualitative agreement or to show the physical existence of some nonlinear phenomenon."

Using only these equations of motion and integrating them on the analogue and digital computers or deriving approximate solutions for them seems to be a popular way of "avoiding" the difficulties of relating back to the real world. It eliminates the many problems that are routinely encountered in any experimental work, and avoids the embarrassment of trying to explain why the theory and the experiment do not correlate. However, the experimental work is essential to our understanding of such phenomena, and therefore should not be overlooked or underestimated.

1.3.2 Solution of the Equations

The general theory and methods of dealing with linear equations constitute a highly developed branch of mathematics, whereas very little (by comparison) of a general nature is known about nonlinear equations. With few exceptions, closed form solutions do not exist for nonlinear equations. Consequently, the study of nonlinear equations is confined to a variety of very special cases, and the method of solution usually involves one or more of a limited number of different methods of approximation. These perturbation solutions are generally valid for only a limited range of parameter variation, usually one or more of the

parameters must be kept small, and the motion must be confined to small but finite amplitudes about a given state. For motions that exceed these constraints, one must seek other approximate solutions if they can be found, or resort to simulation on the analogue or digital computer. For the latter, it is usually a "hunt and peck" procedure that is often costly and time consuming. Every parameter in the governing nonlinear equation constitutes another permutation factor, which makes the total number of possible combinations of system parameters to consider many times larger. For this reason, and also to ascertain if certain parameters are indeed small, the governing differential equations are usually put into nondimensional form. Then, fixed values are assigned to the system's parameters while one is varied; this way we can gauge its effect on the system's response and characterize the system's behavior.

In many cases the parametric and nonlinear terms are relatively small, and any of the "small parameter" methods ranging from the straightforward expansion procedure to the more sophisticated averaging methods and multiple time expansions can be considered for obtaining an approximate solution. The harmonic balance method is quite popular and is fairly easy to use, but we must know a priori the nature of the solution to effectively use this method, otherwise the solution may be seemingly correct, but is actually incorrect. The method of multiple time scales has been used effectively to obtain approximate solutions for nonlinear equations, and will be used in this dissertation.

The end result of applying a perturbation analysis to the original differential equation is a set of reduced variational equations which

are hopefully more tractable. These reduced equations, which govern the modulation of the amplitudes and phases, are typically nonlinear and may also have variable coefficients, and hence cannot be solved explicitly. However, they lend themselves to the solution of the fixed points, which correspond to a constant amplitude steady-state vibration in the original equations. Other periodic solutions can be obtained by integrating these reduced equations directly.

Integrating the reduced equations and even the original equations on the digital or analogue computer is quite popular, especially the reduced equations since they are simpler and consequently faster to integrate. However, the digital integration of nonlinear coupled (and uncoupled) equations is not always straightforward. It may be difficult to determine the accuracy of the integrated solution. Stability of numerical codes is especially important in integrations of parametrically excited systems because an exponential growth of an algorithm instability may be difficult to distinguish from an exponential growth of a genuine parametric instability.

Analogue computer simulation is neither susceptible to digital code stability nor accumulation of truncation errors and hence lends itself well to the study of nonlinear problems. Currently, its two main drawbacks are its limited accuracy--which is four digits at best--and its limited dynamic range. Consequently, we must localize the problem to be studied and then scale it accordingly. This makes it cumbersome to study the whole system at one time, because when a large amplitude vibration experiences a jump down to a small amplitude vibration, or

vice versa, the problem usually needs to be rescaled. However, the advantages far outweigh the drawbacks. We can lock onto a limit cycle and observe the real time solution on an oscilloscope. Once we latch onto a particular attractor, we can vary any one of the system parameters and observe the instantaneous effects in real time. The time can also be scaled to either speed up or slow down the response.

The analogue computer finds its major use in getting a "feel" for the problem and mapping out domains of attraction for all possible solutions. This is usually accomplished much more quickly than on the digital computer. Once all of the solutions have been found, any needed accuracy is quickly obtained on the digital computer. Another convenient use of the analogue computer is verifying the regions of parametric resonance.

The analogue computer has had an interesting history. When the digital computer made its debut three decades ago, scientists and engineers immediately recognized its tremendous potential, and the demand for faster and more powerful machines was second only to the demand for the computers themselves. As their speed and accuracy continued to increase, the digital computer quickly replaced the analogue computer, essentially making the analogue computer obsolete for computational purposes. The thrust to improve and modernize the analogue computer gradually dwindled to a trickle, such that today there are only a few manufacturers of analogue computers in the United States.

Recently, however, the picture has begun to change. The increased interest in nonlinear dynamics is, in part, responsible for the revival

of the analogue computer. In fact, some enterprising engineers have even developed software to emulate the analogue computer on the digital computer! With multiple solutions inherent in nonlinear systems, the analogue computer is proving itself to be an effective and efficient tool in the analysis and understanding of nonlinear systems.

1.4 Literature Review

In the review that follows, we consider single-degree-of-freedom (1DOF) systems, two-degree-of-freedom (2DOF) systems, and multi-degree-of-freedom (MDOF) systems that are parametrically excited in part or in whole. Random parametrically excited systems will not be included here unless the work also includes periodic parametric excitation. Works dealing with bifurcations and chaos in parametrically excited system were quite scarce by comparison to externally excited systems.

The occurrence of parametric resonance as described by the Mathieu equation was observed as early as 1831 when Faraday noted that surface waves in a fluid-filled vertically oscillating cylinder have one-half the frequency of the excitation. Meld (1859) was the first to perform experiments on a structural element; he excited a string longitudinally along the axis by attaching the free end to a tuning fork, and found for various combinations of the system parameters that transverse out-of-plane vibrations occurred at one-half the frequency of excitation. Strutt (1887) performed further experiments similar to Meld's, and provided a theoretical basis for these observations; the diagram

depicting the stable regions of the Mathieu equation sometimes bears his name.

Stephenson (1906) extended the work of Strutt and observed the possibility of exciting vibrations when the frequency of the applied axial excitation is a rational multiple of the fundamental frequency of the lateral vibration of the string, not just at twice the resonant frequencies previously observed.

Since these early days, many researchers have investigated different aspects of parametrically excited systems. McLaclan [1964] was the first to summarize the known work on Mathieu equations. Bolotin's [1964] extensive English translation presented the most complete summary of parametric phenomena. He investigated the parametric instability regions which were identified more than 100 years ago by the French mathematician Floquet [1883]. According to Floquet, a second-order differential equation with time-varying coefficients has two sets of harmonic solutions; these form the limit between stable and unstable solutions. One set of solutions has a basic frequency equal to the natural frequency (Period T) of the system, and the second set has solutions that have one-half the natural frequency of the system (Period $2T$).

Hsu [1963] summarized the work on parametric instability of MDOF systems. He found that in a system of coupled Mathieu equations, there can exist, in addition to the known unstable regions (Periods T and $2T$) a new set of unstable regions corresponding to "combination resonances." Valdeev [1963] also published a paper warning of combination resonances.

It was not until Evan-Iwanowski [1976] published his book that a comprehensive treatment of resonance in mechanical systems was compiled in one work. He devotes one chapter to principal parametric resonance and one chapter to principal parametric and combination resonance in structures. Ibrahim and Barr [1978] summarized the work on parametric systems in a series of five review articles on both linear and nonlinear systems, and Barr [1980] summarized some developments in parametric stability in nonlinear systems. Their work was followed by that of Nayfeh and Mook [1979] which provides a review of the literature in the field of nonlinear oscillations; their text presents the most comprehensive application of the method of multiple time scales to the solution of nonlinear equations. They devote one chapter to parametric resonances of linear and nonlinear systems. Although the text by Ibrahim [1985] deals with random parametric vibration, his first chapter has a general discussion on parametric vibration. The most recent text on nonlinear vibrations by Schmidt and Tondl [1986] considers parametric resonances in two chapters and devotes one chapter to autoparametric coupling. Since Nayfeh and Mook [1979] gives a comprehensive review of the literature up to 1978, the following literature review will concentrate on the literature published since 1978.

1.4.1 Single-Degree-of-Freedom Systems

Sato et al [1978] investigated the steady-state response of a parametrically excited, simply supported horizontal beam carrying a concentrated mass. They included the nonlinear terms arising from the

moderately large curvatures caused by gravitational loading, longitudinal inertia of the beam and concentrated mass, and rotatory inertia of the concentrated mass. They applied Galerkin's method and used the method of harmonic balance to solve the resulting equations, and they found that in addition to the parametric resonances, a fundamental parametric resonance also occurs because of the initial static deflection.

Zajaczkowski and Lipinski [1979] examined the vibrations and stability of parametrically excited linear systems using Bolotin's [1964] approach.

Hsieh [1980] investigated the influence the influence of damping on the stability of the Mathieu equation.

Holmes and Rand [1981] investigated the feasibility of modeling the Mathieu equation containing a cubic stiffness nonlinearity with two nonlinearly coupled oscillators, and Month and Rand [1982] investigated the bifurcation of 4:1 subharmonics in the same nonlinear Mathieu equation.

Hagedorn [1981] considered a nonlinear Mathieu equation containing quadratic and cubic nonlinearities as an example for applying Liapunov's stability criteria.

In two papers, Yano [1984a,b] considered parametric excitations in a self-excited system with dry friction governed by

$$\ddot{u} + (c_1 u^2 - c_2) \dot{u} + c_3 \operatorname{sgn} \dot{u} + u + \alpha u^3 + g u \cos \omega t = 0 .$$

This equation models the vibrations of a rotor with an asymmetric shaft rigidly supported by bearings and the vibrations of a pipe conveying a two-phase gas and liquid flow subjected to self-excitation caused by harmonically pulsating flow.

In a series of three papers, Yano [1984c, 1985, 1984d] investigated parametric excitation in self-excited systems governed by

$$\ddot{u} + (c_1 u^2 - c_2) \dot{u} + \delta u^2 + g u \cos 2\Omega t + \delta g u^3 \cos 2\Omega t = 0 .$$

He found subharmonic resonances of order 1/2 and 1/3 and superharmonic resonances of order two. In the neighborhood of these resonances, he found a beat phenomenon. He notes that the vibration phenomena of systems subjected to both self-excitation and parametric excitation are not clear, and are not fully known even in the case of a 1DOF system; moreover, he notes that studies on subharmonic vibrations due to a parametric excitation are as important as those due to an external harmonic force in nonlinear systems, but that they have not been made except by Tondl [1978].

Kotera and Yano [1985] investigated periodic solutions in the regions of fundamental and principal parametric resonances of

$$\ddot{u} + (c_1 u^2 - c_2) \dot{u} + u + \alpha u^3 + g u \cos \Omega t = 0,$$

and Yano, Kotera, and Hiramatsu [1986b] investigated principal parametric resonance using two approximate methods. The method of harmonic balance gave poor results but the method of averaging gave very good results.

Yano, Kotera, and Hiramatsu [1986a] investigated asymmetric parametric excitation in self-excited systems governed by

$$\ddot{u} + (c_1 u^2 - c_2) \dot{u} + u + \delta u^2 + \alpha u^3 + g u \cos \Omega t + \delta g u^2 \cos \Omega t + \alpha g u^3 \cos \Omega t = 0.$$

The results of the above eight papers by Yano et al can be briefly summarized as follows: (a) resonance phenomena are induced by the product $u^n \cos 2\Omega \tau$ where $n = 1, 2, 3, \dots$, (b) the mechanisms of the occurrence are evidently different from those of nonlinear forced vibration systems, (c) in self-excited van der Pol systems with only $u \cos 2\Omega \tau$ as the excitation, principal and fundamental resonances occur in the regions of frequencies corresponding to the unstable regions of principal and fundamental resonances in a linear Mathieu equation, and (d) subharmonic resonances of orders 1/2 and 1/3 with frequencies $\Omega/2$ and $\Omega/3$ respectively, and subsuperharmonic ones of order 2/3 besides orders of one and two occur in a self-excited system with a cubic excitation term $(u^3 \cos 2\Omega \tau)u$. An example of this type of problem is considered in Nayfeh and Mook [1979].

Gürgoze [1986] analyzed parametric vibrations of a restrained beam with an end mass under a displacement excitation at the other end. Using a one mode approximation and applying Galerkin's method, he reduced the governing partial differential equation to a Mathieu equation containing a cubic nonlinearity in the restoring force. He obtained an approximate solution for the case of principal parametric resonance.

HaQuang [1986] and HaQuang et al [1987] investigated the response of 1DOF and MDOF systems having quadratic and cubic nonlinearities in the restoring force to harmonic parametric excitation, to harmonic external excitation, and to combined harmonic parametric and external excitations. He found solutions characterized by period multiplying bifurcations and chaos.

Sueoka, et al [1986] investigated both analytically and experimentally the combined external and parametric harmonic resonance phenomena of a roller chain. The chain was stretched vertically and was regarded as a system with many degrees of freedom; the analysis also included stretching of the chain. They used the method of harmonic balance.

Eisinger and Merchant [1979a] investigated the response of a combined parametrically and externally excited, clamped beam carrying a lumped mass located at the center. The parametric excitation was fundamental (i.e., the frequency of excitation was near the system fundamental resonance) and was applied as a compressive load with static and dynamic components; the external excitation was transverse support motion at frequencies much lower than the fundamental resonance. In this work and another [1979b] they found a higher order phenomenon that they identified as secondary parametric amplification; its occurrence was characterized by a frequency of the parametric excitation of the order $2\omega_0/n$, where ω_0 is the undamped natural frequency and $n = 1, 2, 3, \dots$.

Mook et al [1979] investigated resonant interactions of harmonic axial and transverse loads.

Nayfeh [1984] investigated the interaction of principal parametric resonances and subharmonic resonances of order one-half in a 1DOF system with quadratic and cubic nonlinearities in the stiffness. He found that in some cases, neither the parametric nor the subharmonic resonance is excited; for other cases two stable solutions coexist. Under certain conditions, he showed that a parametric resonance can be quenched by the addition of a subharmonic excitation having the proper amplitude and phase, and vice versa.

Kojima, et al [1985] analyzed the nonlinear vibrations of a horizontal beam with an end mass subject to a periodic electromagnetic force acting on the mass; the governing equation has both external and parametric excitations. Using the harmonic balance method, they found second order superharmonic and one-half order subharmonic vibrations, as well as the expected harmonic response. Their theoretical results were complemented with experiments.

Bajaj [1987] investigated the bifurcations in a principal parametrically excited non-linear (van der Pol and Duffing) oscillator.

1.4.2 Multi-Degree-of-Freedom Systems

MDOF systems are by far the most interesting of the parametrically excited class of vibrations. Additionally, and more importantly, most real structures encountered in engineering practice are MDOF structures. Some examples are shown in Figure 1.7 and 1.8. MDOF

systems possess all of the features of 1DOF systems, but allow modal interactions through linear coupling terms which are not possible in 1DOF systems. MDOF systems can also have very interesting and complex behavior due to interaction of the various modes through the nonlinear coupling terms. They can also have repeated natural frequencies, which further complicate the response. Such a system was considered by Tezak et al [1982]. Fu and Nemat-Nasser [1977] observed the similarity between the "coincidence" problem in jet engines and combination resonance in the classical theory of parametric excitation.

Nayfeh [1983a] analyzed 2DOF systems subject to multifrequency parametric excitations. He considered the case of four simultaneous resonances: principal parametric resonances of the two modes, combination resonance of the sum type, and combination resonance of the difference type.

Nayfeh [1983b] investigated 2DOF systems with internal resonance and quadratic stiffness nonlinearities subject to a principal parametric excitation to the second mode. He found that the second mode became saturated, and under some conditions a sub-critical instability was present. He also analyzed [1983c] the response of MDOF systems with quadratic nonlinearities to a principal parametric resonance in the presence of combination internal resonances. He found under certain conditions that the excited mode becomes saturated and that multiple stable steady-state solutions exist. New results show that most of the saturated modes are unstable.

Nayfeh and Zavodney [1986] investigated the response of coupled 2DOF systems with quadratic stiffness nonlinearities to a combination parametric resonance using the method of multiple scales (see Chapter VI). They evaluated the effect of detuning the internal resonance and the parametric resonance. The results show that for certain ranges of the phase of the excitation to the second mode, the combination resonance can be quenched. Hard forcing to the second mode saturates it and causes the first mode to respond with a large amplitude. Some steady-state solutions experience a Hopf bifurcation as the excitation level increases, and some limit cycles of the amplitude modulation equations were observed to experience period doubling bifurcations.

Nayfeh and Jebril [1987] analyzed a 2DOF system with quadratic and cubic stiffness nonlinearities subjected to weak multifrequency parametric excitations. They considered principal parametric resonances of both modes and combination resonances of the sum and difference type. The equations considered can model a simply-supported uniform shallow arch whose rise consists of the lowest two modes. They found regions where parametric resonances are excited, regions where a subcritical instability exists, and regions where the nonlinearity causes a finite amplitude oscillation to occur. In the case of combination resonance of the difference type, the effective nonlinearity (which limits amplitude growth) may vanish and the response may be very large. In the case of two simultaneous principal parametric excitations, the coupling between the two modes produces a stable

solution; for moderately large excitation amplitudes, the response was not periodic.

As discussed in section 1.3.2, the analogue computer is finding increasing use in the study of nonlinear dynamics. Szemplińska-Stupnicka [1978] studied combination resonances in parametrically excited multi-degree-of-freedom systems. Using Bolotin's [1964] method and the method of harmonic balance, she presented a generalization of the method of harmonic balance applied to the case of the combination resonance. Her work includes simulation of a two-degree-of-freedom system on an analogue computer.

Zajaczkowski and Lipiński [1979] examined the vibrations of linear MDOF parametrically and externally excited systems. They used Bolotin's approach to examine stability and thus found the boundaries of the regions of instability. Using these derived formulas, they estimated the amplitude of the steady-state forced response amplitude.

Watanbe [1984] analyzed the forced vibration of nonlinear systems with symmetrical piecewise-linear characteristics. He simulated the system on an analogue computer and found the results to agree with the Fourier series solution.

Bajkowski and Szemplińska-Stupnicka [1986] studied two-degree-of-freedom systems with cubic stiffness nonlinearities and an internal resonance. They used the analogue computer to verify the application of the averaging method and the Ritz method.

1.4.3 Lumped Mass Systems

Many structures are fabricated from beams and bars, and many complicated structures are modeled with beam elements and lumped masses. Consequently, the theoretical analysis of the vibration of beams and masses and their experimental verification comprise a significant portion of structural mechanics.

A very interesting work is that of Haddow, Barr, and Mook [1984]. Their work on a simple two beam-two mass model considered the effect of an internal resonance on a 2DOF structure (see Figure 1.7) that was primarily externally excited and had a small parametric excitation due to the asymmetrical geometry. They obtained an approximate solution using the method of multiple scales and found excellent qualitative agreement with the results of the experiments. They predicted and measured the nonlinear response and observed saturation of the second mode. This structure also exhibits superharmonic resonances (see Haddow, et al [1985]) and subharmonic combination resonances as well. These phenomena were reproduced in the vibration laboratory at VPI & SU.

A second interesting work involving both combination and internal resonances is that by Bux and Roberts [1986]. They considered a model consisting of two beams and one mass; the first beam is cantilever mounted in the horizontal direction like that of Haddow et al, and the second beam is attached to the end of the first beam in an upright position but is rotated 90° with respect to its centerline such that transverse vibrations occur out of the plane of the two beams (see Figure 1.7). With a large mass attached to the top of the second beam,

the four lowest modes of vibration consist of (a) out-of-plane bending of the second upright beam occurring at frequency ω_B , (b) in-plane first mode bending of the first beam occurring at frequency ω_1 , (c) torsion of the mass and second beam occurring at frequency ω_T , and (d) in-plane second mode bending of the first beam. The equations of motion (a) possess quadratic nonlinearities due to the geometry, (b) show that planar rotational motion at the coupling point causes coupled parametric excitation of the torsion mode (mode 3) and out-of-plane bending mode of the second beam (mode 1), and (c) show that transverse motion of the coupling point causes direct parametric excitation of the out-of-plane bending mode of the second beam. The motion of the structure is further complicated when external and internal resonances exist, such as $\Omega \approx \omega_2$, and $\omega_2 \approx \omega_B + \omega_T$, where Ω is the frequency of the external excitation. When $\omega_2 \approx \omega_B + \omega_T$ a combination resonance exists. When $\omega_2 \approx \omega_B + \omega_T$ and $\Omega \approx 2\omega_2$ exist simultaneously, it is possible for the linear resonance of a directly excited mode to be absorbed with an accompanying steady-state vibration in one or more of the indirectly (i.e., autoparametrically) excited modes at frequencies other than the excitation frequency. The motion of the structure is further complicated when the internal resonance $2\omega_B \approx \omega_1$ condition is satisfied. In this case, the first bending mode will accompany the three mode interaction. This is an example of autoparametric interaction because the sinusoidal excitation and subsequent response of one mode appears as a parametric coefficient to one or more other modes. To obtain approximate solutions to these equations, they used

the method of multiple scales. The theoretical analysis was complemented by experiments.

1.4.4 Pendulum Systems

The simple pendulum is a SDOF system with a well defined nonlinearity and has been used extensively to explain parametric instability. It has also been used as a mathematical model to represent such real systems as a missile on its support base or a building subject to vertical ground motion. The simple pendulum has also been used in the development of several mathematical theories.

In a series of papers, Hatwal, Mallik, and Ghosh [1982, 1983a,b] investigated the harmonically forced vibration of a spring-mass-damper system with a parametrically excited pendulum hinged to the bottom of the mass. The system has two degrees of freedom: the primary system consisting of the mass, linear viscous damper, and linear spring, and the secondary system consisting of the damped pendulum. For some experiments, the restoring force of the pendulum due to gravity was supplemented by a torsional spring. The linear natural frequencies of the two systems were adjusted to cause a 2:1 internal resonance. The primary mass was excited by a harmonic force, and due to the internal resonance, the pendulum was autoparametrically excited. Using the method of harmonic balance, they found that a second order approximation was necessary and sufficient to predict stability. Experiments were performed to verify the parameters for which the pendulum exhibited the following different motions when disturbed from its static equilibrium

position: the pendulum (a) returned to its equilibrium position, (b) reached a harmonic steady state, or (c) oscillated randomly even after a long time (apparently chaos). Only the motion of the primary system was recorded; the motion of the pendulum was observed visually. Hatwal [1982] proposed adding an additional degree of freedom to the pendulum vibration absorber for the purpose of suppressing the peaks of the primary system at resonance (via autoparametric coupling) by replacing the inelastic pendulum rod with a damped elastic pendulum.

The parametrically excited pendulum in these papers has a practical use as a vibration absorber. Haxton and Barr [1972] studied a similar system; it had a cantilever beam mounted in a vertical position with an end mass mounted on top. They called the secondary mass system an autoparametric vibration absorber.

Schmidt [1981] added a degree of freedom to the pendulum excited by base excitation by allowing the mass to rotate on the suspension bar. The mass was constrained from translation on the bar and was attached to a torsional spring.

Levin et al [1985] performed some experiments on a pendulum (hanging down) that was hinged to a support that was harmonically excited in the vertical direction. They observed periodic and chaotic type aperiodic motions and used a strobe light to obtain Poincaré maps which showed period doubling bifurcations enroute to chaos.

A pendulum with an elastic instead of an inextensible suspension is one of the simplest models of an autonomous, conservative, oscillatory system of several degrees of freedom with nonlinear coupling; it can

also have a 2:1 internal resonance. The interesting feature of the elastic pendulum is that the centrifugal force completes two cycles for every pendulum cycle; it will thus autoparametrically excite the suspension mode if the suspension natural frequency is close to twice the pendulum frequency. This is easily seen in a simple experiment where one can tune the system and observe the energy exchange. Although the simple system looks like a toy, its behavior is quite complex because the suspension motion periodically alters the pendulum length, and hence the pendulum period. The process is nonlinear even when the spring is ideal and angular displacements are small such that $\sin \theta \approx \theta$, so that the motion cannot be represented by a linear superposition of normal modes. Witt and Gorelik [1933] seem to be the first to study this problem. Recently, the elastic pendulum attached to a fixed support and constrained to move in a plane was studied by Brietenberger and Mueller [1981] using the method of averaging and obtained solutions with remarkable accuracy when compared to numerically integrated solutions (one percent difference after 100 cycles).

Schmidt [1980, 1981, 1983] investigated the response of the elastic pendulum when the pivot support was given a periodic rectilinear oscillation in the plane of motion. Using the method of averaging, he obtained first-order solutions for a variety of cases including both a fixed direction and a constantly rotating direction of the oscillating support.

Yoshizama et al [1984] investigated theoretically and experimentally the transverse vibrations of a simply-supported beam that

was excited by a moving body with a pendulum attached; the body traversed the beam with a constant velocity. When the natural frequency of the beam is twice the natural frequency of the pendulum, internal resonance can occur due to the nonlinear coupling terms in the equations of motion. Using the method of multiple scales, they considered the case of internal resonance and found remarkable agreement with their experimental results.

Other recent pendulum related works can be found by Miles [1985] who considered the parametric excitation of a 2:1 internally resonant double pendulum.

1.4.5 Beams, Bars, Rods, and Strings

Elastic members such as beams, bars, rods and columns are essential parts of many structural systems. They usually carry various types of loads, and parametric excitations can cause resonances and structural failure.

Dugundji and Mukhopadhyay [1973] demonstrated that combination resonances can be excited in a horizontally positioned cantilever beam with the largest plane of rigidity in the vertical direction (see Figure 1.7); the shaker oscillates the beam clamp in the vertical direction. They parametrically excited a combination resonance by using a frequency close to the sum of the first bending and the first torsional modes. Dokumaci [1978] investigated theoretically and experimentally some of the parametric resonances that occur in this model. His calculated and measured stability boundaries for the onset of a parametric resonance

are in close agreement. Of experimental interest, he determined the damping of the torsional mode by determining the critical stability boundary of parametric resonance and made a direct calculation of the damping from the theoretical prediction of the stability boundary. Mukhopadhyay [1980] investigated combination resonances of parametrically excited coupled second-order systems with nonlinear damping of the fluid dynamic type (proportional to the square of the velocity). Using the Krylov-Bogoliubov-Mitropolsky method, he found regions where parametric instabilities exist. Using his previous model (similar to that of Dokumaci's [1978]), he compared the theoretical results to experimental results of the following combination resonances: (a) the first bending and first torsional modes, and (b) the second bending and first torsional modes.

Tezak et al [1978] analyzed parametrically excited transverse vibrations of columns and considered the nonlinear effect caused by stretching of the neutral axis. They used the method of multiple scales and considered two cases: with and without an internal resonance.

There are many machine components that can experience vibrational instabilities during operations caused by axially moving parts (e.g., saw blades and belt drives). They are sometimes subjected to tension fluctuations that can be caused by a wheel eccentricity or by joints and flaws in the band. Wu and Mote [1986] investigated parametric vibrations of a simply-supported beam with the largest plane of rigidity in the vertical direction. The top edge supported an axially moving band which caused a periodic edge loading. This model simulates band

saws, belts, magnetic tapes, and other systems under edge forces. They excited simple torsional parametric resonances and combination torsional-bending parametric resonances.

Many structures such as machines have rods and bars that oscillate axially. A beam that oscillates axially and subjected to a variable axial load was investigated by Elmaraghy and Tabarrok [1975]. This problem is complicated further if part of the beam or rod travels into a hole in a rigid support because then the length is varied simultaneously. The parametric instability of the motion of a beam with a periodically varying length was investigated by Zajaczkowski and Lipiński [1979]. The length was varied by sliding the beam into a motionless support by applying a force to the end of the beam inside the support. If the force causing the motion is applied to the other end, then there are two system parameters that are affecting the resonant transverse frequencies -- the length and the axial load. However, Zajaczkowski and Yamada [1980a] showed that the effect of relocating the force to the simple support was minimal. Zajaczkowski [1981] also investigated the parametric vibration of a beam excited by a reciprocating simple support. In this case, the friction force from the support is the source of parametric excitation in the same manner as an axial end load.

Like the oscillating bar with a time varying length, a string can exhibit a parametric instability caused by an oscillating support that periodically stretches the string. Furthermore, the other end of the string can pass through a small hole in a rigid plate that is also

oscillating, thus causing a length change of the string without disturbing the tension. Tagata [1983] investigated such a problem, and he retained the nonlinear terms caused by stretching of the string during large amplitude vibration. He investigated the first three modes of vibration using the method of harmonic balance, and determined the regions of parametric instability using the Routh-Hurwitz stability criterion.

Foryś and Nizioł [1984] considered a plane system of three rods arranged in such a way that the transverse forces at the ends of neighboring rods appear as parametric forces (see Figure 1.7). They considered the case of internal resonance. They retained the nonlinear damping and nonlinear inertia terms in the governing equations and used a procedure equivalent to the method of harmonic balance, and compared the results with those obtained using the Poincaré small parameter method. Foryś [1986] considered combination resonances in the same structure.

A cantilever beam with a tangential force acting on the free end was first studied by Beck [1952] and hence is commonly referred to as Beck's problem. Bolotin [1965] investigated parametric resonances of the Beck-type problem under the action of a periodic tangential force; he obtained the instability regions for the first and second modes. Sugiyama et al [1970] used an analogue computer to investigate the parametric instability regions of the Beck-type problem. In addition to the simple resonances, they found that there exists an important region of combination resonance. It was not until 1982 that Sugiyama et al

[1982] provided a theoretical basis for the existence of the combination resonance using Hsu's [1963] method. Crespo da Silva [1978] and Nayfeh and Mook [1979] consider the Beck problem and include nonlinear terms in the analysis.

1.4.6 Rotating Shafts

The dynamics of rotating shafts and associated instabilities are important considerations in machine design. Excessive vibration and instability during operation are caused primarily by asymmetries in shafts and their support bearings. Instabilities can occur at driving speeds that are some fraction (subharmonic) of a critical speed. The interaction of the symmetric parameters of a rotor and its bearing is expressed by time-dependent coefficients in the equations of motion.

Parametric instabilities can be induced in rotating systems due to pulsating torques. The torque transmitted by a shaft is usually pulsating about a mean value; it can arise from many sources, such as worn gears or transmission of torque through a Hookean (common universal) joint when the centerlines of the shaft are not collinear. Eshleman [1967] formulated the problem of pulsating torque transmission by developing the equation of motion and specifying the boundary conditions, but he did not solve the equation. However, he did show experimentally, using a shaft-disk system, that a fundamental parametric resonance consisting of a first beam mode can be excited with a pulsating torque. Unger and Brull [1981] extended the work of Eshleman

[1967] and Eshleman and Eubanks [1969] by including the cases of principal combination and parametric resonances.

1.4.7 Plates and Shells

If beam elements can be considered to constitute the primary building elements in models and structures, then plate elements constitute secondary elements. Many structures, such as an airplane, are frame structures fabricated from beam elements and covered with plates and shells. As these structures flex and bend, the plates are sometimes subjected to transverse excitation caused by inplane forces or moments.

In many respects, plate behavior is a three-dimensional extension of two-dimensional beam behavior. Inplane forces on plates are quite similar to axial loads on beams when parametric instability is considered. Plates are susceptible to all the resonances of beams, plus more that are associated with the additional dimension. With the additional spatial dimension come more possibilities of internal resonances and combination resonances. The study of inplane forces on plates goes back to Einaudi [1936] and was followed by less than two dozen papers, including a chapter in the book by Bolotin [1964], in the four decades that followed! The dynamic stability of cylindrical shells was first considered by Markov [1949].

Carlson [1974] experimentally investigated principal and fundamental parametric resonances in a thin plate subjected to tensile loads that consist of static and harmonically varying dynamic

components. The plate had a cracklike opening in the center. Although his primary objective was to investigate the instability boundaries, he measured quantitatively the frequency response and obtained a hardening type curve that he attributed to midplane stretching due to bending. Datta [1978] extended the results of Carlson to include different size openings. He found that a more circular hole tended to reduce the instability regions. Attempts to provide a theoretical framework were made by Datta [1981]. He modeled the plate with a 1DOF equation since the lowest eigenvalue was well separated from the other eigenvalues. He obtained the form of the nonlinear stiffness qualitatively from previous studies.

Meritt and Willems [1973] investigated the response of a stiffened simply supported skew plate that was loaded by an inplane force consisting of a constant component and a harmonic component. This type of loading leads to an equation of motion with time-dependent coefficients similar to the Mathieu equation (see also Evan-Iwanowski [1976]).

Takahashi [1985] analyzed the response of a rectangular plate subjected to an inplane moment which consists of a static component and a sinusoidal component. He applied Galerkin's method to the stress function and obtained coupled Mathieu equations which he numerically integrated by the Runge-Kutta-Gill method. In addition to fundamental and principal parametric resonances, he also found combination resonances of the additive type. The combination resonance instability regions were much larger than the regular parametric instability

regions. When he included the nonlinear terms, he found their effect was to limit the unbounded growth (predicted by linear theory) to finite amplitude values. This problem is quite similar to a beam with an axial end load because the application of an inplane moment reduces to an axial end load on a single fiber in the plate.

Tani and Nakamura [1978] investigated principal and combination parametric resonances in a thin annular plate. They excited the plate along the inner and outer edges with inplane forces of different frequencies. They found that the principal parametric resonance had a larger instability region when compared to the combination resonance instability region.

Just as an oscillating beam can exhibit parametric instability, plates also can exhibit similar behavior. Evan-Iwanowski [1976] discusses the problem and reviews the literature on the subject. If the oscillating beam or plate is allowed to enter an opening in a motionless support, then the free length is also time-varying. Zajackowski and Yamada [1980b] considered a plate that was simply-supported on two edges. The applied force moving the plate was applied to the edge which was sliding inside the motionless support. They determined the boundaries of the instability regions.

1.4.8 Flow-Induced Parametric Vibration

The study of flow-induced vibrations (FIV) and fluid-elastic instabilities of structural components has been receiving increased attention in recent years. One reason is that the repeated equipment

failures in the power generating industry (especially tubes in heat exchangers) are quite costly both in terms of replacement and of down time. FIV in articulated and continuous tubes conveying fluid have been studied extensively beginning with the work of Benjamin [1961a,b] on articulated tubes. Most of the early work was limited to linear models of initially straight tubes undergoing planar motion conveying fluid flowing at a constant rate. Nonlinear analysis for linearly unstable planar motions was conducted by Holmes [1977], Rousselet and Herrmann [1977], and Bajaj, Sethna, and Lundgren [1980]. Bajaj and Sethna [1982] extended the analysis and considered three-dimensional motions.

Whenever the velocity of a fluid flowing through a pipe is not constant but has harmonic fluctuations superimposed on a mean value, a parametric resonance can be excited. Since pipes are typically MDOF systems, combination resonances can also be excited. These were first studied by Natanzon [1962].

Bohn and Herrmann [1974] showed that when the flow rate through the tubes is periodic, both parametric and combination resonances can occur, especially when the mean flow is near a critical value. The case of continuous tubes with periodic flow was investigated by Paidoussis and Issid [1974], Ginsberg [1973], and Paidoussis and Sundararajan [1975]. Recently Singh and Mallik [1979] determined the principal and fundamental parametric instability regions for the first two modes of a simply-supported two span pipe. Mallik et al [1984] investigated ways to reduce parametric resonances in pipes conveying fluid by installing vibration absorbers on the pipe hangers, and Bajaj [1984] investigated

the interactions between self and parametrically excited motions in articulated tubes.

Parametric resonances can be excited in pipes that have fluid flowing around them. Although most tube failures associated with FIV are caused by cross-flow, cases of axial FIV have been shown to be important. These parametric excitations can be caused by pulsations in the mean flow caused by a variety of sources such as the harmonic pressure fluctuations in a pump, thermo-hydraulic instabilities in two-phase flows, or by periodic vortex shedding somewhere upstream. Paidousis et al considered theoretically [1980a] and experimentally [1980b] the parametrically excited vibrations of slender cylinders to external axial flow.

1.4.9 Structures Containing Liquid

Since the advent of aerospace vehicles, the problem of liquid sloshing has received considerable attention. Fuel containers of rockets and missiles are subjected to vertical excitation due to dynamic coupling between the structure and the engine thrust. Fuel tanks in aircraft experience vertical excitation while taxiing, taking off, and landing due to travel over uneven track, and also during flight due to air turbulence. The free surface oscillations of liquid propellants inside fuel tanks exert forces and moments on the vehicle, and these can interact with the dynamics of the control system or the structural system, or with both simultaneously. The DC-3 was particularly susceptible to wing flapping in flight, and was nick-named the "Gooney

Bird." The danger of this type of resonant oscillation of the wings and hence the fuel tanks is the possibility of exciting parametric resonances on the free surface of the fuel. Railway tank cars, tank trucks, and automotive vehicles carrying liquid as cargo or fuel are also subjected to vertical excitation due to track roughness. Even dams and overhead tanks of all types experience vertical motion during earthquakes. Consequently, there are many fluid related structures that are susceptible to parametric vibration.

Parametric resonances were first observed by Faraday [1831] in the surface oscillations of liquids in containers. Faraday [1831] and Lord Rayleigh [1883a,b] studied such "crispations" experimentally and noted that the surface oscillation frequency was typically one-half that of the excitation frequency. Benjamin and Ursell [1954] derived an infinite set of Mathieu equations to describe the linear vibrations of the liquid surface; their stability analysis provided a theoretical basis for the frequency demultiplication observed by Faraday and Rayleigh. Dodge et al [1965] gave a finite-amplitude analysis for free surface vibrations of a liquid in a vertically excited cylindrical container, but Miles [1984] pointed out that "their equations of motion for the modal amplitudes violate reciprocity conditions that are implicit in the underlying (Newtonian) mechanics." Ockendon and Ockendon [1973] extended the analysis of Benjamin and Ursell [1954] to small but finite amplitudes, but did not calculate the parameter that measures the effects of nonlinearity. Miles [1984] extended the analysis of Ockendon and Ockendon [1973] by giving an explicit

expression for this parameter; he also included linear damping and analyzed the case of a perfectly tuned 2:1 internal resonance when the lower mode was excited by a principal parametric excitation. Henstock and Sani [1974] also gave a finite-amplitude analysis, but they applied the free-surface boundary conditions at the equilibrium rather than the disturbed surface and obtained a nonlinear correction to the frequency that was of first order rather than second order in amplitude. Nayfeh [1987] analyzed the nonlinear response of the free surface of a liquid in a cylindrical container to a harmonic vertical oscillation in the presence of a 2:1 internal resonance. He used the method of multiple scales to determine the amplitude and phase modulation of the two modes involved in the internal resonance when the lower mode was excited by a principal parametric excitation. He found trivial, limit cycle, amplitude- and phase-modulated sinusoidal, and chaotic responses.

Recently, a number of experiments have been conducted to investigate the free-surface vibrations of liquids in vertically oscillating containers. Ibrahim and Barr [1975a,b] and Ibrahim [1976] investigated both theoretically and experimentally the response of a fluid-filled cylindrical structure, looking particularly at two- and three-mode interactions of the fluid and the structure which was mounted on an elastic support.

Keolian et al [1981, 1984] used liquid helium and water in thin annular troughs and observed period doubling as well as quasiperiodic surface waves involving three modes.

Khandelwal and Nigam [1981] investigated the free surface of a liquid in a rectangular container with a flexible base under a vertical periodic excitation. They used Bolotin's method to determine the regions of principal and fundamental parametric resonance (instability regions). The flexible base reduced the regions of parametric instability of the free surface.

Hashimoto and Sudo [1984] performed a series of experiments to investigate the dynamic behavior of the gas-liquid interface in a cylindrical container subject to vertical vibration. Gollub and Meyer [1983] examined the loss of stability of a single axisymmetric mode and its period-doubling bifurcations. At relatively high amplitudes, they observed temporal chaos with azimuthal spatial modulation. Ciliberto and Gollub [1984, 1985] examined the case in which the excitation amplitude and frequency are near the interaction of the stability boundary between two degenerate modes and found that they can compete to produce either periodic or chaotic motion.

Since parametric resonances can occur on the free surface of a liquid in a vertically moving container, a principal design problem is that of eliminating or suppressing the large amplitude resonant response when it occurs. If detuning the system or incorporating a flexible tank bottom is not a feasible option, another method must be considered. Hasegawa and Kondah [1986] investigated the possibility of adding a small amount of fluid of lower density and higher viscosity to the original fluid; such a fluid would come to rest as a top surface layer, and being more viscous than the underlying fluid, would tend to have

stabilizing effects. Their predicted responses of increased stability were confirmed by experiments. This phenomenon has been observed in stormy seas when oil has been sprinkled (or spilled by accident) on the surface; the amplitude of the wave motion was observed to decrease.

1.4.10 Parametric Instability

As noted in Section 1.2.4, one principal engineering problem is determining the boundaries of the instability regions. The classical methods for doing this, such as Hill's infinite determinant, are well documented in the literature. Recently, modifications of the classical methods as well as new methods have been reported.

Kotera [1980] used Lyapunov's theorem to obtain characteristic equations, and from these equations used a simple approximate method to estimate the eigenvalues. He included combination resonances of the sum type, subharmonic combination resonances, superharmonic resonances, and subharmonic resonances in his example.

Sinha et al [1979] discussed an approximate method for determining the stability boundaries of second-order linear systems with periodic coefficients. The periodic functions were approximated during the first period of motion by functions of time such that the resulting approximate equations had known closed form solutions. The stability criteria was determined from the solution of the approximate system and Floquet theory.

Takahashi [1981,1982] investigated parametric instability in a linear MDOF system of coupled Mathieu equations by using the method of

harmonic balance; he assumed a Fourier series with periods T and $2T$ for the solutions. His analysis also included cases of combination resonance.

Papastavridis [1982] investigated a variational method based on Hamilton's principle to determine the stability boundaries of Mathieu's equation. He generalized the conventional Hamilton's principle by treating the time-dependent parameters in the system as additional generalized coordinates and subjected them to similar variations.

Noah and Hopkins [1982] described a method for investigating the stability of the trivial solution of a general system of linear second-order differential equations. The method was based on a generalization of Hill's infinite determinant method and was illustrated on a MDOF discretized system describing pipes conveying pulsating fluid.

Hansen [1985] described a method for investigating the stability of the trivial solution of coupled Mathieu equations. His method involved infinite determinants but used symbolic manipulation to rewrite the determinants as polynomials in the desired variables, the zeros of which were found by root searching. Using this approach, he was able to generate stability diagrams that were not confined to only small parameters.

1.5 Summary and Purpose

In this introductory chapter, we have defined parametrically excited systems and discussed many of the unique features of parametric resonance; we have also seen that parametric vibration is as important

as conventional vibration even though it is not as common. Some features of parametric resonances have counterparts in both linear and nonlinear systems, and other features are unique to parametric systems. Hence, there are cases where parametric systems need to be analyzed as parametric systems because any attempt to model them as externally excited systems can lead to erroneous results.

The literature review summarizes the work that has been accomplished in the last decade. The work in the United Kingdom is notable for its scholarship and accompanying experimental results, and the work in Japan is notable for its relatively large number of papers that report experimental results. The work in the United States is notable for its many scholarly theoretical works in the field. The theoretical findings often motivates the experimentalist to look for new behavior or provide an explanation for observed behavior not predicted by simple theory; and it also happens that the experimental results have motivated the theoretician to improve his model. Thus, a thorough investigation into the nonlinear dynamic behavior of a structure will include both the theoretical analysis and experimental observation.

There are several observations to be made regarding the literature review. First, there is virtually no experimental work being performed in the USA in the area of harmonic parametric vibration; Ibrahim [1985] is performing experimental work in the area of random parametric vibration and is making a contribution to the literature. Second, most of the theoretical and experimental work presently being performed in the area of nonlinear dynamics is with external excitation. Literature

dealing with bifurcations and chaotic behavior in parametrically excited system is scarce in the journals that typically publish works relevant to theoretical and experimental mechanics. It is possible that literature on chaotic behavior in parametric systems does exist in other journals, but these were not searched in this review.

In this dissertation, we will investigate parametrically excited structures that can be modeled by 1DOF and 2DOF mathematical models. Nonlinear terms in the governing differential equations will be retained. The theoretical investigation will include developing perturbation solutions using the method of multiple scales. These approximate solutions will be compared with solutions obtained by integrating the original differential equations on the analogue and digital computers. The theoretical results will be compared with the experimental results obtained by shaking models consisting of beams and masses.

In one sense, the experimental aspect of this dissertation provides the "proof" of any assumptions deemed necessary in the mathematical modeling of structures. Experiments performed on actual physical systems involve the least amount of idealization, and hence give the most realistic picture of the "real world". As we have seen, any time an equation is written to describe a structure or system, assumptions must be made and a certain amount of idealization occurs. All subsequent analysis performed using these idealized equations will be constrained to the behavior of these equations, which may or may not describe the original physical system in all respects. For these

reasons, the experimental data--even with systematic, random, and human error present--will provide the benchmark with which to gage the theoretical model. Historically, the experimental study of structural vibration has provided a major contribution to our efforts to understand and to control the many vibration phenomena encountered in practice. Since the early days of awareness of vibrations, experimental observations have been made for the two major objectives of determining the nature and extent of vibration response levels and verifying theoretical models and predictions. The work in this dissertation falls into the second category.

Thus, the purpose of this dissertation is to investigate--both theoretically and experimentally--the nature of parametric resonances in structures that are most accurately modeled by nonlinear equations with time-dependent coefficients. In MDOF systems, the possibility of internal resonances and combination resonances exist, which allows modal interaction to occur. Chaotic behavior and period-doubling bifurcations leading to chaos in parametrically excited systems have been observed in mathematical models, but they have been demonstrated on pendulums only. We have demonstrated chaotic behavior on parametrically excited long flexible beams in the vibration laboratory at VPI & SU. Hence, one of the thrusts of this dissertation will be to compare the mathematical model of a structure with the experimental observations in the laboratory. If we can predict behavior and then observe it, then our understanding of the causes, and hence some cures, of parametric resonance will have been advanced.

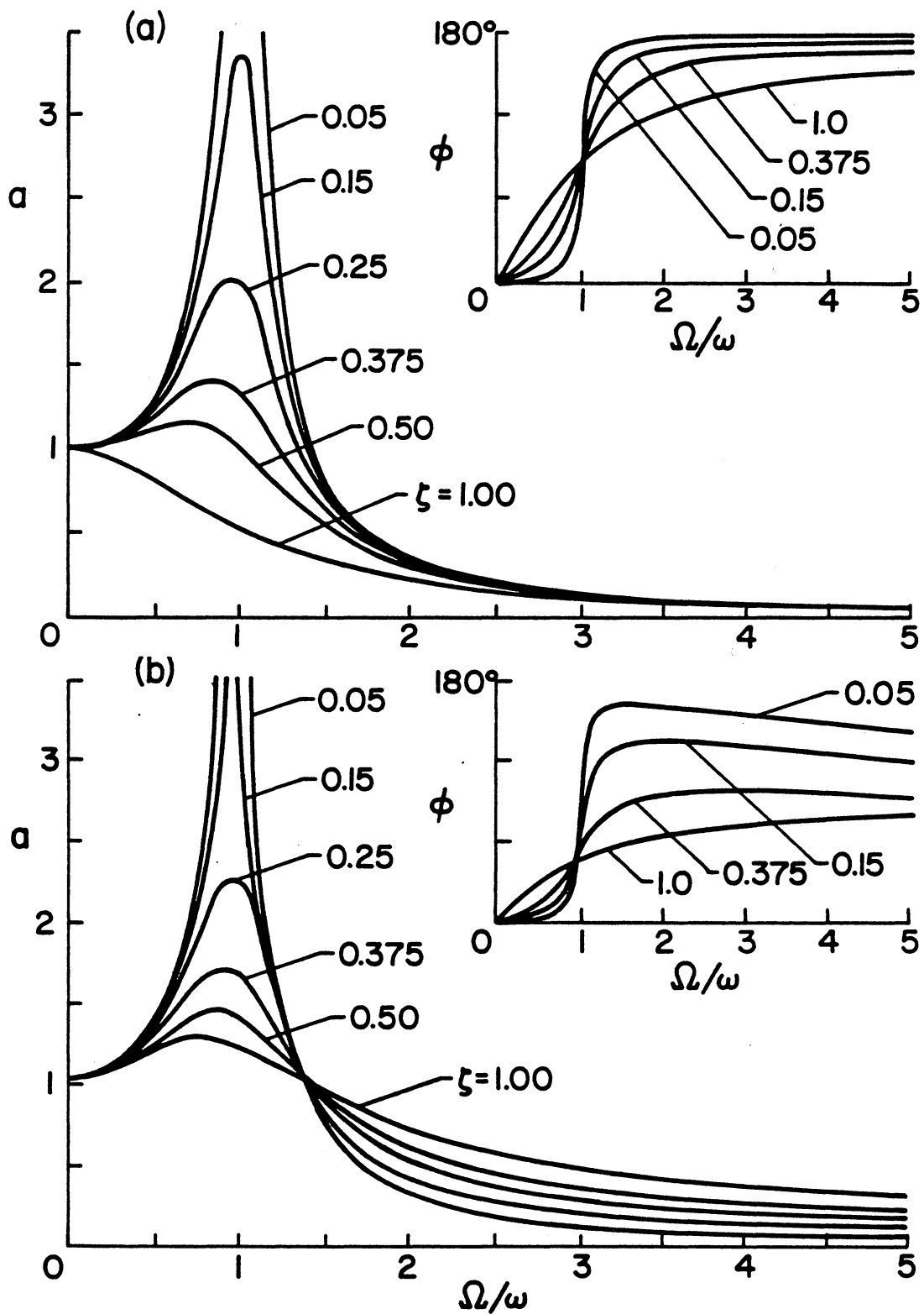


Figure 1.1 Frequency response function of a spring-mass-damper to an (a) external sinusoidal force and (b) external sinusoidal base displacement for different values of the damping coefficient ζ (Thompson, 1965).

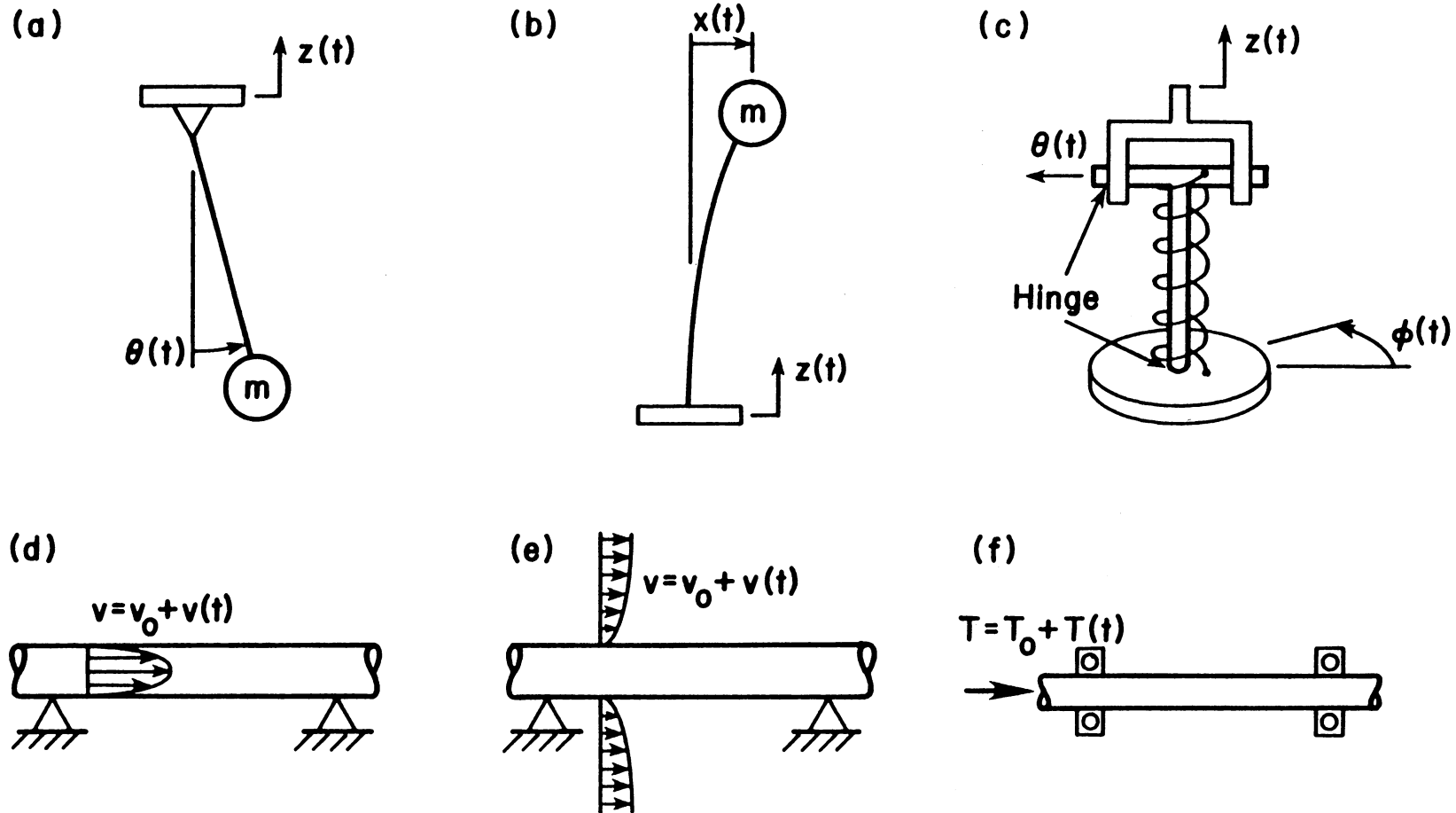


Figure 1.2 Examples of dynamic systems subjected to parametric excitation: (a) pendulum with a moving hinge, (b) cantilevered beam carrying a lumped mass clamped to a moving support, (c) torsional pendulum with a moving hinge (Schmidt, 1981), (d) tubes conveying fluid, (e) tubes with external axial flow, (f) shafts transmitting torque.

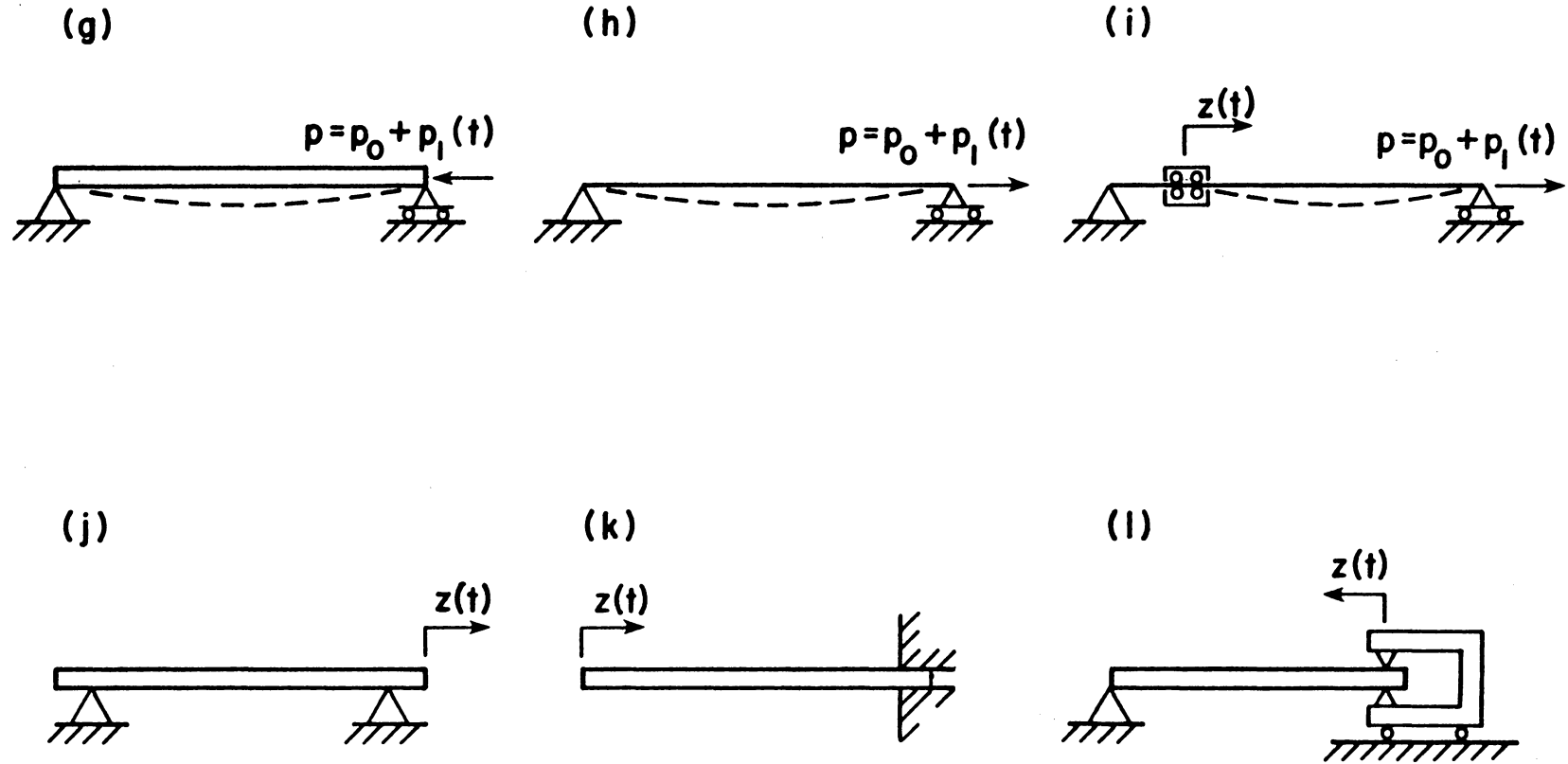


Figure 1.2 continued, (g) rod with axial loads, (h) string with variable tension, (i) string with variable tension and length, (j) moving rod, (k) moving rod with variable length, (l) rod with moving support.

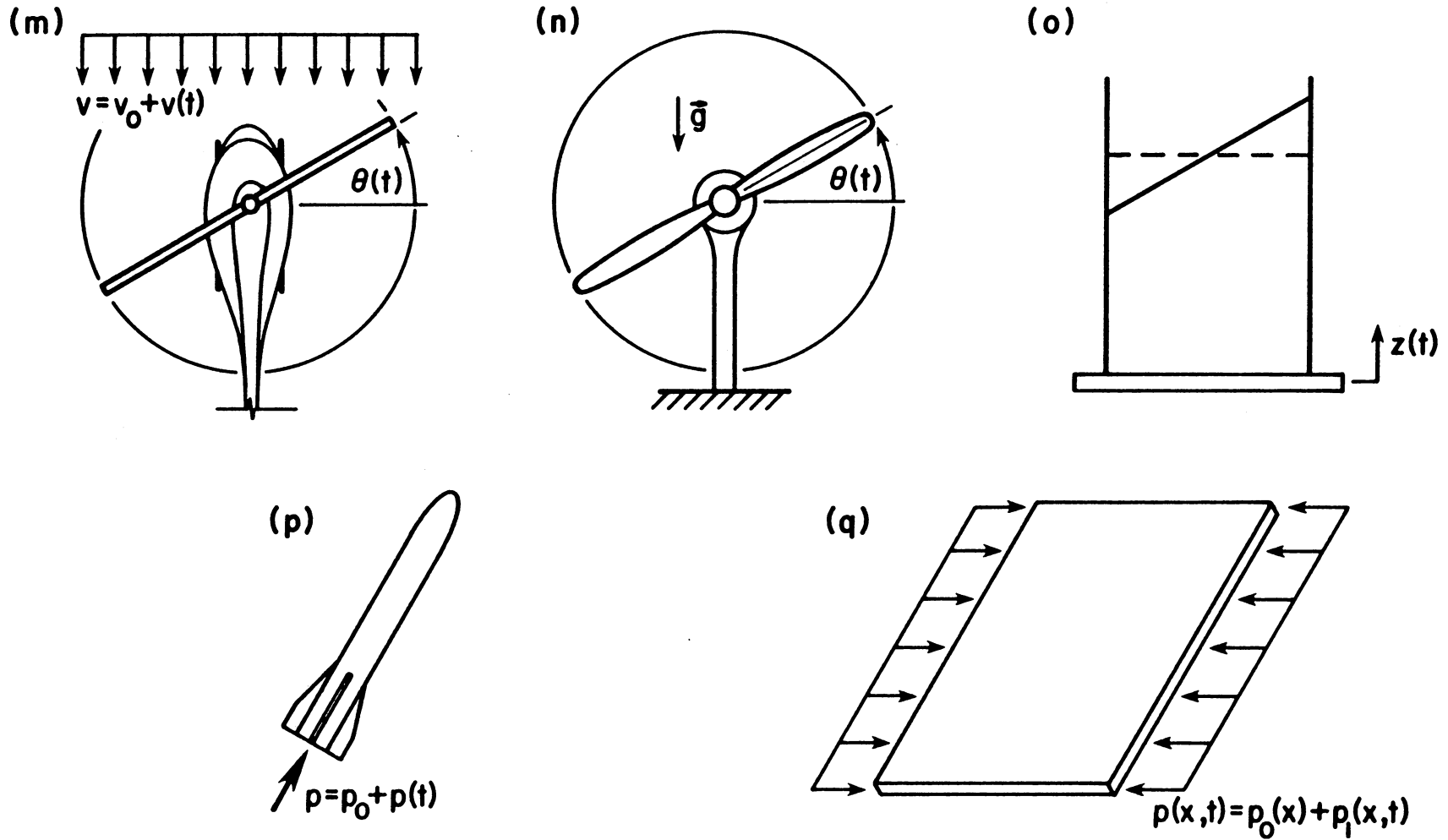


Figure 1.2 continued, (m) helicopter rotor blade in forward flight, (n) wind turbine blade in a gravity field, (o) liquid free surface sloshing under vertical support motion, (p) flexible missile under pulsating thrust, (q) plate under longitudinal loading with pulsating component.

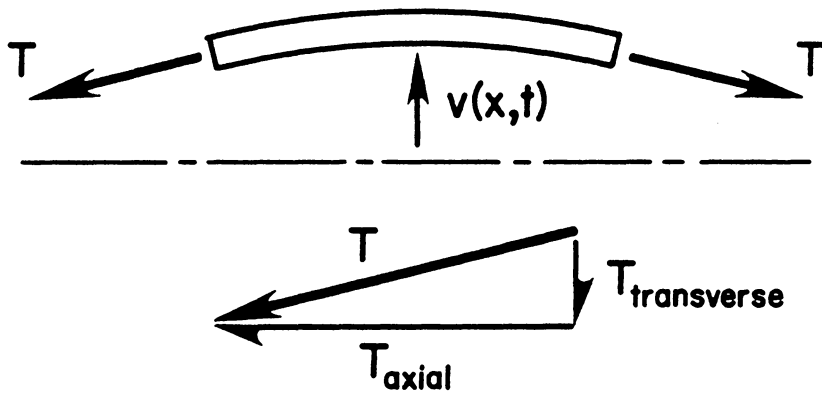


Figure 1.3 Free-body diagram of a string element in a displaced position.

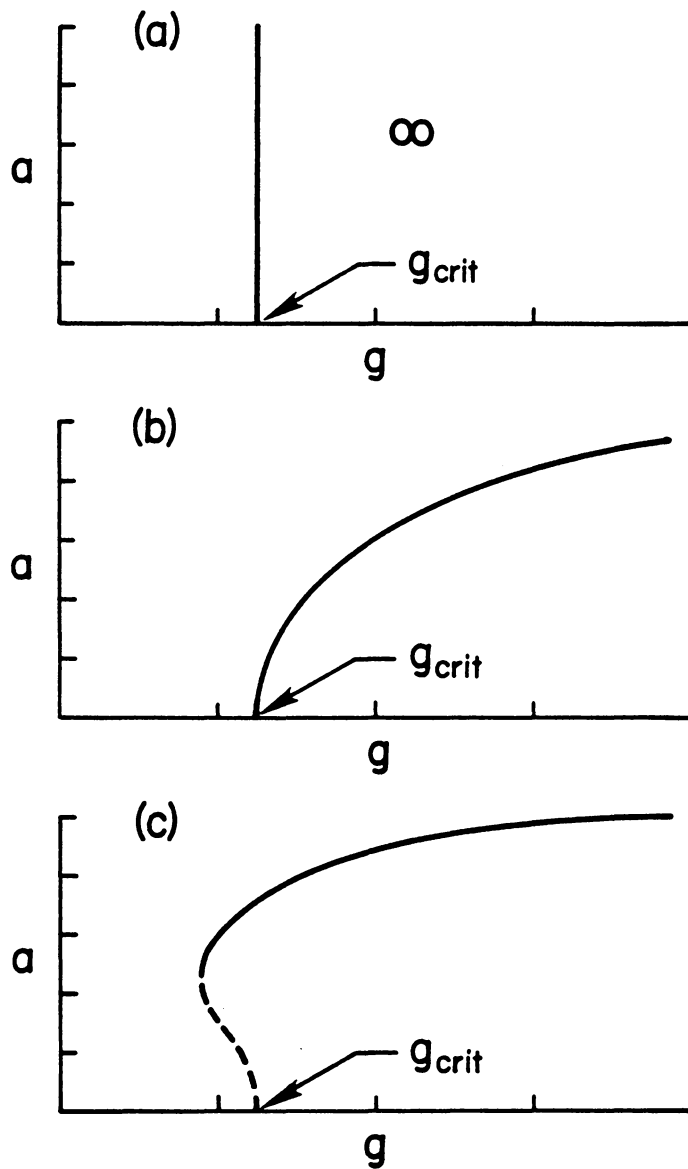


Figure 1.4 Response amplitude to a parametric excitation for (a) a linear system, (b) a nonlinear system, and (c) a nonlinear system that possesses a subcritical instability.

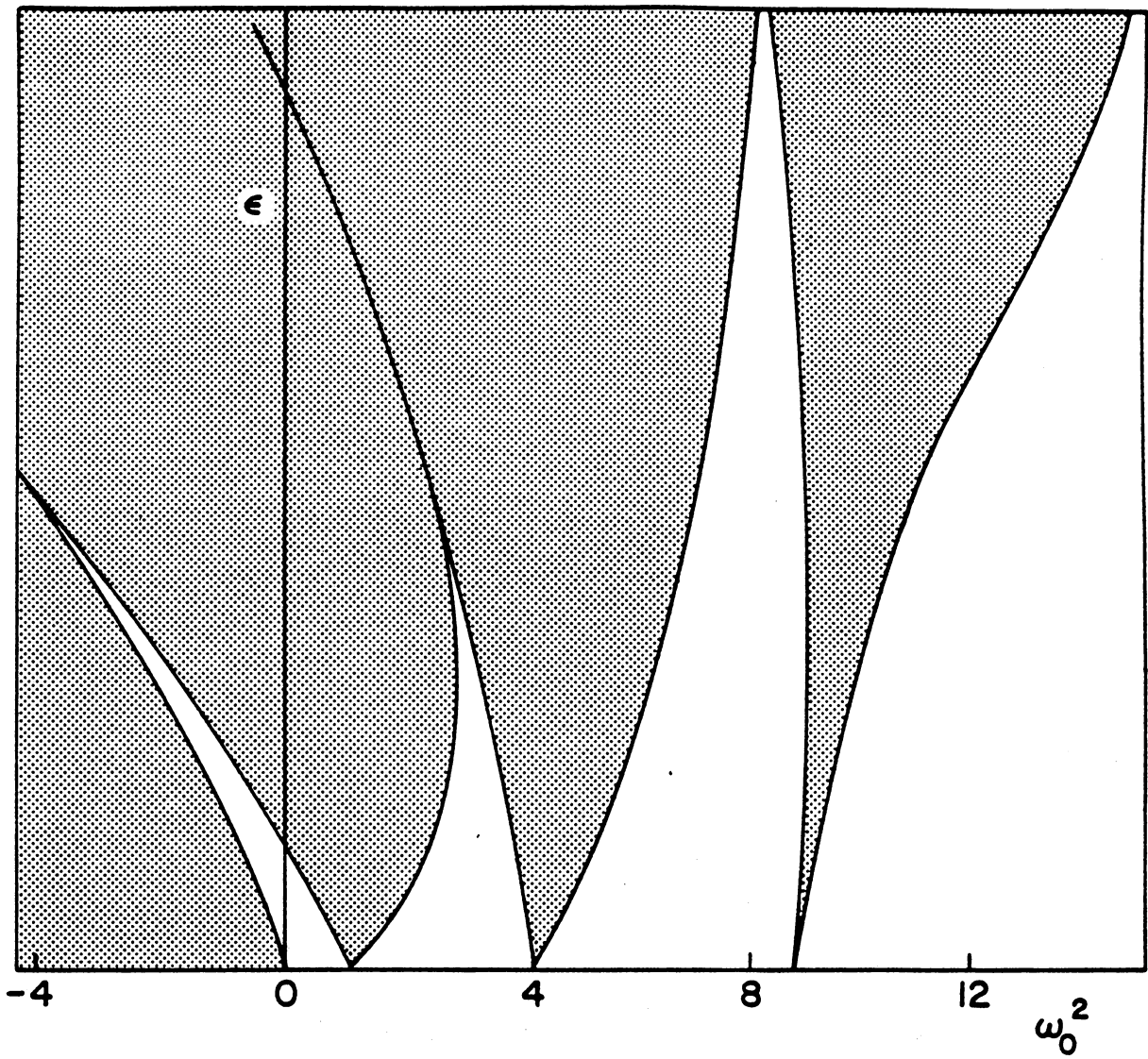


Figure 1.5 Stability diagram of the undamped Mathieu oscillator, also known as the Strutt diagram.

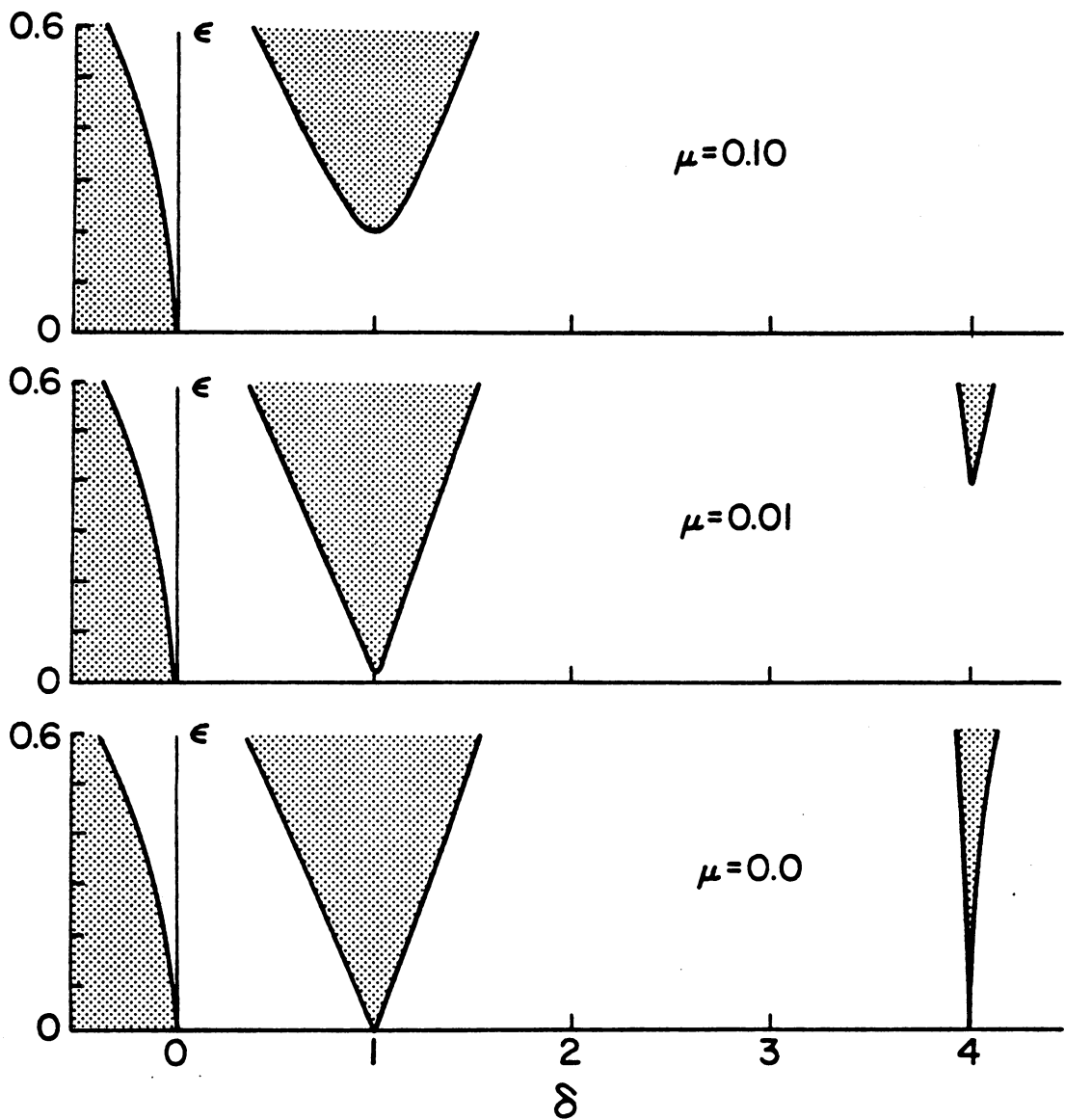


Figure 1.6 Effect of damping on the instability regions of Figure 1.5 (Nayfeh and Mook, 1979).

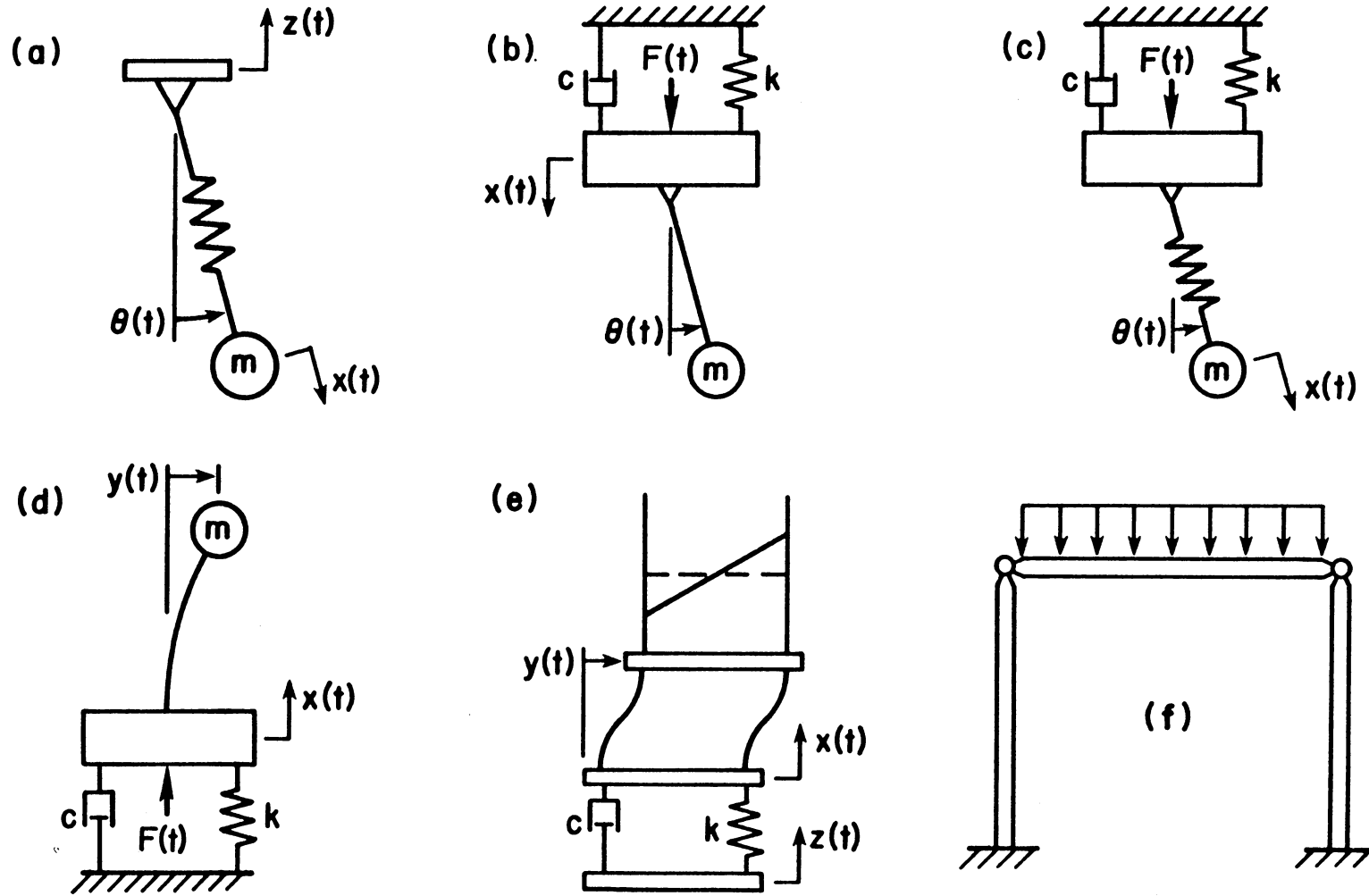


Figure 1.7 Examples of dynamic systems with autoparametric interaction caused by internal resonance: (a) elastic pendulum, (b) 2DOF system (Hatwal, et al, 1982, 1983), (c) 3DOF system (Hatwal, 1982), (d) vibration absorber (Haxton and Barr, 1973), (e) elastic structure carrying a liquid tank (Ibrahim and Barr, 1975), (f) system of rods (Forys and Nizioł, 1984).

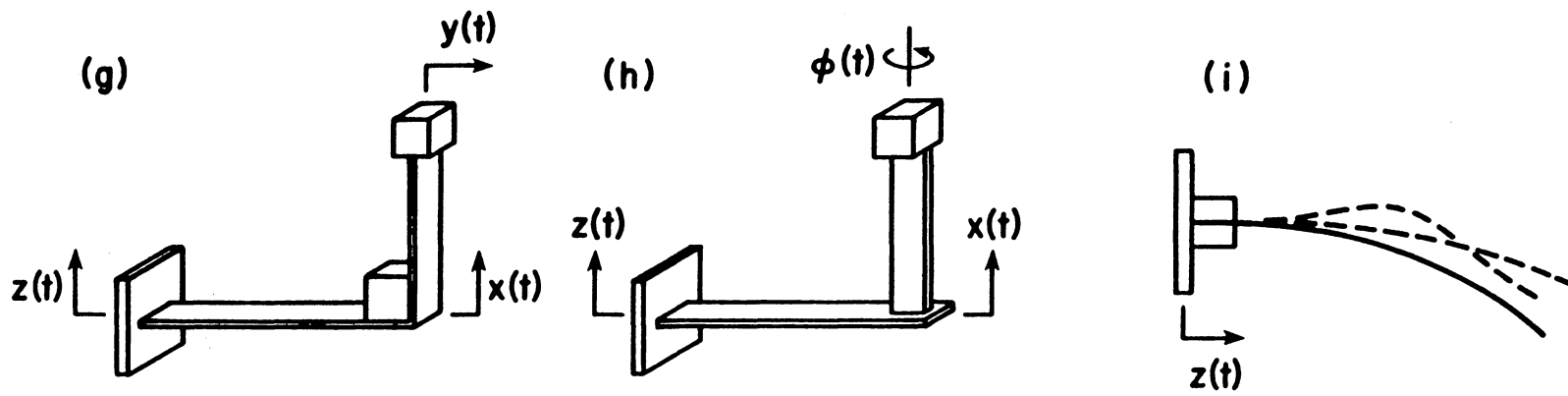


Figure 1.7 continued, (g) 2DOF system with 2:1 internal resonance (Haddow, Barr, and Mook, 1984), (h) 4DOF system with internal resonances (Bux and Roberts, 1986), (i) MDOF flexible beam with 2:1 internal resonance between the 3rd and 4th modes, (Zavodney, 1987).

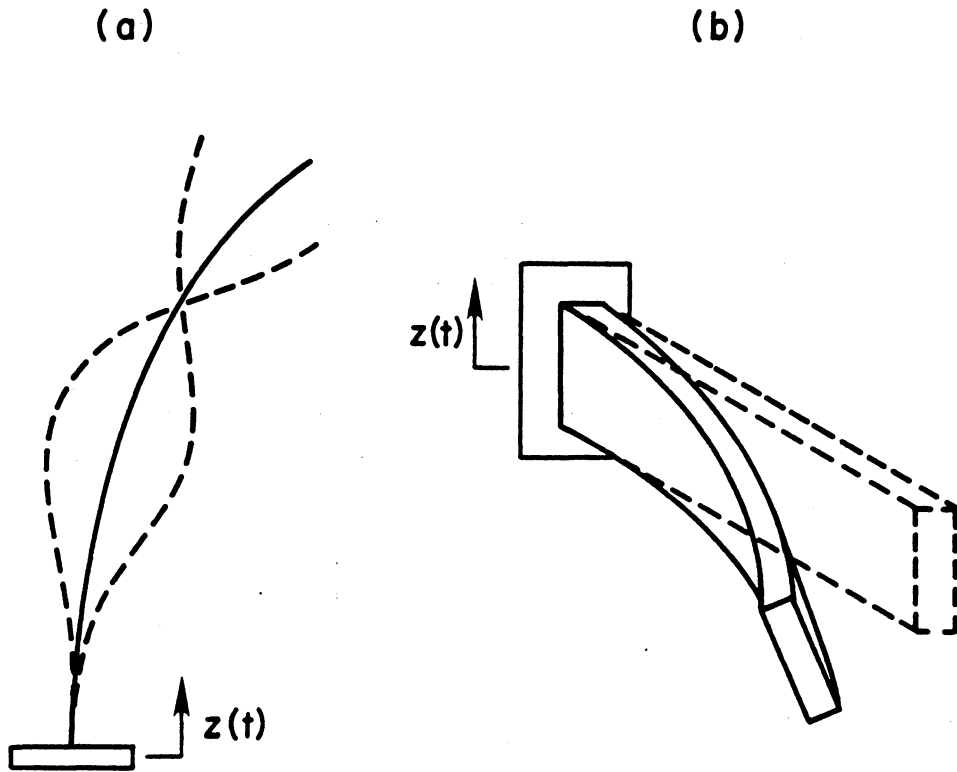


Figure 1.8 Examples of dynamic systems susceptible to combination resonances caused by parametric excitation: (a) vertical flexible cantilever beam responding with two modes (Jaeger and Barr, 1966), (b) horizontal cantilever beam responding with transverse and torsion modes (Dugundji and Mukhopadhyay, 1973).

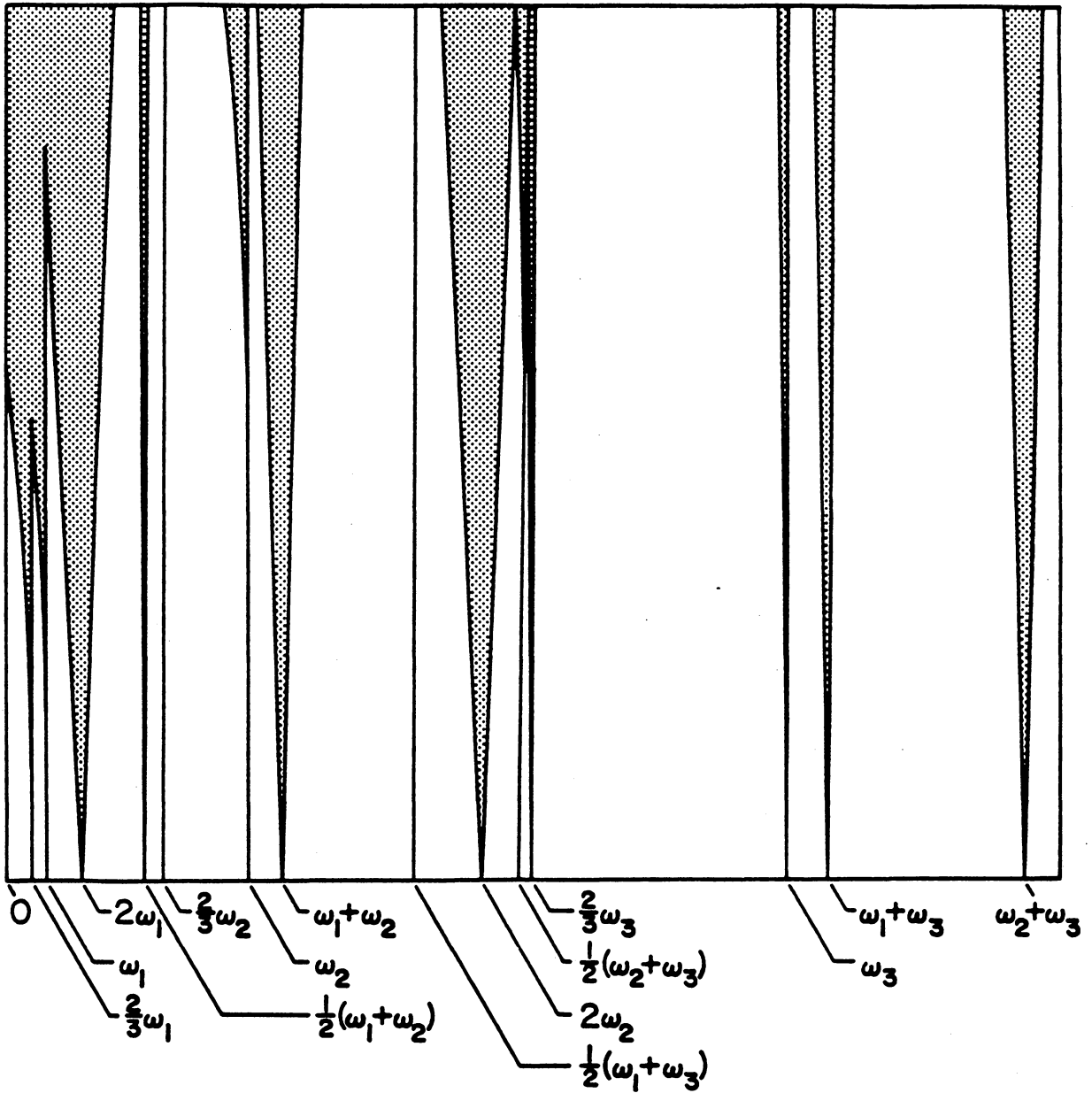


Figure 1.9

Stability diagrams of a multi-degree-of-freedom system showing the combination resonances that exist in a particular system.

CHAPTER II

FUNDAMENTAL PARAMETRIC RESONANCE IN A SINGLE-DEGREE-OF-FREEDOM SYSTEM

This chapter considers the response of one-degree-of-freedom systems with quadratic and cubic nonlinearities to a fundamental parametric resonance. The problem is governed by

$$\ddot{u} + 2\epsilon\mu\dot{u} + [\omega_0^2 + \epsilon\delta u + \epsilon^2\alpha u^2 + \epsilon g \cos\Omega t]u = 0, \quad (2.1)$$

where the dots indicate differentiation with respect to time, ϵ is a small dimensionless parameter, and μ , ω_0 , δ , α , g and Ω are constants. The quadratic term may be due to curvature or an asymmetric material nonlinearity whereas the cubic term may be due to mid-plane stretching or a symmetric material nonlinearity. The parametric term may be due to a harmonic axial load.

2.1 Multiple Scales Analysis

A second-order uniform solution of (2.1) is sought using the method of multiple scales (Nayfeh [1973, 1981, 1985]) in the form

$$u(t;\epsilon) = u_0(T_0, T_1, T_2) + \epsilon u_1(T_0, T_1, T_2) + \epsilon^2 u_2(T_0, T_1, T_2) + \dots, \quad (2.2)$$

where $T_0 = t$ is a fast scale associated with changes occurring at the frequencies ω_0 and Ω , and $T_1 = \epsilon t$ and $T_2 = \epsilon^2 t$ are slow scales associated with modulations in the amplitude and phase caused by the

nonlinearity, damping, and resonances. In terms of the T_n , the time derivatives become

$$\frac{d}{dt} = D_0 + \epsilon D_1 + \epsilon^2 D_2 + \dots , \quad (2.3)$$

$$\frac{d^2}{dt^2} = D_0^2 + 2\epsilon D_0 D_1 + \epsilon^2 (2D_0 D_2 + D_1^2) + \dots ,$$

where $D_n = \frac{\partial}{\partial T_n}$. Substituting (2.2) and (2.3) into (2.1) and equating coefficients of like powers of ϵ , we obtain

$$D_0^2 u_0 + \omega_0^2 u_0 = 0 , \quad (2.4)$$

$$D_0^2 u_1 + \omega_0^2 u_1 = - 2D_0 D_1 u_0 - 2\mu D_0 u_0 - g u_0 \cos \Omega T_0 - \delta u_0^2 , \quad (2.5)$$

$$D_0^2 u_2 + \omega_0^2 u_2 = - 2D_0 D_2 u_0 - D_1^2 u_0 - 2D_0 D_1 u_1 - 2\mu D_0 u_1 - 2\mu D_1 u_0 - g u_1 \cos \Omega T_0 - 2\delta u_0 u_1 - \alpha u_0^3 . \quad (2.6)$$

The solution of (2.4) can be expressed in complex form as

$$u_0 = A(T_1, T_2) e^{i\omega_0 T_0} + \bar{A}(T_1, T_2) e^{-i\omega_0 T_0} , \quad (2.7)$$

where \bar{A} is the complex conjugate of A . Then, (2.5) becomes

$$D_0^2 u_1 + \omega_0^2 u_1 = - 2i\omega_0 (D_1 A + \mu A) e^{i\omega_0 T_0} - \frac{1}{2} g A e^{i(\Omega + \omega_0) T_0} - \frac{1}{2} g A e^{-i(\Omega - \omega_0) T_0} - \delta A^2 e^{2i\omega_0 T_0} - \delta \bar{A} A + cc . \quad (2.8)$$

Any particular solution of (2.8) contains secular terms and small-divisor terms when $\Omega \approx 2\omega_0$ (i.e., principal parametric resonance). For the case of fundamental parametric resonance (i.e., $\Omega \approx \omega_0$), there are

no terms in (2.8) that lead to small-divisor terms. Then, eliminating the terms that lead to secular terms yields

$$D_1 A = -\mu A . \quad (2.9)$$

Consequently, the solution of (2.8) becomes

$$\begin{aligned} u_1 = & -\frac{\delta A \bar{A}}{\omega_0^2} + \frac{gA}{2\Omega(\Omega+2\omega_0)} e^{i(\Omega+\omega_0)T_0} + \frac{g\bar{A}}{2\Omega(\Omega-2\omega_0)} e^{i(\Omega-\omega_0)T_0} \\ & + \frac{\delta A^2}{3\omega_0^2} e^{2i\omega_0 T_0} + cc . \end{aligned} \quad (2.10)$$

Substituting (2.7) and (2.9) into (2.6) yields

$$\begin{aligned} D_0^2 u_2 + \omega_0^2 u_2 = & - \left[2i\omega_0 D_2 A + D_1^2 A + 2\mu D_1 A + \left(3\alpha - \frac{10\delta^2}{3\omega_0^2} \right) A^2 \bar{A} \right. \\ & + \left. \frac{g^2 A}{2(\Omega^2 - 4\omega_0^2)} \right] e^{i\omega_0 T_0} - \left[\frac{1}{6\omega_0^2} + \frac{1}{\Omega(\Omega-2\omega_0)} \right] \delta g A e^{-2i(\Omega-2\omega_0)T_0} \\ & + \left[\frac{1}{\omega_0^2} - \frac{2}{\Omega^2 - 4\omega_0^2} \right] \delta g A e^{-i\Omega T_0} - \frac{g^2 \bar{A}}{4\Omega(\Omega-2\omega_0)} e^{i(2\Omega-\omega_0)T_0} + cc \\ & + \left[\text{terms having the frequencies } \pm 2\omega_0, \right. \\ & \left. \pm (\Omega - \omega_0), \pm 3\omega_0, \pm (\Omega + 2\omega_0), \pm (2\Omega + \omega_0) \right] . \end{aligned} \quad (2.11)$$

Any particular solution of (2.11) will contain small-divisor terms when $\Omega \approx \omega_0$, $\Omega \approx 2\omega_0$, or $\Omega \approx 3\omega_0$.

To treat the fundamental parametric resonance $\Omega \approx \omega_0$, we introduce the detuning parameter σ according to

$$\Omega = \omega_0 + \varepsilon^2 \sigma , \quad (2.12)$$

and write

$$\Omega T_0 = \omega_0 T_0 + \sigma T_2, \quad (2\Omega - \omega_0)T_0 = \omega_0 T_0 + 2\sigma T_2. \quad (2.13)$$

Then, eliminating the terms that produce secular terms from (2.11) yields

$$\begin{aligned} 2i\omega_0 D_2 A + D_1^2 A + 2\mu D_1 A + \left(3\alpha - \frac{10\delta^2}{3\omega_0^2}\right) A^2 \bar{A} - \frac{g^2 A}{6\omega_0^2} \\ - \frac{5\delta g A^2}{6\omega_0^2} e^{-i\sigma T_2} - \frac{5\delta g \bar{A} A}{3\omega_0^2} e^{i\sigma T_2} - \frac{g^2 \bar{A}}{4\omega_0^2} e^{2i\sigma T_2} = 0, \end{aligned} \quad (2.14)$$

where Ω was replaced with ω_0 . Using (2.9) to eliminate $D_1 A$ from (2.14) yields

$$\begin{aligned} 2i\omega_0 D_2 A - \left(\mu^2 + \frac{g^2}{6\omega_0^2}\right) A + \left(3\alpha - \frac{10\delta^2}{3\omega_0^2}\right) A^2 \bar{A} - \frac{5\delta g A^2}{6\omega_0^2} e^{-i\sigma T_2} \\ - \frac{5\delta g \bar{A} A}{3\omega_0^2} e^{i\sigma T_2} - \frac{g^2 \bar{A}}{4\omega_0^2} e^{2i\sigma T_2} = 0. \end{aligned} \quad (2.15)$$

We can easily verify that (2.9) and (2.15) are the first two terms in a multiple-scales analysis of

$$\begin{aligned} 2i\omega_0 (\dot{A} + \epsilon\mu A) + \epsilon^2 \left[- \left(\mu^2 + \frac{g^2}{6\omega_0^2}\right) A + \left(3\alpha - \frac{10\delta^2}{3\omega_0^2}\right) A^2 \bar{A} \right] - \frac{5\epsilon^2 \delta g A^2}{6\omega_0^2} e^{-i\epsilon^2 \sigma t} \\ - \frac{5\epsilon^2 \delta g \bar{A} A}{3\omega_0^2} e^{i\epsilon^2 \sigma t} - \frac{\epsilon^2 g^2 \bar{A}}{4\omega_0^2} e^{2i\epsilon^2 \sigma t} = 0. \end{aligned} \quad (2.16)$$

At this point it is convenient to express the complex function A in polar form as

$$A = \frac{1}{2} a e^{i\beta}. \quad (2.17)$$

Substituting (2.17) into (2.16) and separating real and imaginary parts yields

$$\dot{a} = -\epsilon\mu a + \frac{5\epsilon^2 \delta g a^2}{24\omega_0^3} \sin\gamma + \frac{\epsilon^2 g^2 a}{8\omega_0^3} \sin 2\gamma, \quad (2.18)$$

$$a\dot{\beta} = \epsilon^2 \left[\left(\frac{\mu^2}{2\omega_0} + \frac{g^2}{12\omega_0^3} \right) a - \alpha_e a^3 \right] + \frac{5\epsilon^2 \delta g a^2}{8\omega_0^3} \cos\gamma + \frac{\epsilon^2 g^2 a}{8\omega_0^3} \cos 2\gamma, \quad (2.19)$$

where

$$\alpha_e = \frac{3\alpha}{8\omega_0} - \frac{5\delta^2}{12\omega_0^3}, \quad \gamma = \epsilon^2 \sigma t - \beta. \quad (2.20)$$

Substituting (2.7) and (2.10) into (2.2) yields

$$u = a \cos(\omega_0 t + \beta) + \epsilon \left\{ \frac{\delta a^2}{6\omega_0^2} \cos(2\omega_0 t + 2\beta) + \frac{ga}{2\Omega(\Omega+2\omega_0)} \cos[(\Omega + \omega_0)t + \beta] \right. \\ \left. + \frac{ga}{2\Omega(\Omega-2\omega_0)} \cos[(\Omega - \omega_0)t - \beta] - \frac{\delta a^2}{2\omega_0^2} \right\} + \dots, \quad (2.21)$$

where a and β are given by (2.18) and (2.19).

It follows from (2.18)-(2.21) that, to the second approximation, the nonlinearity has three effects: (a) a shift $\epsilon^2 \alpha_e a^2$ in the natural frequency, (b) the generation of the second harmonic in the response, and (c) a drift $-\epsilon\delta a^2/2\omega_0^2$ in the response. The last two effects are produced by the quadratic nonlinearity, whereas the frequency shift is a combined effect of the cubic and quadratic nonlinearities according to (2.20). When $\alpha_e > 0$, the frequency increases with amplitude and the nonlinearity is called a hardening nonlinearity. On the other hand, when $\alpha_e < 0$, the frequency decreases with amplitude and the nonlinearity is called a softening nonlinearity. Although the cubic nonlinearity may

have a softening or hardening effect, depending on the sign of α , the quadratic nonlinearity always has a softening effect, regardless of the sign of δ . The overall effect of the nonlinearity depends on the sign and magnitude of α_e , which in turn depends on the sign of α and the relative magnitudes of $|\alpha|$ and $|\delta|$.

Periodic solutions of (2.1) correspond to the fixed points (i.e., constant solutions) of the modulation equations (2.18) and (2.19), which in turn correspond to $\dot{a} = 0$ and $\dot{\gamma} = 0$. It follows from (2.18) and (2.19) that periodic solutions correspond to either $a = 0$ or

$$\mu = \frac{5\epsilon\delta g a}{24\omega_0^3} \sin\gamma + \frac{\epsilon g^2}{8\omega_0^3} \sin 2\gamma, \quad (2.22)$$

$$\sigma + \left[\frac{\mu^2}{2\omega_0} + \frac{g^2}{12\omega_0^3} - \alpha_e a^2 \right] = -\frac{5\delta g a}{8\omega_0^3} \cos\gamma - \frac{g^2}{8\omega_0^3} \cos 2\gamma. \quad (2.23)$$

In this case, for a given σ and g , (2.22) and (2.23) need to be solved numerically to determine a and γ .

To determine the stability of the trivial fixed points, we investigate the solutions of the linearized form of (2.16); that is,

$$2i\omega_0(\dot{A} + \epsilon\mu A) - \epsilon^2\left(\mu^2 + \frac{g^2}{2}\right)A - \frac{\epsilon^2 g^2}{4\omega_0^2} A e^{2i\epsilon^2\sigma t} = 0. \quad (2.24)$$

Letting

$$A = (B_r + iB_i)e^{i\epsilon^2\sigma t} \quad (2.25)$$

in (2.24) and separating real and imaginary parts, we obtain

$$2\omega_0(B_r + \epsilon\mu B_r) - \epsilon^2\left[\mu^2 + \frac{g^2}{6\omega_0^2} + 2\omega_0\sigma - \frac{g^2}{4\omega_0^2}\right]B_i = 0, \quad (2.26)$$

$$2\omega_0(\dot{B}_i + \epsilon\mu B_i) + \epsilon^2\left[\mu^2 + \frac{g^2}{6\omega_0^2} + 2\omega_0\sigma + \frac{g^2}{4\omega_0^2}\right]B_r = 0. \quad (2.27)$$

Equations (2.26) and (2.27) admit solutions of the form

$$(B_r, B_i) = (b_r, b_i)e^{\epsilon\lambda t} \quad (2.28)$$

provided that

$$\lambda = -\mu \pm \frac{\epsilon}{2\omega_0} \left[\frac{g^4}{16\omega_0^4} - \left(2\omega_0\sigma + \mu^2 + \frac{g^2}{6\omega_0^2} \right)^2 \right]^{\frac{1}{2}}. \quad (2.29)$$

Consequently, a trivial fixed point is unstable when

$$\frac{g^4}{16\omega_0^4} - \left(2\omega_0\sigma + \mu^2 + \frac{g^2}{6\omega_0^2} \right)^2 > \frac{4\omega_0^2\mu^2}{\epsilon}. \quad (2.30)$$

Otherwise, it is stable.

To determine the stability of the nontrivial fixed points, we let

$$a = a_0 + a_1(t), \quad \gamma = \gamma_0 + \gamma_1(t), \quad (2.31)$$

where a_0 and γ_0 correspond to a nontrivial fixed point, and a_1 and γ_1 are perturbations which are assumed to be small compared with a_0 and γ_0 . Substituting (2.31) into (2.18) and (2.19) and linearizing the resulting equations, we obtain

$$\dot{a}_1 = \left[\frac{5\epsilon^2 \delta g a_0}{24\omega_0^3} \sin\gamma_0 \right] a_1 + \left[\frac{5\epsilon^2 \delta g a_0^2}{24\omega_0^3} \cos\gamma_0 + \frac{\epsilon^2 g^2 a_0}{4\omega_0^3} \cos 2\gamma_0 \right] \gamma_1, \quad (2.32)$$

$$\begin{aligned} \dot{\gamma}_1 = & - \left[2\varepsilon^2 \alpha_e a_0 - \frac{5\varepsilon^2 \delta g}{8\omega_0^3} \cos\gamma_0 \right] a_1 - \left[\frac{5\varepsilon^2 \delta g a_0}{8\omega_0^3} \sin\gamma_0 \right. \\ & \left. - \left[\frac{5\varepsilon^2 \delta g a_0}{8\omega_0^3} \sin\gamma_0 + \frac{\varepsilon^2 g^2}{4\omega_0^3} \sin 2\gamma_0 \right] \gamma_1 \right. \end{aligned} \quad (2.33)$$

Consequently, a nontrivial fixed point is stable if and only if the real parts of both eigenvalues of the coefficient matrix in (2.32) and (2.33) are less than or equal to zero.

In general, the stability of the fixed points is a continuous function of the system parameters. As one of the parameters of the system, say α or δ or g or ω , is varied, it may happen that the corresponding fixed point may undergo a change in stability. For positive damping (i.e., $\mu > 0$), the system changes stability in one of two ways. First, one real eigenvalue of (2.32) and (2.33) passes from the left to the right half of the complex plane through the origin. This corresponds, under some nondegeneracy conditions (see Guckenheimer and Holmes [1983]), to a turning point in the response curves and gives rise to the jump phenomenon. Second, the eigenvalues of (2.32) and (2.33) are complex conjugates and the fixed points lose their stability as the eigenvalues cross the imaginary axis from the left to the right half of the complex plane. This corresponds to the Hopf bifurcation (see Marsden and McCracken [1986]). Based on the Hopf bifurcation theorem (see Hale [1963]), we expect the modulation equations (2.18) and (2.19) to exhibit limit cycle oscillations near the Hopf bifurcation

parameters and hence the original equation to exhibit amplitude- and phase-modulated motions (i.e., a torus).

2.2 Numerical Results of Approximate Solution

Before considering the system response to a parametric excitation, we investigate the free response. The singular (equilibrium) points of the system are calculated from (2.1) by setting the excitation g and all derivative terms equal to zero. The roots of the reduced equation are then given by

$$u = 0, \frac{1}{2\epsilon\alpha} [-\delta \pm (\delta^2 - 4\omega_0^2\alpha)^{\frac{1}{2}}] . \quad (2.34)$$

For the cases analyzed in the present paper, we chose $\omega_0 = 1.0$, $\alpha = 4.0$, and $\epsilon = 0.10$. When $\delta = 5.0$ there are two stable equilibrium points (foci) and one unstable equilibrium (saddle) point. When $\delta = 4.0$, there are only two equilibrium points since the radical vanishes causing the left focus and saddle point merge to form a cusp (repeated root); when $\delta = 3.0$, the only real root is the origin. Phase plane plots and potential energy diagrams are shown in Figure 2.1 for these three cases. The perturbation analysis was applied to motions about the equilibrium point at the origin.

In the presence of damping and excitation, an approximate expression for the response is given by (2.21). The steady-state response amplitude a and phase γ used to calculate $u(t)$ are determined numerically from (2.22) and (2.23). The value of γ is determined numerically from

$$\begin{aligned}
F(\gamma) = & \sigma + \frac{\mu^2}{2\omega_0} + \frac{g^2}{12\omega_0^3} - \alpha_e \left(\frac{24\omega_0^3\mu}{5\epsilon\delta g \sin\gamma} - \frac{3g \sin 2\gamma}{5\delta \sin\gamma} \right)^2 \\
& + \frac{5\delta g \cos\gamma}{8\omega_0^3} \left(\frac{24\omega_0^3\mu}{5\epsilon\delta g \sin\gamma} - \frac{3g \sin 2\gamma}{5\delta \sin\gamma} \right) + \frac{g^2 \cos 2\gamma}{8\omega_0^3} = 0, \quad (2.35)
\end{aligned}$$

and then the amplitude a is calculated directly from (2.22). The stability of each solution, including the trivial solution, is determined from (2.30), (2.32), and (2.33). In the following discussion, we examine how the response depends on the system parameters. Since we are examining the response near the singular point at the origin, only the first case with one equilibrium point (of the system parameters shown in Figure 2.1) will be considered. All three cases have stable trajectories about the origin which are quite similar in nature. The differences become apparent when the amplitude of the motion becomes large enough to be affected by the homoclinic orbit (i.e., the separatrix of the unforced, undamped system); however at these amplitudes, the small amplitude assumption underlying the perturbation solution ceases to be valid. The latter portion of this paper discusses two techniques for investigating large amplitude responses and considers the third case which has three equilibrium positions.

The effect of the excitation g is determined in the manner described above; that is, by solving for the roots of (2.35) and calculating the amplitude a as g is varied. The results of one choice of system parameters are shown in Figure 2.2. There are several interesting features characterizing the response. As expected, the

excitation amplitude must exceed a threshold (critical) value in order to excite a parametric resonance. Neglecting the nonlinear terms, we find from (2.24)-(2.30) that the threshold value predicted by the linear theory is given by (2.30) with the inequality sign being replaced with an equality. In this case, the linear threshold value is $g_3 = 10.6006$. It follows from Figure 2.2 that the threshold value predicted by the linear analysis is higher than the threshold value $g_1 = 9.8321$ predicted by the nonlinear analysis, a phenomenon called sub-critical instability. Another interesting feature of the response is that there are four bifurcation values of g that divide the g axis into five distinct intervals. In region I ($g < g_1$), there is only one trivial solution which is stable. In II ($g_1 < g < g_2$, where $g_2 = 10.3327$), there are three possible solutions: the trivial solution, which is stable, and two nontrivial solutions, the larger of which is stable. In III ($g_2 < g < g_3$), there are five possible solutions: the trivial solution, which is stable, and four nontrivial solutions, two of which are stable. In IV ($g_3 < g < g_4$, where $g_4 = 11.1394$), there are also five possible solutions: the trivial solution, which is unstable, and four nontrivial solutions, three of which are stable. In V ($g > g_4$), there are three possible solutions: the trivial solution, which is unstable, and two nontrivial solutions, which are stable.

The interesting behaviors in Figure 2.2 were verified by numerically integrating both the amplitude- and phase-modulation equations (2.18) and (2.19) and the original governing equation (2.1) using a 5th and 6th order Runge-Kutta-Verner algorithm. For $g = 5.0$,

the perturbation solution predicts one solution -- a stable trivial solution (region I). The long-time solution of the original equation (2.1) shown in Figure 2.3 verifies the perturbation result. When $g = 15.0$ (region V), we found two steady-state amplitudes of vibration, again verifying the perturbation analysis.

The most interesting behavior occurs in regions II, III, and IV of Figure 2.2. In region IV, the perturbation solution predicts three stable and two unstable responses. The long-time behavior of the solutions of the modulation equations (2.18) and (2.19) is shown in Figure 2.4, and we see three stable steady-state amplitudes, as predicted by the analysis. We note that the trajectory that is attracted to the largest fixed point (corresponding to the largest steady-state response) may spend some time in the neighborhood of the unstable nontrivial fixed point on its way. The three solutions (attractors) predicted by the perturbation analysis for $g = 11.0$ and calculated using (2.21) are shown in Figure 2.5. The corresponding attractors obtained by numerically integrating (2.1) are shown in Figure 2.6. We note the striking similarity in the qualitative nature of each of the small attractors. The long-time traces of the perturbation solutions in Figure 2.5 and the numerical simulations in Figure 2.6 are superimposed in Figure 2.7. Even though ϵ is quite large, the approximate solution accurately predicts the number and the nature of the solutions and suffers only in accurately predicting the steady-state amplitude. Surprisingly, the largest response amplitude has the least peak-to-peak error.

Figure 2.8 shows a typical frequency-response curve. In this case, the nonlinear frequency shift is $\varepsilon^2 \alpha_e a^2 = -2.25\varepsilon^2 a^2$ and hence the overall nonlinearity of the system is of the softening type as seen in the figure. This is due to the quadratic nonlinearity even though the coefficient of the cubic nonlinearity is positive (hardening). There are five bifurcation values of σ that divide the σ axis into six distinct intervals. When $\sigma > \sigma_5$, where $\sigma_5 = 24.3657$, only the trivial solution is possible, which is stable. When $\sigma_4 < \sigma < \sigma_5$, where $\sigma_4 = 20.5624$, there are three possible solutions: the trivial solution, which is stable, and two nontrivial solutions, the larger of which is stable. When $\sigma_3 < \sigma < \sigma_4$, where $\sigma_3 = 7.0372$, there are five possible solutions: the trivial solution, which is stable, and four nontrivial solutions, two of which are stable. When $\sigma_2 < \sigma < \sigma_3$, where $\sigma_2 = 6.3027$, there are five possible solutions: the trivial solution, which is stable, and four nontrivial solutions, three of which are stable. When $\sigma_1 < \sigma < \sigma_2$, where $\sigma_1 = -45.5372$, there are three possible solutions: the trivial solution, which is unstable, and two nontrivial solutions, both of which are stable. When $\sigma < \sigma_1$, there are three possible solutions: the trivial solution, which is stable, and two nontrivial solutions, one of which is stable.

The effect of the strength of the perturbation coefficient ε on the steady-state amplitude is shown in Figure 2.9. It shows a behavior similar to that of Figure 2.2.

The effect of damping on the response is shown in Figure 2.10. From this figure we conclude that a fundamental parametric resonance can be excited only if the damping coefficient is below a certain critical value. This critical value is larger than that predicted by the linear analysis (i.e., corresponding to the loss of stability of the trivial solution).

Next, we discuss the influence of the coefficients α and δ of the cubic and quadratic nonlinearities on the steady-state amplitude. As discussed earlier, the nonlinearities influence the steady-state amplitudes through the nonlinear frequency shift $\varepsilon^2 \alpha_e a^2$, where α_e is defined in (2.20). When $\alpha_e = 0$, the influence of the nonlinearity on the steady-state amplitude disappears and the parametric resonance produces an exponential growth of the response if condition (2.30) is satisfied. This growth is not limited by the damping and only nonlinearities can limit it. The larger α_e is, the larger is the limiting effect and hence the the steady-state amplitude is smaller. We note that the present analysis is not valid when $\alpha_e \approx 0$, and higher-order nonlinear effects must be included to limit the response.

The effect of the coefficient α of the cubic nonlinearity on the system response is shown in Figure 2.11. It is asymmetric with respect to the origin. The effect of the coefficient δ of the quadratic nonlinearity on the system response is shown in Figure 2.12. It is symmetric with respect to the origin. We note that it is only the larger of the two amplitudes that is affected when α_e approaches zero. Outside this region, the large amplitude predicted by the perturbation

solution can be more accurate than the small "unaffected" amplitude, as seen in Figure 2.7.

In summary, we have seen in this section that the perturbation solution predicts the complete nature of the response, including the total number of steady-state solutions and their qualitative features. As the perturbation coefficient ϵ gets larger, or the effective nonlinearity α_e approaches zero, the perturbation solution breaks down. We have also seen that even if the qualitative features of the perturbation solution in the phase plane deteriorate for the larger amplitude response, the peak amplitude of vibration predicted by the perturbation solution may be quite accurate.

2.3 Analogue Computer Simulation

The perturbation solution is good for small amplitude motions about one of the foci and improves as the value of ϵ decreases. In general, when there is more than one focus, the free motion can be attracted to any of the stable foci. Figure 2.1 shows three classes of solutions. For the analysis in this section and the next, we consider the more interesting case of two foci and one saddle shown in Figure 2.1(c), corresponding to a double-well potential. In addition to small amplitude oscillations about the focus at the origin, we allow oscillations about the other focus and large amplitude motions encircling both foci and the saddle point.

Equation (2.1) was simulated on an analogue computer for fixed values of ϵ , δ , α , μ , ω_0 , and Ω . Although many experiments were

performed varying all of the parameters, we present here only the free response and the effect of varying the magnitude g of the parametric excitation. The laboratory setup is shown in Figure 2.13 and the computer program is shown in Figure 2.14.

The analogue computer, although not as accurate as the digital computer, was extremely useful in several areas. For example, to locate the separatrices and equilibrium positions, we used the repetitive operate mode. This mode automatically cycles the computer from the initial conditions to the run mode, so that the response trajectory can be observed up to several times a second on the oscilloscope, depending on the selected integration time. The time in the fast mode was scaled to run 400 times faster. The initial displacement and velocity can be easily changed so that locating the equilibrium positions (point attractors) and separatrices usually takes no more than a few minutes. The slow speed mode is used to make a permanent copy of the solution on the analogue plotter. When the system is forced, the steady-state response may be a point, a limit cycle, a torus, or a chaotic attractor. When multiple attractors coexist, the initial conditions determine the final state. The attractors and their domains (basins) of attraction can be quickly mapped out on the analogue computer if the boundaries are not fractal.

Near the bifurcation points, achieving a steady-state solution requires many cycles, and this can be expensive on a digital computer. For example, to achieve a steady-state solution may require 50,000 cycles (of the excitation) with 100 points per cycle using a 5th and 6th

order Runge-Kutta-Verner algorithm. However, on the analogue computer, these bifurcation points can be easily located. Only seconds are needed to achieve a steady-state solution when operating in the high speed mode. Once a steady state has been achieved, any system parameter can be varied continuously, thus only slightly disturbing the system from its steady-state response. In this manner, an attractor that has a very small domain of attraction and/or domain of existence may be realized by starting with system parameters that enlarge its domain of attraction and/or existence. This approach must be used to analyze a particular attractor near the bifurcation values because its domain of existence and domain of attraction are extremely small. Otherwise the transient response may have sufficient disturbance to prevent the trajectory from settling onto the desired attractor, even if the initial conditions are chosen on the attractor itself! We found that initial conditions on the positive displacement axis (i.e., zero velocity) coinciding with the trajectory are the best ones for attracting specific limit cycles, because the ensuing motion of the system followed the steady-state trajectory quite closely. This approach had to be used to attract some of the exotic trajectories such as the tripled period (3x) trajectory. Otherwise, we might have to wait up to one hour (in the slow mode) for some of the trajectories to settle down to their steady state.

Equation (2.1) was programmed on the analogue computer with the parametric term programmed as a van der Pol oscillator (to maintain a constant amplitude). Figure 2.15 shows the results of varying only the amplitude of the excitation. These results show multiple attractors

(steady-state solutions), including the simultaneous coexistence of a limit cycle and a chaotic response, the familiar period doubling bifurcations leading both to chaos and extinction, and unexpected 3x, 6x, 7x, and 12x bifurcations. In addition, the frequency spectra obtained by an FFT analyzer are shown in column B for the large-amplitude attractors enclosing the three equilibrium positions, in column C for the small-amplitude attractors encircling the right focus, and in column D for the nontrivial attractor enclosing the left focus. For the larger excitations, enlarged trajectories about the origin are shown in column D since the two limit cycles overlap, making it difficult to distinguish between the two.

The free response of the system is shown in Figure 2.15(a)-A, where portions of the two inbound separatrices are shown. If the separatrices were extended further, the figure would take on an appearance similar to that of the shell plot in Dowell and Pezeshki [1986]. The narrow banded region between the two separatrices is the domain of attraction of the origin and the wide region between the separatrices is the domain of attraction of the left focus. This phase plane plot locates all equilibrium points: two stable foci at -10.0 and 0.0 and one unstable saddle point at -2.5. The displacement vs. time for the upper separatrix approaching the saddle point and going to the two foci is shown in Figure 2.15(a)-C. Note that the frequency of the free response about the origin is nearly one-half that of the left focus. Since the analogue computer is a physical device, it is not possible to get on the separatrix exactly. We got as close as possible,

then in the repeated runs we saw the solution going to the left or right focus in a random fashion. Sometimes it would set on the saddle point for 30 seconds (in the slow mode), but eventually would leave, as expected. As the excitation is increased from zero, the left equilibrium position becomes an attractor for limit cycles that have the same frequency as the excitation because it has in addition to the parametric excitation an external excitation driving the system at the excitation frequency. The origin however, remains a point attractor because it is purely a parametric resonance which requires a critical amplitude of excitation before a response can occur.

As g is increased, a new limit cycle becomes stable--one that encloses all three equilibrium positions. Figure 2.15(c) shows two limit-cycle attractors and a point attractor. Since all three of them are stable, the initial conditions will determine the response. By the time g reaches 6.0 the left limit cycle vanishes; this happens when the limit cycle trajectory gets close to the separatrices. The trajectory crosses over and is instantly attracted to the larger limit cycle that encloses all the equilibrium positions.

A period doubling bifurcation is easily seen by the time $g = 6.25$ in Figure 2.15(d). The usual splitting of the trajectory is seen, and the octave between ω and 2ω is observed to split into two equal parts by the presence of a spectral line at $3\omega/2$. In fact, all the octaves are observed to divide into two equal parts. The presence of the spectral line at $\omega/2$ (subharmonic bifurcation) shows that the period has now doubled. In Figure 2.15(e), the bifurcated trajectory becomes more

established, and the magnitudes of these halving spectral lines consequently increase. Increasing g further causes the previous pattern to repeat; a splitting of each of the previous harmonic bands into two bands. Now, the first spectral line occurs at $\omega/4$, implying a period quadrupling, as shown in Figure 2.15(f). We anticipate that this series of bifurcations, if continued, would lead to chaos. The numerical simulation shows what may be chaos, and it is possible that we do have chaos before the trajectory becomes unstable, but the range of g is so small, that it was not observed; instead, the trajectory bifurcated a number of times and became unstable. So, in this case the bifurcations end in an extinction. Figure 2.15(g) shows that the only limit cycle occurs at the origin.

When an outer limit cycle does again become stable, it appears as a period doubled trajectory, but it takes on a new loop because a strong attraction still exists at the left focus. We see that it is that part of the trajectory coming the closest to the focus that is affected. This trajectory becomes stable for $g = 11.3$, and is shown for $g = 11.5$ in Figure 2.15(h). Increasing g causes period doubling bifurcations leading to chaos, as shown in Figures 2.15(i)-2.15(k). Figure 2.15(j) shows what appears to be a chaotic response, but upon a closer examination it shows that the final steady-state response is only the limit cycle about the origin. This is sometimes called transient chaos in the literature. Increasing g causes the outer limit cycle to reappear, only to repeat the period doubling bifurcations leading to chaos. This is shown in Figures 2.15(l) -2.15(p).

An unexpected limit cycle appears in an island bounded by chaos on both sides, as shown in Figures 2.15(p)-2.15(s). Figure 2.15(q) shows a 6x limit cycle. This is a marked departure from the previous 2x, 4x, 8x, etc., pattern usually encountered and well documented in the literature. This trajectory bifurcates in the normal manner into a 12x limit cycle. Further bifurcations eventually lead to chaos.

Two other unexpected limit cycles appear, again bounded by chaos on either end, and are shown in Figures 2.15(t)-2.15(w). Figure 2.15(u) shows a 7x limit cycle, and Figure 2.15(v) shows a 3x limit cycle. The spectra of these two attractors show that the octave between 0 and ω is divided into 7 bands (6 spectral lines) and into 3 bands (2 spectral lines), respectively. The transition (caused by very slowly varying g) from chaos to 7x and from 3x to chaos was observed to be a jump phenomenon; we did not observe the normal period doubling bifurcations. Likewise, the transition from 7x to 3x and from 3x to 7x was also observed to be a jump phenomenon. Increasing g very slowly and then decreasing it very slowly showed that there were regions of coexistence (overhangs) of different attractors, thereby giving rise to the jumps.

Increasing g further shows another island of non-chaotic response in the midst of chaotic motion. Figures 2.15(x)-2.15(aa) show the banding of the chaotic response leading eventually to another tripled period limit cycle which eventually jumps into chaos.

Figures 2.15(bb)-2.15(dd) show the system response coming out of chaos through the normal period demultiplying bifurcations, culminating

in yet another new limit cycle. The limit cycle surrounding just the origin has maintained stability throughout the entire range of g , and aside from the small lobe, it has simply increased in amplitude. It is a separate attractor from the larger outer attractor, even though they seem to overlap. Although we have not shown it here, further increases in g causes this outer attractor to bifurcate again, become unstable, and eventually give rise to yet another new limit cycle that encircles all three equilibrium positions.

There is a second outer attractor coexisting with the previous outer attractor (shown in Figure 2.15(x) and following) that is distinctly different but having the same period as the excitation, and it contains the same frequency components. This attractor becomes stable for $g \geq 25.0$ and exists through $g = 50.0$, although it changes profile and bifurcates before it becomes unstable. We did not study this or other large excitation responses in detail on the analogue computer. Two of these limit cycles are shown in Figures 2.15(ee) and 2.15(ff), and more are shown later in the next section.

Figure 2.15(q) shows a 6x period response for $g = 20.57$. When $g = 26.3$, the 3x response of Figure 2.15(z) experiences a period doubling bifurcation, resulting in a 6x period response. Although the spectral components are at the same frequencies, their magnitudes are quite different.

Figure 2.16 shows selected time histories of the attractors described in Figure 2.15, with the relative phase between the excitation and the response preserved. The period multiplying bifurcations of the

response are not as obvious on the time history plots as they are on the phase plane plots, but careful examination of the amplitudes of the peaks will reveal the bifurcations.

There are at least two more solutions that are not documented here, one encircling the left focus approaching the separatrix and a second encircling the origin coexisting with the limit cycle shown above. The two attractors at the origin were discussed in Section 2.2.

In summary, we were able to gain insight into the various attractors, locate their domains of existence, and map out their domains of attraction much more quickly on the analogue computer than on the digital computer. In fact, we found some solutions on the analogue computer that we missed on the digital computer; consequently we went back and found them on the digital computer. With the help of the analogue computer, we were able to locate the domains of attraction using the digital computer.

We were also able to vary the excitation (and all other parameters as well) after achieving a steady-state condition. This is something not usually done on the digital computer. With the real time solution being displayed on the oscilloscope, the visual impact of a bifurcation accompanied by the instantaneous change of the frequency spectrum displayed in real time is quite illuminating and fascinating.

We did not achieve exact numerical correspondence in the value of g from the simulation on the digital computer with those on the analogue computer because there are many variables in this problem. It appears that all the error was associated with the value of g because it was the

system parameter that was varied. Actually, there is some error in all of the other parameter settings, and it simply appears to be accumulated in the setting of g . The trends, trajectories, and bifurcations were observed on the digital computer also, but at slightly different values of g .

There still remain some details that need attention to improve the analogue computer results in accuracy and consistency at the fast and slow speeds. We experienced slight variations in the day-to-day results of identical tests when we were near critical points. Even though this is a fairly simple one-degree-of-freedom problem, the computer program uses a number of amplifiers, resistors, capacitors, and multiplier networks, each with its own peculiarities and drift rates, that contribute to accuracy and repeatability problems. For this reason the analogue computer, as an experimental apparatus, is best used as an instrument to locate and observe all possible solutions and map out trends. Then, we can use the digital computer to finalize the results if greater precision is needed.

2.4 Digital Computer Simulation

Equation (2.1) was simulated on the digital computer using a 5th and 6th order Runge-Kutta-Verner algorithm. The effect of varying the amplitude of the excitation and the initial conditions was studied in great detail, with only representative figures shown below. For chaotic and bifurcated responses, Poincaré maps were also plotted. This analysis essentially parallels that of the analogue computer simulation

and provides the numerical accuracy that is not available on the analogue computer.

For small values of g , we found three attractors: two limit cycles and a fixed point at the origin (other attractors exist for limited ranges of system parameters, e.g., Figure 2.6). These are shown in Figure 2.17. That there are three attractors immediately raises the question regarding their domains of attraction. Figure 2.18 shows three different initial conditions leading to the three different attractors. By repeating this procedure over the domain ranging from $-25 \leq u \leq 10$ and $-10 \leq \dot{u} \leq 10$ and assigning a color code to the three solutions, a map showing the domains of attraction can be plotted as shown in Figure 2.19. The color red denotes trajectories attracted to the left inner limit-cycle, black denotes the large outer limit-cycle, and white denotes the trivial attractor at the origin. From this figure we see that the basins are fractal because there are no well defined boundaries separating the domains of attraction, as was observed in Figure 6.10 in Chapter VI. Even if a finer resolution were used, they would still appear as continuous but intertwined domains of attraction. If we continue to enlarge a small section, it will display a well defined structure. We conclude, then, that this system is quite sensitive to initial conditions. Even changing the step size or the error tolerance in the algorithm affected the steady-state response to which the system was attracted when the chosen initial conditions were near a boundary.

In the following discussion, we show other responses that, for the most part, were not discussed in the analogue computer simulation. The

large outer trajectory is the most interesting attractor because it experiences several stages of period multiplying bifurcations, leading both to chaos and extinction. One sequence leading to extinction occurs when $g = 5.80$; at this level a period doubling is visible in the phase plane. By the time $g = 6.50$, another doubling occurs, followed by increased banding, and by the time $g = 6.80$, the attractor appears to be chaotic. However, the Poincaré map shows only a small attractor, as shown in Figure 2.20. It is possible that we are seeing a finite number of period doubling bifurcations. By the time $g = 7.00$, this attractor has become unstable and vanished, leaving only the point attractor at the origin, as was observed in Figure 2.15.

When this outer trajectory again appears, it exhibits a period doubled bifurcation (as seen in Figure 2.15). Increasing g causes further period multiplying bifurcations, leading to chaos at $g = 13.0$. At $g = 15.0$, we have a stable double period trajectory that experiences the previously observed period doubling bifurcations, leading to chaos when $g = 19.0$. Figure 2.21 shows this strange attractor in the phase plane and corresponding Poincaré map. The state of the system chosen for this Poincaré map corresponds to the maximum value of the excitation (phase $\phi = 0.0$). Figure 2.22 shows eight discrete Poincaré maps at different phases of the excitation. Although it appears as eight disjointed maps, it actually changes smoothly as ϕ varies from 0° to 360° .

Figure 2.23(a) shows the limit-cycle attractor at the origin experiencing its first period doubling bifurcation when $g = 29.8$; when g

= 30.5, Figure 2.23(b) shows the bifurcation to be well established and on the verge of disappearing. For larger values of g , this attractor becomes unstable and gives rise to yet a new larger limit-cycle attractor that encircles the origin once and then executes a trajectory that encircles both foci. This bifurcation is quite unusual because one normally sees an entire trajectory becoming unstable, causing something drastic to happen. In this case, only a portion of the trajectory becomes unstable (i.e., one of the two orbits constituting the periodic cycle) and bifurcates; the other (i.e., the inner) portion of the trajectory remains essentially as it was.

Another outer trajectory appears simultaneously (when using appropriate initial conditions) when $g = 24.0$ and continues as g increases. Although it has a small loop, it has a period equal to that of the excitation (see Figures 2.15(ee) and 2.16(ee)). Figure 2.24 shows three different response trajectories for increasing levels of excitation for this alternate outer trajectory.

Figure 2.21 shows the original outer trajectory in a chaotic state. When g is increased, this trajectory eventually settles down to a 5x response when g approaches 24.0. This is shown in Figure 2.25 with the corresponding Poincaré map showing five points. Note that this 5x response exists at the same level of excitation as the 1x response shown in Figure 2.24. The initial conditions determine which attractor will be achieved. We could not obtain this 5x solution on the analogue computer. Holmes [1979] was able to obtain a 5x solution on the analogue computer using a Duffing equation.

Figure 2.26 shows the numerical simulation of the $7x$ response seen in the analogue computer simulation in Figure 2.15(u); it required over 3000 cycles to finally settle down. The Poincaré map shows 7 points.

2.5 Chapter Summary

The method of multiple scales was used to obtain a uniform second-order expansion for the response of a one-degree-of-freedom system with quadratic and cubic nonlinearities to a fundamental parametric excitation. Steady-state solutions were obtained for small but finite amplitude oscillations around the origin, and it was shown that the results qualitatively describe the system response for the parameters chosen. For large amplitude oscillations, the equation was integrated on both the digital and analogue computers. The response of the system modeled on the analogue computer was analyzed using a Fast Fourier Transform (FFT) Analyzer.

The perturbation solution predicts a threshold value of the amplitude g of the excitation for which a fundamental parametric resonance about the origin can be excited; it also predicts a subcritical instability. The perturbation solution predicts the number of stable limit cycles and qualitatively agrees with the digital and analogue computer simulations, especially for the smaller amplitudes of vibration.

The more interesting problem is the case of the double-well potential, having a stable limit-cycle attractor in each well (at different levels of excitation) and a large amplitude attractor about

both foci consisting of stable limit cycles and chaotic oscillations. Most attractors were observed on both the digital and analogue computers. The analogue computer was found to be extremely useful in locating possible attractors and defining their domains of attraction and existence. Once a trajectory was established, it was possible to locate its bifurcations by slowly varying any of the system parameters. The bifurcated and chaotic responses were observed on the oscilloscope and FFT analyzer. Although the analogue computer is a useful tool in the study of nonlinear systems, it does not have the numerical accuracy of a digital computer, which was used to determine more accurately the bifurcations after the survey work was completed on the analogue computer.

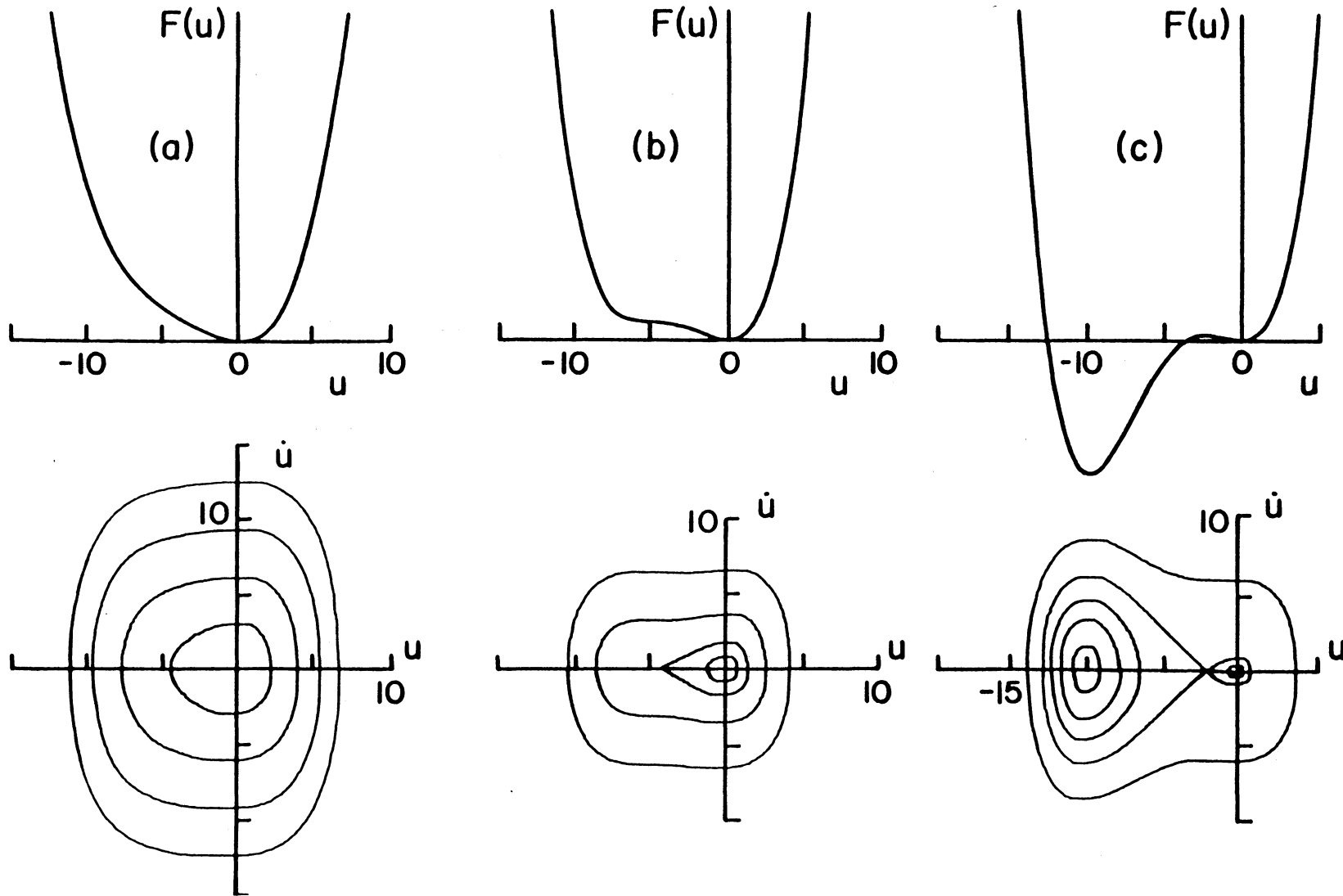


Figure 2.1 Potential wells and corresponding phase-plane portraits for three distinct cases: (a) $\delta = 3.0$, (b) $\delta = 4.0$, and (c) $\delta = 5.0$ for $\alpha = 4.0$, $\mu = 1.0$, $\epsilon = 0.10$. The phase-plane portraits were obtained using the analogue computer.

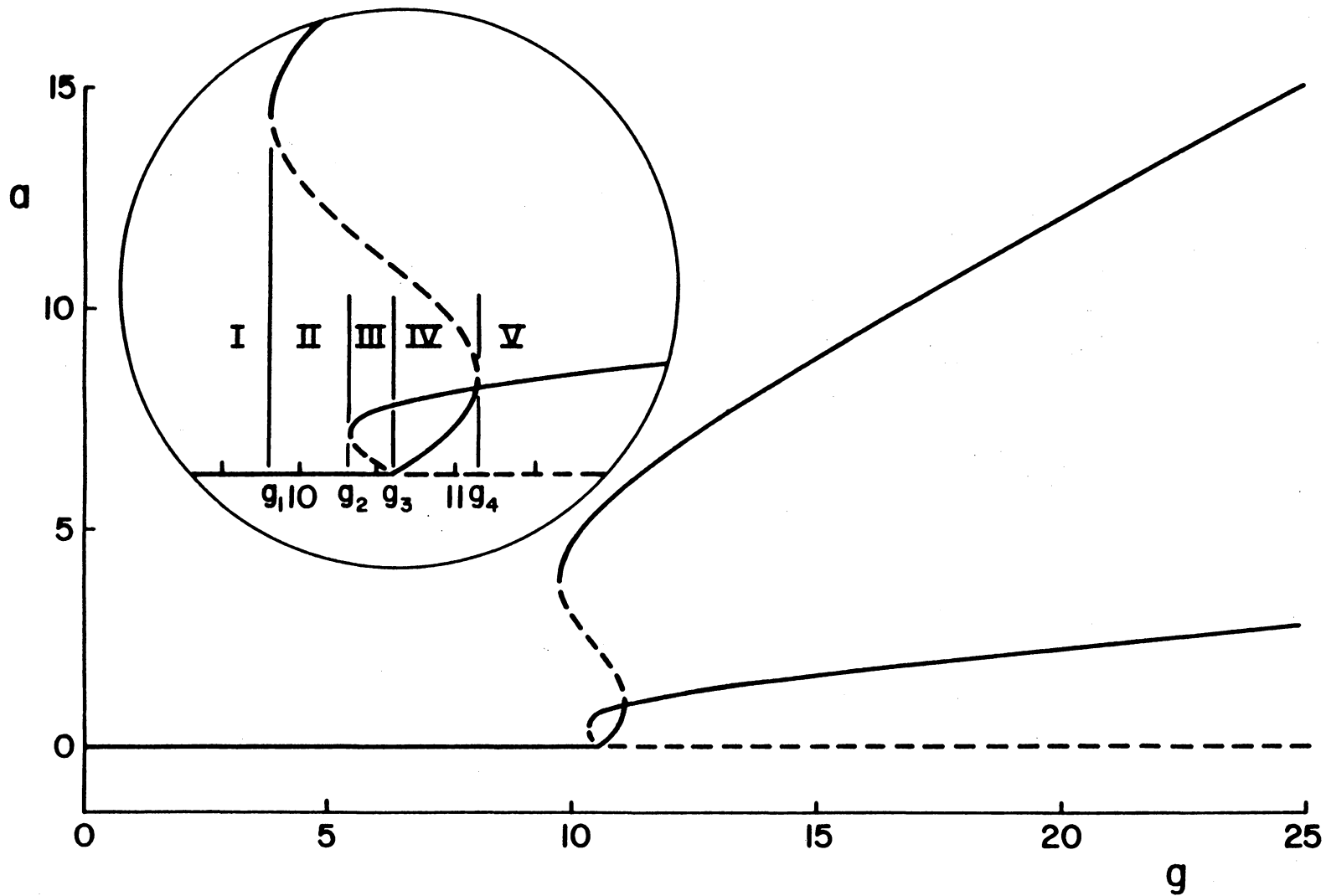


Figure 2.2 Variation of the steady-state response amplitude a with the excitation g :
 (—) stable, (---) unstable, $\sigma = 0.0$, $\alpha = 4.0$, $\delta = 3.0$, $\mu = 1.0$, $\epsilon = 0.10$.

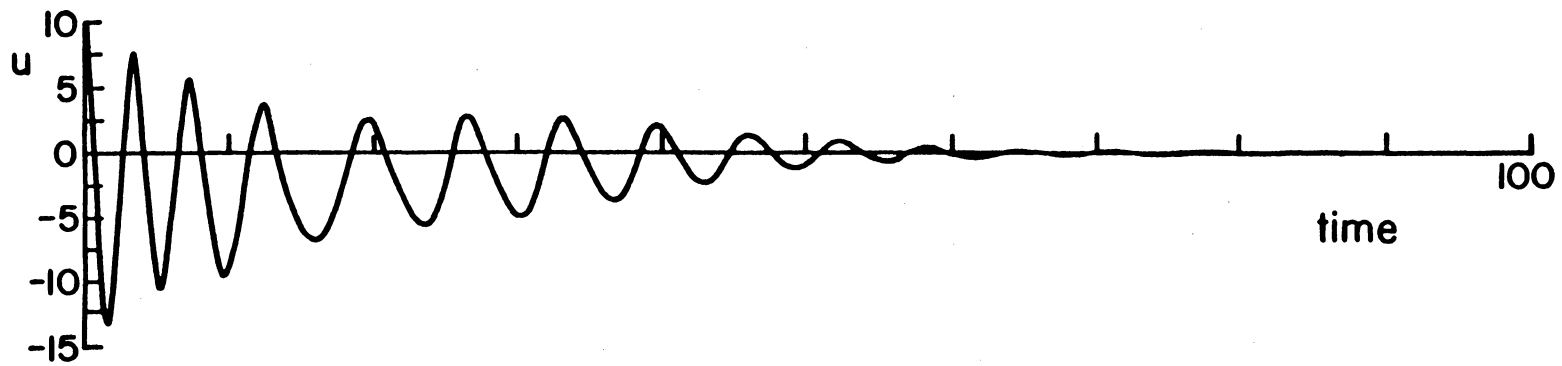


Figure 2.3 Time history of u showing the response decaying to the stable trivial response, as predicted by the perturbation solution: $\sigma = 0.00$, $\alpha = 4.0$, $\delta = 3.0$, $\mu = 1.0$, $g = 5.0$, $\epsilon = 0.10$.

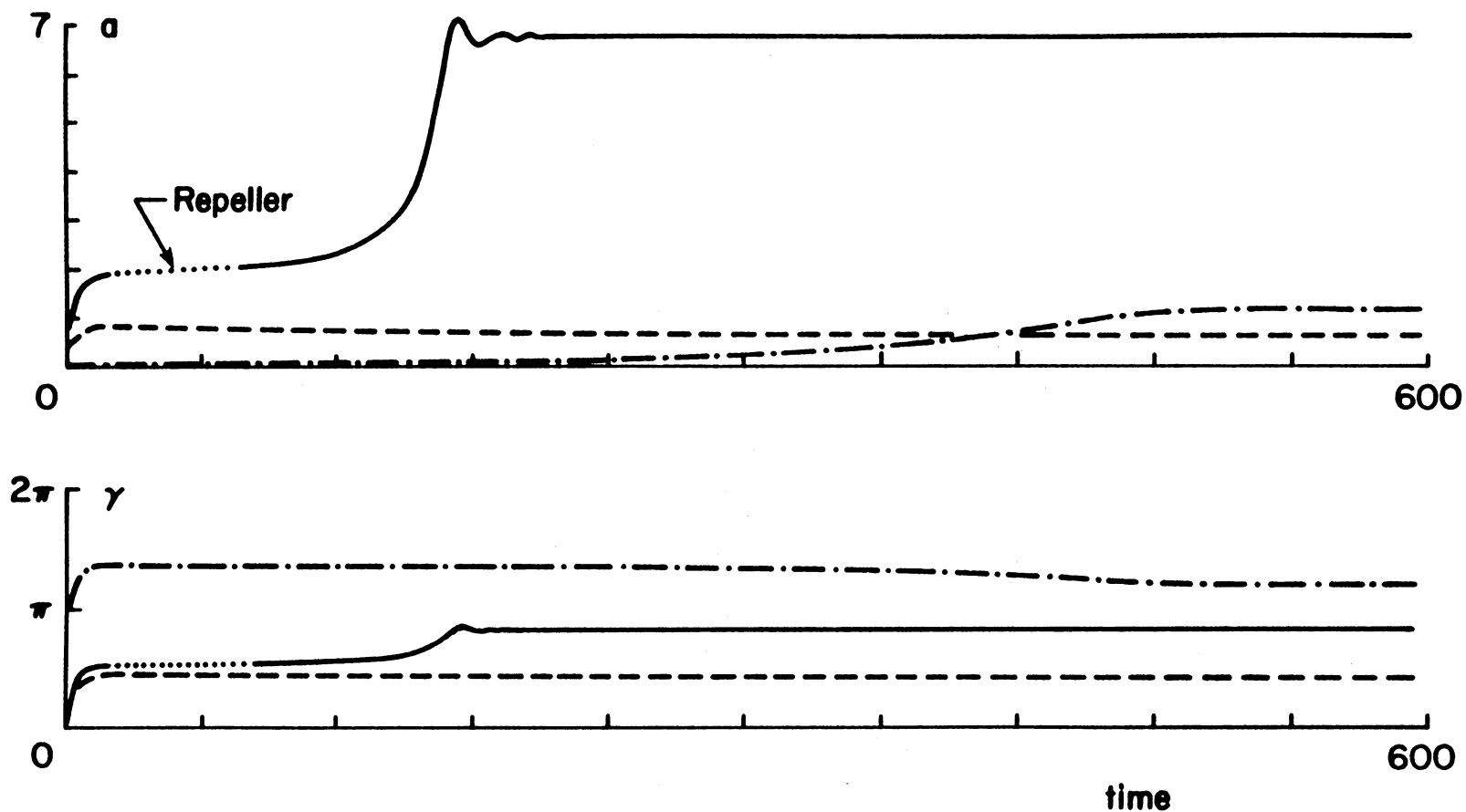


Figure 2.4 Long-time history of the amplitude and phase, obtained by numerically integrating the amplitude- and phase-modulation equations (2.18)-(2.20): $\sigma = 0.0$, $\alpha = 4.0$, $\delta = 3.0$, $\mu = 1.0$, $g = 11.0$, $\epsilon = 0.10$. The three attractors correspond to the three stable solutions shown in Figure 2.2 at $g = 11.0$ (region IV). The largest amplitude response is first attracted to the unstable solution before arriving at its steady state. The steady-state amplitudes are (---) 0.623, (-.-) 1.078, and (—) 6.763 and correspond to Figures 2.5(a), 2.5(b), and 2.5(c), respectively.

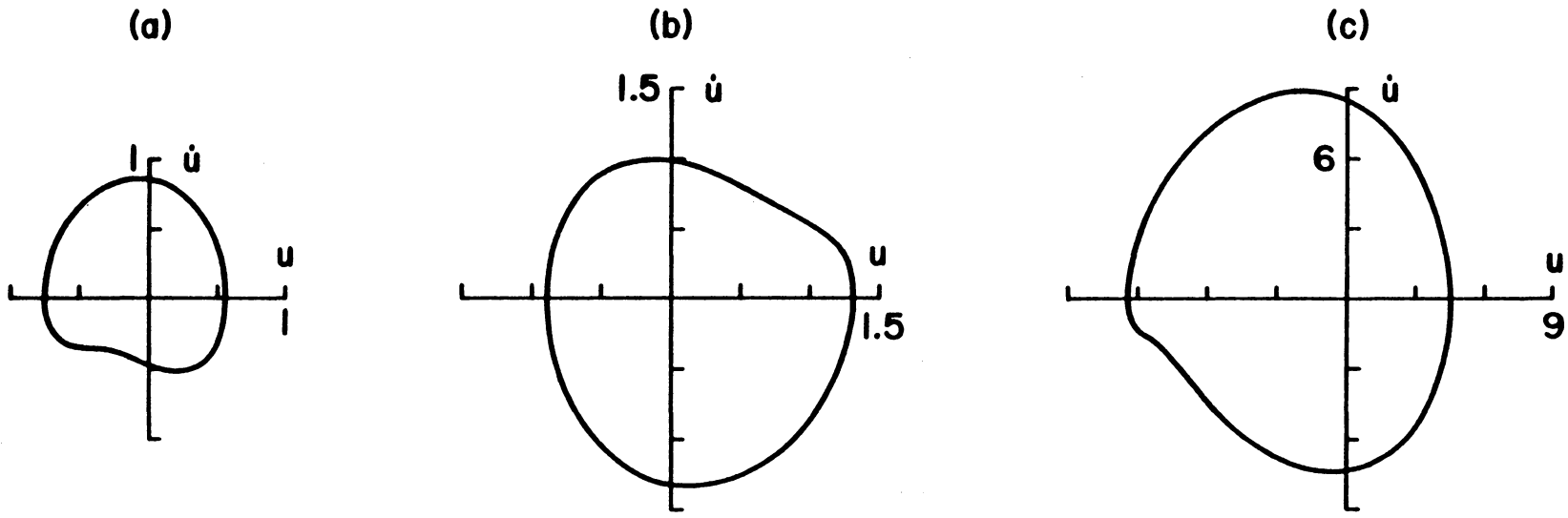


Figure 2.5 Phase-plane portraits of the three steady-state solutions predicted by the perturbation solution shown in Figures 2.2 and 2.4: $\sigma = 0.0$, $\alpha = 4.0$, $\delta = 3.0$, $\mu = 1.0$, $g = 11.0$, $\epsilon = 0.10$.

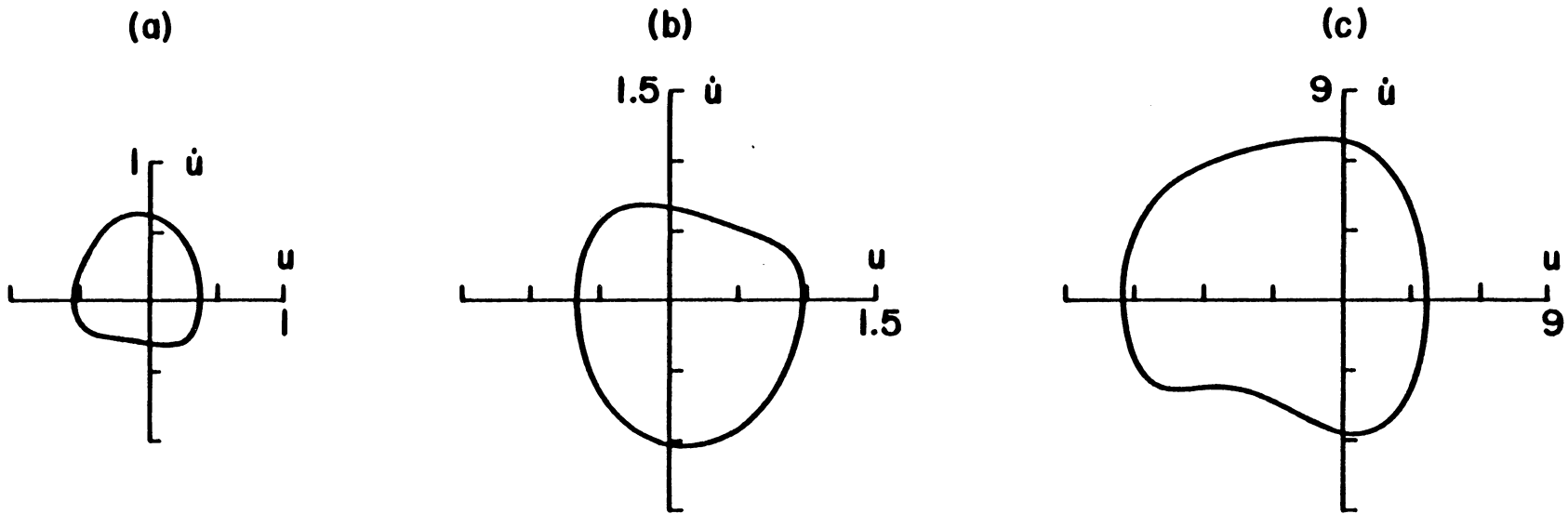


Figure 2.6 Phase-plane portraits of the three steady-state solutions obtained by numerical integration of (2.1) for the system parameters used in Figure 2.5.

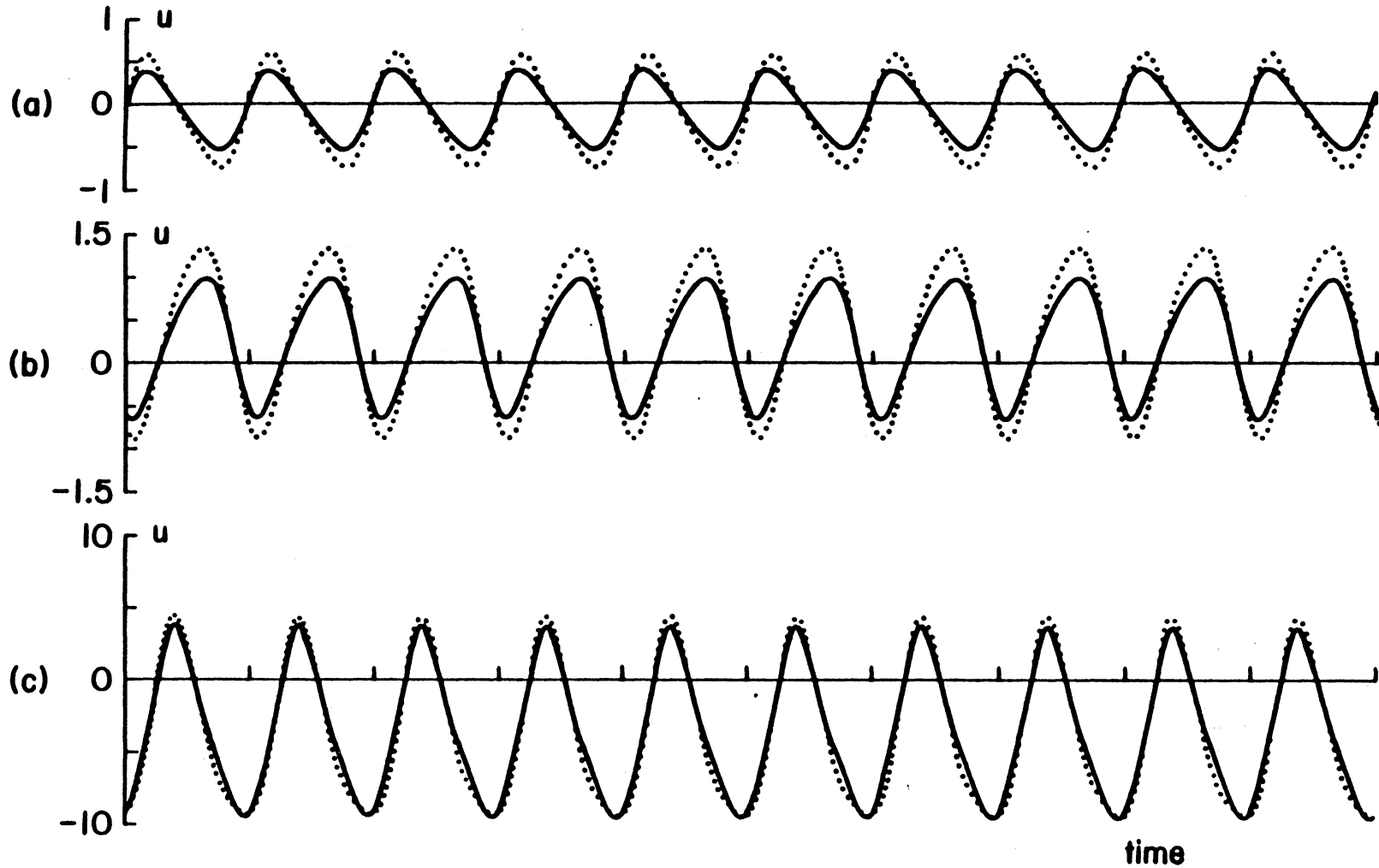


Figure 2.7

Comparison of the time history of the response obtained using the perturbation solution (\dots) with that obtained by numerically integrating (---) the original equation for the three distinct solutions shown in Figures 2.2, 2.4, 2.5, and 2.6.

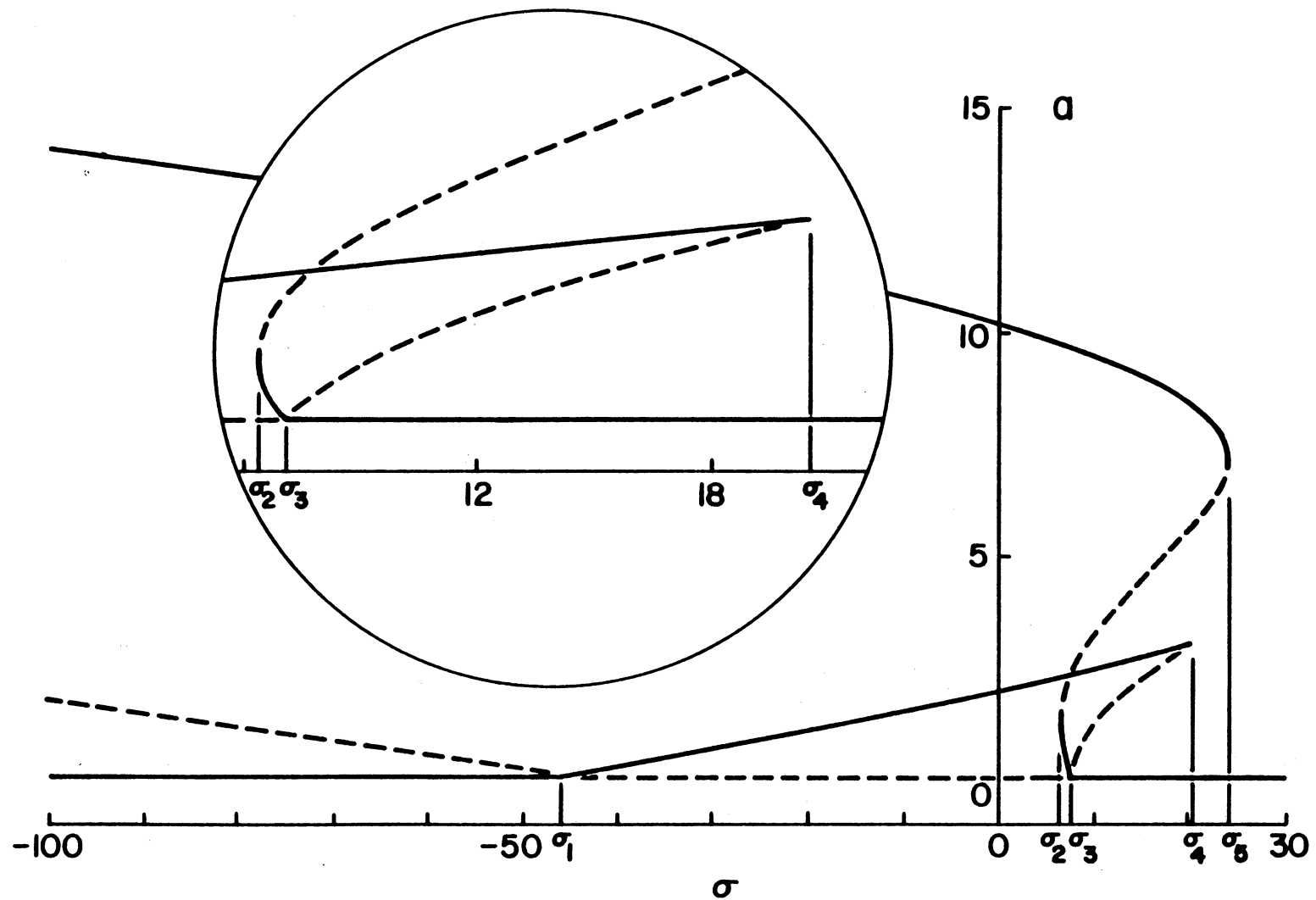


Figure 2.8 Variation of the steady-state amplitude a with the frequency detuning σ : (—) stable, (---) unstable, $\alpha = 4.0$, $\delta = 3.0$, $\mu = 1.0$, $g = 15.0$, $\epsilon = 0.10$.

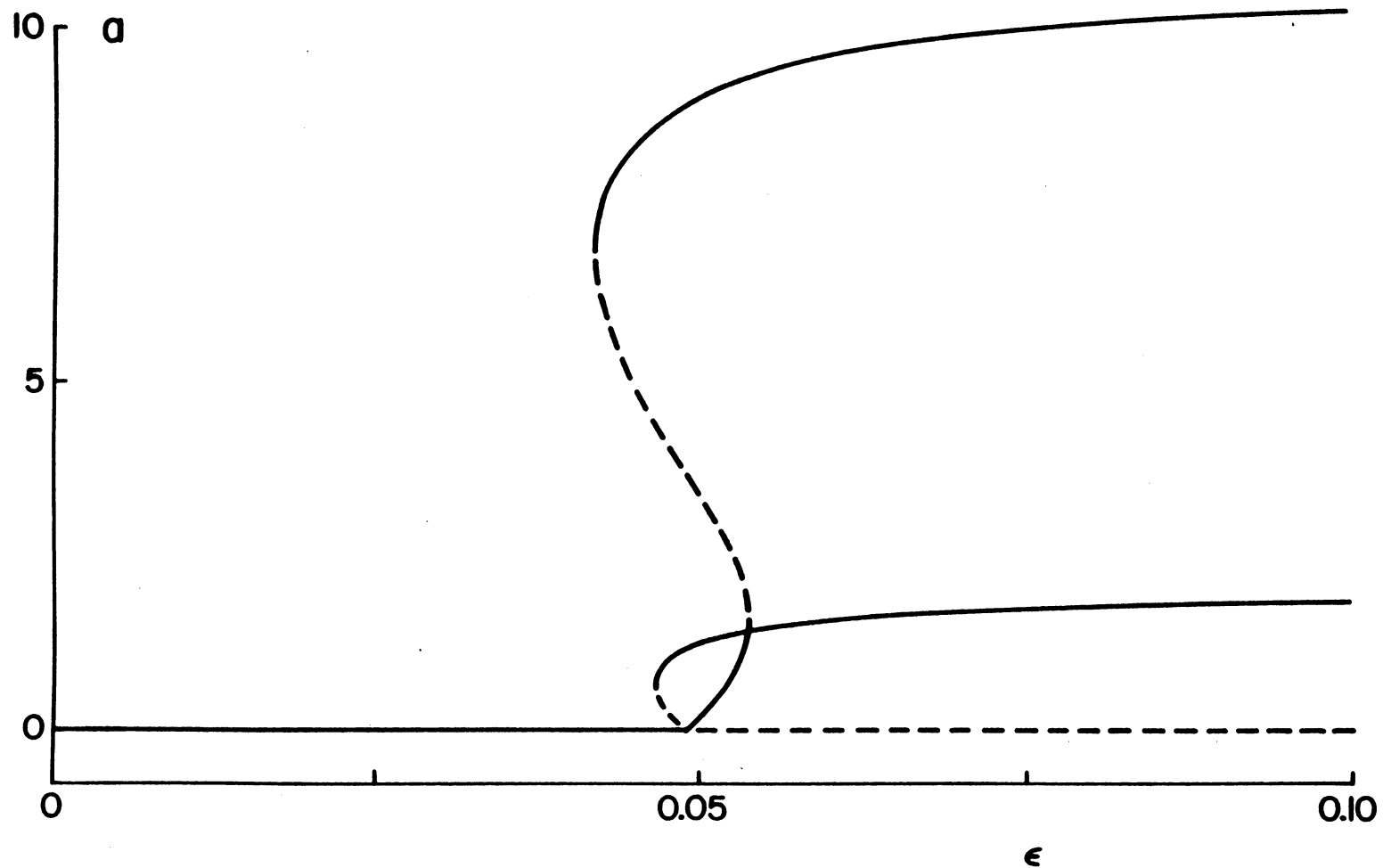


Figure 2.9

Variation of the steady-state amplitude a with the perturbation parameter ϵ : (—) stable, (---) unstable, $\sigma = 0.0$, $\alpha = 4.0$, $\delta = 3.0$, $\mu = 1.0$, $g = 15.0$.

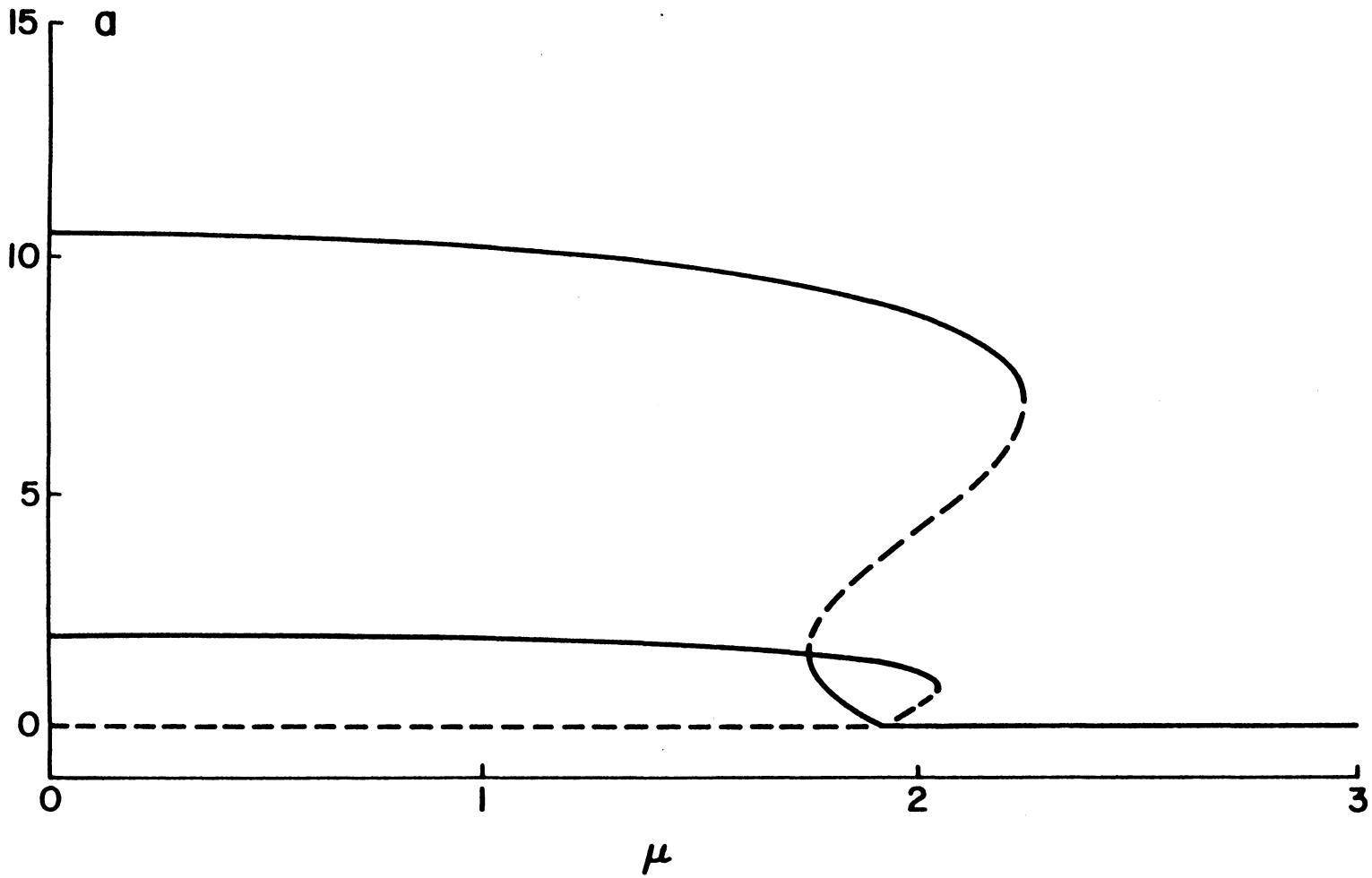


Figure 2.10 Variation of the steady-state amplitude a with the damping coefficient μ : (—) stable, (---) $\sigma = 0.0$, $\alpha = 4.0$, $\delta = 3.0$, $g = 15.0$, $\epsilon = 0.10$.

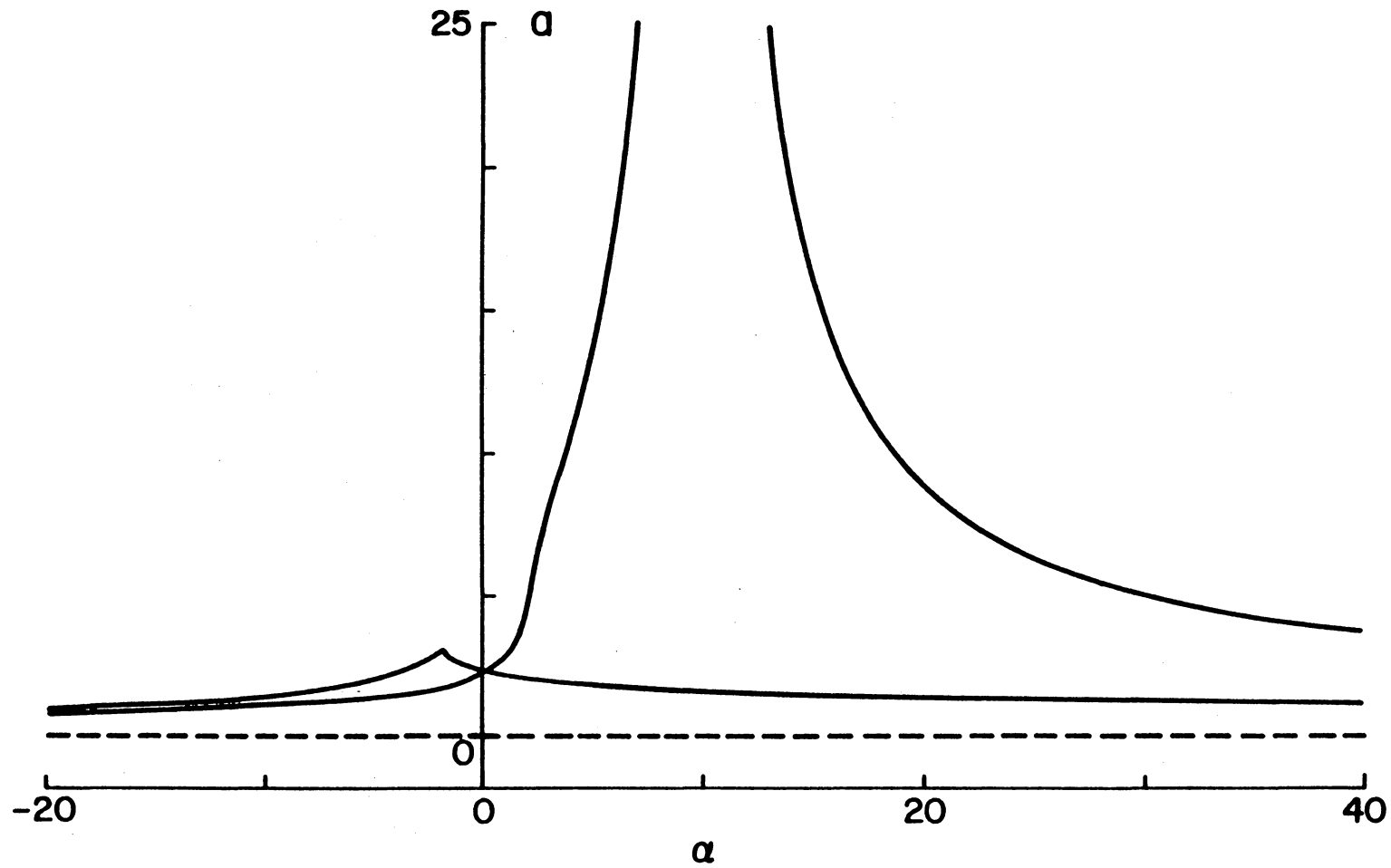


Figure 2.11 Variation of the steady-state amplitude a with the coefficient α of the cubic nonlinearity: (—) stable, (---) unstable, $\sigma = 0.0$, $\delta = 3.0$, $\mu = 1.0$, $g = 15.0$, $\varepsilon = 0.10$.

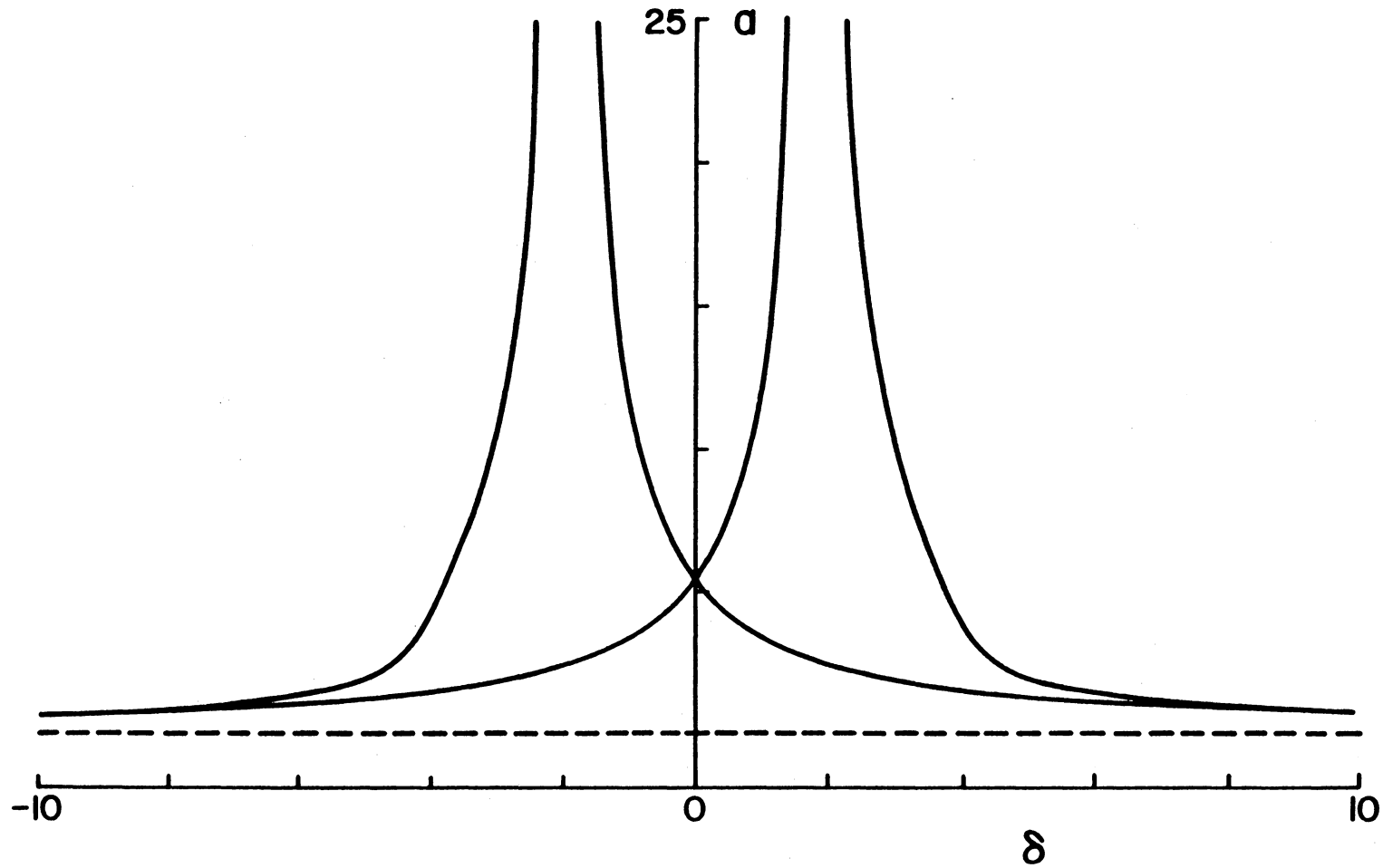


Figure 2.12 Variation of the steady-state amplitude a with the coefficient δ of the quadratic nonlinearity: (—) stable, (---) unstable, $\sigma = 0.0$, $\alpha = 4.0$, $\mu = 1.0$, $g = 1.50$, $\epsilon = 0.10$.

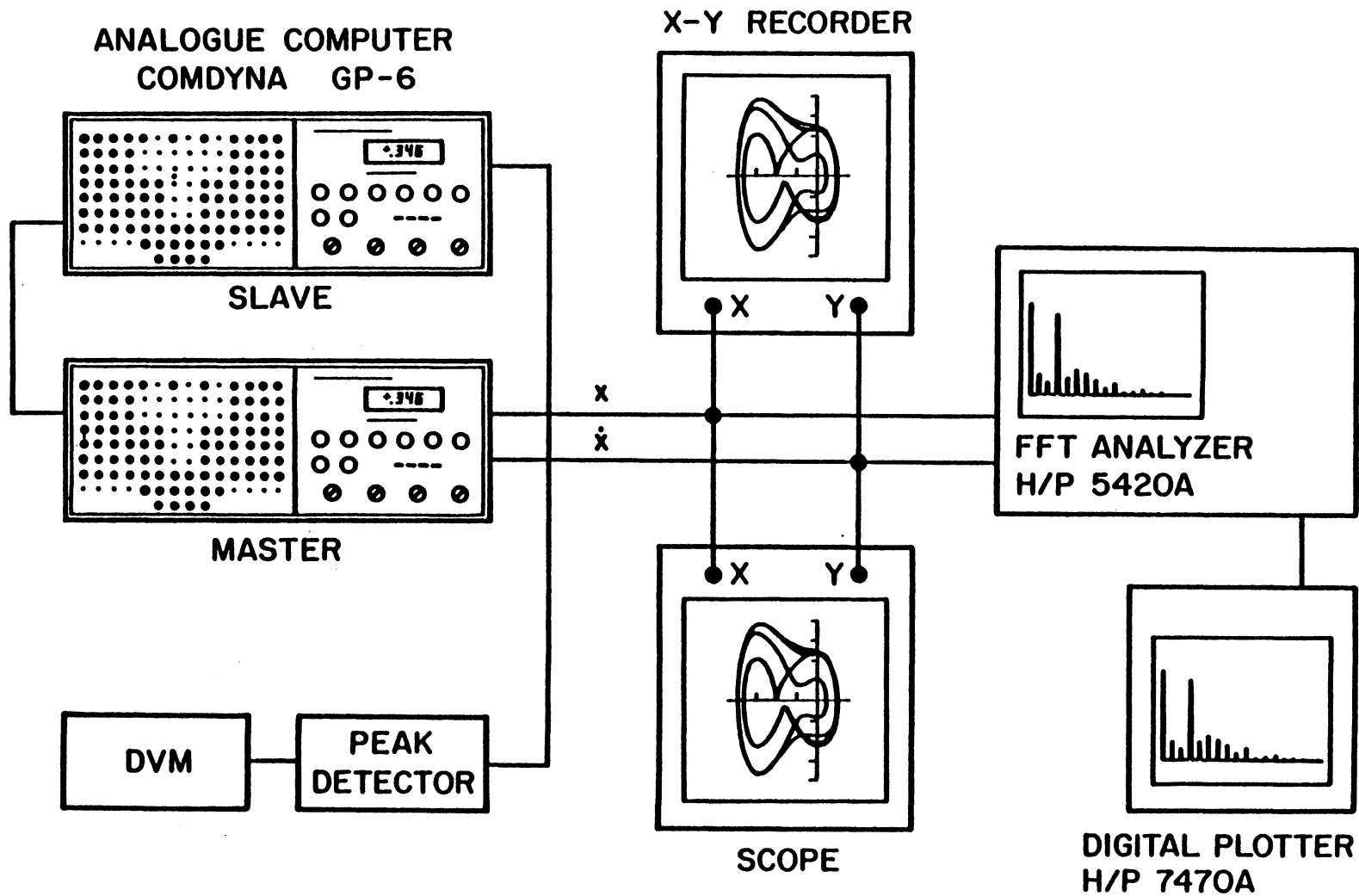


Figure 2.13 Laboratory setup showing the analogue computers and instrumentation. The X-Y recorder was used only in the slow speed mode.

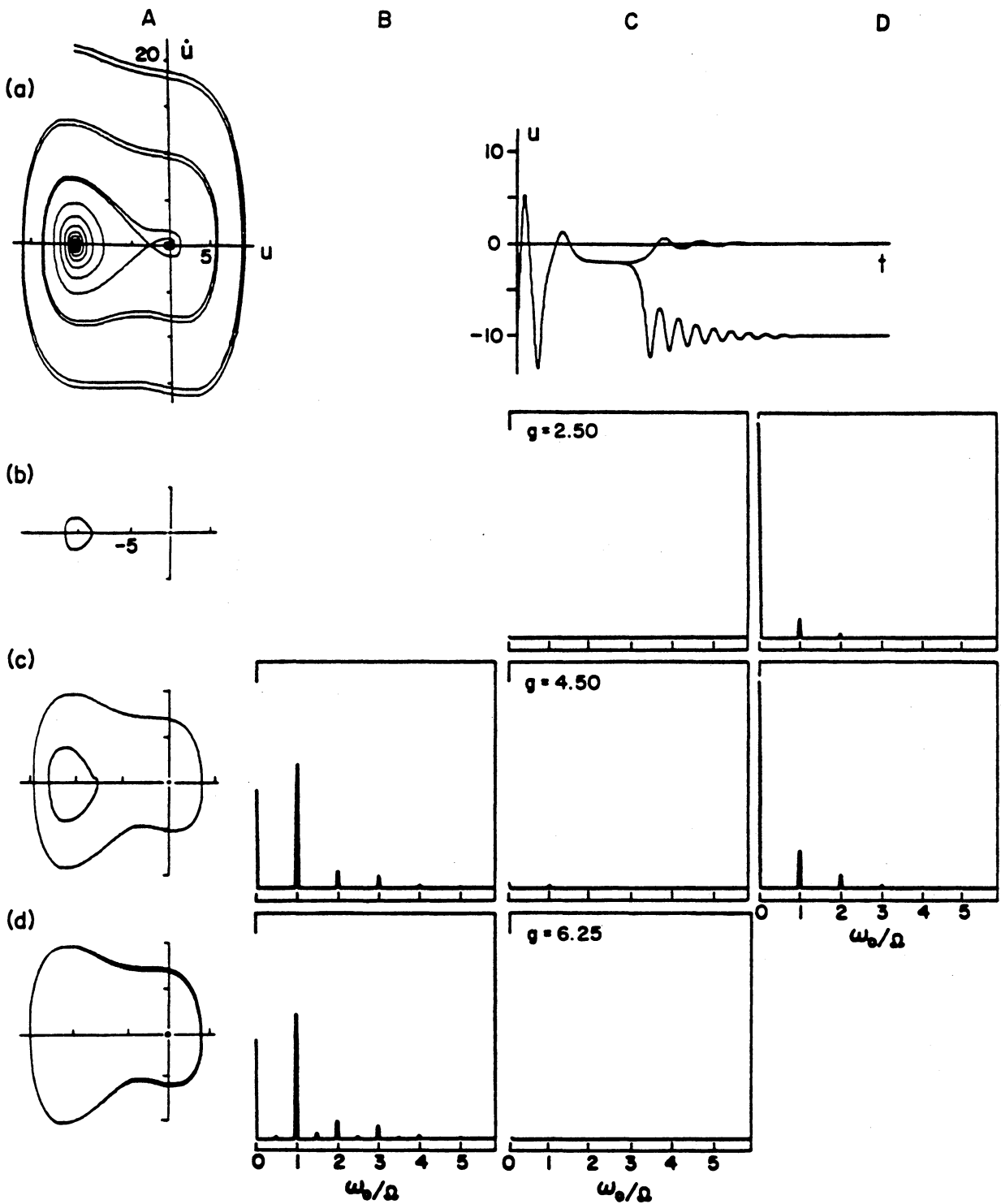


Figure 2.15 Phase-plane portraits and accompanying frequency spectra of the system response, obtained by analogue computer simulation: $\sigma = 0.0$, $\alpha = 4.0$, $\delta = 5.0$, $\mu = 1.0$, $\epsilon = 0.10$. The excitation g varies from 0.0 to 32.0. These results were also obtained by numerical simulation on the digital computer.

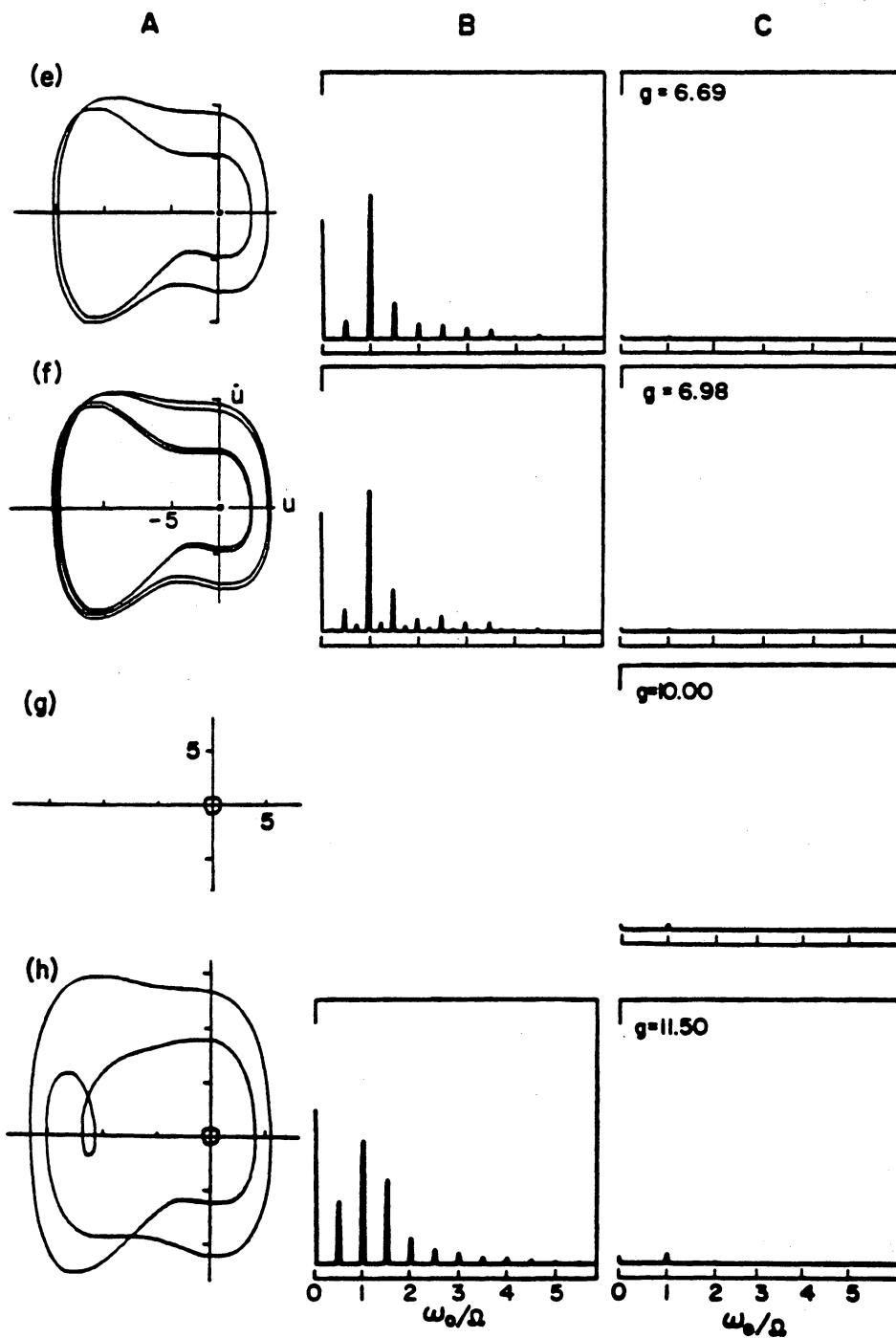


Figure 2.15 continued

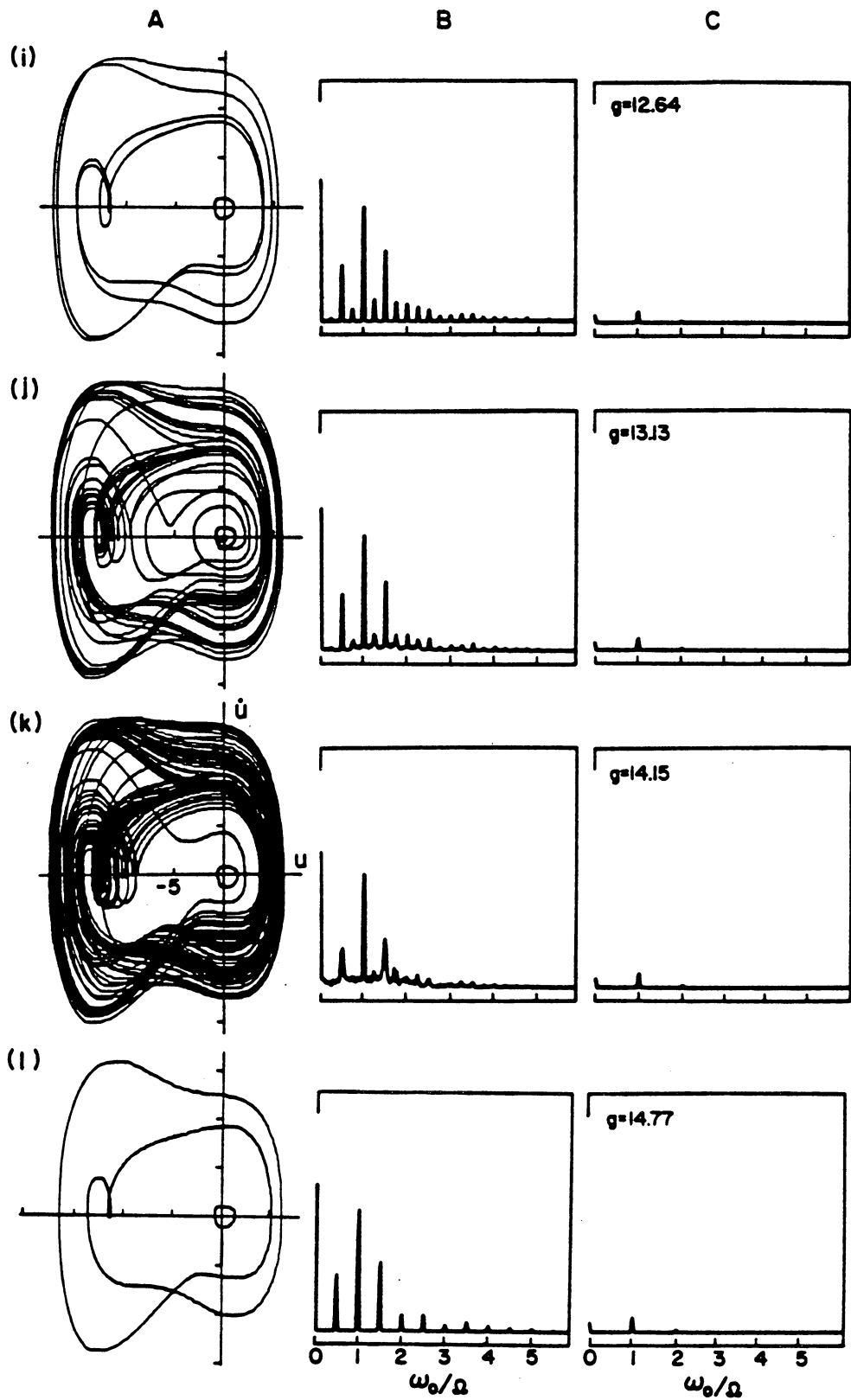


Figure 2.15 continued

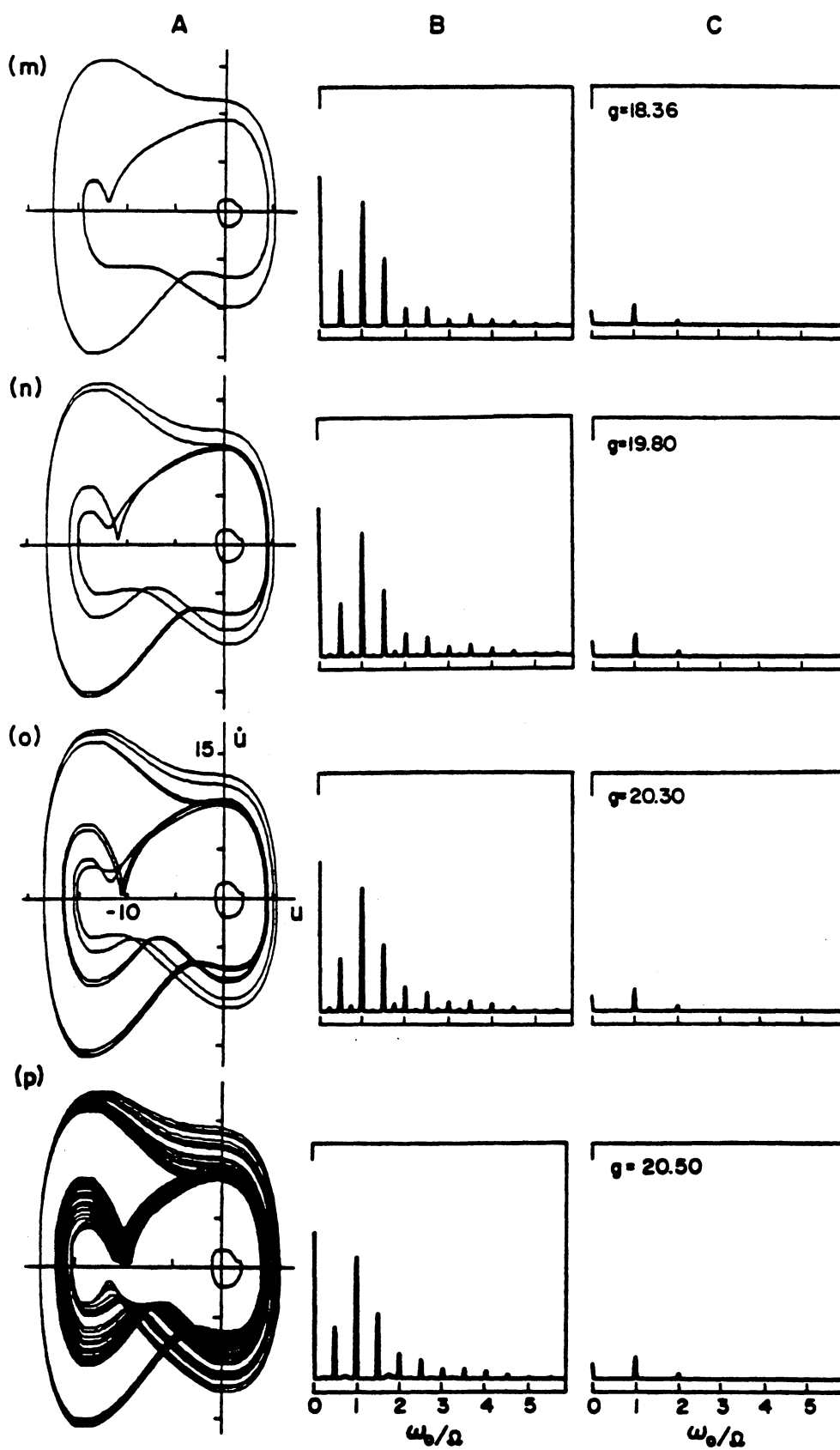


Figure 2.15 continued

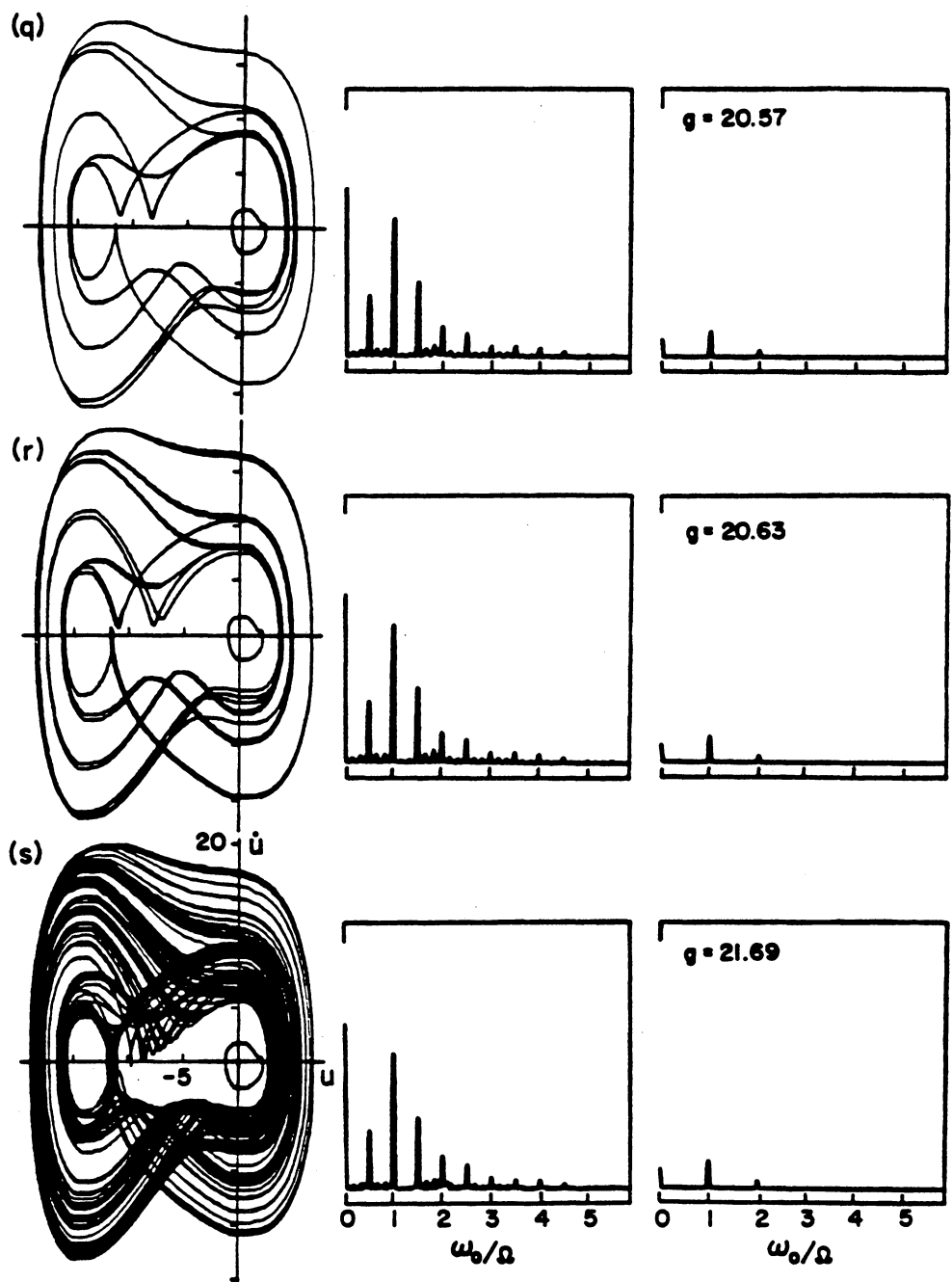


Figure 2.15 continued

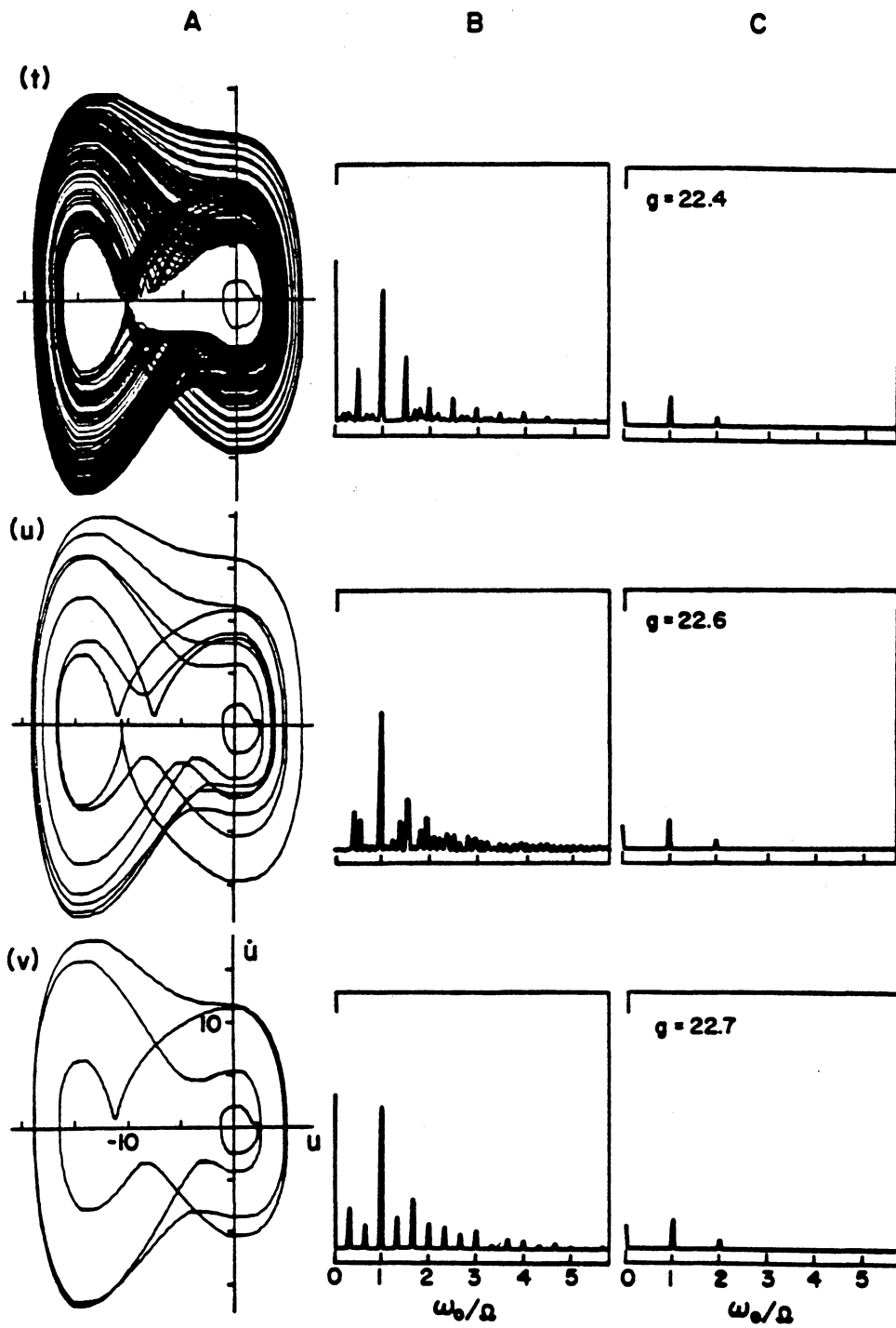


Figure 2.15 continued

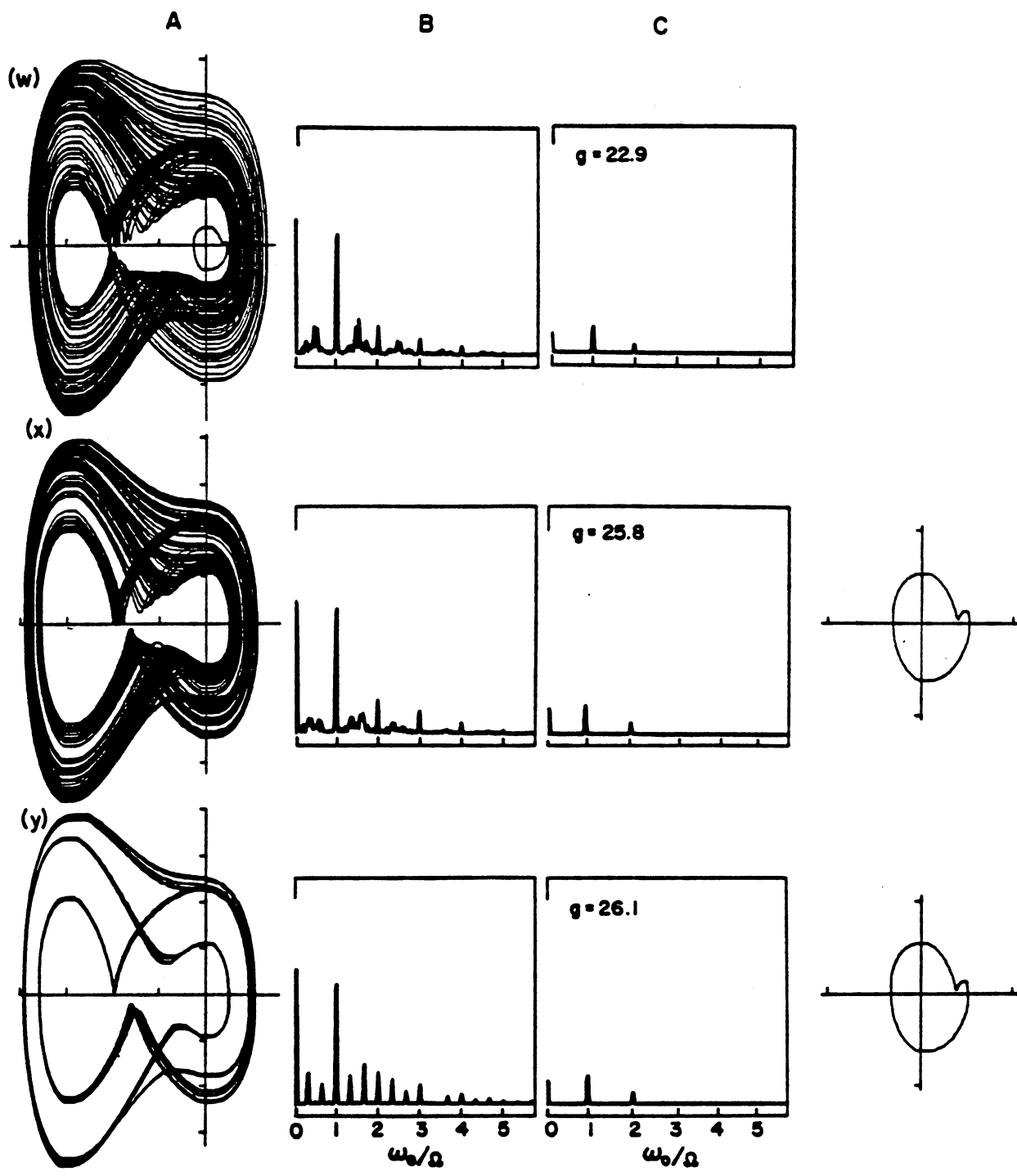


Figure 2.15 continued

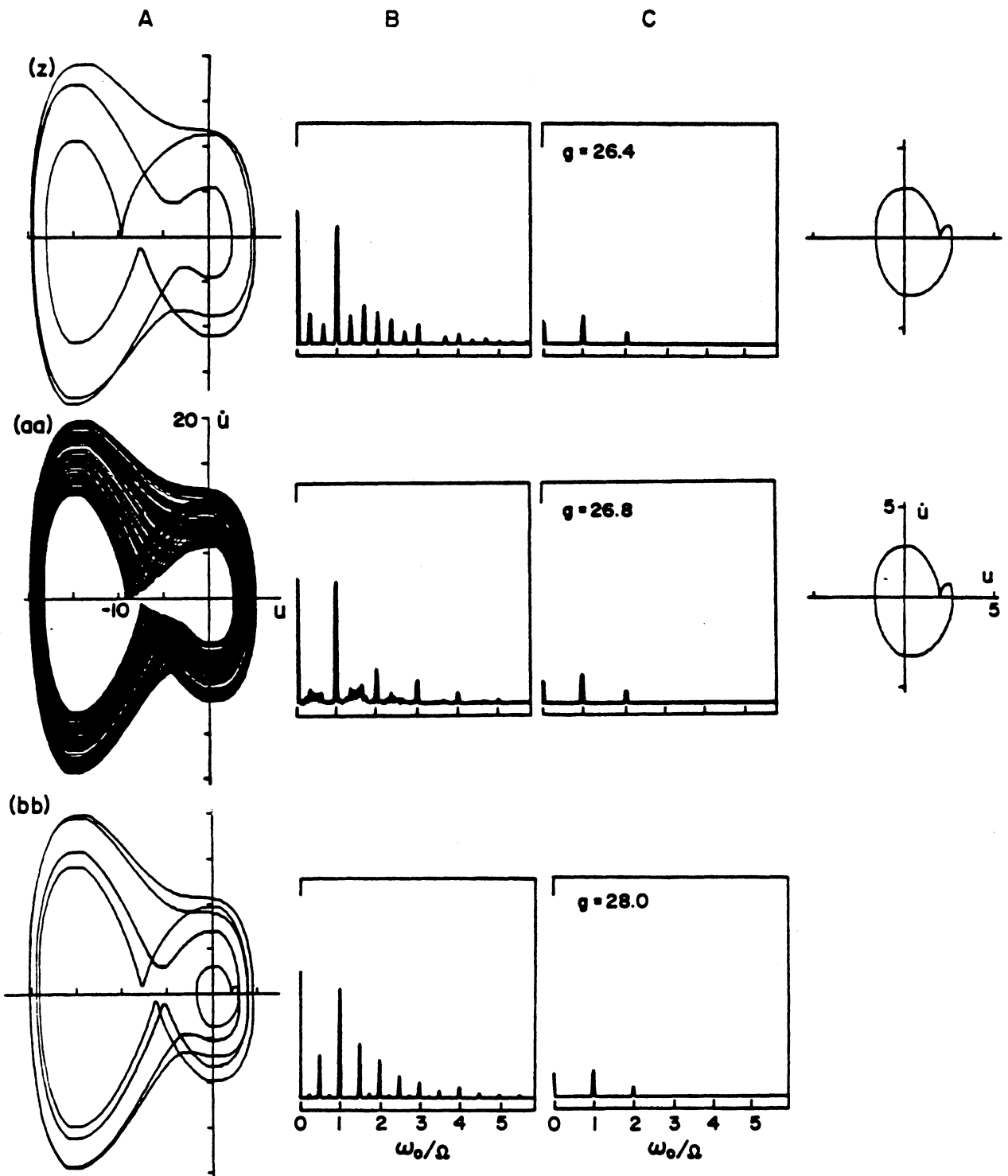


Figure 2.15 continued

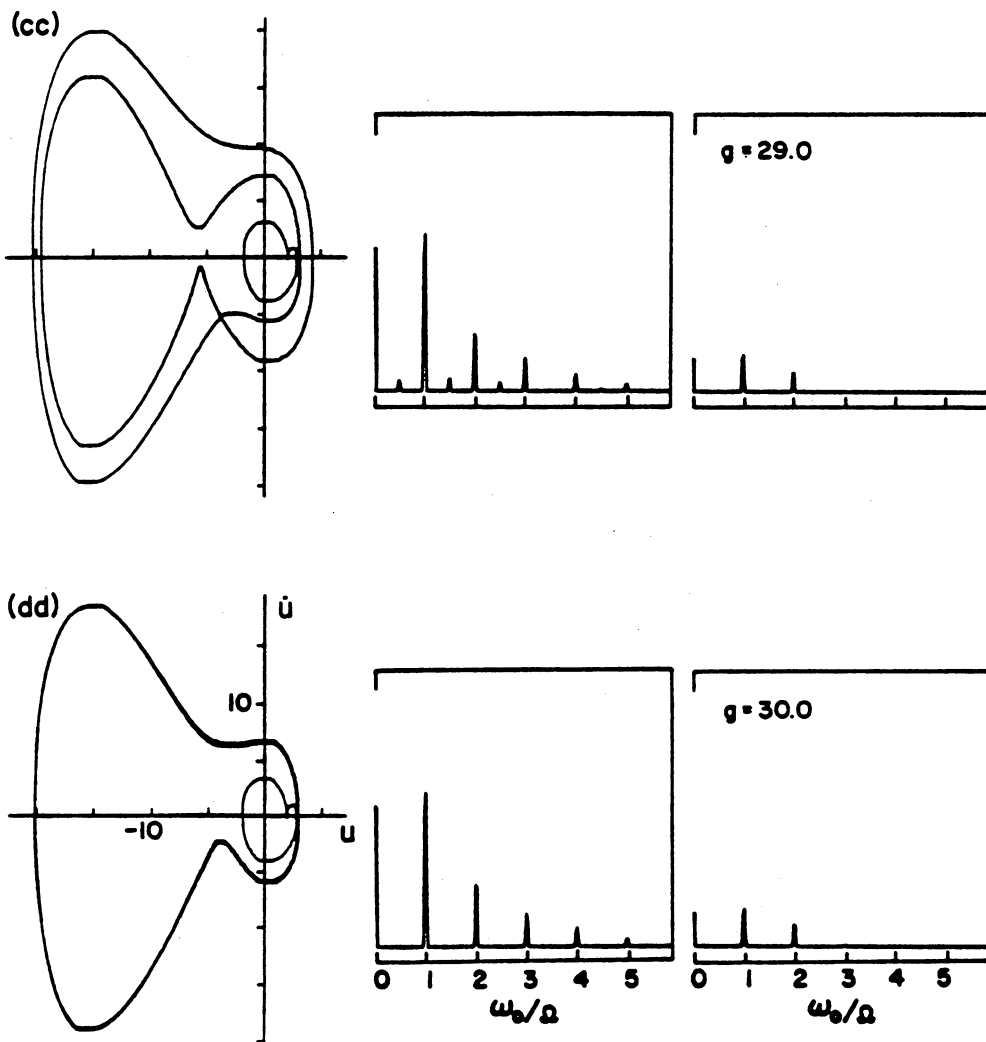


Figure 2.15 continued

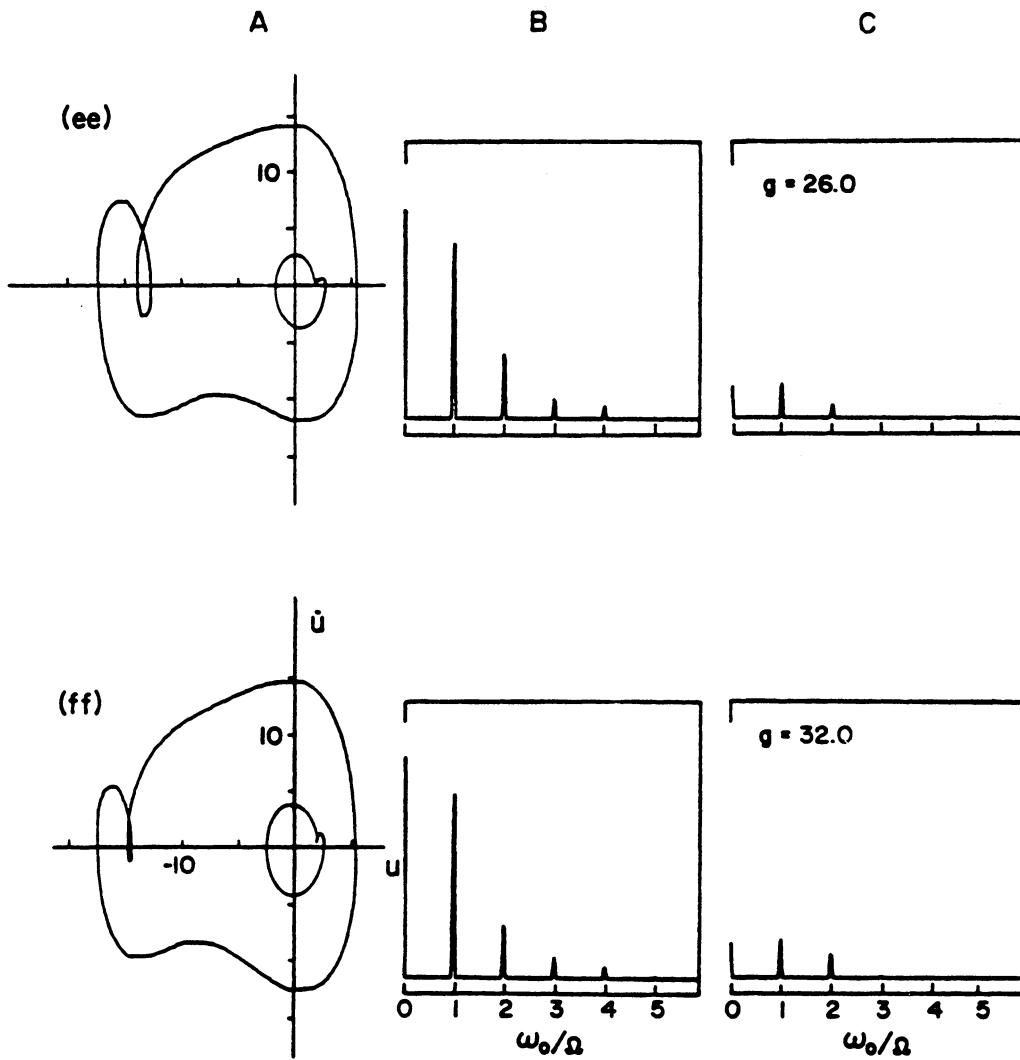


Figure 2.15 continued

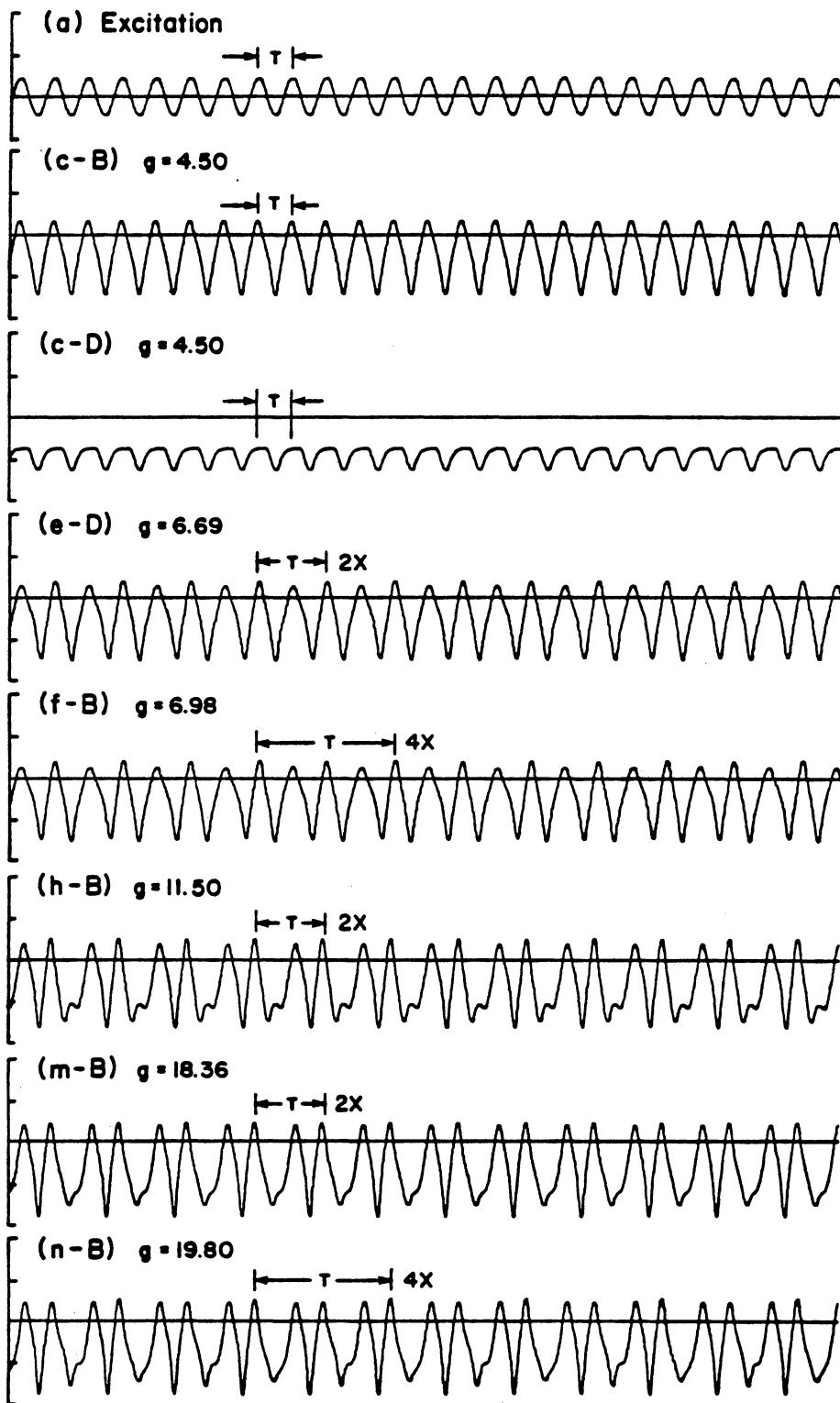


Figure 2.16 Long-time history for selected cases shown in Figure 2.15, obtained by analogue computer simulation, with the relative phase between the excitation and the response preserved.

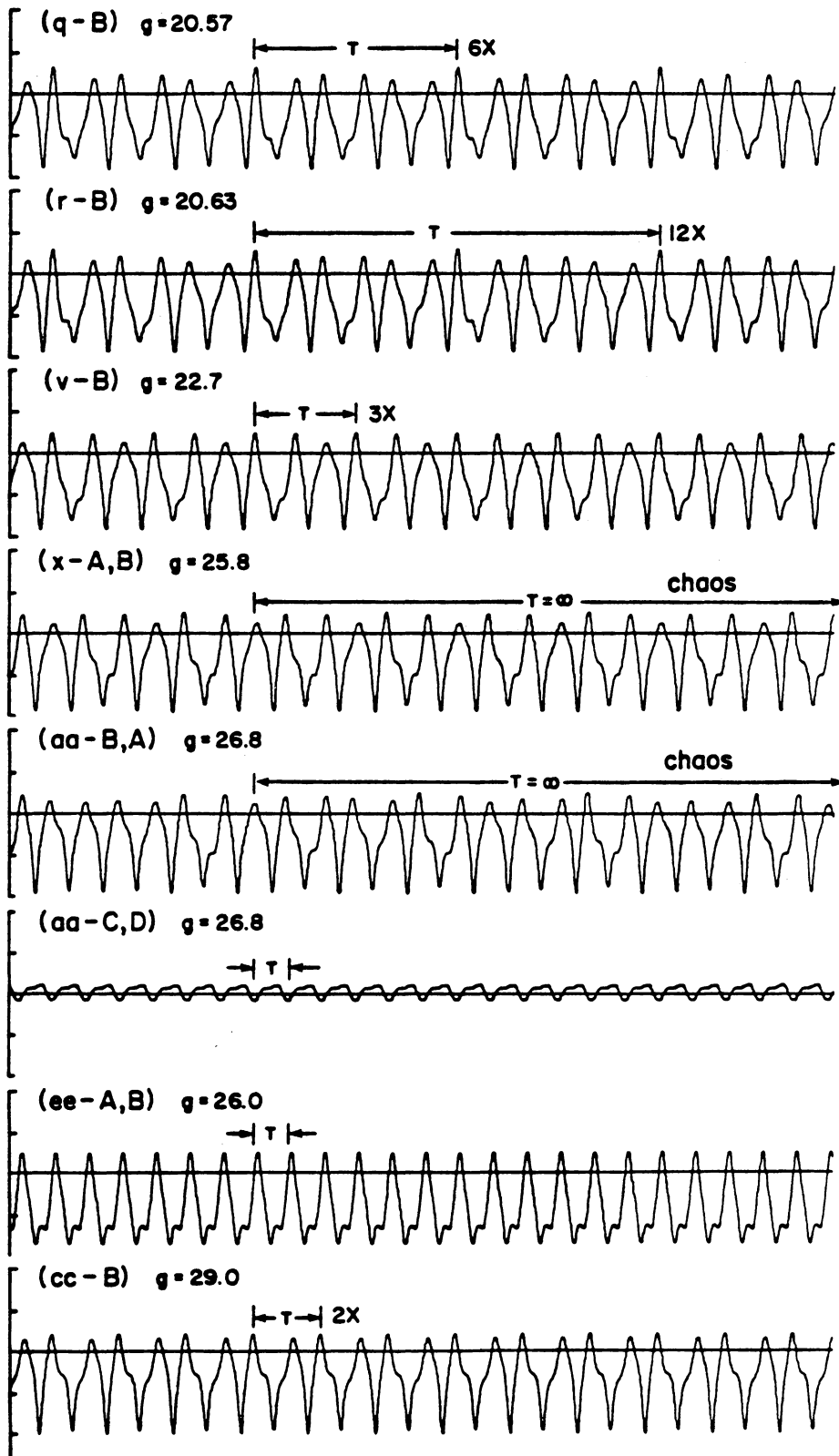


Figure 2.16 continued

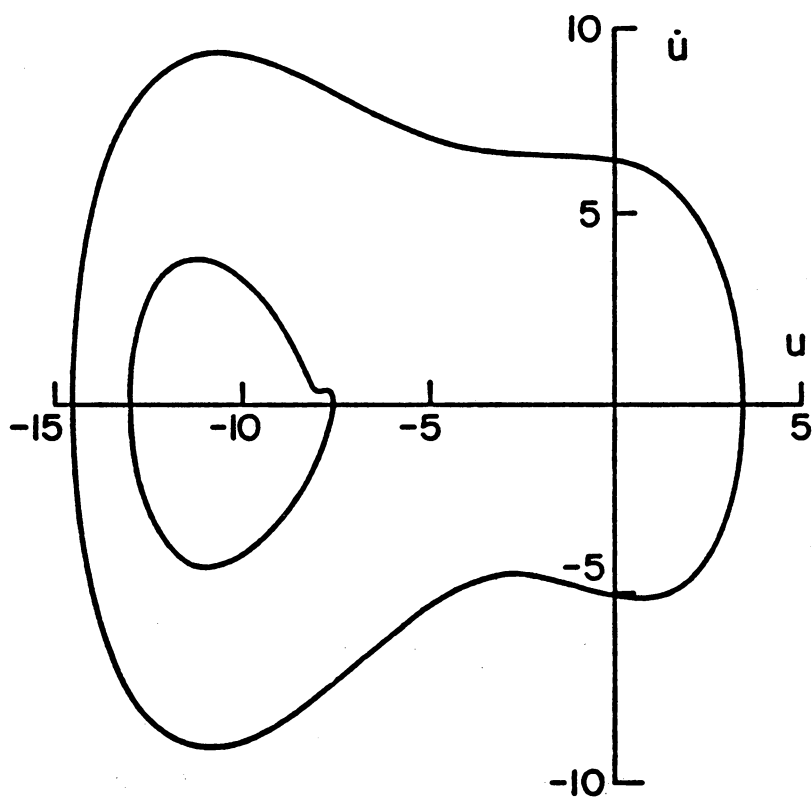


Figure 2.17 Phase-plane portraits of stable steady-state solutions of (2.1) for case (c) shown in Figure 2.1: $\sigma = 0.0$, $\alpha = 4.0$, $\delta = 5.0$, $\mu = 1.0$, $g = 5.0$, $\epsilon = 0.10$.

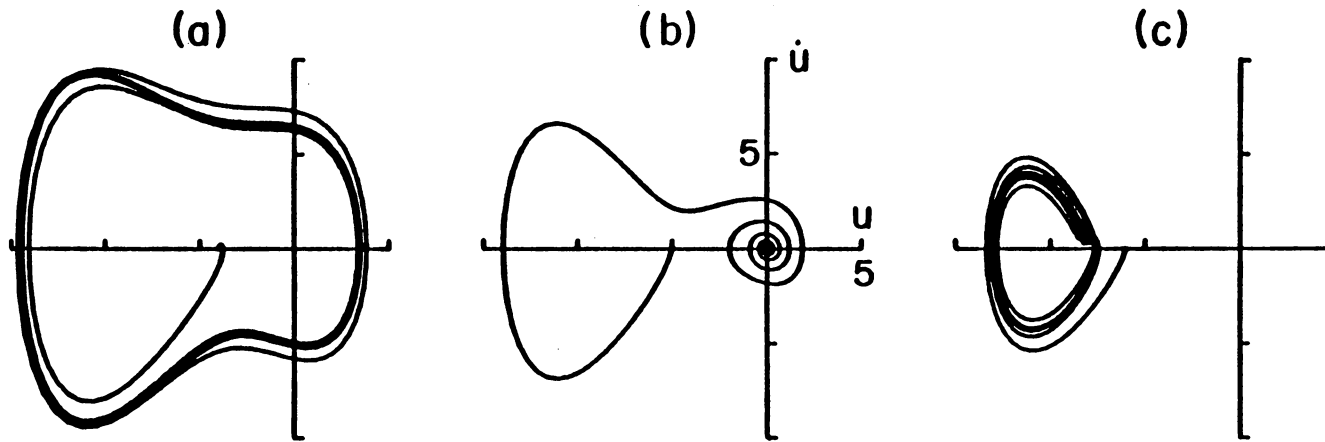


Figure 2.18 Transient responses for each of the three different steady-state responses shown in Figure 2.15, $\dot{u}(0) = 0$: (a) $u(0) = -4.0$, (b) $u(0) = -5.0$, (c) $u(0) = -6.0$.



Figure 2.19 Fractal basin boundary showing domains of attraction for the three attractors shown in Figure 2.18: black-large outer attractor, red limit-cycle attractor about the focus at -10.0 , white-trivial attractor; $-20 \leq u \leq 10$, $-20 \leq \dot{u} \leq 20$.

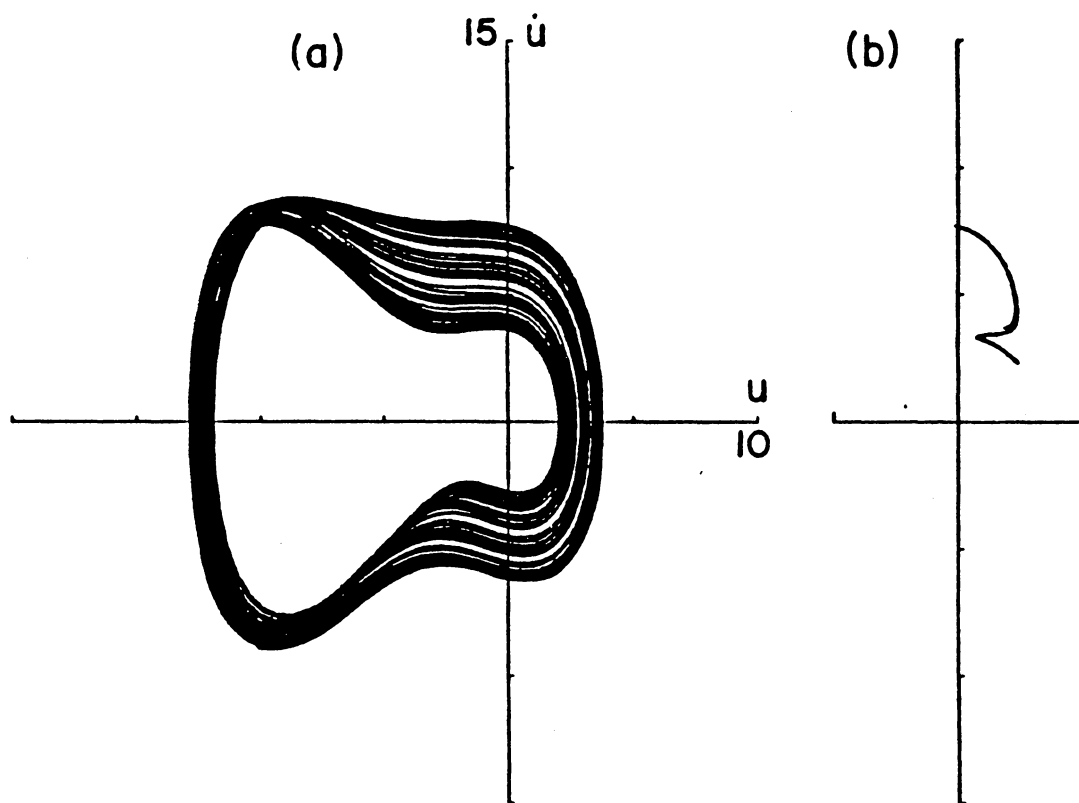


Figure 2.20 (a) Phase-plane portrait and (b) Poincaré map of the system obtained by numerical integration of (2.1) showing what appears to be chaotic response: $\sigma = 0.0$, $\alpha = 4.0$, $\delta = 5.0$, $\mu = 1.0$, $g = 6.80$, $\epsilon = 0.10$. This is the same outer attractor as shown in Figure 2.15, but it becomes unstable and vanishes when g is increased to 7.0.

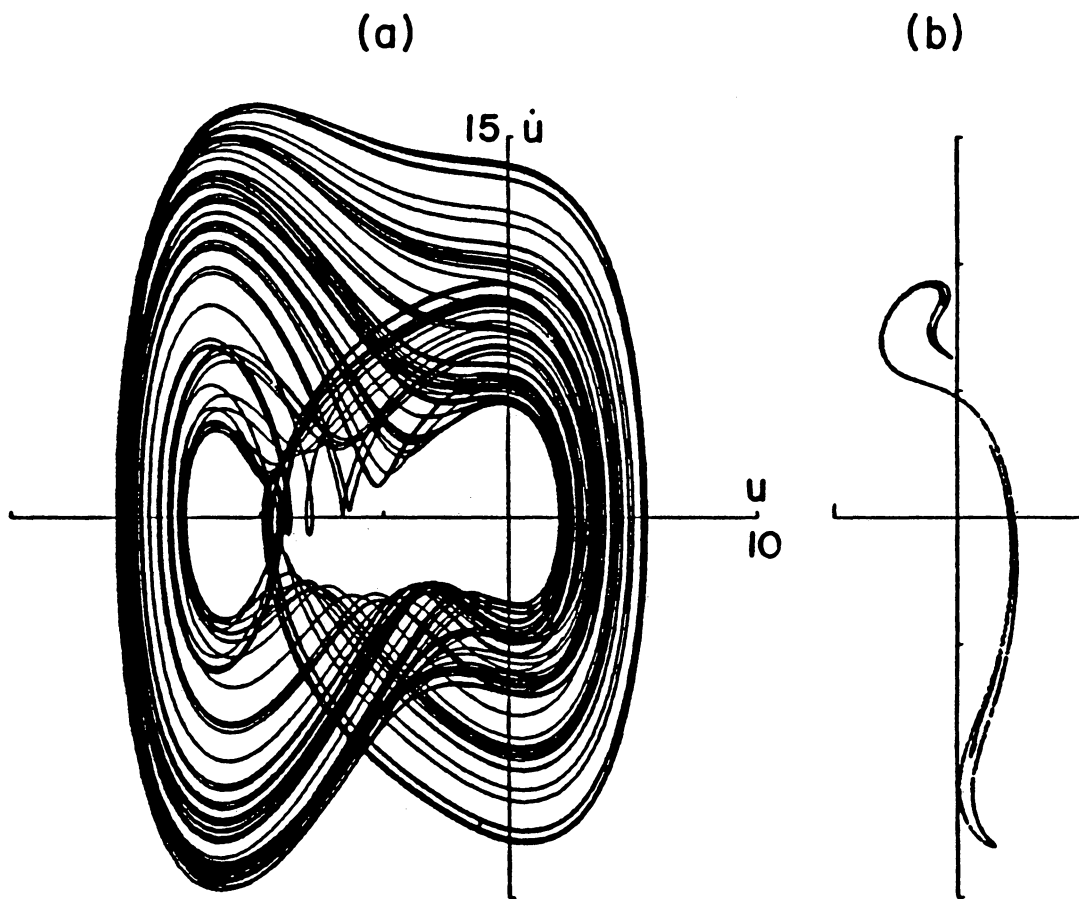


Figure 2.21

(a) Phase-plane portrait and (b) Poincaré map of the system obtained by numerical integration of (2.1) showing chaotic response: $\sigma = 0.0$, $\alpha = 4.0$, $\delta = 5.0$, $\mu = 1.0$, $g = 22.0$, $\epsilon = 0.10$.

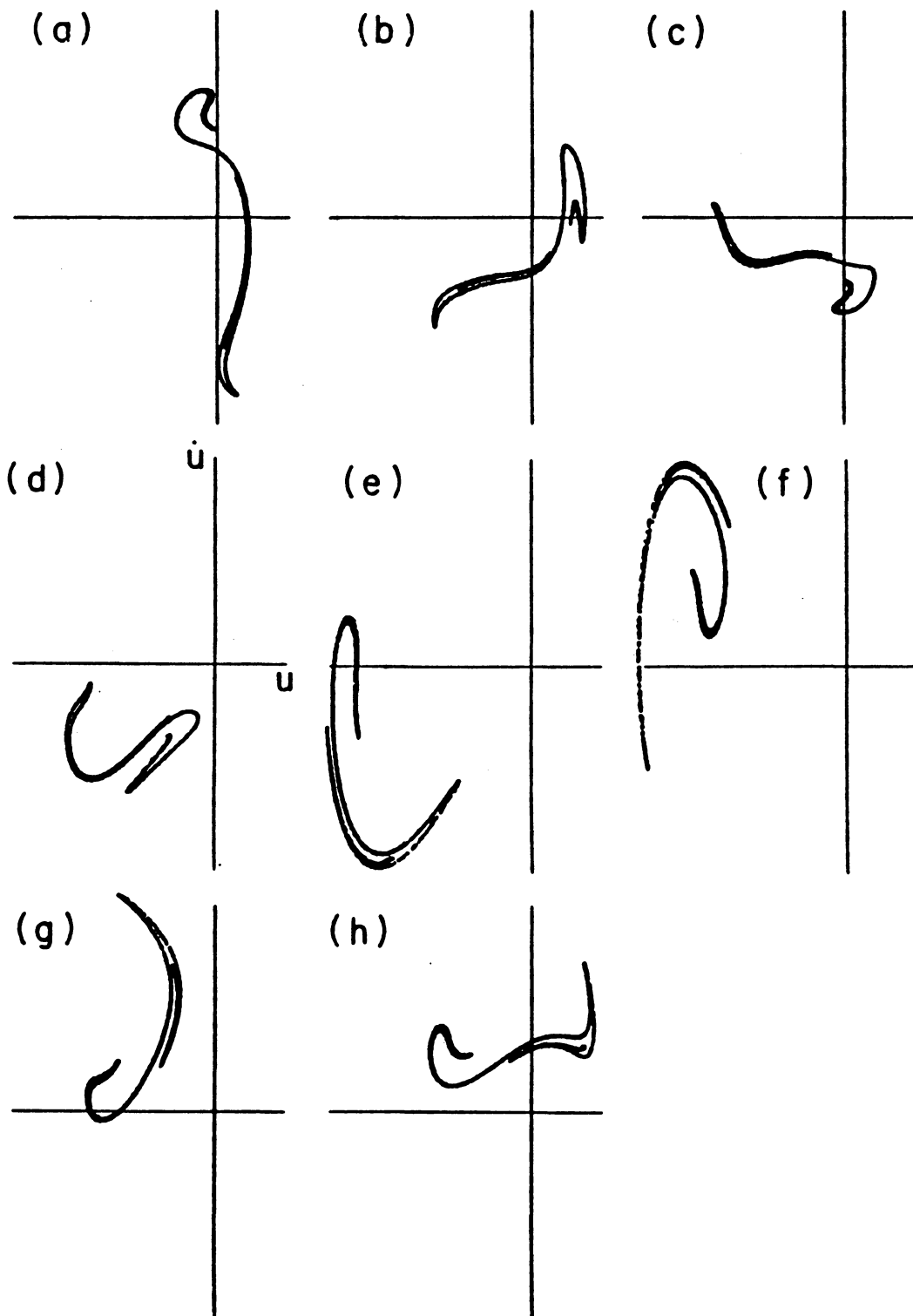


Figure 2.22 Poincaré maps of the chaotic response shown in Figure 2.21 at different phases of the excitation: (a) $\phi = 0^\circ$, (b) $\phi = 45^\circ$, (c) $\phi = 90^\circ$, (d) $\phi = 135^\circ$, (e) $\phi = 180^\circ$, (f) $\phi = 255^\circ$, (g) $\phi = 270^\circ$, (h) $\phi = 315^\circ$.

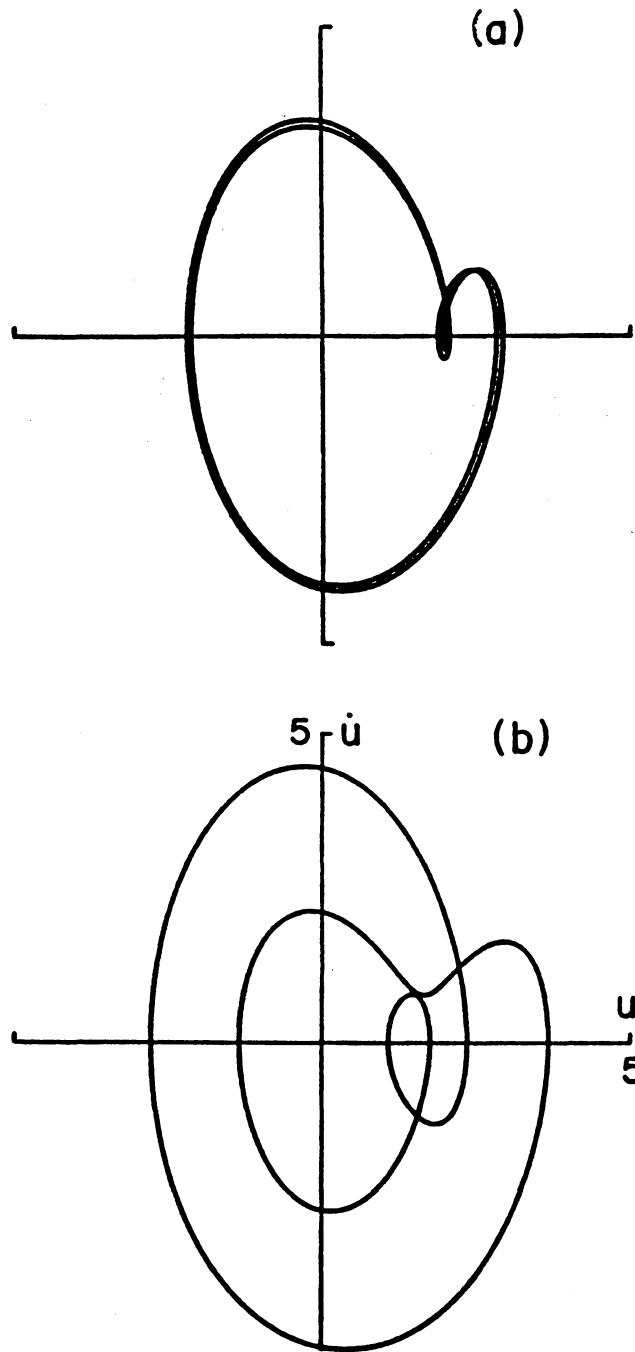


Figure 2.23 Phase-plane portraits of the attractor at the origin showing its first period doubling bifurcation encircling the focus at the origin (a) $g = 29.8$ and (b) $g = 30.5$: $\sigma = 0.0$, $\alpha = 4.0$, $\delta = 5.0$, $\mu = 1.0$, $\epsilon = 0.10$.

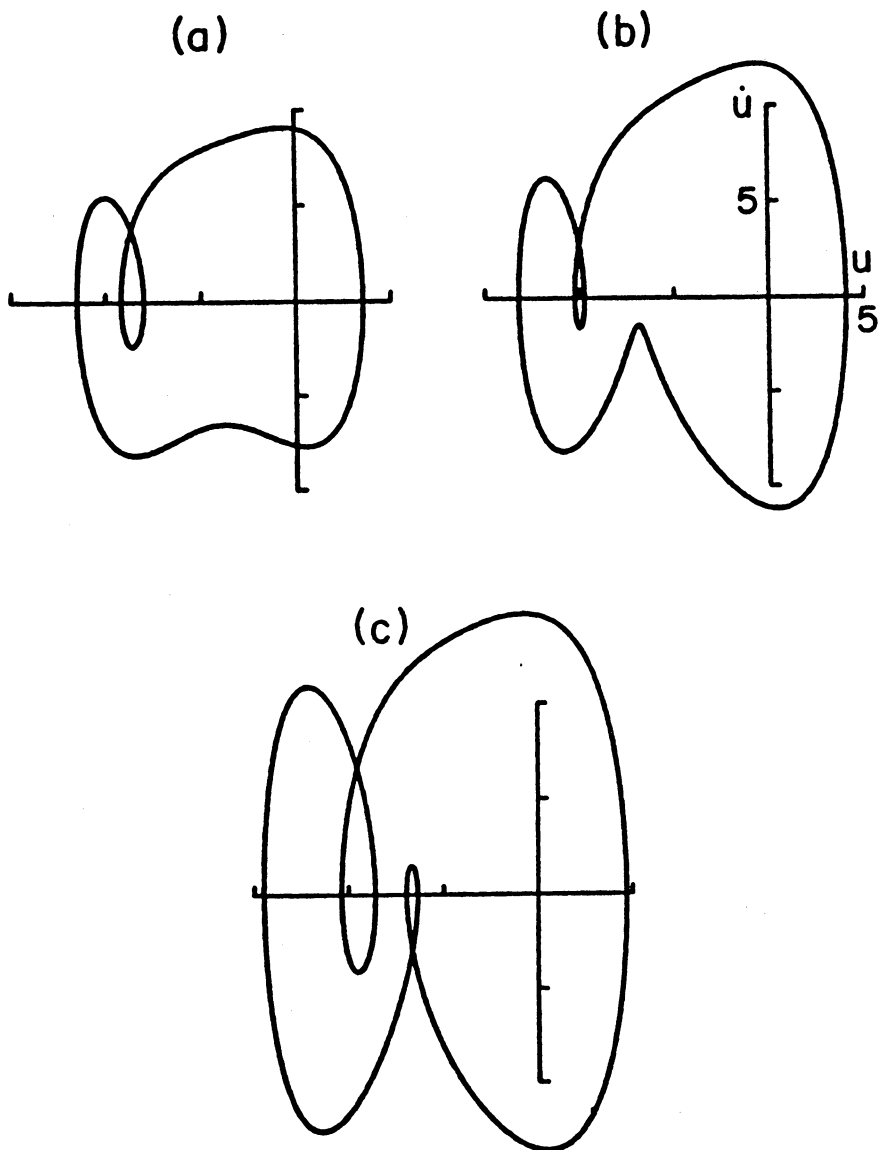


Figure 2.24 Phase-plane portraits of an attractor that coexists with those found earlier (shown as the outer trajectory in Figure 2.15) for (a) $g = 24.0$, (b) $g = 45.0$, and (c) $g = 50.0$: $\sigma = 0.0$, $\alpha = 4.0$, $\delta = 5.0$, $\mu = 1.0$, $\epsilon = 0.10$.

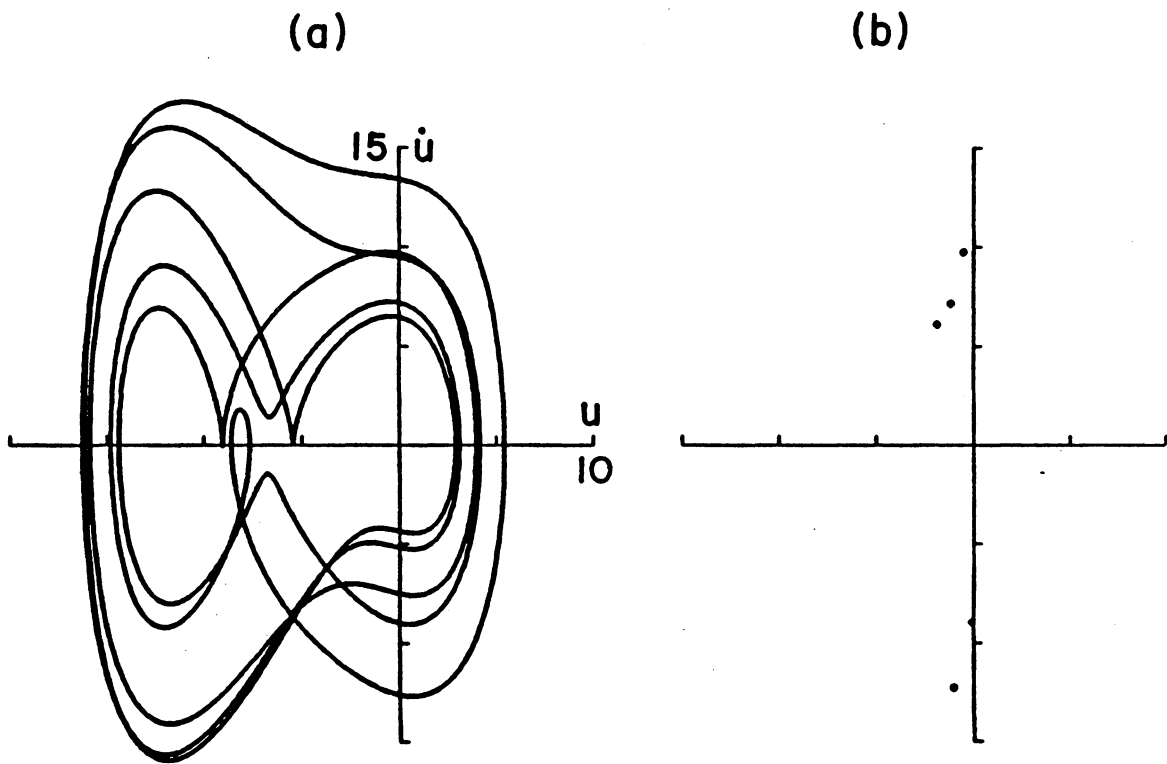


Figure 2.25 (a) Phase-plane portrait and (b) Poincaré map of the system obtained by numerical integration of (2.1) showing a 5x response: $\sigma = 0.0$, $\alpha = 4.0$, $\delta = 5.0$, $\mu = 1.0$, $g = 24.0$, $\epsilon = 0.10$. This response is embedded between chaotic responses. Note that this level of excitation is identical to that in Figure 2.24.

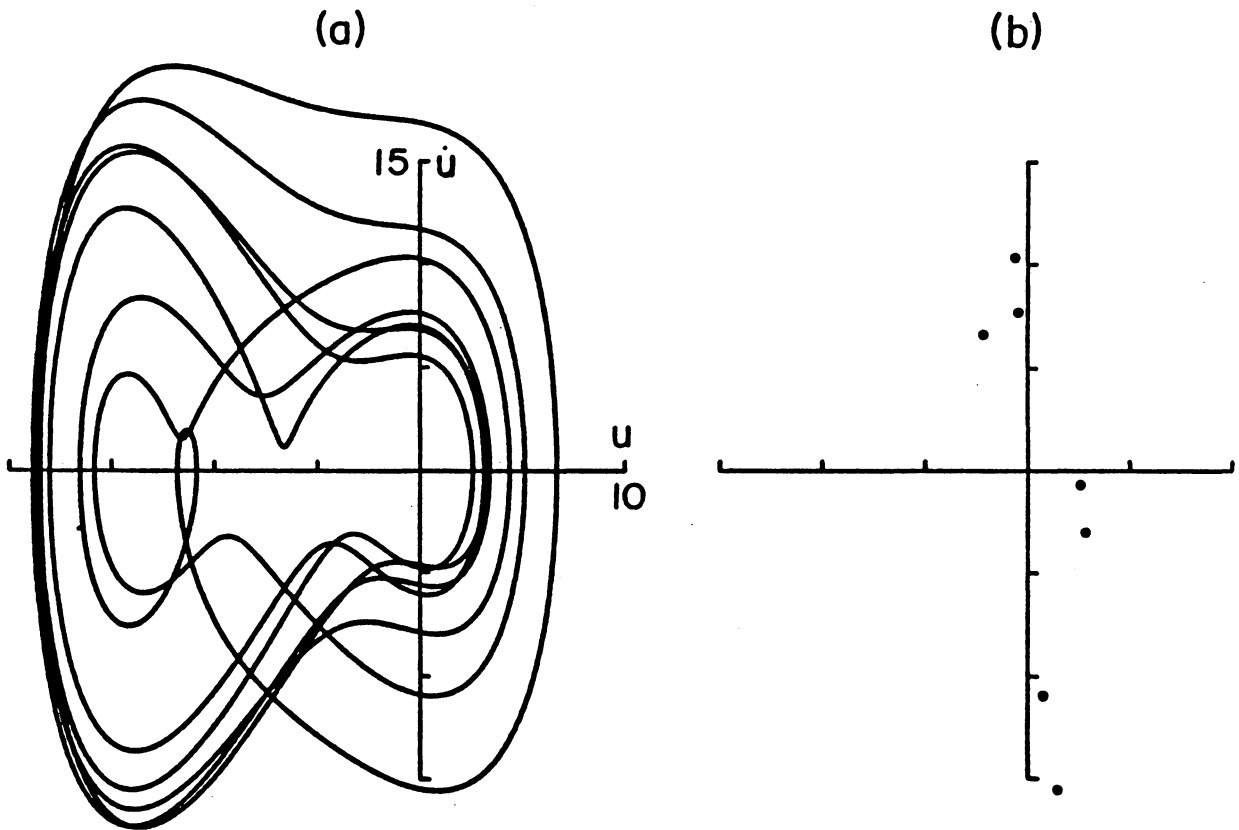


Figure 2.26 (a) Phase-plane portrait and (b) Poincaré map of the system obtained by numerical integration of (2.1) showing a 7x response: $\sigma = 0.0$, $\alpha = 4.0$, $\delta = 5.0$, $\mu = 1.0$, $g = 21.0$, $\epsilon = 0.10$.

CHAPTER III
PRINCIPAL PARAMETRIC RESONANCE IN A SINGLE-DEGREE-OF-FREEDOM
SYSTEM WITH QUADRATIC AND CUBIC NONLINEARITIES

This chapter is concerned with the response of one-degree-of-freedom systems with quadratic and cubic nonlinearities to a principal parametric resonance. The problem is governed by

$$\ddot{u} + 2\varepsilon\mu\dot{u} + [\omega_0^2 + \varepsilon\delta u + \varepsilon^2\alpha u^2 + \varepsilon g \cos\Omega t]u = 0, \quad (3.1)$$

which is the same as (2.1). In this chapter we consider the case when $\Omega \approx 2\omega_0$.

3.1 Multiple Scales Analysis

The analysis in Chapter II can be used up to (2.8). At this point, the particular resonance must be specified because it will affect the solvability conditions. In Chapter II we chose $\Omega \approx \omega_0$, which did not cause any small-divisor terms in (2.8). This happened because $\Omega \approx \omega_0$ is a secondary parametric (fundamental) resonance. However, when we choose $\Omega \approx 2\omega_0$, which is a principal parametric resonance, we do have a small divisor in the particular solution generated by the term containing $\exp[i(\Omega - \omega_0)T_0]$.

To treat this case, we introduce a detuning parameter σ to convert the small-divisor terms into secular terms according to

$$\Omega = 2\omega_0 + \varepsilon\sigma. \quad (3.2)$$

Then, we write

$$(\Omega - \omega_0)T_0 = \omega_0 T_0 + \sigma T_1 . \quad (3.3)$$

Eliminating the terms in (2.8) that produce secular terms in u_1 yields

$$2i\omega_0(D_1 A + \mu A) + \frac{1}{2} g A e^{-i\sigma T_1} = 0 . \quad (3.4)$$

Then, a particular solution of (2.8) is

$$u_1 = -\frac{\delta A \bar{A}}{\omega_0^2} + \frac{g A}{2\Omega(\Omega+2\omega_0)} e^{i(\Omega+\omega_0)T_0} + \frac{\delta A^2}{3\omega_0^2} e^{2i\omega_0 T_0} + cc . \quad (3.5)$$

Substituting (2.7) and (3.5) into (2.6) yields

$$\begin{aligned} D_0^2 u_2 + \omega_0^2 u_2 = & - \left[2i\omega_0 D_2 A + D_1^2 A + 2\mu D_1 A + \frac{g^2 A}{4\Omega(\Omega+2\omega_0)} + 3\alpha A^2 \bar{A} \right. \\ & \left. - \frac{10\delta^2}{3\omega_0^2} A^2 \bar{A} \right] e^{i\omega_0 T_0} + cc + NST . \end{aligned} \quad (3.6)$$

Eliminating the terms that produce secular terms from (3.6) yields

$$2i\omega_0 D_2 A + D_1^2 A + 2\mu D_1 A + \frac{g^2 A}{4\Omega(\Omega+2\omega_0)} + 3\alpha A^2 \bar{A} - \frac{10\delta^2}{3\omega_0^2} A^2 \bar{A} = 0 . \quad (3.7)$$

To eliminate $D_1^2 A$ from (3.7), we differentiate (3.4) with respect to T_1 and obtain

$$D_1^2 A = -\mu D_1 A + \frac{ig}{4\omega_0} D_1 A e^{-i\sigma T_1} - \frac{\sigma g}{4\omega_0} A e^{-i\sigma T_1} . \quad (3.8)$$

Using (3.4) and (3.8) to eliminate $D_1^2 A$ and $D_1 A$ from (3.7), we obtain

$$2i\omega_0 D_2 A + \left(\frac{3g^2}{32\omega_0^2} - \mu^2 \right) A + \left(3\alpha - \frac{10\delta^2}{3\omega_0^2} \right) A^2 \bar{A} - \frac{\sigma g}{4\omega_0} A e^{-i\sigma T_1} = 0 , \quad (3.9)$$

where Ω was replaced with $\Omega \approx 2\omega_0$. We can easily show that (3.4) and (3.9) are the first two terms in a multiple-scales analysis of

$$2i\omega_0(\dot{A} + \epsilon\mu A) + \epsilon^2\left[\left(\frac{3g^2}{32\omega_0^2} - \mu^2\right)A + \left(3\alpha - \frac{10\delta^2}{3\omega_0^2}\right)A^2\bar{A}\right] + \frac{1}{2}\epsilon g\left(1 - \frac{\epsilon\sigma}{2\omega_0}\right)\bar{A}e^{i\epsilon\sigma t} = 0. \quad (3.10)$$

Substituting the polar form

$$A = \frac{1}{2} a e^{i\beta} \quad (3.11)$$

into (3.10) and separating real and imaginary parts, we have

$$\dot{a} = -\epsilon\mu a - \frac{\epsilon g}{4\omega_0}\left(1 - \frac{\epsilon\sigma}{2\omega_0}\right)a \sin\gamma, \quad (3.12)$$

$$a\dot{\beta} = \epsilon^2\left[\left(\frac{3g^2}{64\omega_0^3} - \frac{\mu^2}{2\omega_0}\right)a + \alpha_e a^3\right] + \frac{\epsilon g}{4\omega_0}\left(1 - \frac{\epsilon\sigma}{2\omega_0}\right)a \cos\gamma, \quad (3.13)$$

where

$$\gamma = \epsilon\sigma t - 2\beta, \quad (3.14)$$

and

$$\alpha_e = \frac{3\alpha}{8\omega_0} - \frac{5\delta^2}{12\omega_0^3}. \quad (3.15)$$

Substituting (2.7) and (3.5) into (2.2) yields

$$u = a \cos\left(\frac{1}{2}\Omega t - \frac{1}{2}\gamma\right) + \epsilon\left\{\frac{1}{6}\delta a^2 \cos(\Omega t - \gamma) + \frac{ga}{2\Omega(\Omega+2\omega_0)} \cos\left[\frac{3}{2}\Omega t - \frac{1}{2}\gamma\right] - \frac{1}{2}\delta a^2\right\} + \dots, \quad (3.16)$$

where a and γ are given by (3.12)-(3.14).

It follows from (3.12)-(3.16) that, to the second approximation, the nonlinearity has three effects: (a) a shift $\epsilon^2\alpha_e a^2$ in the natural

the nonlinearity has three effects: (a) a shift $\varepsilon^2 \alpha_e a^2$ in the natural frequency, (b) the generation of the second harmonic in the response, and (c) a drift $-\varepsilon \delta a^2/2$ in the response. The last two effects are produced by the quadratic nonlinearity, whereas the frequency shift is a combined effect of the quadratic and cubic nonlinearities according to (3.15). When $\alpha_e > 0$, the frequency increases with increasing amplitude and the nonlinearity is of the hardening type. On the other hand, when $\alpha_e < 0$, the frequency decreases with increasing amplitude and the nonlinearity is of the softening type. Although the cubic nonlinearity may have a softening or hardening effect, depending on the sign of α , the quadratic nonlinearity is always of the softening type, regardless of the sign of δ . The overall effect of the nonlinearity depends on the sign and magnitude of α_e , which in turn depends on the sign of α and the relative magnitudes of $|\alpha|$ and $|\delta|$.

For steady-state solutions, $\dot{a} = 0$ and $\dot{\gamma} = 0$. Hence, it follows from (3.14) that $\dot{\beta} = \frac{1}{2} \varepsilon \sigma$. Then, it follows from (3.12) and (3.13) that steady-state solutions correspond to the solutions of

$$-\mu a = \frac{g}{4\omega_0} \left(1 - \frac{\varepsilon\sigma}{2\omega_0}\right) a \sin\gamma, \quad (3.17)$$

$$\frac{1}{2} \sigma - \frac{3\varepsilon g^2}{64\omega_0^3} + \frac{\varepsilon\mu^2}{2\omega_0} - \varepsilon\alpha_e a^2 = \frac{g}{4\omega_0} \left(1 - \frac{\varepsilon\sigma}{2\omega_0}\right) a \cos\gamma. \quad (3.18)$$

There are two possibilities: either $a = 0$ or

$$\varepsilon\alpha_e a^2 = \frac{1}{2} \sigma - \frac{3\varepsilon g^2}{64\omega_0^3} + \frac{\varepsilon\mu^2}{2\omega_0} \pm \left[\frac{g^2}{16\omega_0^2} \left(1 - \frac{\varepsilon\sigma}{2\omega_0}\right)^2 - \mu^2 \right]^{\frac{1}{2}}. \quad (3.19)$$

Not all possible steady-state solutions are stable and hence physically realizable. To determine the stability of the trivial

solution, we determine the behavior of the linear solutions of (3.10); that is, the solutions of

$$2i\omega_0(\dot{A} + \epsilon\mu A) + \epsilon^2\left(\frac{3g^2}{32\omega_0^2} - \mu^2\right)A + \frac{1}{2}\epsilon g\left(1 - \frac{\epsilon\sigma}{2\omega_0}\right)\bar{A}e^{i\epsilon\sigma t} = 0. \quad (3.20)$$

Closed-form solutions of (3.20) can be obtained by letting

$$A = (B_r + iB_i)e^{\frac{1}{2}i\epsilon\sigma t}, \quad (3.21)$$

separating real and imaginary parts, and obtaining

$$2\omega_0(\dot{B}_r + \epsilon\mu B_r) - \left[\epsilon\sigma\omega_0 + \epsilon^2\mu^2 - \frac{3\epsilon^2 g^2}{32\omega_0^2} + \frac{1}{2}\epsilon g\left(1 - \frac{\epsilon\sigma}{2\omega_0}\right)\right]B_i = 0, \quad (3.22)$$

$$2\omega_0(\dot{B}_i + \epsilon\mu B_i) + \left[\epsilon\sigma\omega_0 + \epsilon^2\mu^2 - \frac{3\epsilon^2 g^2}{32\omega_0^2} - \frac{1}{2}\epsilon g\left(1 - \frac{\epsilon\sigma}{2\omega_0}\right)\right]B_r = 0. \quad (3.23)$$

Equations (3.22) and (3.23) admit solutions of the form

$$(B_r, B_i) = (b_r, b_i)e^{\epsilon\lambda t}, \quad (3.24)$$

provided that

$$\lambda = -\mu \pm \frac{1}{2\omega_0} \left[\frac{1}{4}g^2\left(1 - \frac{\epsilon\sigma}{2\omega_0}\right)^2 - \left(\sigma\omega_0 + \epsilon\mu^2 - \frac{3\epsilon g^2}{32\omega_0^2}\right)^2 \right]^{\frac{1}{2}}. \quad (3.25)$$

Hence, the trivial solution is stable (i.e., a sink) if the real parts of both roots of λ are less than zero (i.e., $g < g_c$) and unstable (i.e., a saddle) if one of the roots of λ is greater than zero (i.e., $g > g_c$) where g_c is defined from

$$\frac{1}{4}g_c^2\left(1 - \frac{\epsilon\sigma}{2\omega_0}\right)^2 = 4\omega_0^2\mu^2 + \left(\sigma\omega_0 + \epsilon\mu^2 - \frac{3\epsilon g_c^2}{32\omega_0^2}\right)^2. \quad (3.26)$$

For a given μ , (3.26) yields a transition (bifurcation) curve that separates stable (sink) from unstable (saddle) trivial solutions. The region above the transition curve is unstable.

To determine the stability of the nontrivial solutions, we let

$$a = a_0 + a_1(t) \quad \text{and} \quad \gamma = \gamma_0 + \gamma_1(t) , \quad (3.27)$$

where a_0 and γ_0 correspond to a steady-state solution and a_1 and γ_1 are perturbations which are assumed to be small compared to a_0 and γ_0 .

Substituting (3.27) into (3.12)-(3.14), recalling that a_0 and γ_0 correspond to a steady-state solution, and linearizing the resulting equations, we obtain

$$\dot{a}_1 = - \frac{\epsilon g a_0}{4\omega_0} \left(1 - \frac{\epsilon \sigma}{2\omega_0} \right) \gamma_1 \cos \gamma_0 , \quad (3.28)$$

$$\dot{\gamma}_1 = - 4\epsilon^2 \alpha_e a_0 a_1 - 2\mu \gamma_1 . \quad (3.29)$$

Equations (3.28) and (3.29) admit solutions of the form

$$(a_1, \gamma_1) = (c_1, c_2) e^{\epsilon \lambda t} \quad (3.30)$$

provided that

$$\lambda^2 + 2\mu\lambda - \frac{\epsilon g a_0^2}{\omega_0} \alpha_e \left(1 - \frac{\epsilon \sigma}{2\omega_0} \right) \cos \gamma_0 = 0 ,$$

or

$$\lambda = - \mu \pm \left[\mu^2 + \frac{\epsilon g a_0^2}{\omega_0} \alpha_e \left(1 - \frac{\epsilon \sigma}{2\omega_0} \right) \cos \gamma_0 \right]^{1/2} . \quad (3.31)$$

Consequently, a steady-state solution given by (3.19) is unstable (saddle) if

$$\frac{ga_0^2}{\omega_0} \alpha_e \left(1 - \frac{\epsilon\sigma}{2\omega_0}\right) \cos\gamma_0 > 0 ,$$

which upon using (3.18) becomes

$$\alpha_e \left[\frac{1}{2} \sigma - \frac{3\epsilon g^2}{64\omega_0^3} + \frac{\epsilon\mu}{2\omega_0} - \epsilon\alpha_e a_0^2 \right] > 0 \quad (3.32)$$

since ω_0 and a_0 are positive. Consequently, it follows from (3.19) and (3.32) that when $\alpha_e > 0$, the steady-state solution corresponding to the negative sign in (3.19) is unstable (saddle), whereas that corresponding to the positive sign is stable (sink). On the other hand, when $\alpha_e < 0$, the steady-state solution corresponding to the positive sign in (3.19) is unstable (saddle), whereas that corresponding to the negative sign is stable (sink).

We note that, according to (3.19), the amplitude a is of order $\epsilon^{-\frac{1}{2}}$. This result suggests that the assumed expansion for $u(t)$ should have been started with $\epsilon^{\frac{1}{2}}$.

3.2 Numerical Results

Before considering the system response to a principal parametric excitation, we investigate the free response. The singular (equilibrium) points of the system are calculated from (3.1) by setting the excitation g and all derivative terms equal to zero. The roots of the reduced equation are given by

$$u = 0, \frac{1}{2\epsilon\alpha} \left[-\delta \pm (\delta^2 - 4\omega_0^2\alpha)^{\frac{1}{2}} \right] . \quad (3.33)$$

For the cases considered in the following analysis, we choose $\omega_0 = 1.0$, $\alpha = 4.0$, and $\epsilon = 0.005$. When we perform digital and analogue computer simulation for large amplitude responses, we allow ϵ to become as large as 0.10. However, for the principal parametric resonance, we do not need as large an excitation as was required for the fundamental parametric resonance (Chapter II), so we scale the excitation accordingly. In so doing, we also scale the nonlinearity with the excitation. For the case $\delta = 5.0$, there are two stable equilibrium points (foci) and one unstable equilibrium (saddle) point. When $\delta = 4.0$, the radical vanishes causing the left focus and saddle point to merge and form a cusp. When $\delta = 3.0$, the only real root is the origin. Phase-plane plots and potential energy diagrams are shown in Figure 3.1 for these three cases. The perturbation parameter ϵ essentially moves the equilibrium points; by decreasing ϵ , the points move further to the left (c.f., Figure 2.1 when $\epsilon = 0.10$). For $\epsilon = 0.005$, the equilibrium points for $\delta = 5.0$ occur at $u = -175$, -25 , and 0 . The perturbation analysis was applied to motions about the equilibrium point at the origin.

In the presence of damping, excitation, and quadratic and cubic nonlinearity, an approximate expression for the response is given by (3.16). The steady-state amplitude a and phase γ used to calculate $u(t)$ are determined numerically from (3.17) and (3.18). The stability of each solution, including the trivial, is determined from (3.26) and (3.32). In the following discussion, we examine how the response

depends on the system parameters. Since we are examining the response near the singular point at the origin, only the first case with one equilibrium point (of the system parameters shown in Figure 3.1) will be considered. All three cases have stable trajectories about the origin which are quite similar in nature. The differences become apparent when the amplitude of the motion becomes large enough to be affected by the homoclinic orbit; however, at these amplitudes, the small amplitude assumption underlying the perturbation solution ceases to be valid. The latter portion of this chapter discusses two techniques for investigating large amplitude responses and considers the third case ($\delta = 5.0$) for $\epsilon = 0.10$.

The effect of the excitation g on the amplitude of the response for a perfectly tuned excitation is shown in Figure 3.2(a). It shows the classical principal parametric response that requires a critical value to excite a response. When the system is positively detuned ($\sigma > 0$), the amplitude decreases and the curve shifts to the right, which causes the critical value to increase. This happens because the "effective" nonlinearity α_e is of the softening type. When the system is negatively detuned ($\sigma < 0$), the amplitude increases and the top portion of the response curve moves to the left and folds over the lower portion because the critical point remains fixed (for $\sigma < 0$). Hence, the curve becomes double-valued. Since we now have a stable nontrivial response existing at a level of excitation below the critical value, this behavior is called a "sub-critical resonance" or a "sub-critical instability". If we perform an experiment in which an excitation

amplitude greater than the critical value is applied to the structure, a parametric resonance will be excited. If the amplitude of the excitation is slowly decreased, the response amplitude will also decrease as it follows the upper curve to the left. If the response amplitude is decreased below the critical value, a stable response still exists until the turning point is reached. Thus, parametric resonances in nonlinear systems can exist at excitation levels below the critical value predicted by linear theory.

A typical frequency-response curve near the principal parametric resonance is shown in Figure 3.3. It displays the classical softening behavior even though the coefficient α of the cubic nonlinearity is positive (hardening). This is due to the influence of the quadratic nonlinearity which is always of the softening type, irrespective of the sign of its coefficient. It is stronger than the coefficient of the cubic nonlinearity α because the coefficient of the "effective" cubic nonlinearity $\alpha_e = -2.25$ is negative.

The stability of the responses shown in Figures 3.2 and 3.3 was verified by numerically integrating the amplitude and phase modulation equations (3.12) and (3.13) using a fifth- and sixth-order Runge-Kutta-Verner algorithm. The results of two such integrations are shown in Figure 3.4; they verify the perturbation solution. A final check on the perturbation solution was obtained by numerically integrating the original governing equation (3.1). Using the same conditions as those in Figure 3.4, we obtained the results shown in Figures 3.5, 3.6, and

3.7. The perturbation solution is also shown in the latter two figures; the agreement is remarkable.

The effect of damping on the response is shown in Figure 3.8. From this series that also shows the influence of detuning, we conclude that a principal parametric resonance can be excited only if the damping coefficient is below a critical value. In some cases this critical value is larger than that predicted by linear analysis (i.e., corresponding to the loss of stability of the trivial solution). We also note that for small values of damping ($\mu < 2$), the amplitude of the response is quite insensitive to the value of the damping coefficient. For example, when $\sigma = 0.0$, the response amplitude for $\mu = 2.0$ is 20.37, and when μ decreases ten times to 0.2, the amplitude increases to 21.27. Thus, an order of magnitude reduction in the damping coefficient allows a mere 4.4% increase in the response amplitude. This is because the excitation g is relatively large. Referring to (3.19), we see that once g is large relative to μ , modest changes in μ have negligible effect on the amplitude. This behavior has two immediate implications. First, in the field or laboratory, it shows that we do not need an extremely accurate estimate of the damping coefficient to predict a steady-state response if the excitation is large enough. Second, it shows that reduction of the response amplitude to a parametric excitation is possible only if the critical damping coefficient is exceeded. Increasing the damping coefficient by an order of magnitude may achieve only modest reductions in the response amplitude. Although the damping is seen to have only a slight effect on the steady-state

amplitude, it does affect the rate of growth of the instability caused by a parametric resonance.

Next we discuss the influence of the coefficients α and δ of the cubic and quadratic nonlinearities on the steady-state amplitude. As discussed earlier, the nonlinearities influence the steady-state amplitudes through the nonlinear frequency shift $\varepsilon^2 \alpha_e a^2$, where α_e is defined in (3.15). When $\alpha_e = 0$, the influence of the nonlinearity on the steady-state amplitude disappears, and the parametric resonance produces an exponential growth of the response if the trivial solution is unstable (see (3.26)). This growth is not limited to a finite value by the damping, as it is for externally excited systems; only the nonlinearity can limit it. The larger α_e is, the greater the limiting effect is, and hence the smaller the steady-state amplitude is. We note that the present analysis is not valid when $\alpha_e \approx 0$, and higher-order nonlinear effects must be included to limit the response.

The effect of the coefficient α of the cubic nonlinearity for two different values of detuning is shown in Figure 3.9, and the effect of the coefficient δ of the quadratic nonlinearity for the same values of detuning is shown in Figure 3.10. The influence of the coefficient of the cubic nonlinearity is asymmetric with respect to the origin, whereas the influence of the coefficient of the quadratic nonlinearity is symmetric. In both figures, we see the perturbation solution breaking down when $\alpha_e \approx 0$. We also note that detuning the excitation has two effects: (a) it stabilizes the trivial solution, and (b) it turns one stable branch into an unstable branch by folding it about $\alpha_e = 0$,

causing $\alpha_e = 0$ to become an asymptote. The asymptote divides the parameter axis into two regions: (a) a region where only the trivial solution exists, and (b) a region where both trivial and nontrivial solutions exist.

In summary, we have seen in this section that the perturbation solution predicts the response of the system to a principal parametric resonance, including the subcritical instability. As the perturbation coefficient ε gets larger, or the effective nonlinearity α_e approaches zero, the perturbation solution breaks down, as expected.

3.3 Analogue Computer Simulation

Equation (3.1) was simulated on an analogue computer for fixed values of ε , δ , α , μ , ω_0 , and Ω . In the following discussion, we show how the amplitude of the excitation affects the steady-state response. Figure 3.11 shows the phase portraits of distinct attractors; the auto power spectra of the four different attractors are shown in columns B, C, D, and E when they exist. Time traces of selected responses are shown in Figure 3.12.

We begin with the free response of the system, shown in Figure 3.12(a). As g is increased, we see a difference in the behavior of the response in the two wells: the focus at the origin remains trivial, but the focus in the left well gives rise immediately to a nontrivial vibration. This behavior is expected because, according to the governing equation, the system is subject to a purely parametric excitation at the origin, and hence requires a critical amplitude of

excitation (e.g., see Figure 3.2) before a resonance occurs. However, in the left well, an expansion of the governing equation (3.1) about $u = -10$ yields an equation that contains both external and parametric excitations. Consequently, the system responds immediately to the excitation with an attractor in the left well, corresponding to the particular solution. This behavior is illustrated in Figure 3.11(b)-A showing the phase portrait of the only nontrivial solution, in Figure 3.12(b)-D showing the time history, and in Figure 3.11(b)-D showing the frequency spectrum of the response.

By the time $g = 3.40$, a new stable attractor appears that encircles both of the stable foci. We note that it is a principal parametric resonance because its period is one-half that of the excitation. The phase portrait shows a distorted trajectory in Figure 3.11(c)-A. This distortion is caused by the nonlinearity and consists largely of the second and third harmonics. The time trace is shown in Figure 3.12(c)-B. The small amplitude vibration in the left well shows only a slight growth in amplitude.

The first period-doubling bifurcation occurs to the large outer trajectory and is well established by the time $g = 4.63$. It is easily seen in the phase portrait, shown in Figure 3.11(d)-A, and just barely seen in the time trace shown in Figure 3.12(d)-B. The spectrum also shows the bifurcation with the presence of new frequency components at $\omega_0/2$, $3\omega_0/2$, $5\omega_0/2$, etc. The response at the origin remains trivial, and the vibration in the left well grows slightly in amplitude.

When $g = 4.77$ the trajectory about the left focus has also bifurcated and is well established when $g = 4.96$. At this level of excitation we also have a parametric resonance about the origin because we have exceeded the critical value. These three responses are shown in Figures 3.11(f)-A, 3.12(f)-B, 3.12(f)-C, and 3.12(f)-D.

As g continues to increase, the outer trajectory continues to experience period-doubling bifurcations while the left inner trajectory experiences a subharmonic bifurcation and then becomes extinct. This transition is seen in the spectra and the time traces. The outer trajectory experiences a cascade of period-doubling bifurcations culminating in chaos; then it disappears. Figures 3.11(g)-A, 3.11(g)-B, and 3.12(g)-B show this trajectory when its period is 16 times the period of the excitation, and Figures 3.11(j)-C, 3.12(j)-B, and 3.12(j)-C show a transient chaotic response as it is attracted to the origin. When $g = 5.60$, only the attractor at the origin remains.

When the large outer attractor again appears, it is chaotic, as shown in Figures 3.11(l)-B and 3.12(l)-B. We can follow it through a series of period-demultiplying bifurcations as it returns to a principal parametric resonance as shown in Figure 3.11(t). During this transition, the trajectory at the origin begins to experience period-multiplying bifurcations leading to chaos and eventually to extinction. This is seen in Figure 3.11(q) where the only stable trajectory is the large outer one. When $11.30 < g < 14.00$, this attractor remains periodic. However, when $g = 15.00$ it begins another round of period-multiplying bifurcations culminating in chaos, as shown

in Figures 3.11(z)-B and 3.12(z)-B. Further increases in g cause the chaotic response to become less deterministic (compare Figures 3.12(z)-B with 3.12(cc)-B) and eventually unstable, so that by the time $g = 16.50$, it vanishes.

We note the existence of a new larger outer trajectory that appears when $g = 13.10$. This attractor coexists with the principal parametric attractor, but it has the same period as the excitation, as shown in Figures 3.11(u)-E and 3.12(u)-E. It remains periodic even though the smaller amplitude attractor becomes chaotic, as shown in Figure 3.11(v)-3.11(dd). This is an interesting phenomena because both trajectories are similar in amplitude but one has a period equal to that of the excitation and one has a period twice that of the excitation. When the inner attractor, shown in Figure 3.11(dd), becomes chaotic its largest amplitude excursions actually exceed the other coexisting attractor shown in Figure 3.11(ee), yet they are distinct in their orbits and frequency content. Eventually the inner trajectory becomes unstable, and only one outer attractor remains. This is shown in Figure 3.11(ff). We note that it contains only slight second harmonic distortion caused by the nonlinearity.

In summary, we have characterized the general response of the system by presenting the phase portraits, the frequency spectra, and the time histories of representative samples. We have chosen system parameters such that there are three equilibrium positions (double well) and a large ϵ . As the amplitude of the excitation increases, we have observed new solutions appearing and existing solutions bifurcating into

chaos or extinction, to the extent that none of the original three attractors remains when $g = 18.00$. We also have seen the coexistence of regular limit cycles with bifurcated limit cycles and bifurcated limit cycles with chaotic responses. Whenever multiple attractors coexist, the initial conditions determine the response. Mapping out the domains of attraction is best done on the digital computer when the basin is fractal. Fractal basins and Poincaré maps will be shown later. However, mapping out the domains of existence, bifurcation boundaries, and chaotic boundaries is best done on the analogue computer. These results are discussed next.

3.4 Bifurcation Diagram

The analogue computer results described in section 3.3 comprise the solution space for the principal parametric resonance ($\Omega \approx 2.0$) when the amplitude of the excitation g is used as a parameter, and proper sets of initial conditions are specified to map all the existing attractors. The analogue computer results of Chapter II comprise a portion of the solution space for the fundamental parametric resonance. A global survey of the effect of the excitation on these attractors can be found by alternatively varying the amplitude and frequency of the excitation, and mapping the domains of the attractors in the g - Ω plane. This process generates regions of stable solutions enclosed by lines of bifurcation.

A periodic orbit of a dissipative system with a two-dimensional Poincaré map is known to lose stability through two types of

bifurcations (e.g., Swift and Wisenfeld [1984])--period-doubling or saddle-node. Therefore, domains of stable nontrivial solutions in the g - ω plane are bounded by lines of one or the other bifurcation, as shown in Figure 3.13, where the bifurcation diagram for the attractors described in section 3.3 for $g < 5$ is presented. The solid curves in Figure 3.13 indicate where period-doubling bifurcations occur and the dashed curve marks the occurrence of a saddle-node instability. The inserts (a)-(d) in Figure 3.13 show typical phase portraits of the stable attractors found in this portion of the parameter space. Regions A, B, and C represent the corresponding domains of stability for the orbits (a), (b), and (c) respectively, which show that for a given set of parameters (g, ω) in a stable domain, there is a nonzero basin of attraction for the particular orbit. Furthermore, the solutions undergo the aforementioned bifurcations when any of the parameters is varied such that we move across the boundaries of the region.

The qualitative results shown in Figure 3.13 can be compared with the more detailed sequence of solutions in Figure 3.12(a)-(g) for $\omega = 2.0$, and increasing values of g . The orbit shown in insert (a) of Figure 3.13 goes through a period-doubling bifurcation across boundary 1-2 and shortly thereafter a saddle-node instability (not shown in Figure 3.13 but seen in Figure 3.12(h) and (i)) makes the attractor unstable. The orbit in Figure 3.13(b) undergoes period-doubling bifurcations across the boundary 3-5 and becomes unstable across the boundary 3-4. Insert (c) shows the stable $2T$ period orbit which bifurcates again into a $4T$ orbit across the boundary 3-6, and undergoes

a period-doubling cascade culminating in chaos very shortly thereafter. The circles denote the sampled locations where chaos was observed. In addition to the attractors shown in Figure 3.13(a)-(c), the origin remains a stable attractor throughout this portion of the parameter space, as indicated by the insert (d), so no bifurcation curve is present for this point attractor at the origin.

A variety of peculiarities in the behavior of the solutions can be inferred from Figure 3.13; we can see that multi-stability is expected at the intersections of stable domains for different attractors. Some other relevant predictions that we can make are the location of saddle-node instabilities that produce jumps in the solution, and the behavior to be observed following the jumps, which could be that of another attractor if multi-stability is present in the neighborhood or even a divergence to infinity if no other solution is reachable.

Following the previously described scheme, analogue computer simulations were carried out for a broad portion of the parameter space $g-\Omega$. The results are summarized in Figures 3.14 and 3.15, where again, lines of bifurcation mark the limits of stability of the attractors whose phase portraits are shown in the inserts. A new type of bifurcation is present in this region, which represents the loss of stability of the point attractor at the origin to form a periodic cycle, better known as the Hopf bifurcation. It is denoted by dotted curves which identify the boundary where the periodic attractor shrinks to a fixed point.

Figure 3.14 shows the multiplicity of resonances that can be obtained by changing the excitation parameters in the governing equation (3.1). The stable domains of the solutions have shapes known as Arnold "tongues" (Arnold [1983]), and the superstructure formed in the bifurcation diagram has been conjectured to be universal for a large class of nonlinear oscillators by Parlitz and Lauterborn [1985]. Figure 3.15 is actually part of Figure 3.14 and is shown separately to avoid obscuring Figure 3.14; it should be considered to be an overlay. The bifurcation structure in Figures 3.14 and 3.15 should be interpreted as a qualitative description of the global behavior of the system rather than as an exact stability map. In some portions of the parameter space, particularly in the superharmonic region, the coexistence of many attractors with complicated attracting sets makes it difficult to precisely define and present the stability regions. Figure 3.15 shows some phase portraits whose stability regions are marked by just one bifurcation curve. In these cases the attractor was found in the portion of space below the curve; near the edges of the region below the curve the attractor would slowly transform into the shape of a neighboring one.

We see that this system is very rich in attractors, some of which coexist with others. In these cases, the initial conditions determine which attractor comprises the response. In some cases increasing a parameter, say g , causes a loss of stability and the solution goes to another attractor, but decreasing the parameter to its original value may not recover the original attractor. Hence, to return to the

original attractor required moving into the domain of the attractor and then finding initial conditions (by trial and error) that were in the basin of attraction. The process is quite tedious and time-consuming, but would be much more so on a digital computer.

3.5 Digital Computer Simulation

The results in sections 3.3 and 3.4 show the possible solutions of (3.1) for the case of principal parametric resonance. The digital computer gave the same solutions but with increased accuracy. Hence in this section we will present a representative sample of a Poincaré map and show the transition of a smooth basin boundary to a fractal boundary. The analogue computer lends itself well to plotting Poincaré maps, but it is not practical to use to determine fractal basin boundaries.

When $g = 14.5$, the outer attractor is chaotic and is shown in Figure 3.16, with a Poincaré map and a representative time trace. Because it is a subharmonic of order $\frac{1}{2}$, we must sample the state of the system at time intervals of $2T$, otherwise we get a superposition of two Poincaré maps.

We saw in Figure 3.11(a) that the system has two foci and that the left focus gives rise to limit cycles immediately because it is subject to a combined parametric and external excitation. The domains of attraction for the unforced case shown in Figure 3.11(a) are well defined by the inbound separatrices. By integrating the governing equation using different initial conditions, the domains of attraction

for the trivial attractor and the limit cycle attractor can be plotted. For the case of $g = 0.0$, there are two point attractors, and the basins of attraction shown in Figure 3.17 obtained by the digital computer are identical to those obtained by the analogue computer. As the excitation is increased, the left focus gives rise to limit cycles. The basin of attraction for $g = 1.50$ when $\phi = 2.000$ is shown in Figure 3.18, and it shows the outbound separatrices deformed, but they are still smooth. When $g = 2.00$, the basin boundaries become fractal, as shown in Figure 3.19. Increasing the excitation amplitude to $g = 2.50$ and $g = 3.00$ increases the fractal dimension of the basin, as shown in Figures 3.20 and 3.21, respectively. Figure 3.11(c) shows a new attractor is present when $g = 3.40$. The basin of attraction for the three attractors for the case of $g = 4.2$ is shown in Figure 3.22. The new outer attractor is shown in the color red. An enlarged portion of Figure 3.22 is shown in Figure 3.23 and it reveals a well defined structure. If this procedure were continued, we would continue to see well defined structure at all levels because this is the nature of a fractal boundary.

3.6 Chapter Summary

The method of multiple scales was used to obtain a uniform second-order expansion for the response of a one-degree-of-freedom system with quadratic and cubic nonlinearities to a principal parametric excitation. Steady-state solutions were obtained for small but finite amplitude oscillations around the origin, and it was shown that the

results qualitatively describe the system response for the parameters chosen. For large amplitude oscillations, the equation was integrated on both the digital and analogue computers. The response of the system modelled on the analogue computer was analyzed using an FFT analyzer.

The perturbation solution predicts a threshold value of the amplitude g of the excitation for which a principal parametric resonance about the origin can be excited; it also predicts a subcritical instability. The perturbation solution predicts the number of stable limit cycles and agrees with the digital and analogue computer simulation. However, as the perturbation coefficient ϵ becomes larger, the perturbation solution deteriorates.

The more interesting problem is the case of the double-well potential, having a stable limit-cycle attractor in each well (at different levels of excitation) and a large amplitude attractor about both foci consisting of stable limit cycles and chaotic oscillations. The analogue computer was used to obtain a global bifurcation map in the g - ω plane for both superharmonic and subharmonic resonances. The digital computer was used to plot Poincaré maps and the transition from a smooth basin to a fractal basin of attraction, including the case of three coexisting attractors. An enlarged plot reveals a complex but well defined structure of the fractal basin.

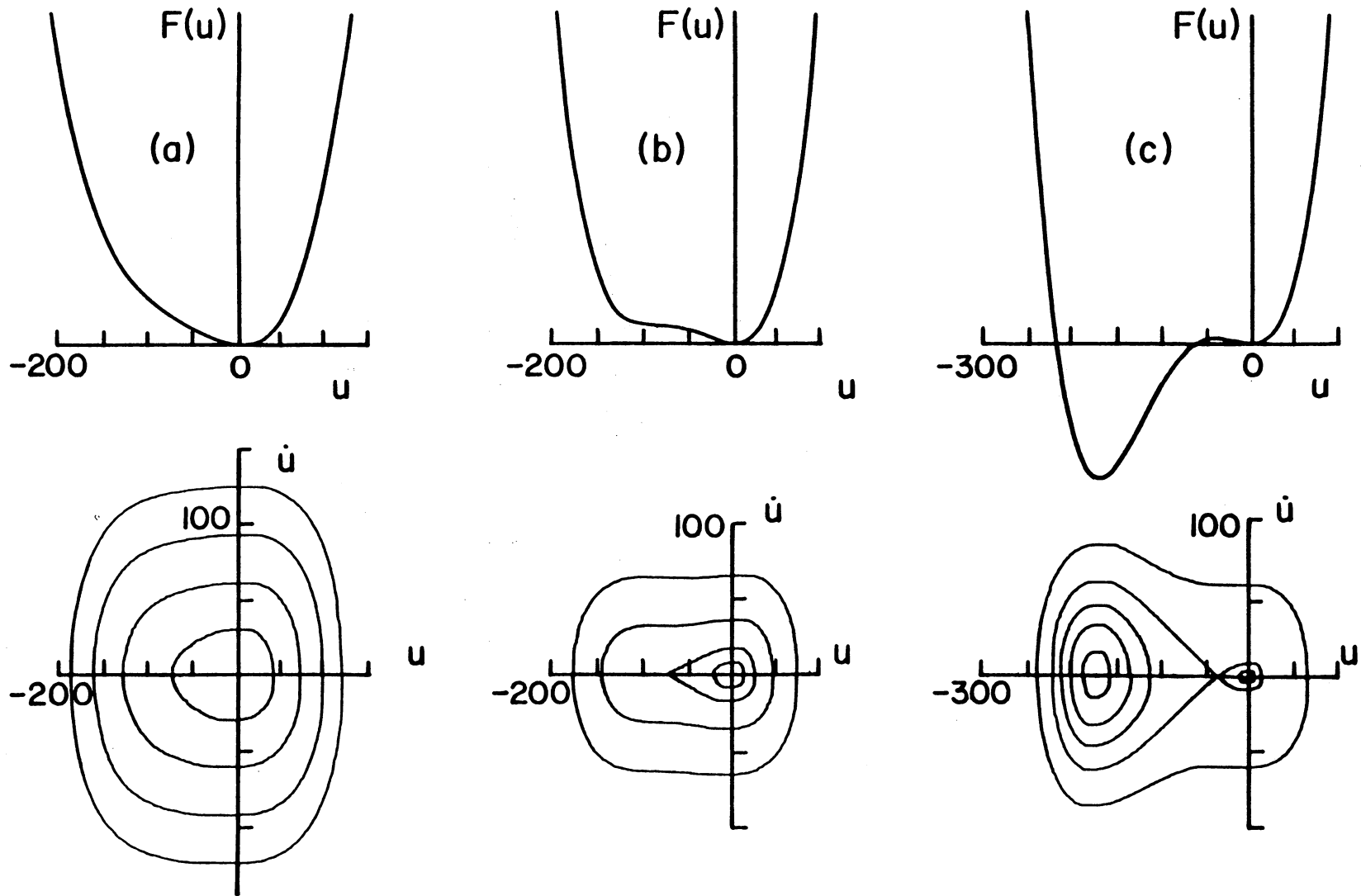


Figure 3.1 Potential wells and corresponding phase-plane portraits for three distinct cases: $\alpha = 4.0$, $\mu = 1.0$, $\epsilon = 0.005$, (a) $\delta = 3.0$, (b) $\delta = 4.0$, (c) $\delta = 5.0$. The phase-plane portraits were obtained using the analogue computer.

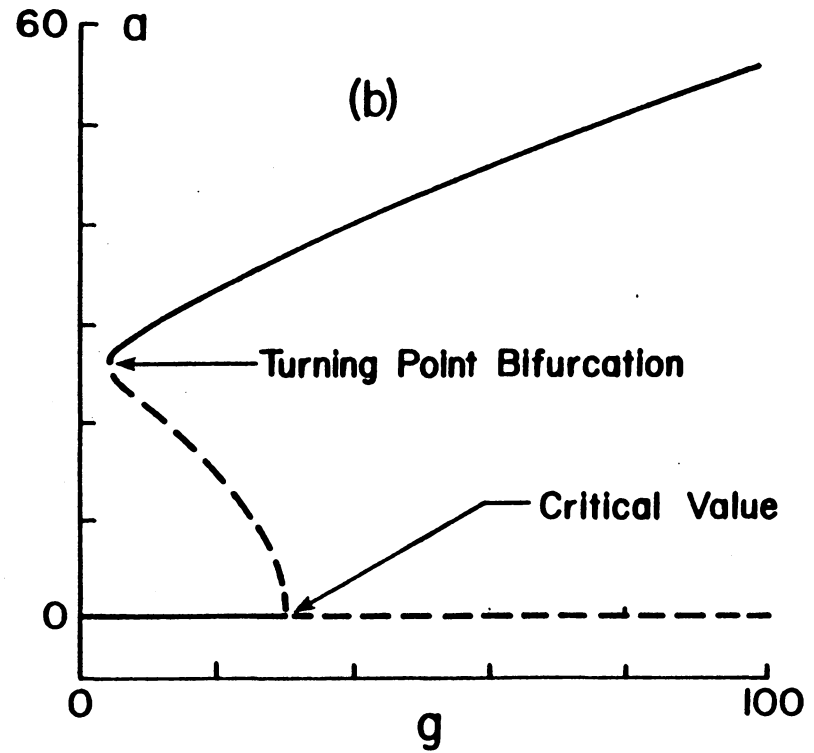
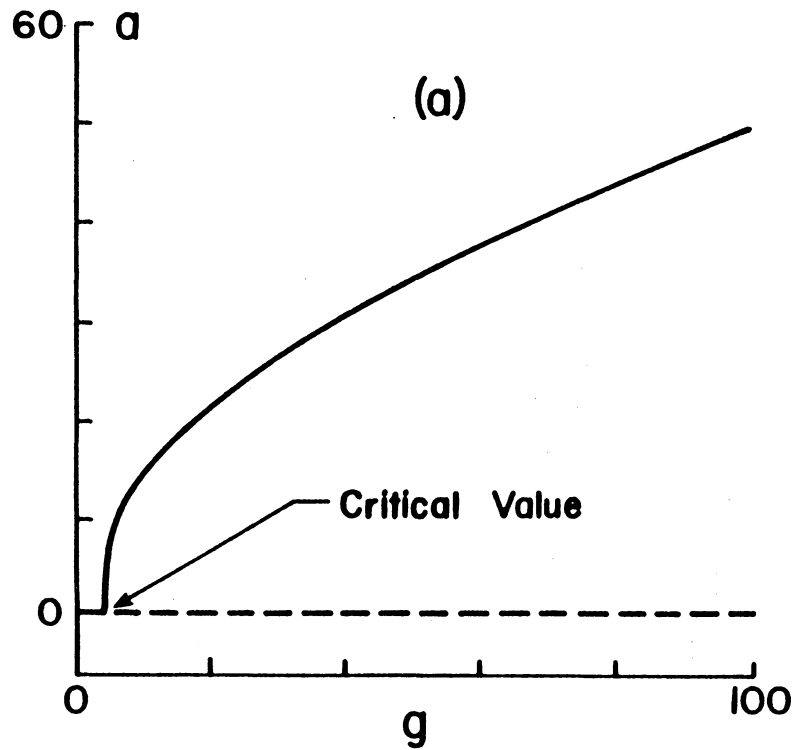


Figure 3.2 Variation of the steady-state response amplitude a with the excitation amplitude g : (—) stable, (----) unstable, $\alpha = 4.0$, $\delta = 3.0$, $\mu = 1.0$, $\epsilon = 0.005$, (a) $\sigma = 0.0$, (b) $\sigma = -15.0$.

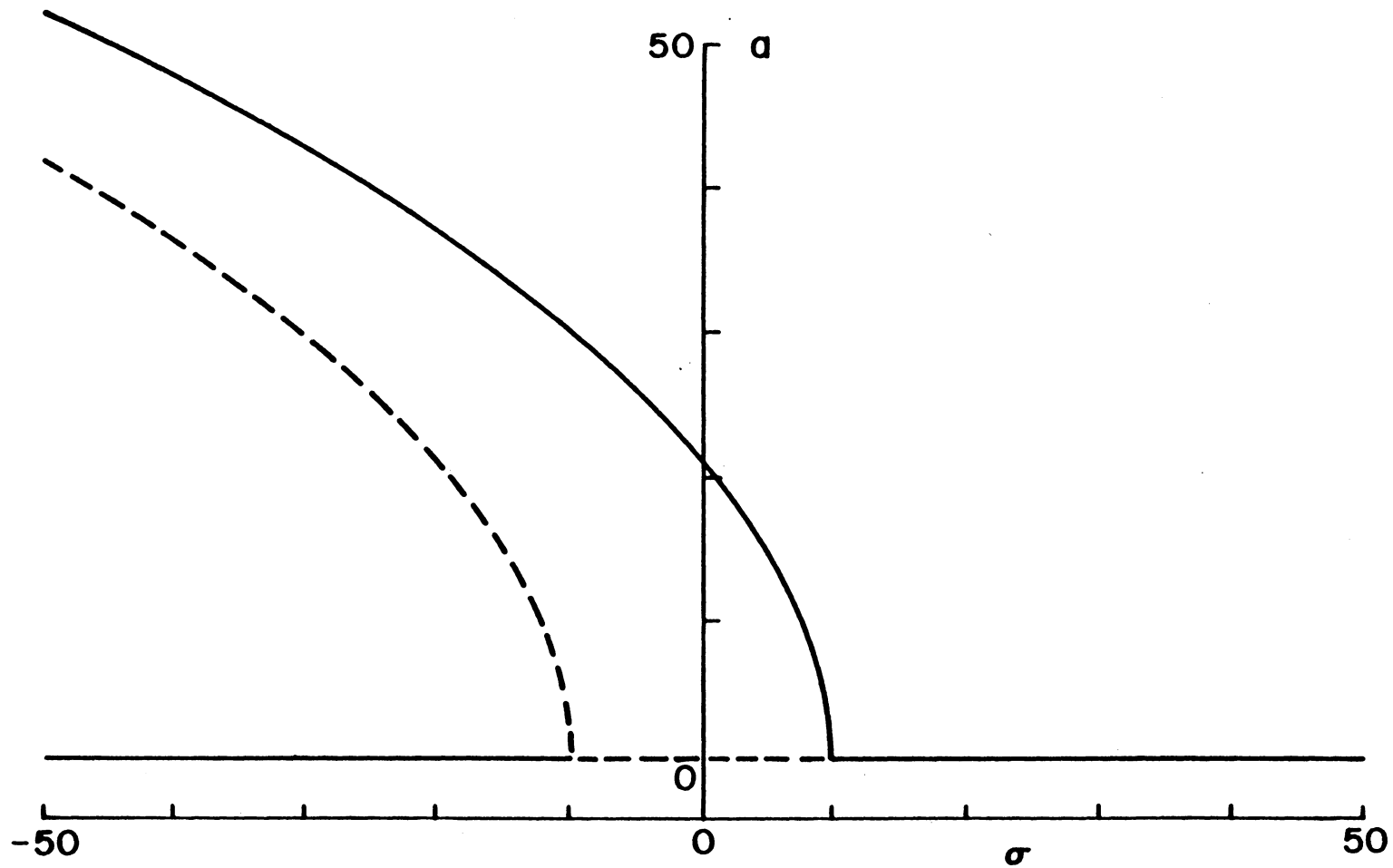


Figure 3.3 Variation of the steady-state response amplitude a with the excitation frequency detuning σ : (—) stable, (----) unstable, $\alpha = 4.0$, $\delta = 3.0$, $\mu = 1.0$, $g = 20.0$, $\epsilon = 0.005$.

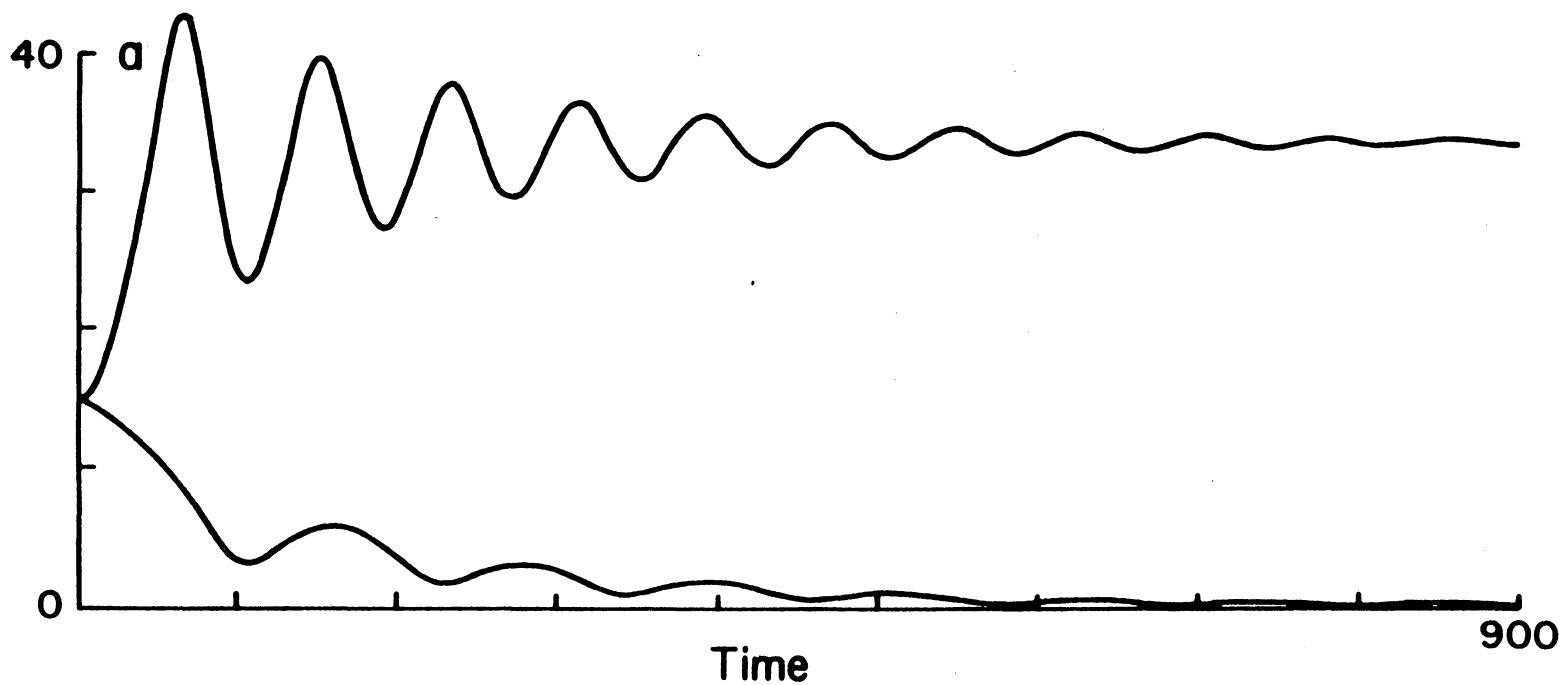


Figure 3.4 Long-time history of the amplitude showing only two stable steady states obtained by numerically integrating the amplitude- and phase-modulation equations (3.12)-(3.14): $\sigma = -15.0$, $\alpha = 4.0$, $\delta = 4.0$, $\mu = 1.0$, $g = 20.0$, $\epsilon = 0.005$. Although $a(0) = 15.0$ for both solutions, $\gamma(0)$ was chosen to attract the two different solutions.

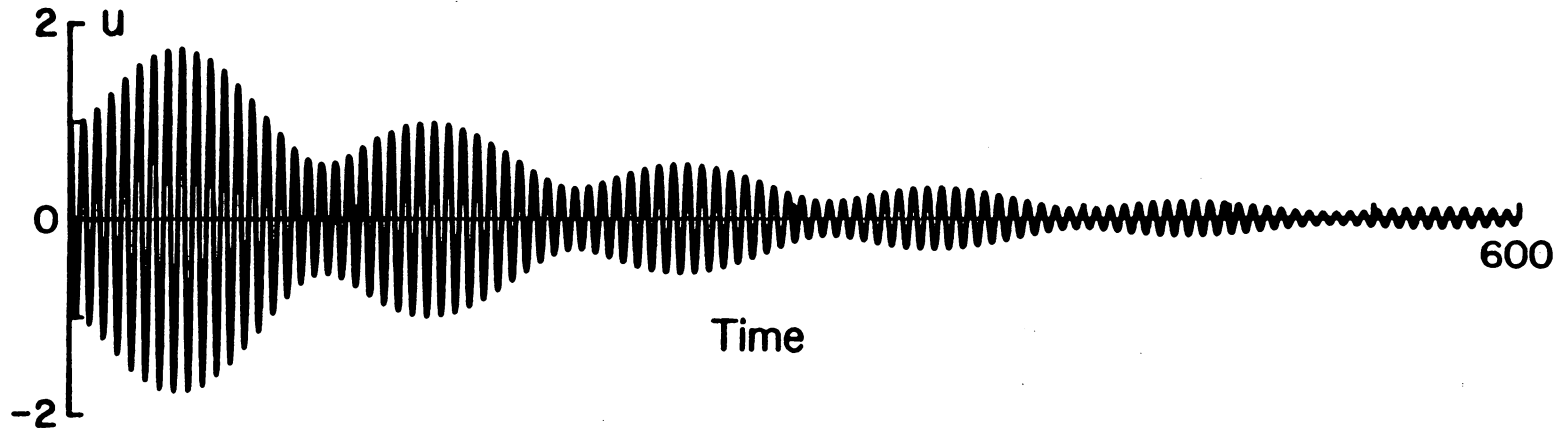


Figure 3.5 Time history of the response as it decays to the trivial solution, which is one of the two stable responses predicted by the perturbation solution shown in Figures 3.2, 3.3, and 3.4: $\sigma = -15.0$, $\alpha = \delta = 3.0$, $\mu = 1.0$, $g = 20.0$, $\epsilon = 0.005$.

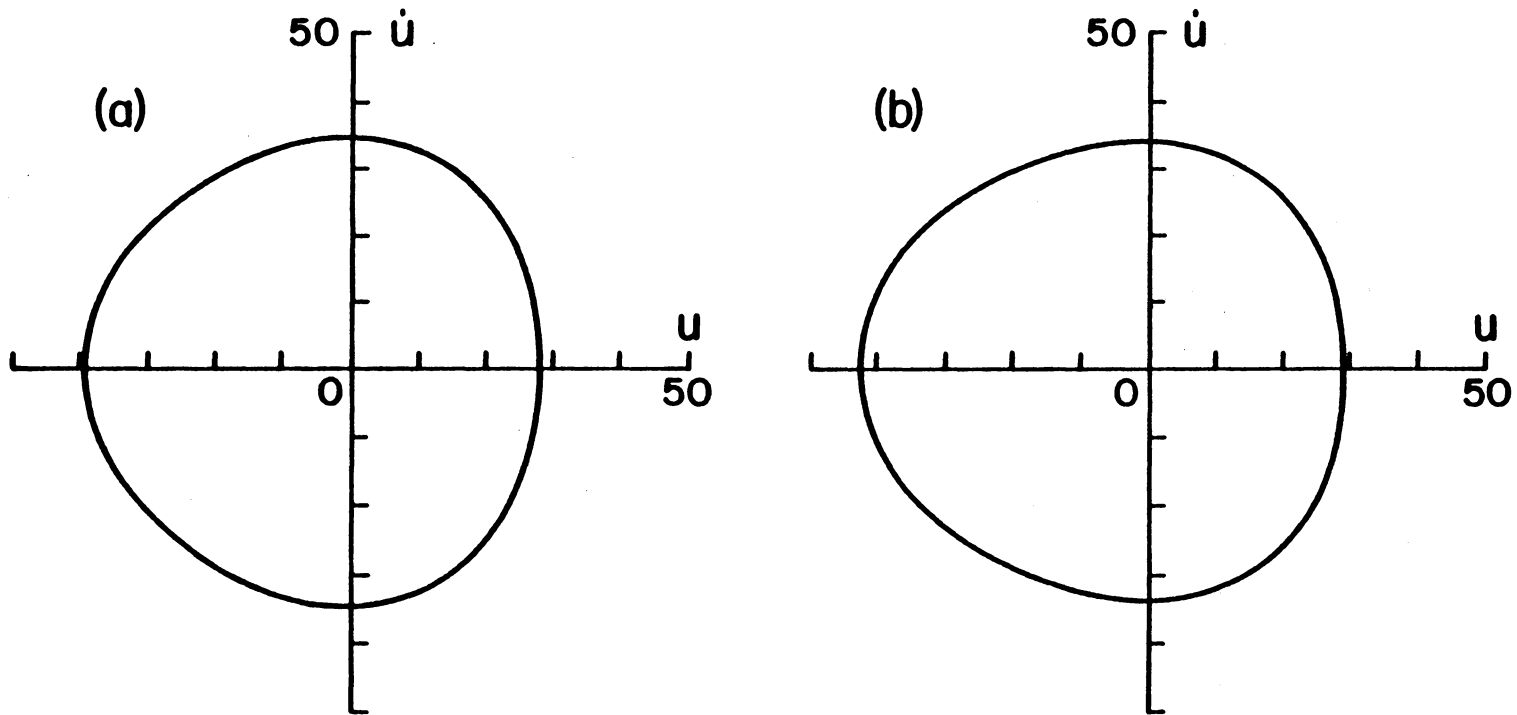


Figure 3.6 Phase-plane plot of the steady-state nontrivial response for the case shown in Figures 3.2, 3.3, and 3.4: $\sigma = -15.0$, $\alpha = 4.0$, $\delta = 3.0$, $\mu = 1.0$, $g = 20.0$, $\epsilon = 0.005$, (a) perturbation solution, (b) numerical integration.

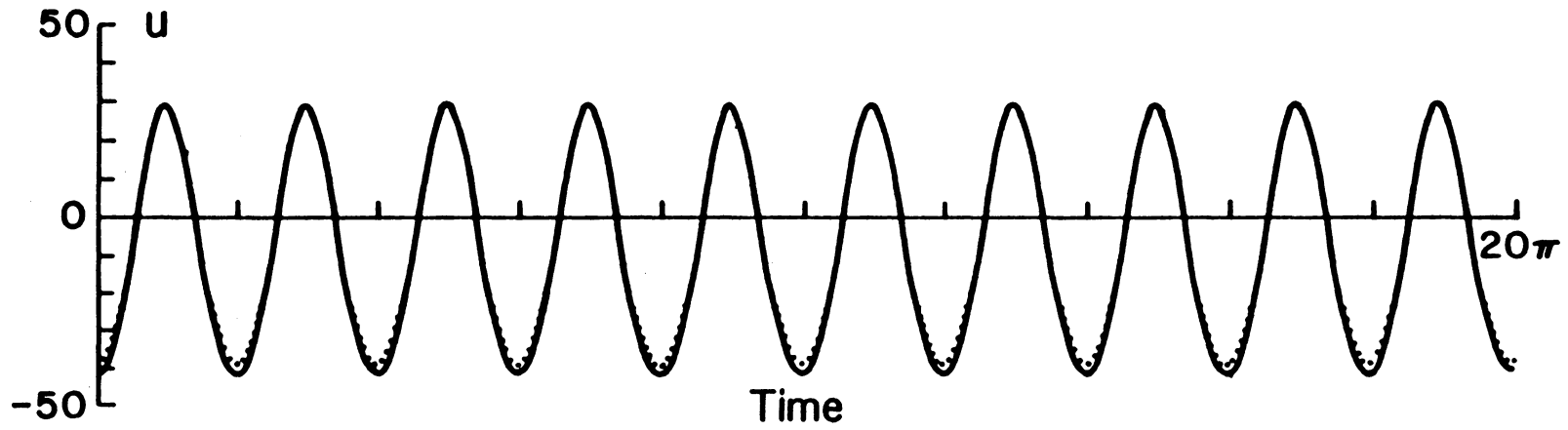


Figure 3.7 Time history of the steady-state response obtained by numerical integration (—) and the response predicted by the perturbation solution (...) for the case shown in Figure 3.6.

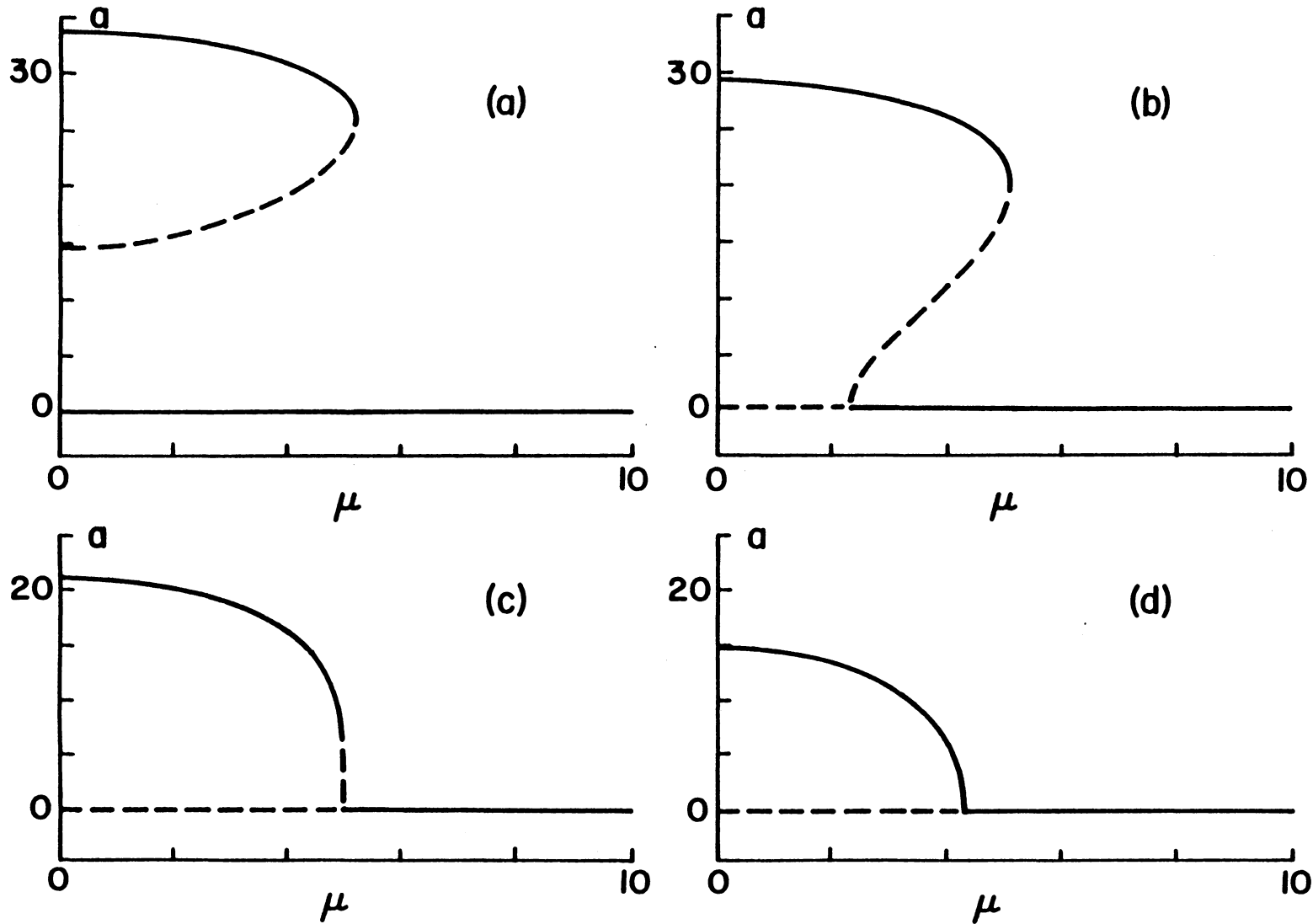


Figure 3.8 Variation of the steady-state response amplitude a with the damping coefficient μ : (—) stable, (----) unstable, $\alpha = 4.0$, $\delta = 3.0$, $g = 20.0$, $\epsilon = 0.005$, (a) $\sigma = -15.0$, (b) $\sigma = -9.0$, (c) $\sigma = 0.0$, (d) $\sigma = 5.0$.

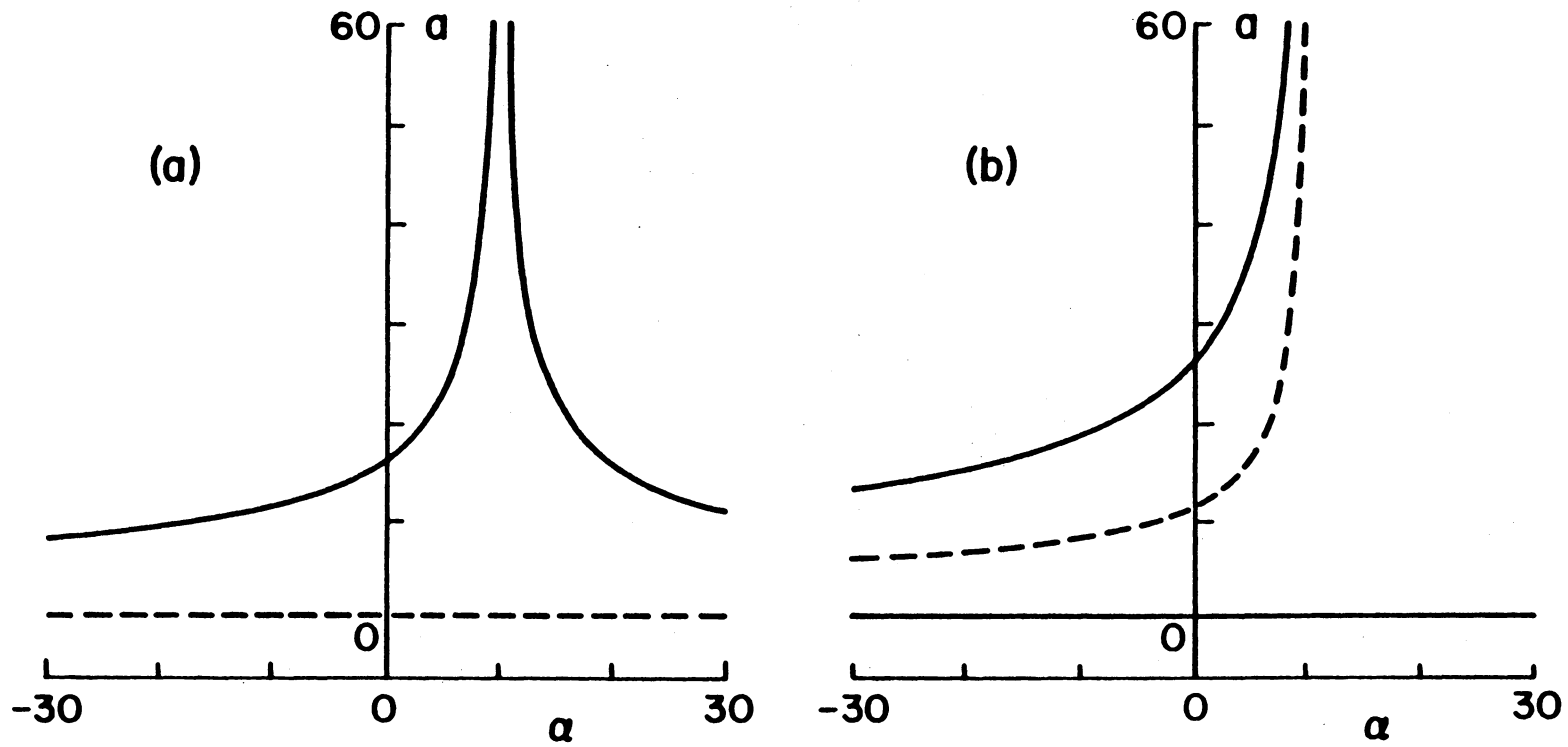


Figure 3.9 Variation of the steady-state response amplitude a with the coefficient α of the cubic nonlinearity: (—) stable, (----) unstable, $\delta = 3.0$, $\mu = 1.0$, $g = 20.0$, $\epsilon = 0.005$, (a) $\sigma = 0$, (b) $\sigma = -15.0$. It is asymmetric with respect to the origin.

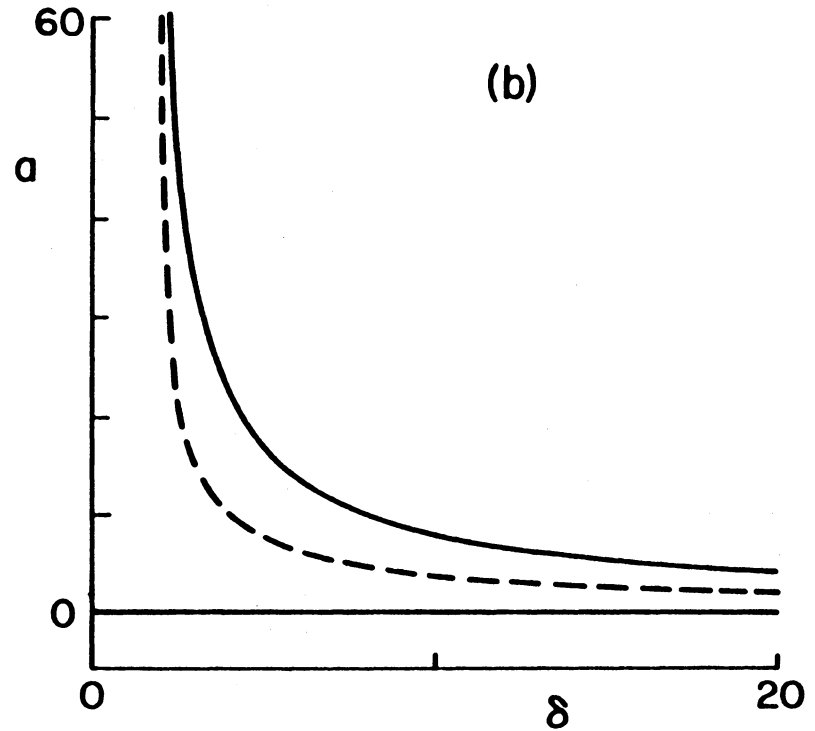
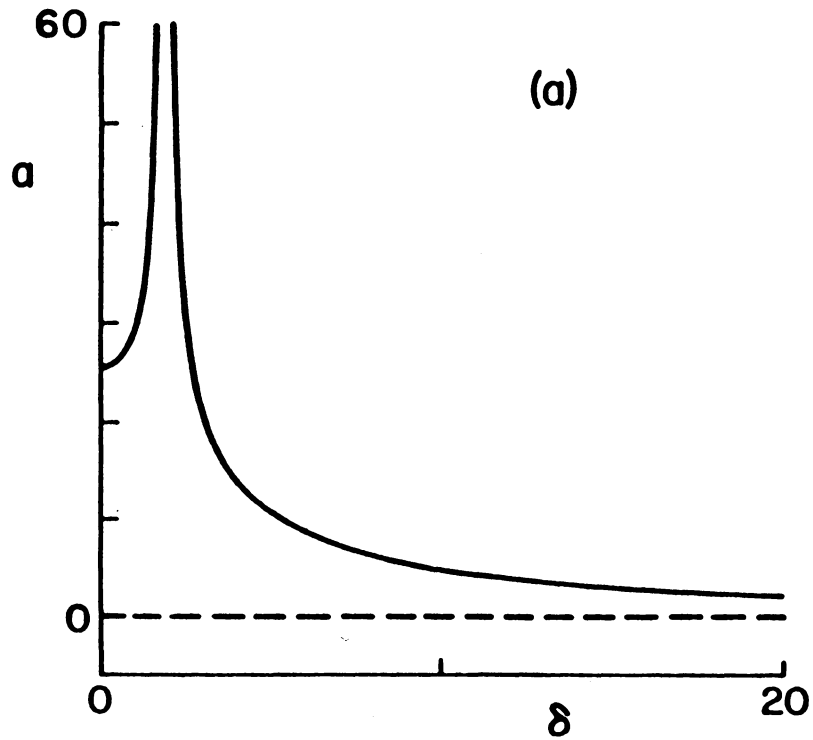


Figure 3.10 Variation of the steady-state response amplitude a with the coefficient δ of the quadratic nonlinearity: (—) stable, (----) unstable, $\alpha = 4.0$, $\mu = 1.0$, $g = 20.0$, $\varepsilon = 0.005$, (a) $\sigma = 0$, (b) $\sigma = -15.0$. It is symmetric with respect to the origin.

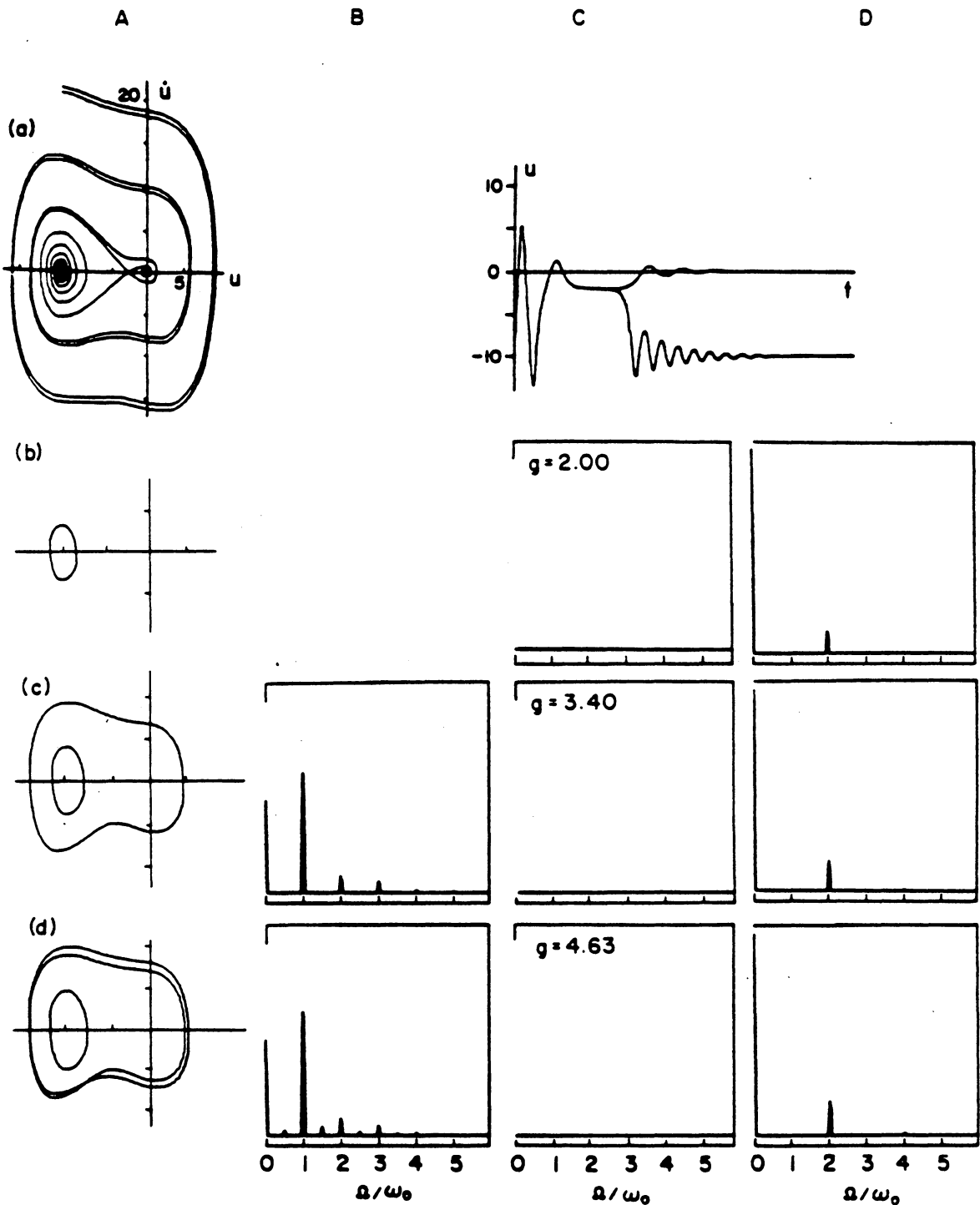


Figure 3.11 Phase-plane portraits and accompanying frequency spectra of the system response, obtained by analogue computer simulation: $\sigma = 0.0$, $\alpha = 4.0$, $\delta = 5.0$, $\mu = 1.0$, $\epsilon = 0.10$. The excitation g varies from 0.0 to 32.0.

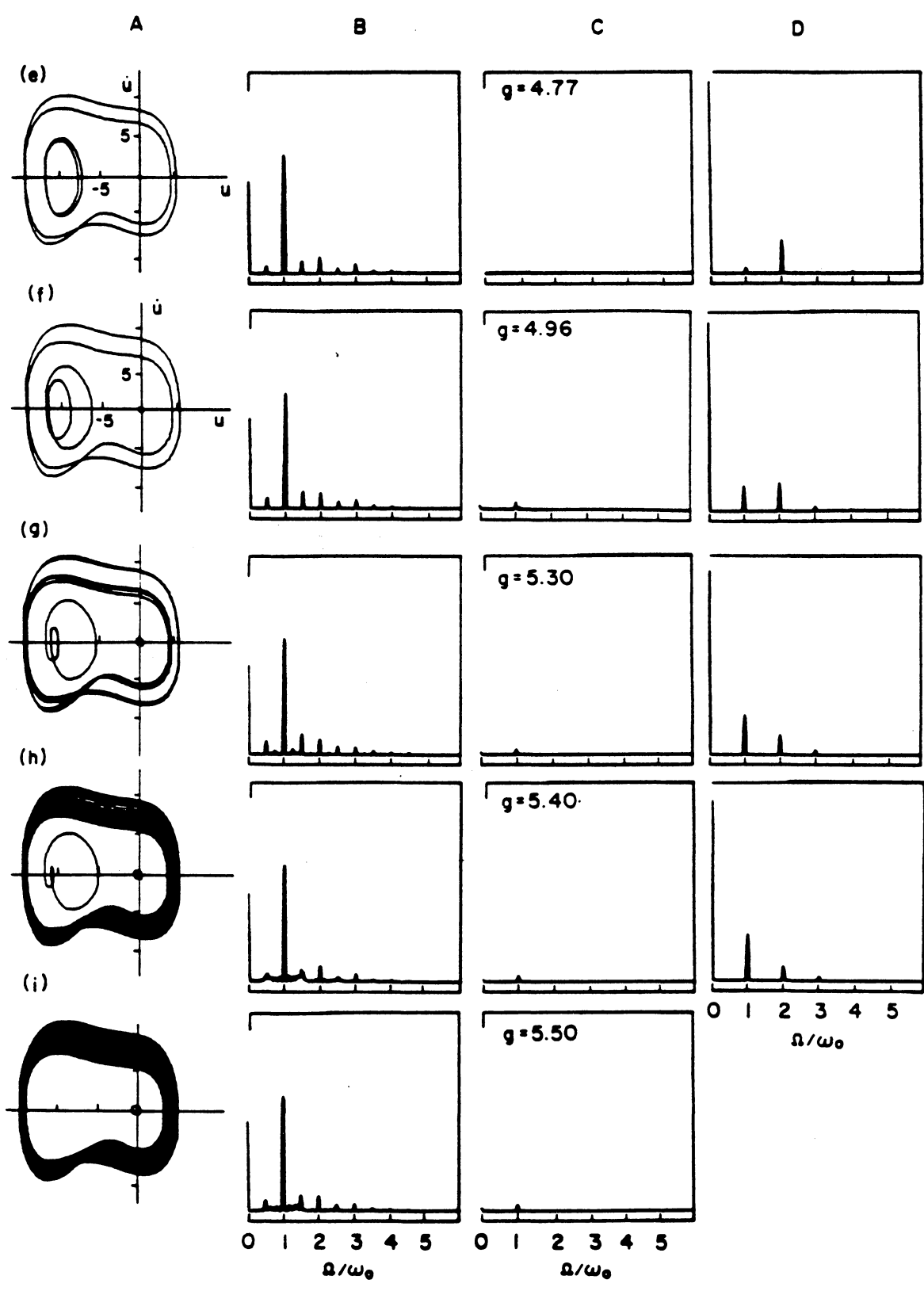


Figure 3.11 continued

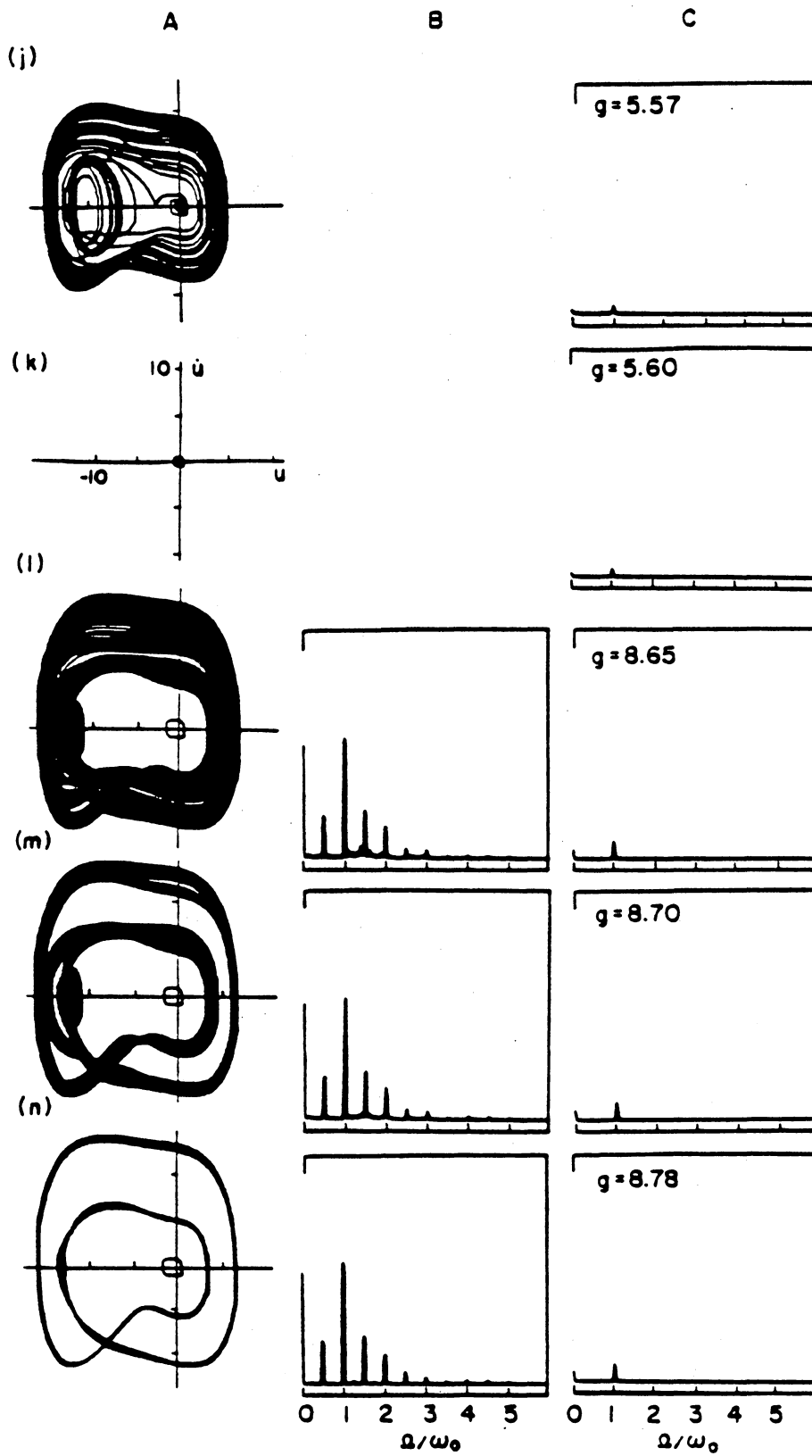


Figure 3.11 continued

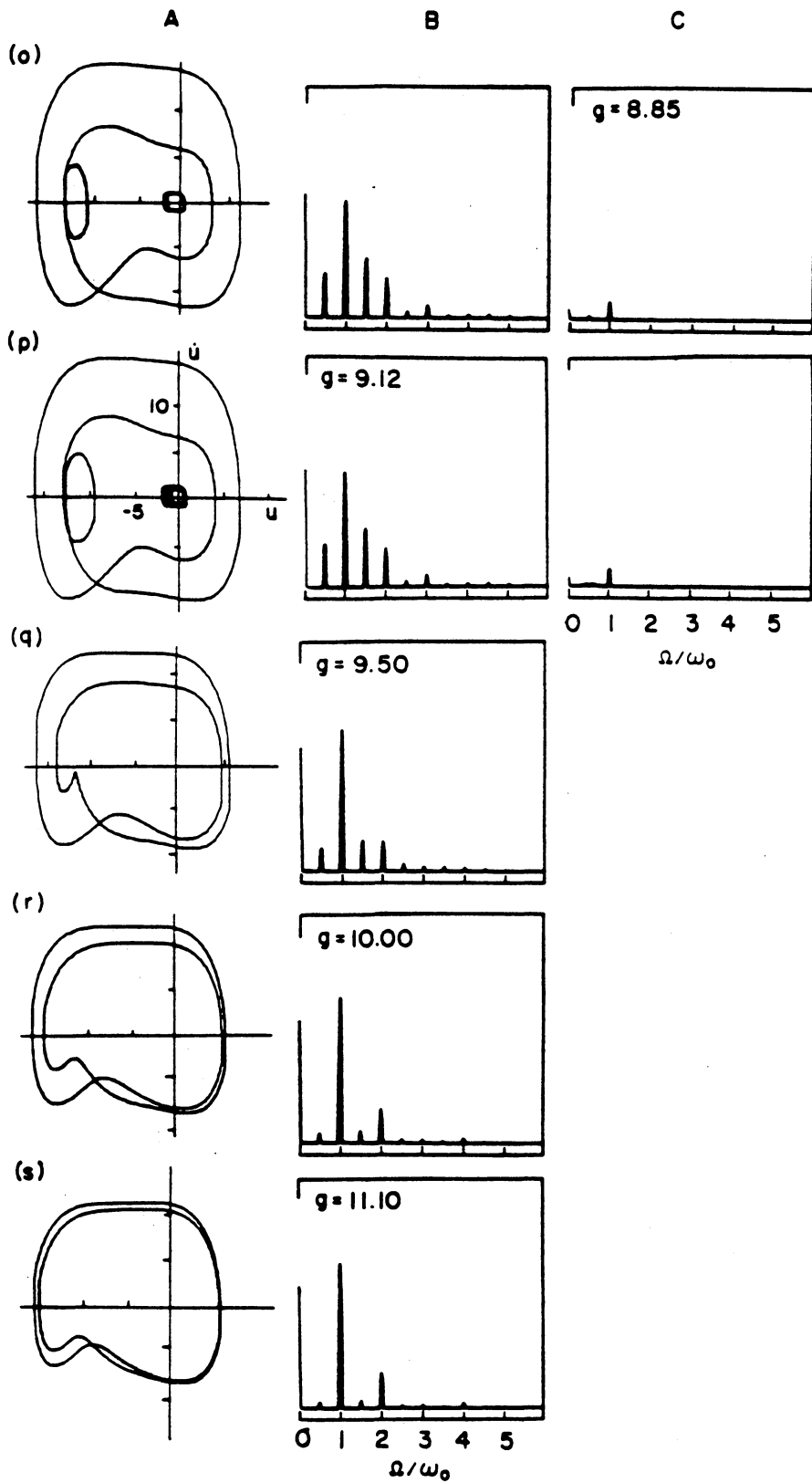


Figure 3.11 continued

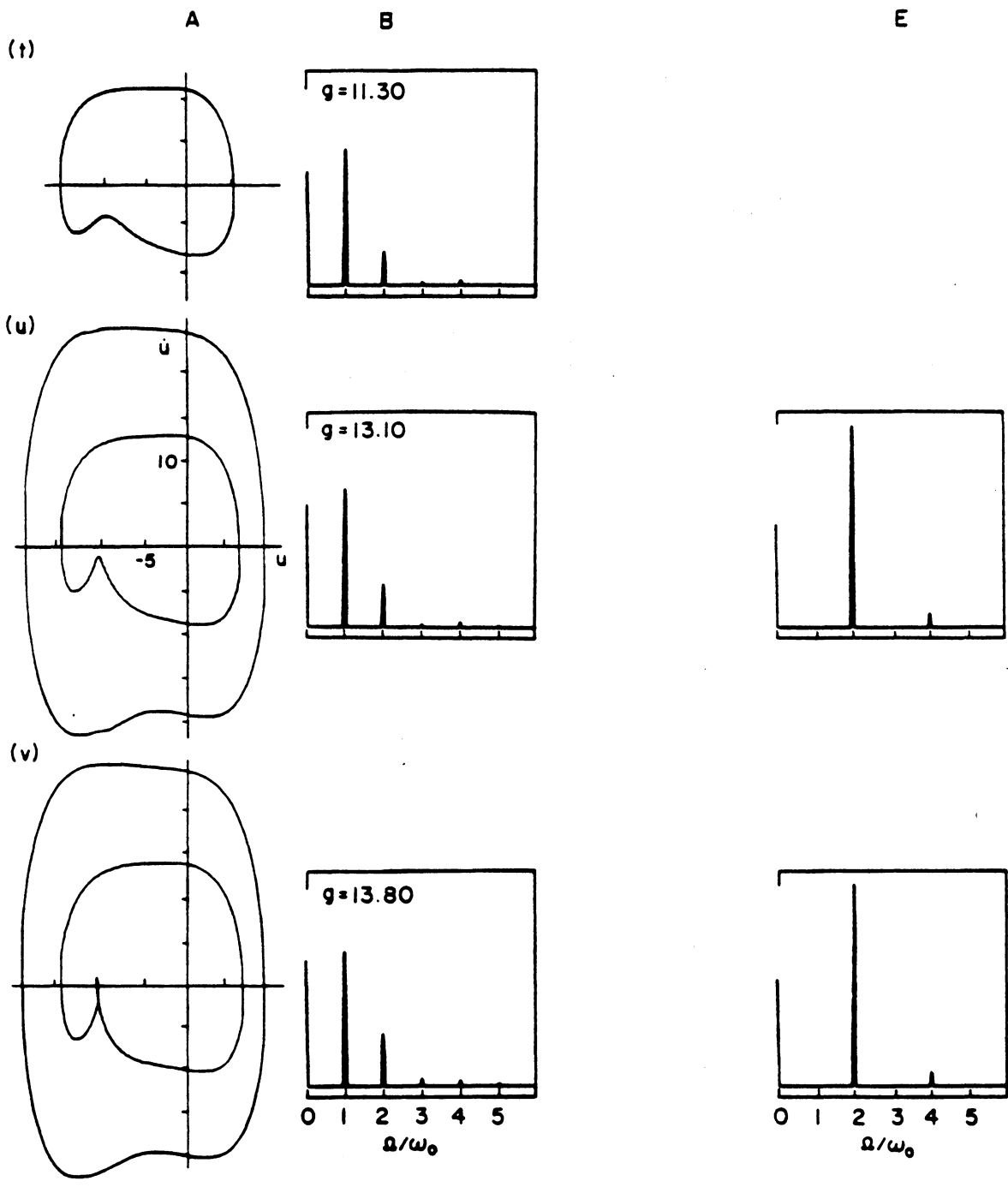


Figure 3.11 continued

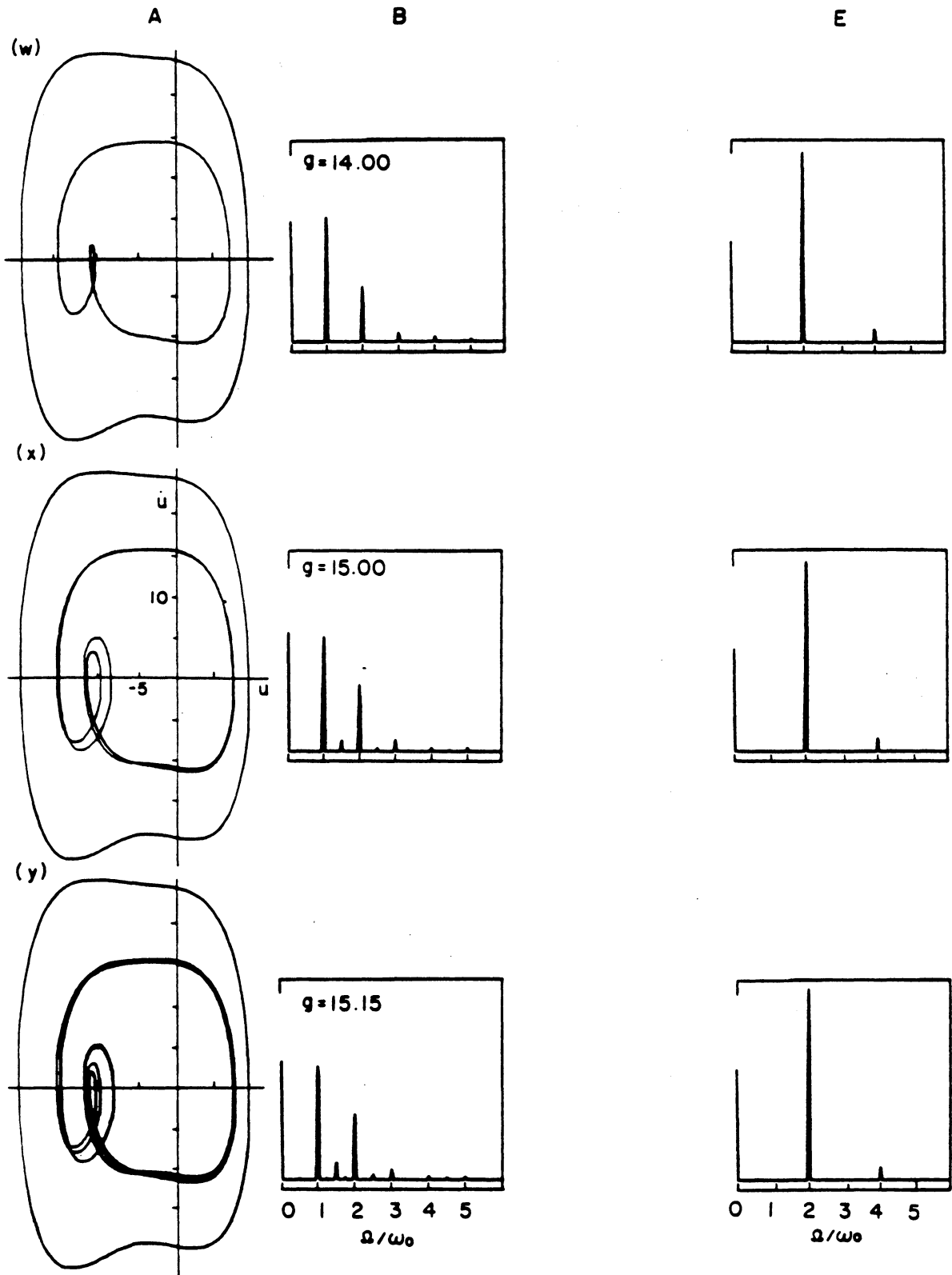


Figure 3.11 continued

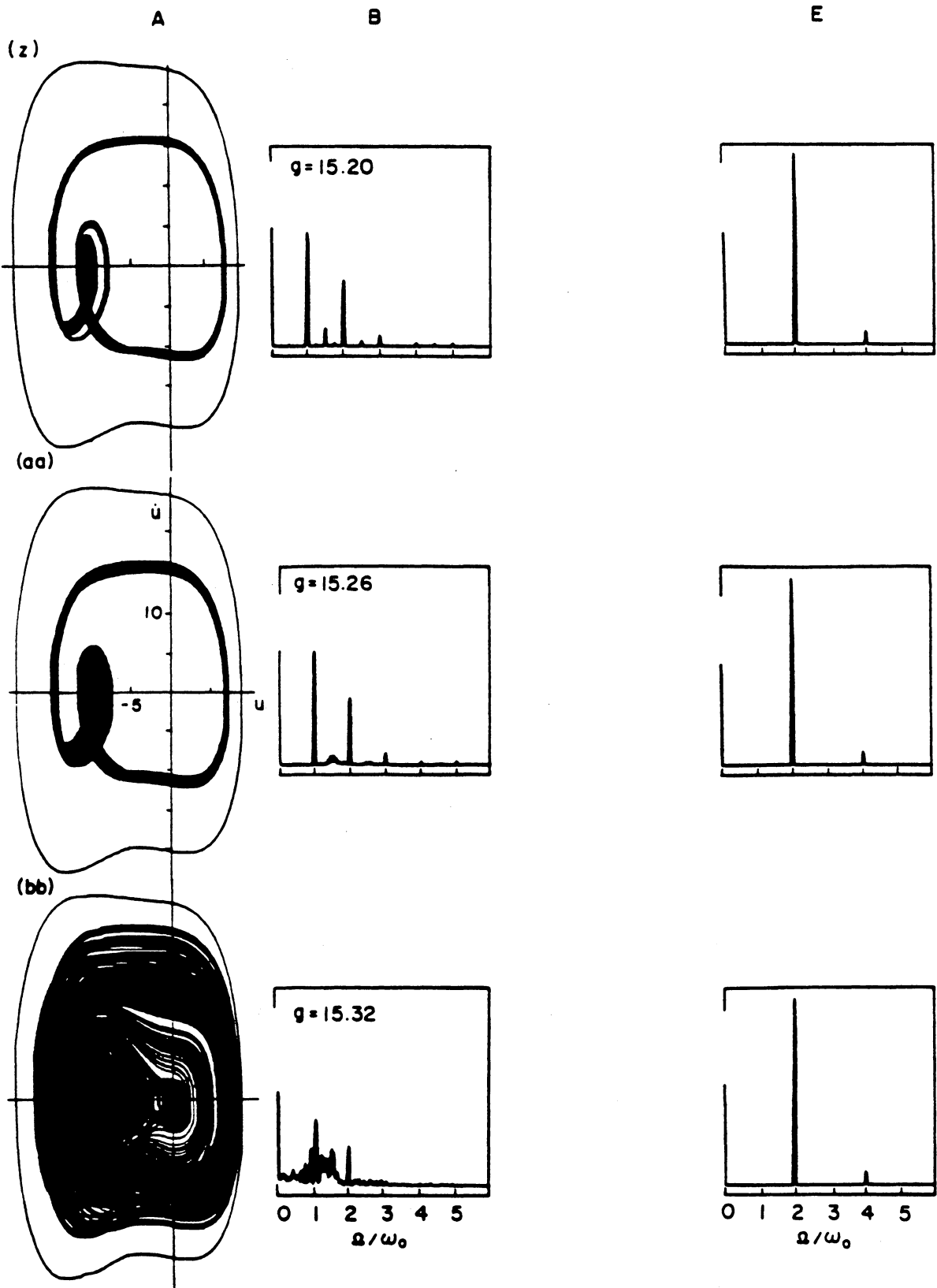


Figure 3.11 continued

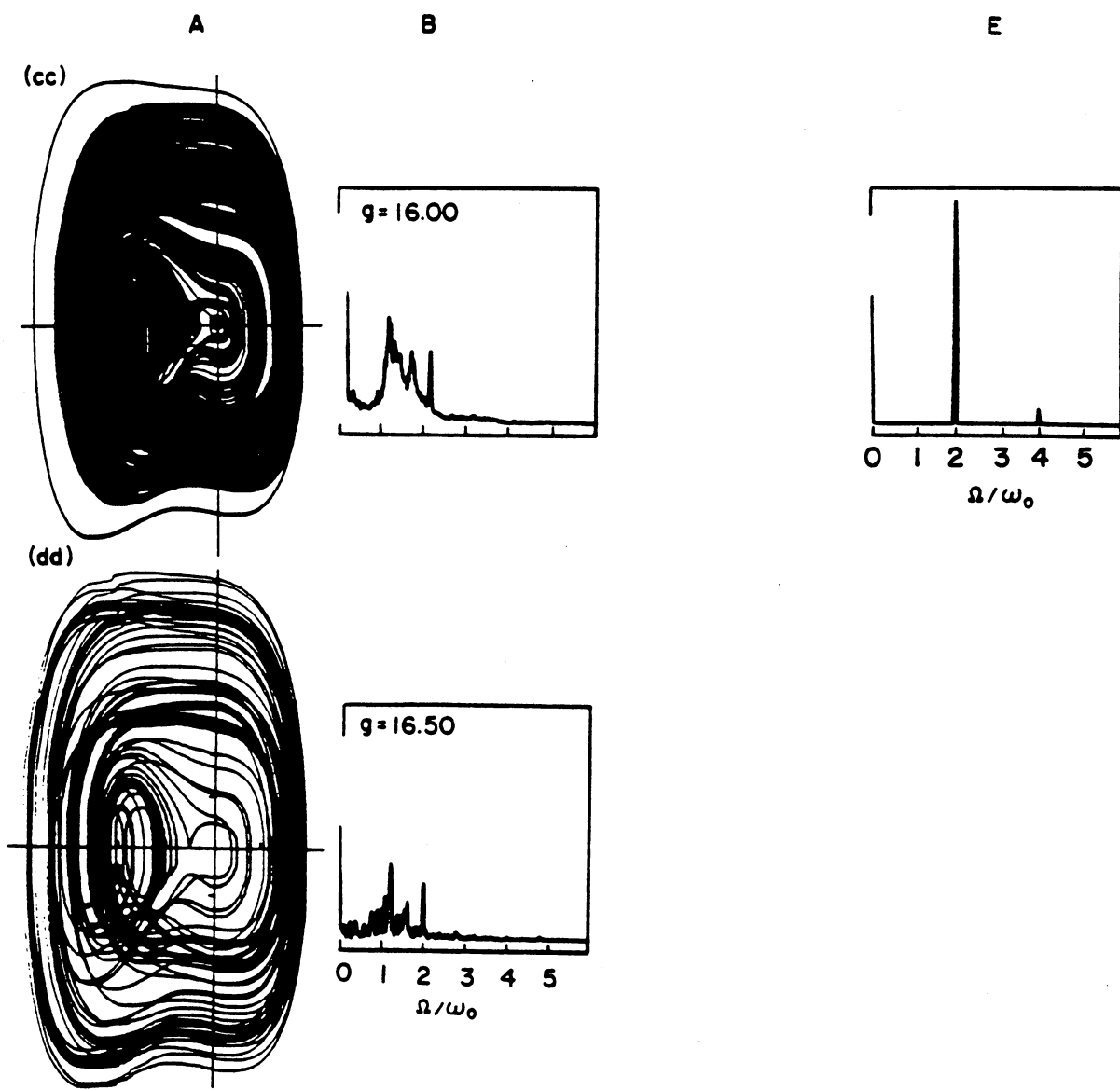


Figure 3.11 continued

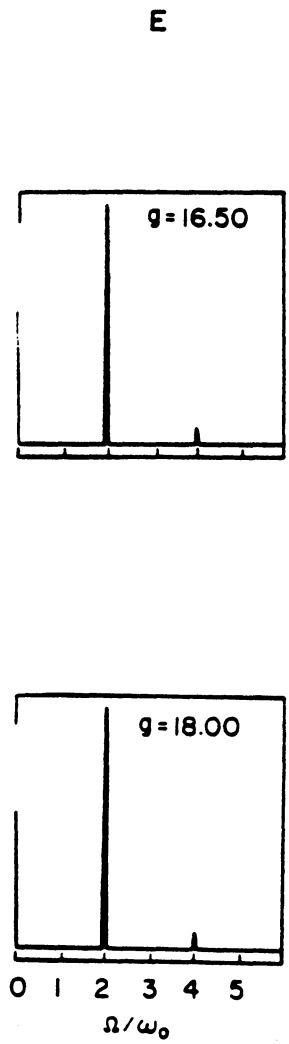
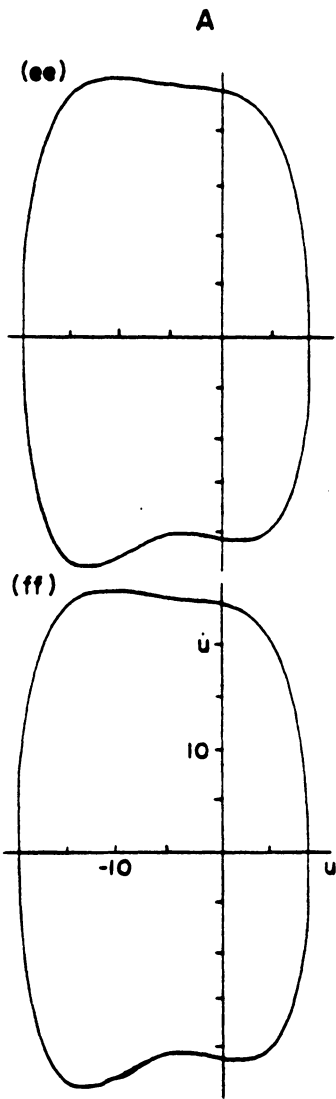


Figure 3.11 continued

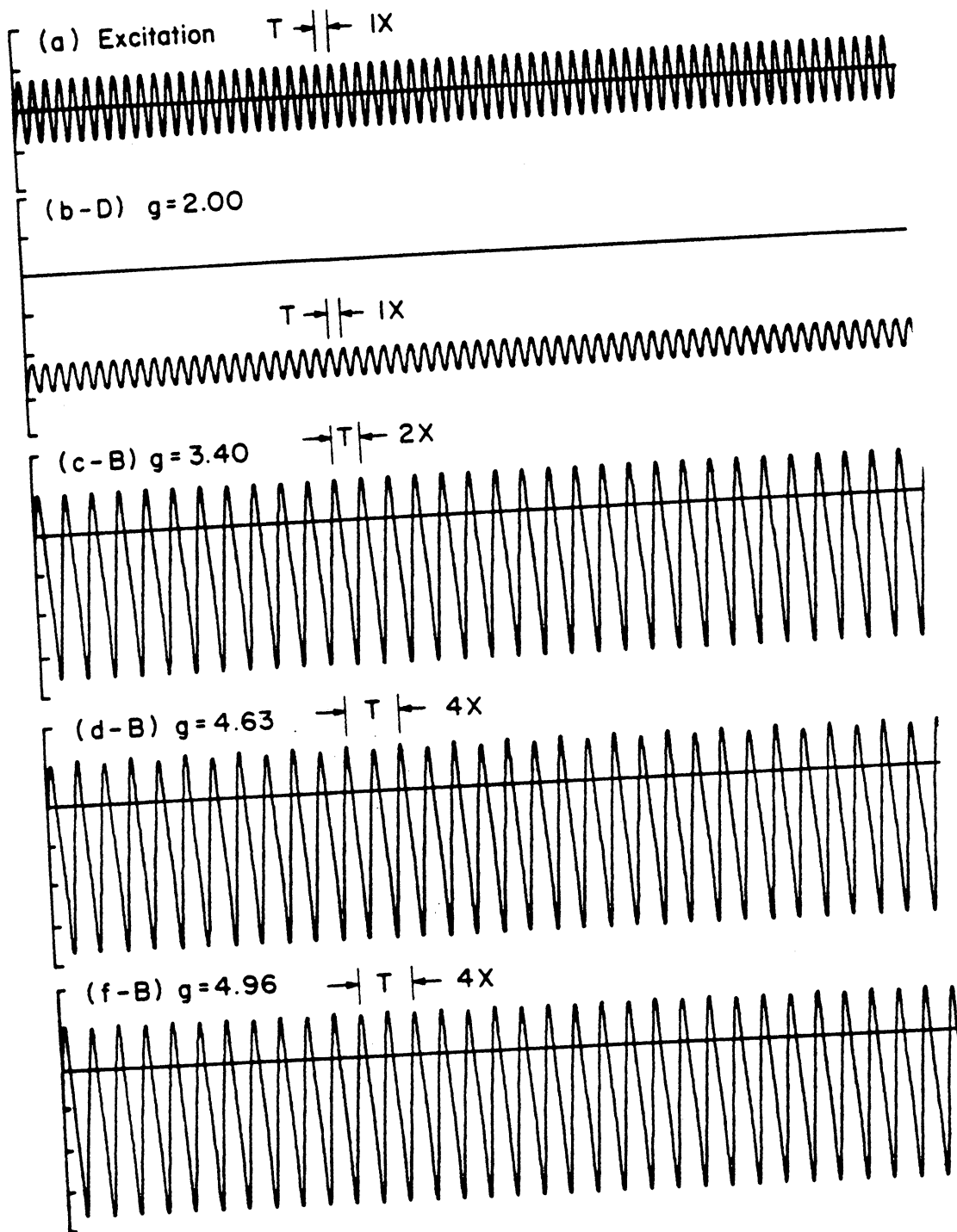


Figure 3.12 Long-time history for selected cases shown in Figure 3.11, obtained by analogue computer simulation, with the relative phase between the excitation and the response preserved.

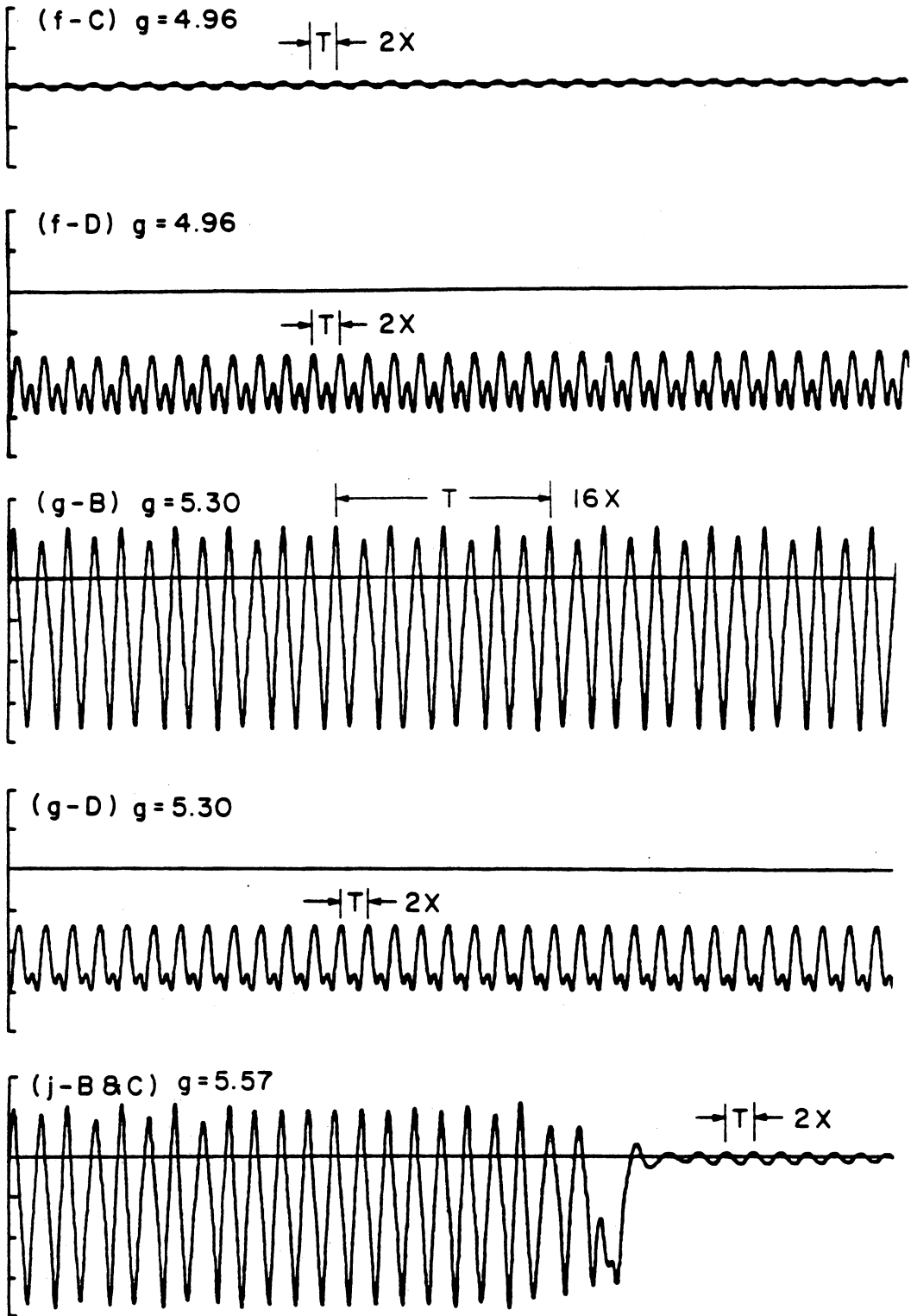


Figure 3.12 continued

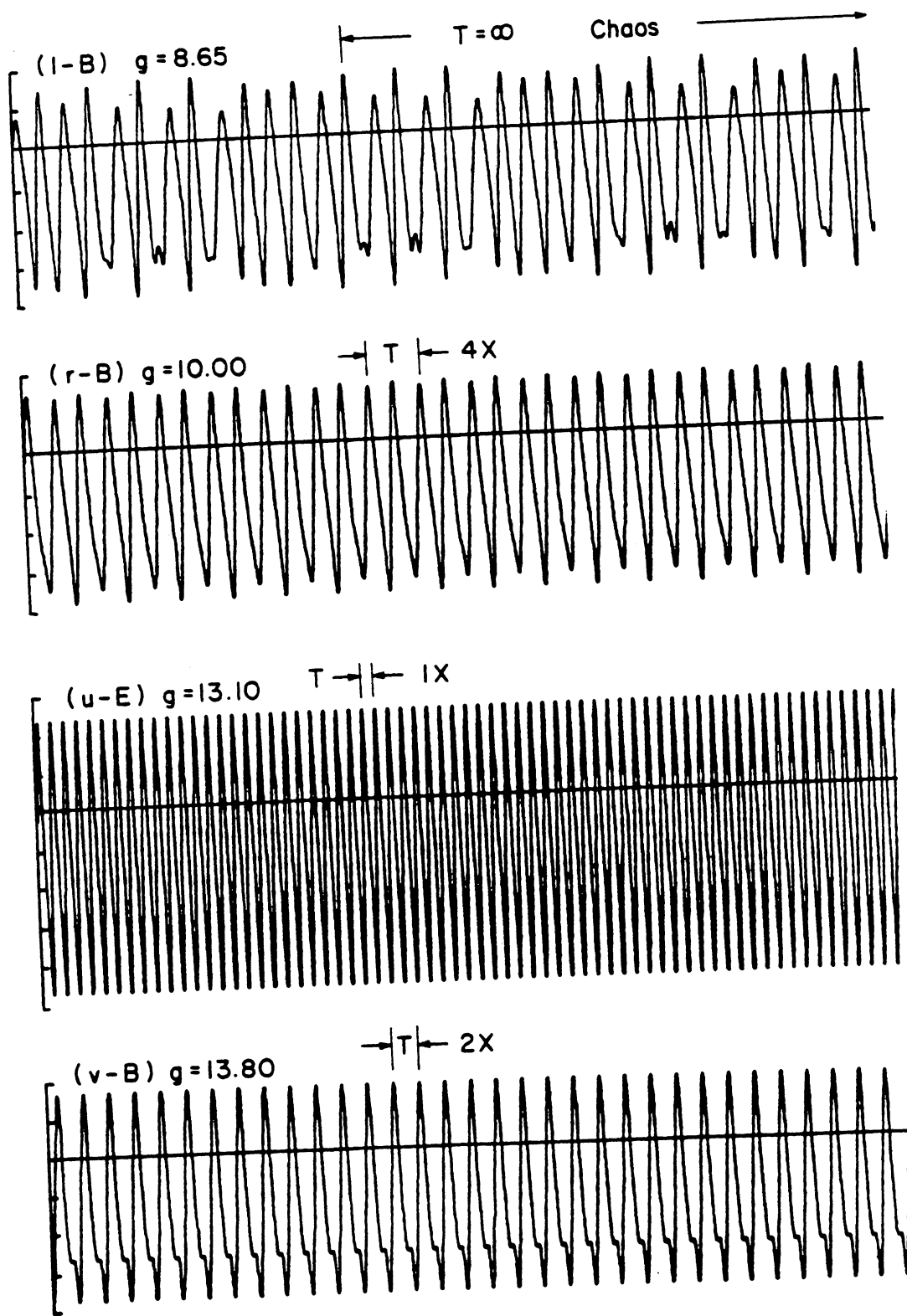


Figure 3.12 continued

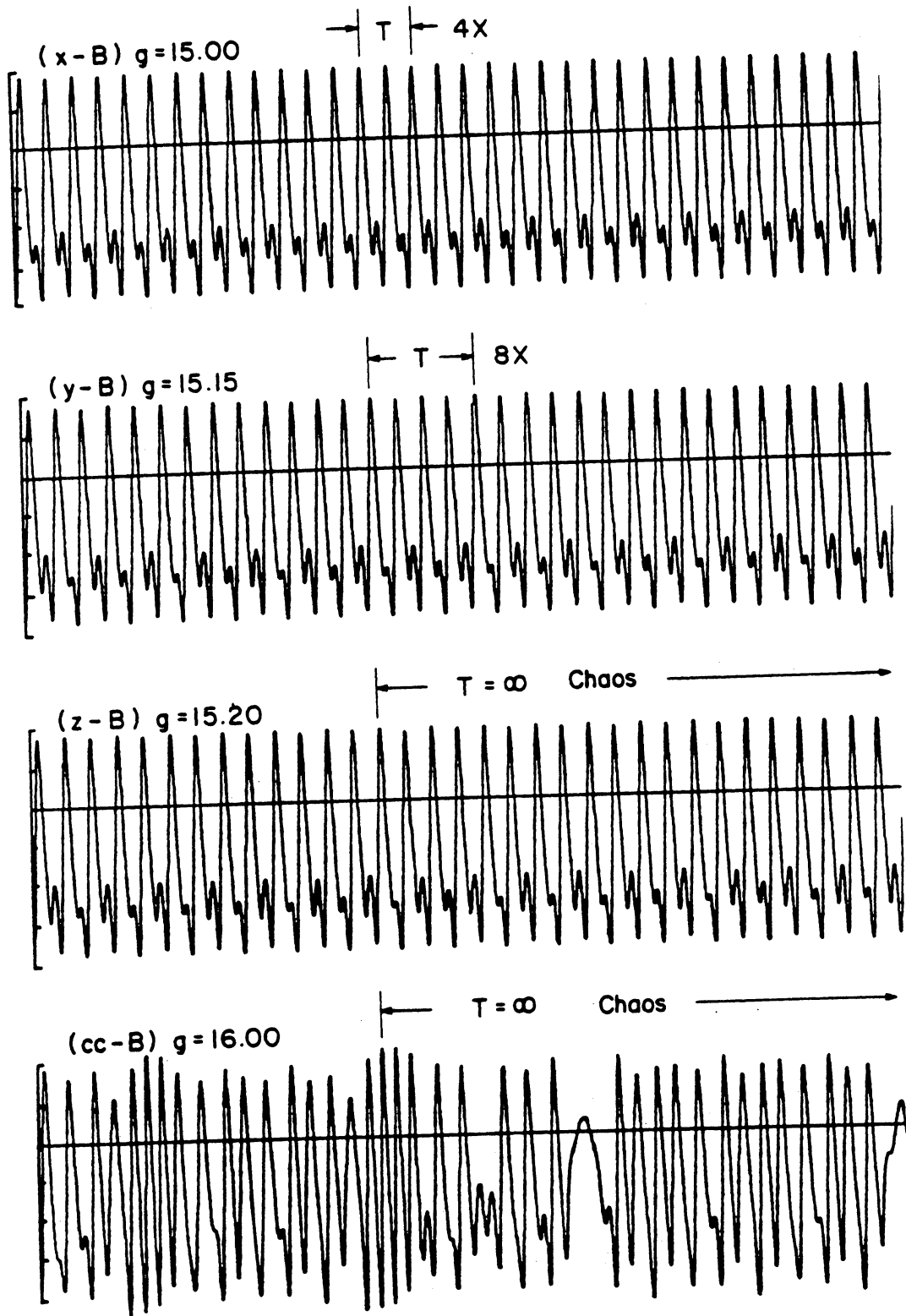


Figure 3.12 continued

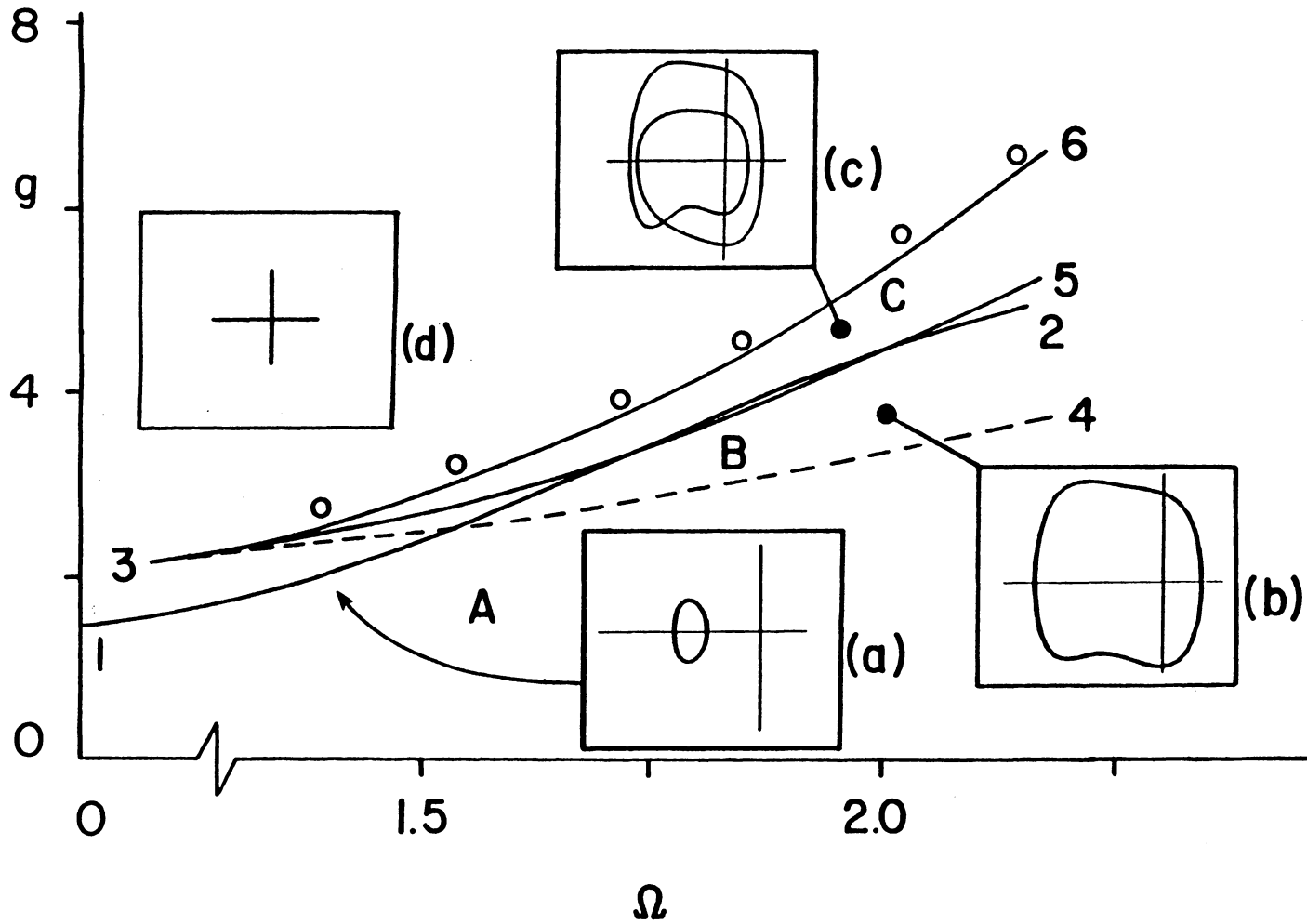


Figure 3.13 Bifurcation map in the g - Ω plane for four of the steady-state attractors shown in Figure 3.11: $\alpha = 4.0$, $\delta = 5.0$, $\mu = 1.0$, $\epsilon = 0.10$.

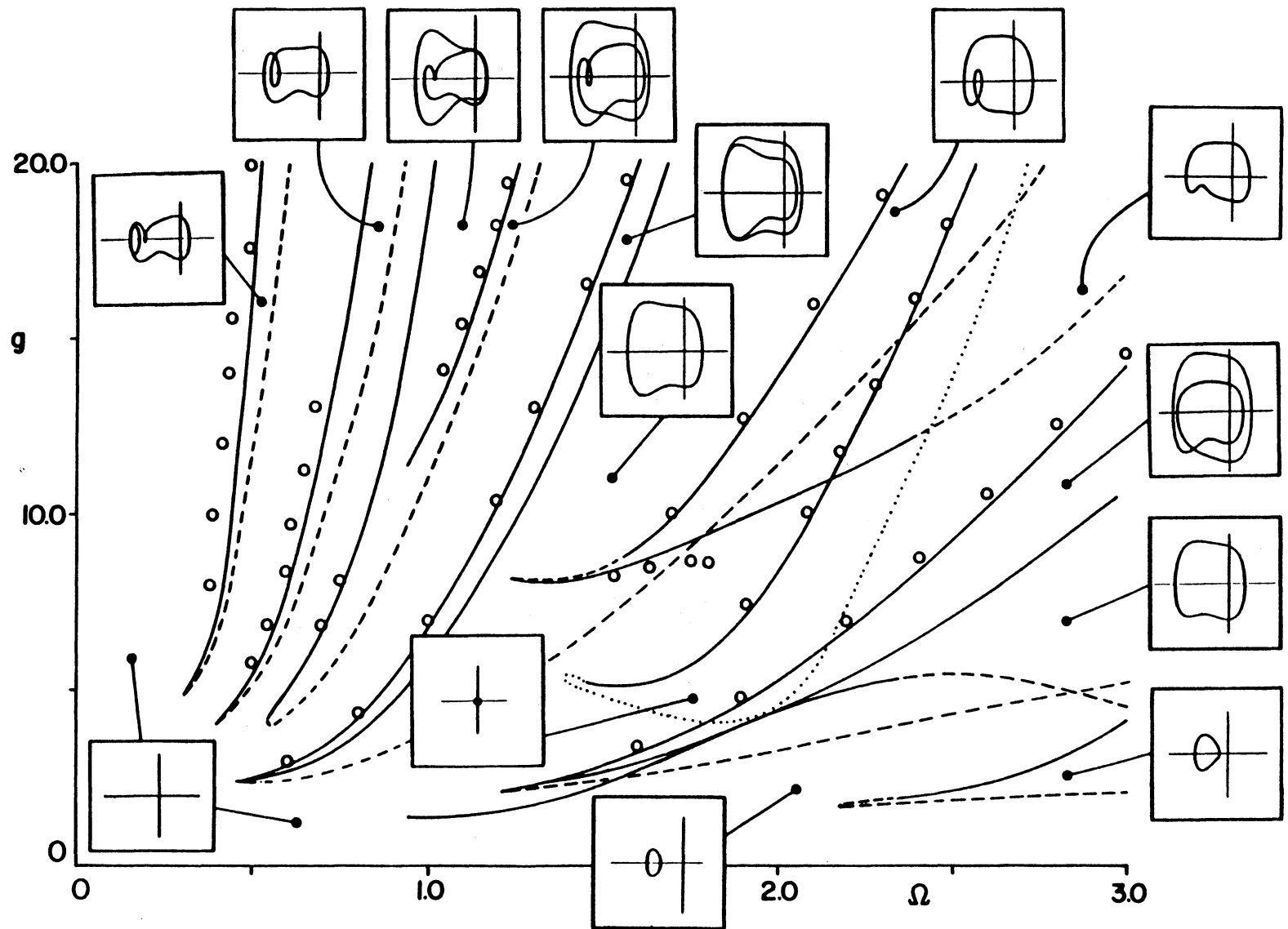


Figure 3.14 Bifurcation map in the g - Ω plane for both superharmonic and subharmonic resonances.

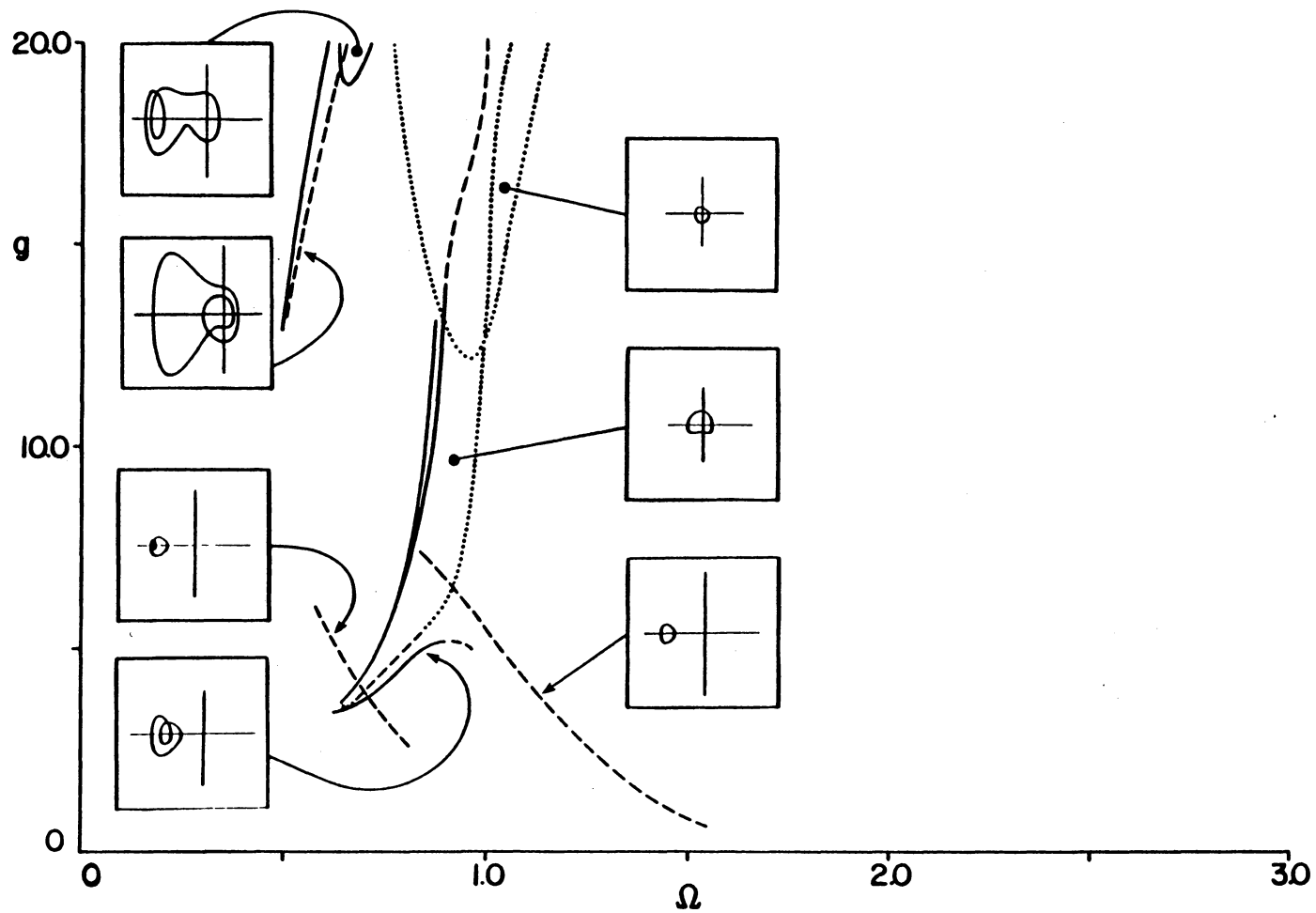


Figure 3.15 Additional attractors and their bifurcation boundaries in the g - Ω plane. This map should be superimposed onto Figure 3.14, but is shown separately to avoid obscuring the map. Note that two of the attractors are shown in Figure 2.6 of Chapter II.

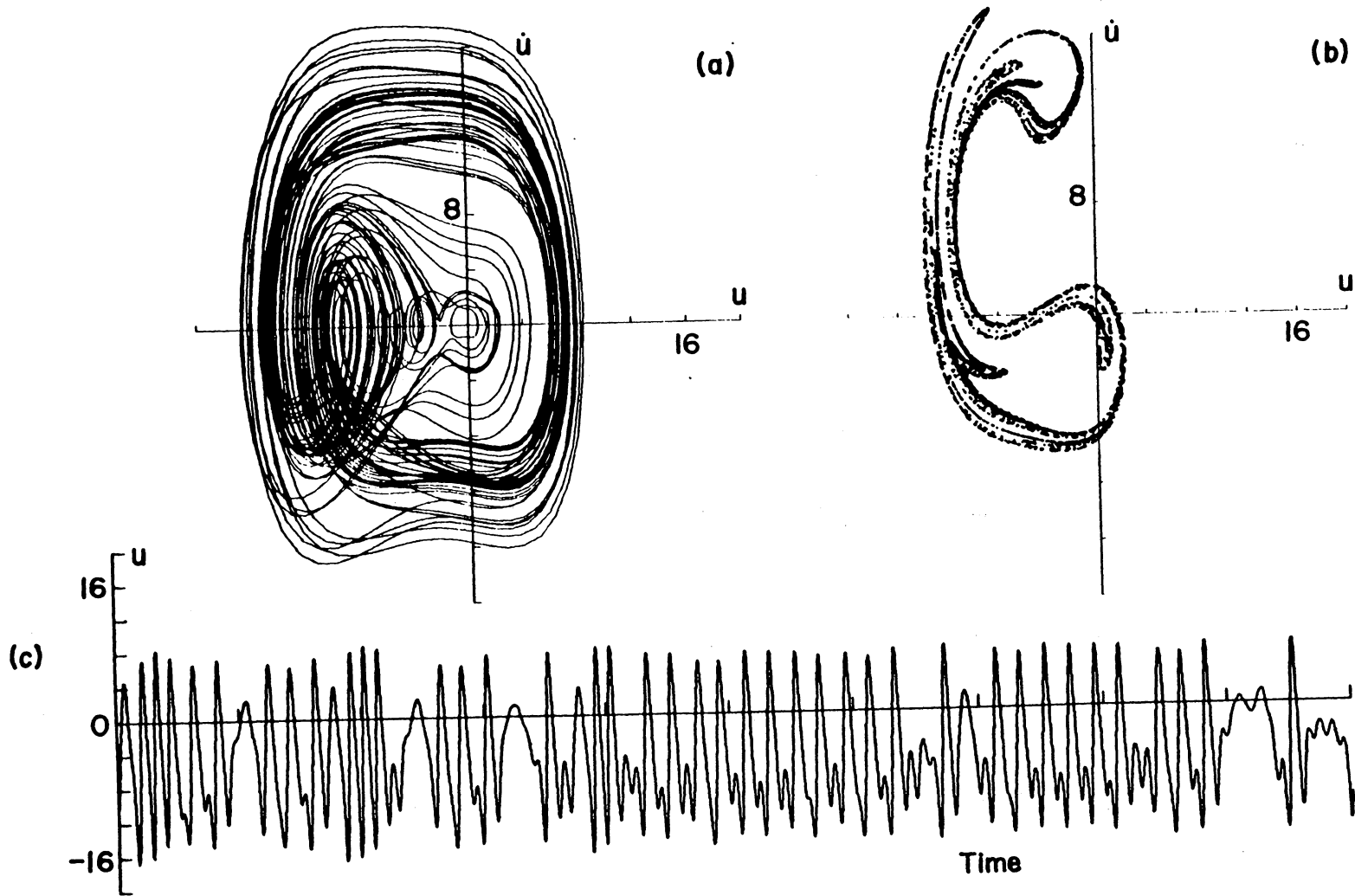


Figure 3.16 (a) Phase portrait, (b) Poincaré map, and (c) representative time history of a chaotic response for the system when $g = 14.5$, $\alpha = 4.0$, $\delta = 5.0$, $\mu = 1.0$, $\epsilon = 0.10$. Because the principal parametric resonance is a subharmonic of order $\frac{1}{2}$, the Poincaré map is obtained by sampling the state at $2T$ intervals instead of T intervals.

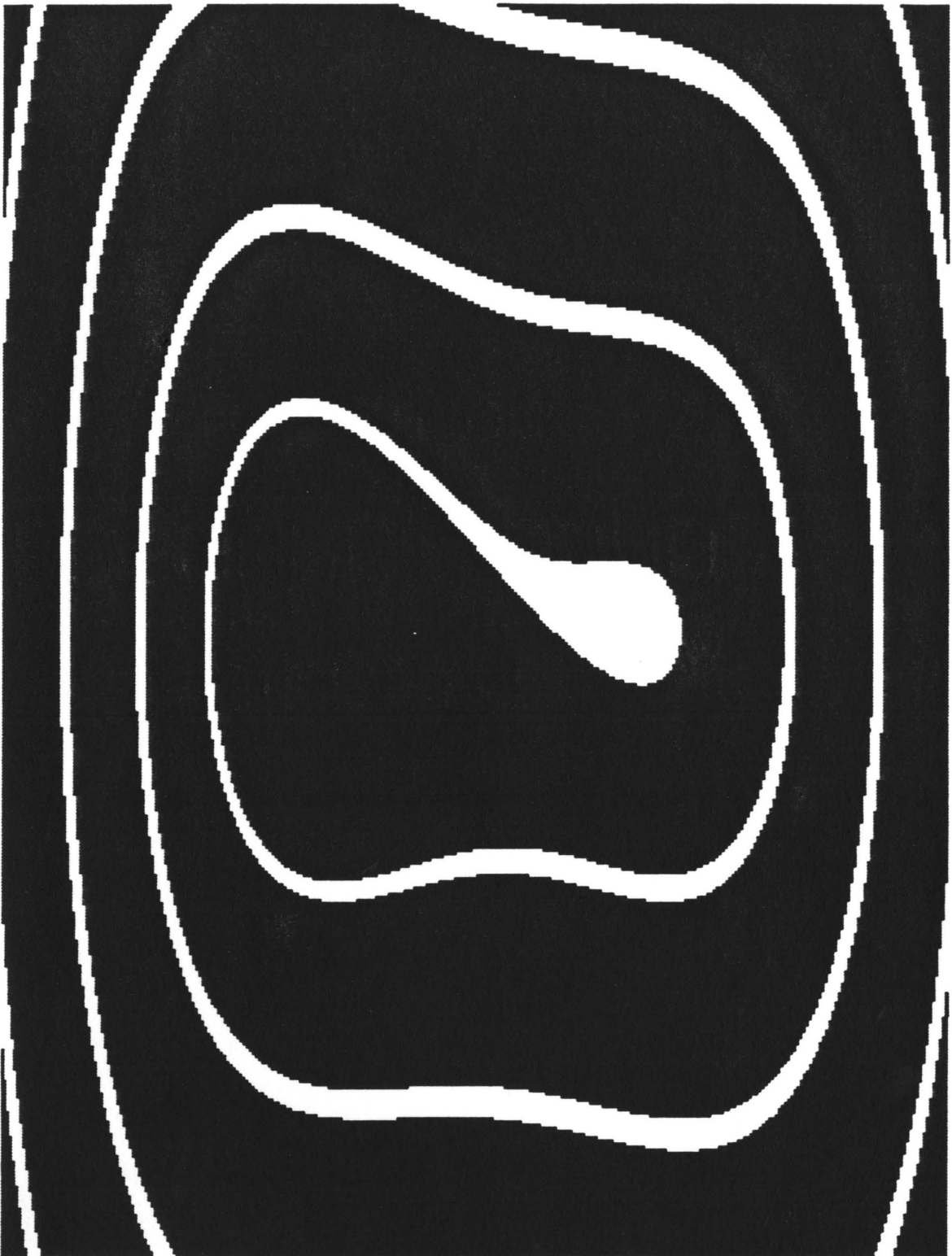


Figure 3.17 Basin of attraction for the system shown in Figure 3.11(a) obtained by numerical integration. The boundaries separating the two basins are the two inbound separatrices approaching the saddle point: $g = 0.0$, $-20 \leq u \leq 10$, $-20 \leq \dot{u} \leq 20$, black-left focus, white-origin.

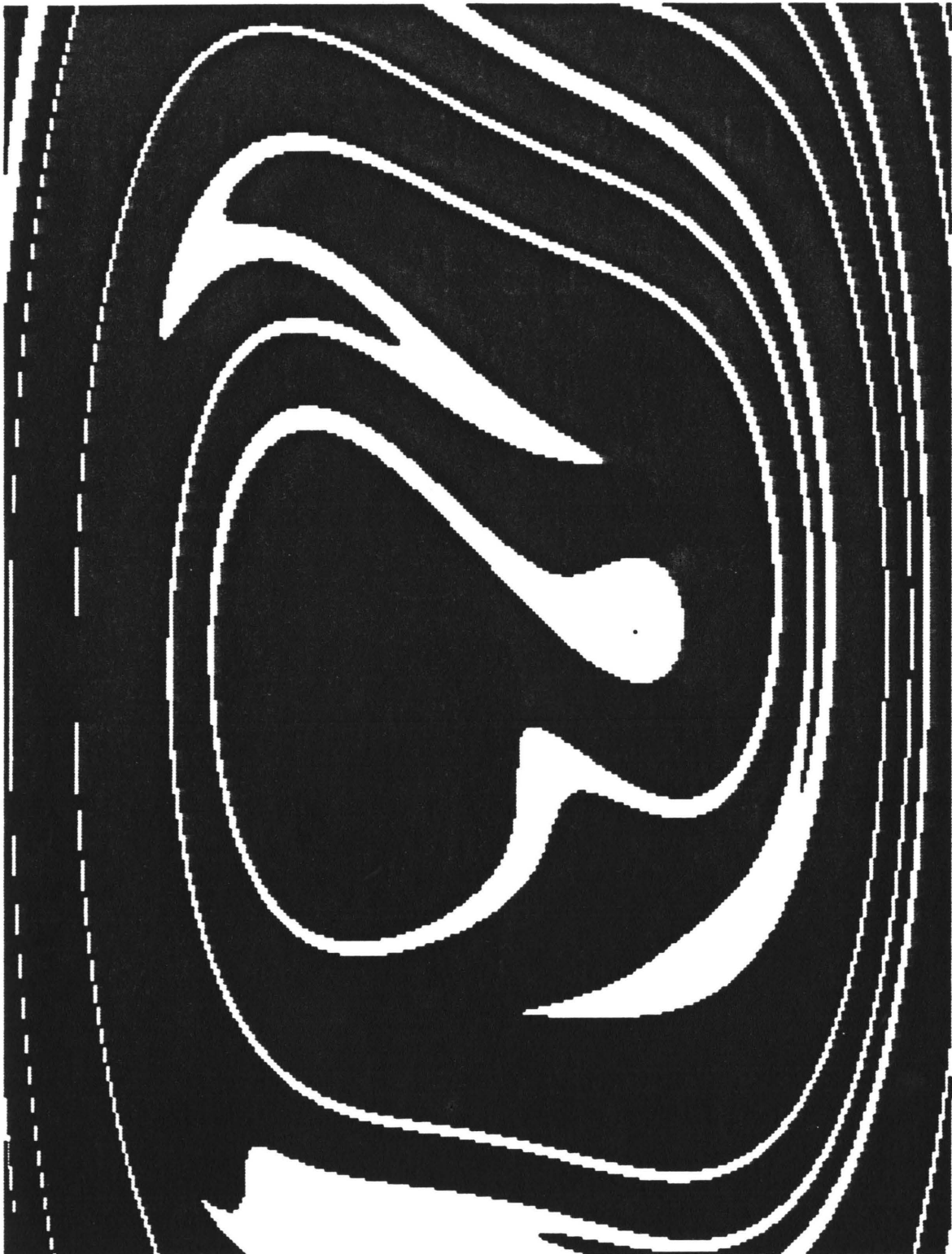


Figure 3.18 Basin of attraction for the system shown in Figure 3.17 for $g = 1.5$, $\phi = 2.000$, black-limit cycle in left well, white-origin.

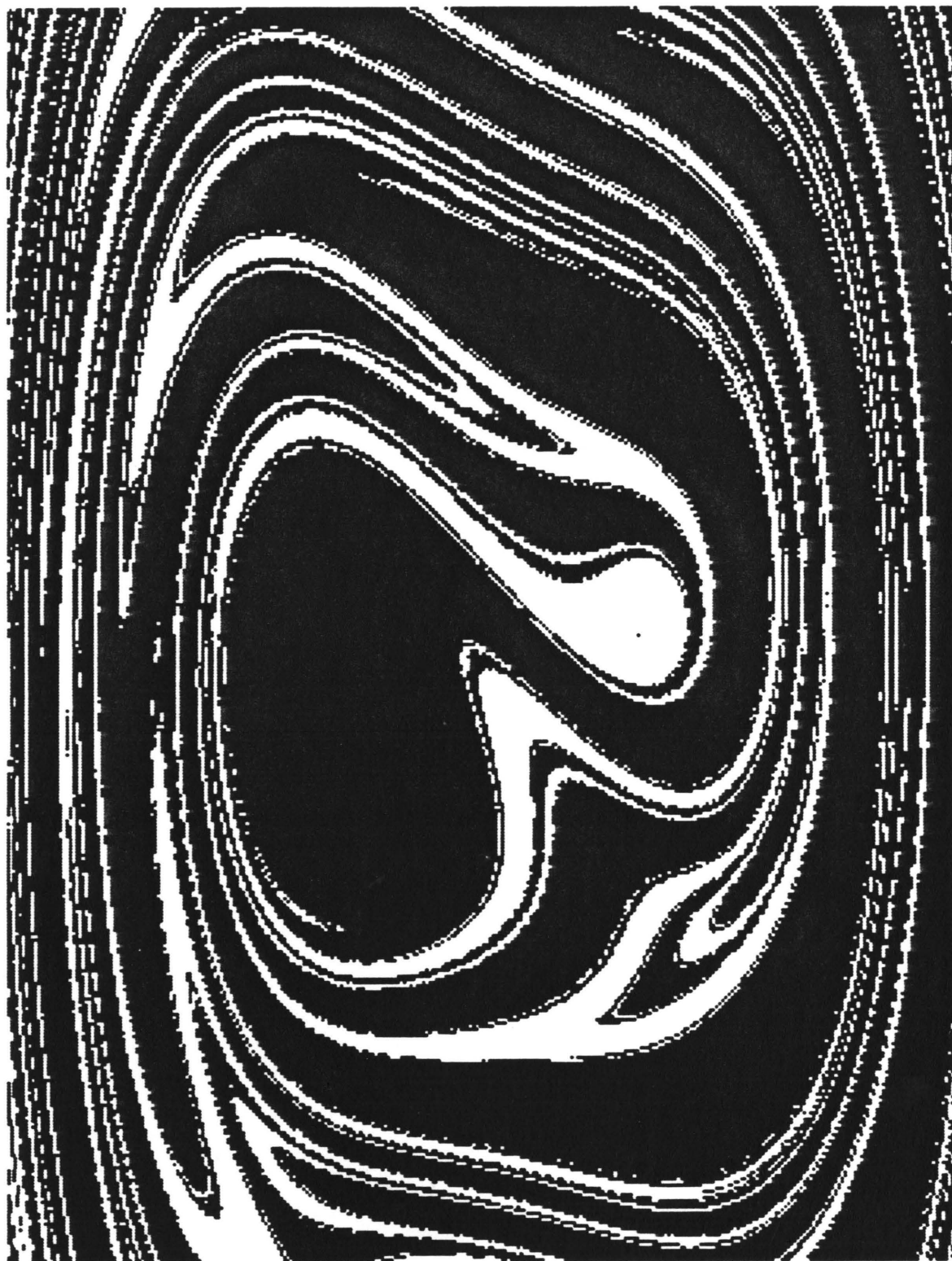


Figure 3.19 Fractal basin of attraction for the system shown in Figure 3.18 for $g = 2.0$.

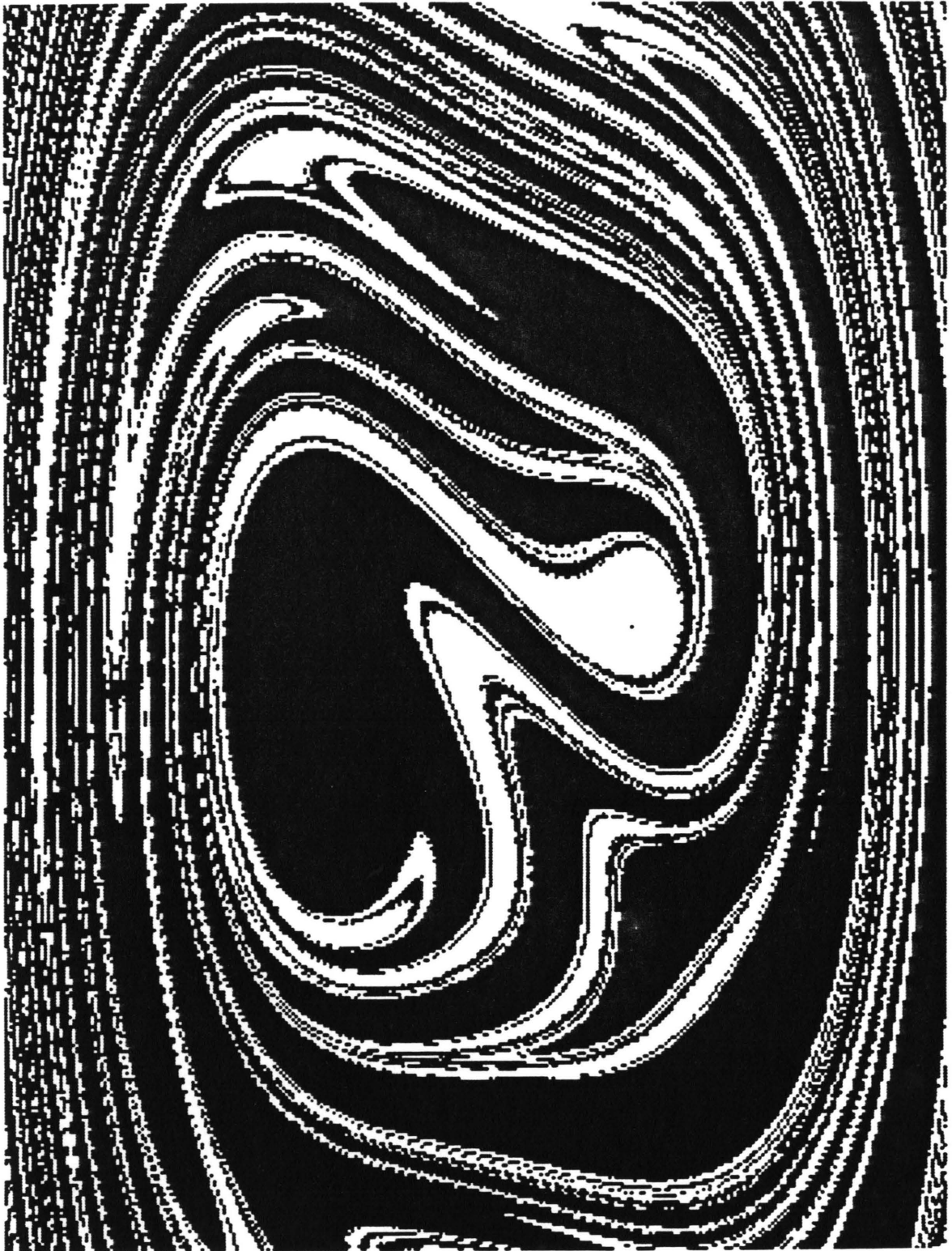


Figure 3.20 Fractal basin of attraction for the system shown in Figure 3.18 for $g = 2.5$.

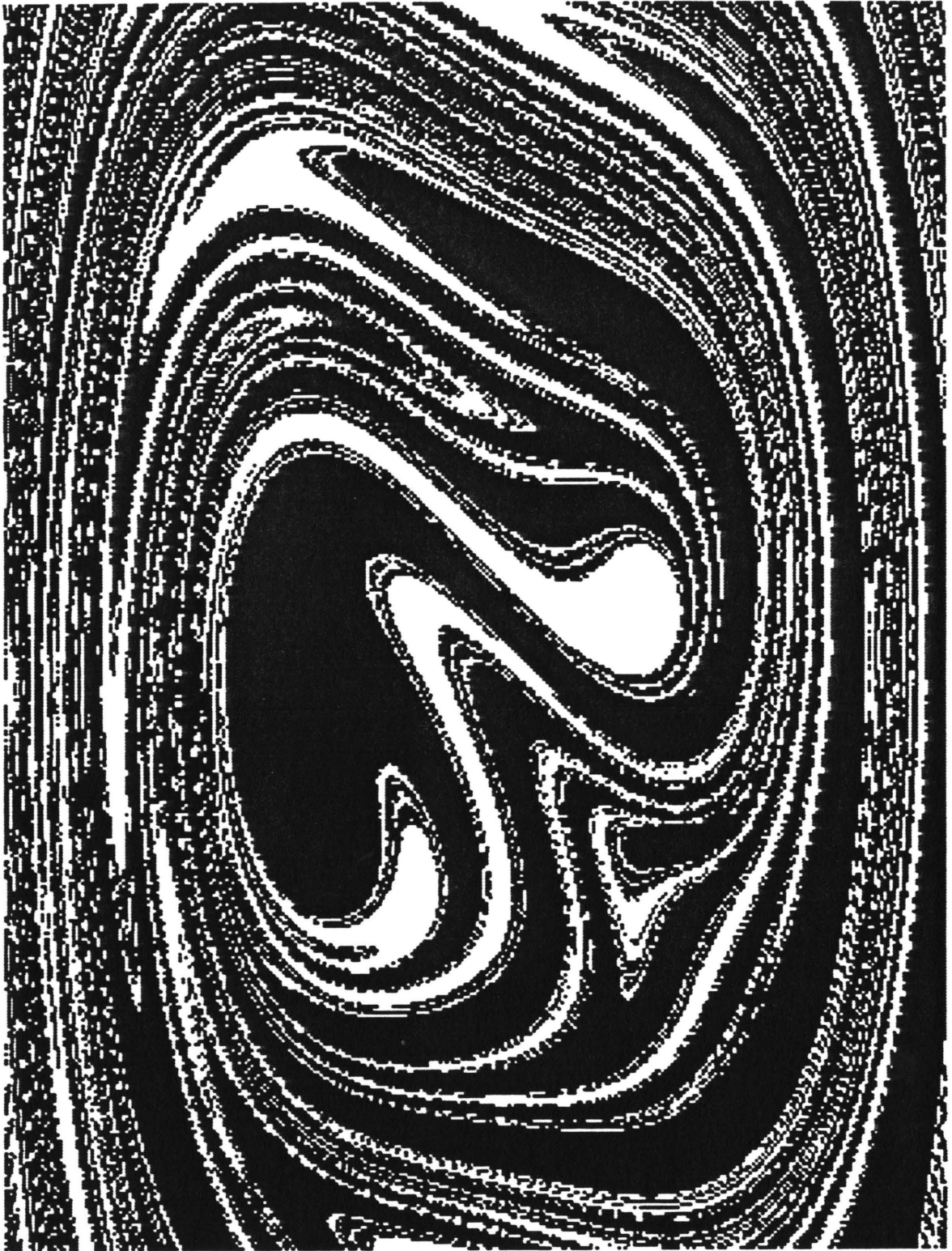


Figure 3.21 Fractal basin of attraction for the system shown in Figure 3.18 for $g = 3.0$.



Figure 3.22 Fractal basin of attraction for the system shown in Figure 3.18 for $g = 4.2$; red denotes the new large outer attractor shown in Figure 3.11(c).

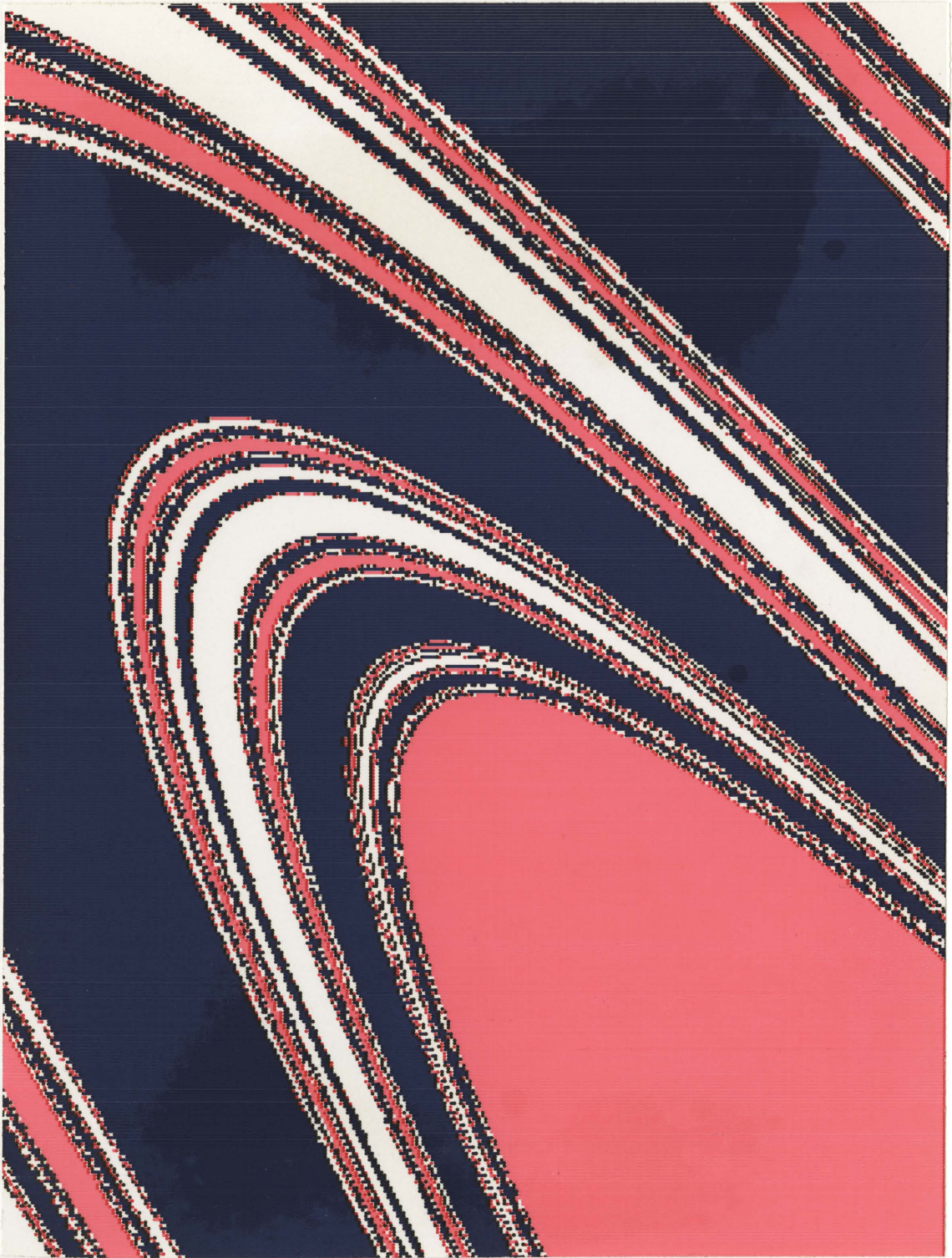


Figure 3.23 Enlarged region of Figure 3.22 showing structure is preserved at the boundaries: $-7.2 \leq u \leq -4.2$, $-2.0 \leq \dot{u} \leq 2.0$.

CHAPTER IV
FORMULATION AND VARIATIONAL SOLUTION OF A SLENDER BEAM CARRYING
A LUMPED MASS SUBJECT TO A PARAMETRIC EXCITATION

Many structural elements can be modelled as a slender continuous beam with concentrated masses located between the ends. When the support undergoes motion, the beam is subject to vibration--either external or parametric, or both. In this chapter we proceed to derive the governing equation for inplane flexural vibration of a thin elastic prismatic cantilever beam subject to parametric vibration at the base. The nonlinear terms arising from the curvature and coupling effects are retained. Galerkin's method is used to discretize the governing nonlinear partial differential equation of motion. The linear eigenvalue problem is solved to determine the eigenvalues, and the eigenfunction is used to determine the coefficients of the time modulation equation. A multiple scales analysis and numerical solutions to these equations are discussed in the next chapter.

4.1 Derivation of the Nonlinear Differential Equation of Motion

In this section we derive the governing equation of motion using the Euler-Bernoulli theory. The beam, shown in Figure 4.1, is cantilevered at the oscillating support, has a length L , and carries a concentrated mass m at an arbitrary distance $s = d$ along the elastic axis of the beam. We assume that the thickness of the beam is so small compared with the length that the effects of shearing deformation and

rotatory inertia of the beam can be neglected. Since we are investigating parametric resonances (transverse vibration), we will not consider axial resonances of the beam since the frequency of excitation will be far below the first axial resonance. If the beam is kept relatively short (< 30 beam widths), the transverse vibration is purely in plane (if the lumped mass is symmetrical with the centerline), and if the excitation frequency is far below the first torsional mode, then we can safely neglect the torsional modes of the beam in the analysis. These assumptions are consistent with observations in the laboratory. Also, we do not observe any combination or internal resonances. When the mass is removed and the length increased by an order of magnitude, we do see combination resonances.

According to the Euler-Bernoulli theory, the bending moment at any cross-section s is given by

$$M(s) = + EI \kappa(s), \quad (4.1)$$

where E is the elastic (Young's) modulus, I is the cross-sectional moment of inertia, and κ^{-1} is the radius of curvature at section s .

From Figure 4.1 we see that

$$\kappa = \frac{\partial \phi}{\partial s} = \phi_s \quad (4.2)$$

and

$$\sin \phi = v_s, \quad (4.3)$$

where $\phi(s)$ is the slope. The subscript s denotes a partial derivative with respect to s , and the subscript t or the overdot denotes a partial derivative with respect to time t . Differentiating (4.3) we obtain

$$\frac{\partial \phi}{\partial s} = \frac{v_{ss}}{\cos \phi} = \frac{v_{ss}}{\sqrt{1-v_s^2}} \quad (4.4)$$

which, when substituted into (4.1), yields the moment at section s as

$$M(s) = EI v_{ss} (1 - v_s^2)^{-\frac{1}{2}}.$$

Expanding the radical, we obtain

$$M(s) = EI v_{ss} \left(1 + \frac{1}{2} v_s^2 + \frac{3}{8} v_s^4 + \dots\right), \quad (4.5)$$

and for the analysis presented here, we will only keep up to third-order terms.

The moment in the beam is the result of three sources:

$$M(s) = M_1 + M_2 + M_3, \quad (4.6)$$

where M_1 is the moment at s due to the lateral inertia of the beam element $d\xi$ and the mass m , M_2 is the moment due to the longitudinal inertia of the beam element $d\xi$ and the mass m , and M_3 is the moment at s caused by the angular acceleration of the mass m due to its mass moment of inertia J .

In the derivation that follows, the following nomenclature will be used:

x,y	-	Newtonian Cartesian reference frame
\bar{g}	-	acceleration of gravity
s	-	reference variable along beam
ξ	-	variable of integration along beam
$d\xi$	-	differential length of beam element
L	-	beam length
w	-	beam width
t	-	beam thickness
d	-	position of mass center of mass m
ρ	-	mass density of homogeneous beam per unit length
c	-	coefficient of viscous damping
m	-	mass of concentrated weight on beam
J	-	polar moment of inertia of mass m
$v(\xi,t)$	-	lateral displacement of beam element $d\xi$
$u(\xi,t)$	-	longitudinal displacement of beam element $d\xi$
$\phi(s)$	-	angle with respect to vertical of beam at s
$\kappa(s)$	-	curvature of beam at s
I	-	cross-sectional moment of inertia of beam
E	-	modulus of elasticity of beam

Using the sign convention indicated in Figure 4.1, we see that the lateral (inertial) force of element $d\xi$ is

$$\rho \ddot{v}(\xi,t) d\xi \rightarrow , \quad (4.7)$$

and the projected moment arm about section s is

$$\int_s^\xi \cos\phi(\eta,t) d\eta . \quad (4.8)$$

Thus, the moment of element $d\xi$ about s is

$$- [\rho \ddot{v}(\xi,t) d\xi] \left(\int_s^\xi \cos\phi(\eta,t) d\eta \right). \quad (4.9)$$

Hence, it follows that the total moment of the beam section from s to L is

$$- \int_s^L \rho \ddot{v}(\xi, t) \left[\int_s^\xi \cos\phi(\eta, t) d\eta \right] d\xi . \quad (4.10)$$

The moment due to m is similarly obtained as

$$- m \ddot{v}(d, t) \left[\int_s^d \cos\phi(\xi) d\xi \right], \quad (4.11)$$

and the moment of the viscous damping is

$$- \int_s^L c \dot{v}(\xi, t) \left[\int_s^\xi \cos\phi(\eta, t) d\eta \right] d\xi . \quad (4.12)$$

Combining these and using the Dirac delta function to locate the mass, we obtain

$$M_1 = - \int_s^L \{ [\rho + m\delta(\xi-d)] \ddot{v} + c\dot{v} \} \left(\int_s^\xi \cos\phi d\eta \right) d\xi . \quad (4.13)$$

In a similar fashion, we obtain

$$M_2 = - \int_s^L \{ \rho [\ddot{u} - g] + m\delta(\xi - d) [\ddot{u} - g] \} \left(\int_s^\xi \sin\phi d\eta \right) d\xi \quad (4.14)$$

and

$$M_3 = - J \ddot{\phi}(d, t) = - \int_s^L J \delta(\xi - d) \ddot{\phi} d\xi . \quad (4.15)$$

The longitudinal displacement caused by the shortening effect is

$$u(\xi, t) = \xi - \int_0^\xi \cos\phi(\eta, t) d\eta , \quad (4.16)$$

which when combined with the displacement $z(t)$ of the base yields the total axial displacement

$$u(\xi, t) = \xi - \int_0^\xi \cos\phi(\eta, t) d\eta + z(t) . \quad (4.17)$$

To obtain the governing differential equation, we differentiate (4.5) and (4.6) twice with respect to s . This involves differentiating (4.13), (4.14), and (4.15) and using Leibnitz' rule. We also need the second time derivative of the axial displacement $u(\xi, t)$, which is obtained by substituting for $\cos\phi$ from (4.3) and differentiating (4.17) with respect to t twice to yield

$$\ddot{u} = \frac{1}{2} \int_0^\xi (v_\eta^2)_{tt} d\eta + \ddot{z}(t) + \dots \quad (4.18)$$

Differentiating (4.13)-(4.15) twice with respect to s and using (4.18) yields

$$\begin{aligned} \frac{\partial^2 M_1}{\partial s^2} = & - \left(1 - \frac{1}{2} v_s^2\right) \{[\rho + m\delta(s-d)]\ddot{v}(s,t) + c\dot{v}(s,t)\} \\ & - v_s v_{ss} \int_s^L \{[\rho + m\delta(\xi-d)]\ddot{v}(\xi,t) + c\dot{v}(\xi,t)\} d\xi, \end{aligned} \quad (4.19)$$

$$\begin{aligned} \frac{\partial M_2}{\partial s} = & v_s \left\{ \rho \int_s^L \left[\frac{1}{2} \int_0^\xi (v_\eta^2)_{tt} d\eta - \ddot{z} \right] d\xi + \rho g(L-s) \right. \\ & \left. + m \int_s^L \delta(\xi-d) \left[\frac{1}{2} \int_0^\xi (v_\eta^2)_{tt} d\eta + \ddot{z} - g \right] d\xi \right\} \\ = & v_s N, \end{aligned} \quad (4.20)$$

where

$$\begin{aligned}
N = & + \frac{1}{2} \rho \int_s^L \left[\int_0^\xi (v_n^2)_{tt} d\eta \right] d\xi - \frac{1}{2} m \int_s^L \delta(\xi - d) \left[\int_0^\xi (v_n^2)_{tt} d\eta \right] d\xi \\
& + m(\ddot{z} - g) \int_s^L \delta(\xi - d) d\xi + \rho L \left(1 - \frac{s}{L}\right) (\ddot{z} - g) , \quad (4.21)
\end{aligned}$$

and

$$\frac{\partial^2 M_2}{\partial s^2} = (Nv_s)_s , \quad (4.22)$$

and

$$\frac{\partial^2 M_3}{\partial s^2} = + \frac{\partial}{\partial s} \left\{ J\delta(s - d) \left[\ddot{v}_s \left(1 + \frac{1}{2} v_s^2\right) + v_s \dot{v}_s^2 \right] \right\} . \quad (4.23)$$

Differentiating (4.5) and (4.6) twice with respect to s and substituting for the $\partial^2 M_n / \partial s^2$ from (4.19), (4.22) and (4.23) yields the governing equation

$$\begin{aligned}
0 = & EI \left(v_{ssss} + \frac{1}{2} v_{ssss} v_s^2 + 3v_s v_{ss} v_{sss} + v_{ss}^3 \right) + \left(1 - \frac{1}{2} v_s^2 - \dots\right) \\
& \cdot \left[\rho + m\delta(s - d) \right] \ddot{v} - \frac{\partial}{\partial s} (Nv_s) + v_s v_{ss} \int_s^L \left[\rho + m\delta(\xi - d) \right] \ddot{v} d\xi \\
& - \frac{\partial}{\partial s} \left\{ J\delta(s - d) \left[\ddot{v}_s \left(1 + \frac{1}{2} v_s^2 + \dots\right) + v_s \dot{v}_s^2 \right] \right\} \\
& + \left(1 - \frac{1}{2} v_s^2 - \dots\right) c\dot{v} + v_s v_{ss} \int_s^L c\dot{v} d\xi . \quad (4.24)
\end{aligned}$$

This field equation is subject to the following boundary conditions:

$$v(0,t) = 0 , \quad (4.25)$$

$$v_s(0,t) = 0 , \quad (4.26)$$

$$v_{ss}(L,t) = 0 , \quad (4.27)$$

$$v_{sss}(L,t) = 0 . \quad (4.28)$$

4.2 Solution of the Linear Problem

The governing problem (4.24)-(4.28) is nonlinear and does not admit a closed-form solution. Therefore, an approximate solution will be sought that satisfies both the equation and the boundary conditions. Since the boundary conditions are spatial and independent of time, we represent the solution of the nonlinear problem in the form

$$v(s,t) = \sum_n r \psi_n(s) G_n(t) \quad (4.29)$$

where r is a scaling factor, $\psi_n(s)$ is the shape function of the n th linear mode, and $G_n(t)$ is the time modulation of the n th mode.

The undamped linear free vibration problem is governed by

$$EIv^{iv} + [\rho + m\delta(s - d)]\ddot{v} = 0, \quad (4.30)$$

subject to the boundary conditions (4.25)-(4.28). Without loss of generality, we will solve explicitly for the first mode, with the understanding that the eigenfunction of the n th mode and its associated eigenvalue correspond to the n th characteristic.

To solve this problem, we break the beam into two parts at the concentrated mass. In the left part, $v = v_1$ where

$$EIv_1^{iv} + \rho\ddot{v}_1 = 0, \quad \text{for } 0 < s < d, \quad (4.31)$$

$$v_1(0,t) = 0, \quad (4.32)$$

$$v_1'(0,t) = 0. \quad (4.33)$$

In the right part, $v = v_2$ where

$$EIV_2^{iv} + \rho \ddot{v}_2 = 0, \quad \text{for } d < s < L, \quad (4.34)$$

$$EIV_2^{i'v}(L,t) = 0, \quad (4.35)$$

$$EIV_2^{i''v}(L,t) = 0. \quad (4.36)$$

To complete the problem formulation, we supplement it with four conditions at the concentrated mass. Two of these conditions demand continuity of displacement and slope; that is,

$$v_1(d,t) = v_2(d,t), \quad (4.37)$$

$$v_1^{i'}(d,t) = v_2^{i'}(d,t). \quad (4.38)$$

The third condition demands the jump in the shear in the two parts of the beam be equal to the inertial force of the mass. It follows from the free body diagram in Figure 4.2 that

$$EIV_1^{i'''} = m\ddot{v}_1 + EIV_2^{i'''}, \quad \text{at } s = d. \quad (4.39)$$

The fourth condition demands the jump in the moment in the two parts of the beam be equal to the inertial moment of the mass; that is,

$$-EIV_1^{i''} = J\ddot{v}_1 - EIV_2^{i''}, \quad \text{at } s = d. \quad (4.40)$$

Assuming a harmonic time variation with frequency ω , we have

$$v_1(s,t) = r\psi_1(s)\cos(\omega t) ,$$

$$v_2(s,t) = r\psi_2(s)\cos(\omega t) . \quad (4.41)$$

Then, it follows from (4.31) that

$$\psi_1^{iv} - \left(\frac{k}{L}\right)^4 \psi_1 = 0 , \quad (4.42)$$

and from (4.32) and (4.33) that

$$\psi_1(0) = 0 , \quad (4.43)$$

$$\psi_1'(0) = 0 , \quad (4.44)$$

where

$$\left(\frac{k}{L}\right)^4 = \frac{\omega^2 \rho}{EI} , \quad (4.45)$$

where k will be defined later. The general solution of (4.42) is

$$\psi_1(s) = C_1 \sin \frac{k}{L} s + C_2 \sinh \frac{k}{L} s + C_3 \cos \frac{k}{L} s + C_4 \cosh \frac{k}{L} s . \quad (4.46)$$

Imposing the boundary conditions (4.43) and (4.44), we can express

C_2 and C_4 in terms of C_1 and C_3 and hence obtain

$$\psi_1(s) = C_1 \left(\sin \frac{k}{L} s - \sinh \frac{k}{L} s \right) + C_3 \left(\cos \frac{k}{L} s - \cosh \frac{k}{L} s \right) . \quad (4.47)$$

We express $\psi_2(s,t)$ as

$$\psi_2(s) = \psi_1(s) + \theta(s) \quad (4.48)$$

so that the represented shape function can be expressed in compact form over the whole interval using the unit step (Heavyside) function.

Substituting (4.48) and (4.41) into (4.34)-(4.40), we obtain

$$\theta^{iv} - \left(\frac{k}{L}\right)^4 \theta = 0, \quad \text{for } d < s < L, \quad (4.49)$$

$$\theta(d) = 0, \quad (4.50)$$

$$\theta'(d) = 0, \quad (4.51)$$

$$EI\theta''(d) = -J\omega^2\psi_1'(d), \quad (4.52)$$

$$EI\theta'''(d) = m\omega^2\psi_1(d), \quad (4.53)$$

$$\theta''(L) = -\psi_1'(L), \quad (4.54)$$

$$\theta'''(L) = -\psi_1''(L). \quad (4.55)$$

The general solution of (4.49) can be expressed as

$$\begin{aligned} \theta(s) = & K_1 \sin \frac{k}{L} (s - d) + K_2 \sinh \frac{k}{L} (s - d) \\ & + K_3 \cos \frac{k}{L} (s - d) + K_4 \cosh \frac{k}{L} (s - d), \end{aligned} \quad (4.56)$$

where the argument $(s - d)$ is chosen for reasons that will become apparent later. Applying the conditions (4.50) and (4.51) relates K_2 and K_4 to K_1 and K_3 , thereby yielding

$$\begin{aligned} \theta(s) = & K_1 \left[\sin \frac{k}{L} (s - d) - \sinh \frac{k}{L} (s - d) \right] \\ & + K_3 \left[\cos \frac{k}{L} (s - d) - \cosh \frac{k}{L} (s - d) \right]. \end{aligned} \quad (4.57)$$

Applying the conditions (4.54) and (4.55) gives us the relationship between the C_i and K_i as

$$\begin{bmatrix} K_1 \\ K_3 \end{bmatrix} = \begin{bmatrix} h_1 & h_2 \\ h_3 & h_4 \end{bmatrix} \begin{bmatrix} C_1 \\ C_3 \end{bmatrix}, \quad (4.58)$$

where

$$\begin{aligned} h_1 &= (k_{22}l_{11} - k_{12}l_{12})/D, \\ h_2 &= (k_{22}l_{12} - k_{12}l_{22})/D, \\ h_3 &= (k_{11}l_{12} - k_{12}l_{11})/D, \\ h_4 &= (k_{11}l_{22} - k_{12}l_{12})/D, \\ D &= -2\left[1 + \cos \frac{k}{L}(L-d) \cosh \frac{k}{L}(L-d)\right], \end{aligned} \quad (4.59)$$

where

$$\begin{aligned} k_{11} &= \sin \frac{k}{L}(L-d) + \sinh \frac{k}{L}(L-d), \\ k_{12} &= \cos \frac{k}{L}(L-d) + \cosh \frac{k}{L}(L-d), \\ k_{22} &= -\sin \frac{k}{L}(L-d) + \sinh \frac{k}{L}(L-d), \end{aligned} \quad (4.60)$$

and

$$\begin{aligned}
x_{11} &= -\sin k - \sinh k , \\
x_{12} &= -\cos k - \cosh k , \\
x_{22} &= \sin k - \sinh k .
\end{aligned} \tag{4.61}$$

Imposing the conditions (4.52) and (4.53) yields

$$C_3 = -\frac{m_{11}}{m_{12}} C_1 = -\Lambda_1 C_1 , \tag{4.62}$$

$$C_3 = -\frac{m_{21}}{m_{22}} C_1 = -\Lambda_2 C_1 , \tag{4.63}$$

where

$$\begin{aligned}
m_{11} &= \frac{2\rho L h_1}{m} + k \left(\sin \frac{kd}{L} - \sinh \frac{kd}{L} \right) , \\
m_{12} &= \frac{2\rho L h_2}{m} + k \left(\cos \frac{kd}{L} - \cosh \frac{kd}{L} \right) , \\
m_{21} &= \frac{2\rho L^3 h_3}{J} - k^3 \left(\cos \frac{kd}{L} - \cosh \frac{kd}{L} \right) , \\
m_{22} &= \frac{2\rho L^3 h_4}{J} + k^3 \left(\sin \frac{kd}{L} + \sinh \frac{kd}{L} \right) .
\end{aligned} \tag{4.64}$$

For a nontrivial solution, $\Lambda_1 = \Lambda_2$, which yields the characteristic equation

$$\begin{aligned}
0 &= \frac{4\rho^2 L^4}{mJ} [h_1 h_4 - h_2 h_3] \\
&+ \left(\frac{2\rho L k^3}{m} \right) [h_1 \left(\sin \frac{kd}{L} + \sinh \frac{kd}{L} \right) + h_2 \left(\cos \frac{kd}{L} - \cosh \frac{kd}{L} \right)] \\
&+ \left(\frac{2\rho L^3 k}{J} \right) [h_4 \left(\sin \frac{kd}{L} - \sinh \frac{kd}{L} \right) - h_3 \left(\cos \frac{kd}{L} - \cosh \frac{kd}{L} \right)] \\
&+ 2k^4 \left(1 - \cos \frac{kd}{L} \cosh \frac{kd}{L} \right) .
\end{aligned} \tag{4.65}$$

The solution can now be stated as the composite function

$$\begin{aligned}
 \psi(s) = & C_1 \left[\left(\sin \frac{k}{L} s - \sinh \frac{k}{L} s \right) - \Lambda \left(\cos \frac{k}{L} s - \cosh \frac{k}{L} s \right) \right] \\
 & + C_1 U(s - d) \left\{ h_1 \left[\sin \frac{k}{L} (s - d) - \sinh \frac{k}{L} (s - d) \right] \right. \\
 & \quad + h_3 \left[\cos \frac{k}{L} (s - d) - \cosh \frac{k}{L} (s - d) \right] \\
 & \quad - \Lambda h_2 \left[\sin \frac{k}{L} (s - d) - \sinh \frac{k}{L} (s - d) \right] \\
 & \quad \left. - \Lambda h_4 \left[\cos \frac{k}{L} (s - d) - \cosh \frac{k}{L} (s - d) \right] \right\}, \quad (4.66)
 \end{aligned}$$

where $\Lambda = \Lambda_1 = \Lambda_2$. It follows from (4.45) that the frequency can be calculated as

$$\omega^2 = \frac{EI}{\rho} \left(\frac{k}{L} \right)^4. \quad (4.67)$$

The shape function given in (4.66) and its derivatives are shown plotted in Figure 4.3. We note that all boundary conditions are satisfied and the discontinuities in the shear and moment are due to the concentrated mass. The displacement is plotted showing the shortening effect while the derivatives are plotted against the variable s . The shape function for the second mode and its derivatives are shown in Figure 4.4.

4.3 Solution of the Nonlinear Differential Equation of Motion

Experiments performed on the beam shown in Figure 4.1 show that the assumed form of solution for the linear problem is valid, and begins to

deteriorate when the amplitude exceeds $L/4$. When the model is excited near the principal parametric resonant frequency, the trivial response becomes unstable when the excitation amplitude exceeds a critical value, and a parametric vibration develops and grows into a steady-state finite amplitude vibration. The amplitude is finite because of nonlinearity (the linear problem predicts an infinite response).

Since we are analyzing the first mode, this continuous system can be discretized by any of the variational methods available such as Rayleigh-Ritz. When the assumed comparison function is the eigenfunction in particular, the procedure is known as Galerkin's method. It requires multiplying each term by the eigenfunction $\psi(s)$ and then integrating from 0 to L . When this procedure is applied to (4.24) we obtain

$$\begin{aligned}
 0 = \ddot{G} + 2\varepsilon\zeta\dot{G} + \theta^2(1 - \varepsilon f \cos\omega t)G + \varepsilon\alpha G^3 + \varepsilon\kappa_1 G\dot{G}^2 \\
 + \varepsilon\kappa_2 G^2\ddot{G} - 2\varepsilon\zeta\nu G^2\dot{G} , \qquad (4.68)
 \end{aligned}$$

where

$$\begin{aligned}
\hat{\zeta} &= \frac{cH_{21}}{2\epsilon\rho[H_{11} + \mu H_{12} + j\lambda^2 H_{13}]}, \\
\theta^2 &= \frac{\frac{EI}{\rho} \left(\frac{k}{L}\right)^4 [H_{31} + \mu H_{32}] - \frac{q}{L} (H_{33} + \mu H_{34})}{[H_{11} + \mu H_{12} + j\lambda^2 H_{13}]}, \\
f &= \frac{\Omega^2 \Gamma [H_{33} + \mu H_{34}]}{\epsilon\theta^2 L [H_{11} + \mu H_{12} + j\lambda^2 H_{13}]}, \\
\hat{\alpha} &= \frac{EI\lambda^2 [k^4 (H_{41} + \mu H_{42}) + H_{43}]}{\epsilon\rho L^4 [H_{11} + \mu H_{12} + j\lambda^2 H_{13}]}, \\
\kappa_1 &= \frac{[H_{51} + \mu H_{52} + \lambda^2 jH_{53}]\lambda^2}{\epsilon[H_{11} + \mu H_{12} + j\lambda^2 H_{13}]}, \\
\kappa_2 &= \frac{[H_{61} - H_{62} + \mu H_{63} - \mu H_{64} + j\lambda^2 H_{65}]\lambda^2}{\epsilon[H_{11} + \mu H_{12} + j\lambda^2 H_{13}]}, \\
v &= \lambda^2 \frac{H_{71}}{H_{21}}, \tag{4.69}
\end{aligned}$$

where

$$\begin{aligned}
H_{11} &= \int_0^1 \psi^2 dx, & H_{12} &= \psi^2(\beta), & H_{13} &= \psi_X^2(\beta), & H_{21} &= H_{11}, \\
H_{31} &= H_{11}, & H_{32} &= H_{12}, & H_{33} &= \int_0^1 (1-x)\psi_X^2 dx, & H_{34} &= \int_0^\beta \psi_X^2 dx, \\
H_{41} &= \frac{1}{2} \int_0^1 \psi^2 \psi_X^2 dx, & H_{42} &= \frac{1}{2} \psi^2(\beta) \psi_X^2(\beta), \\
H_{43} &= \int_0^1 [3\psi \psi_X \psi_{XX} \psi_{XXX} + \psi \psi_{XX}^3] dx, & H_{51} &= \int_0^1 \left\{ \int_x^1 \left(\int_0^\xi \psi_\eta^2 d\eta \right) d\xi \right\} \psi_X^2 dx, \\
H_{52} &= \left(\int_0^\beta \psi_X^2 dx \right)^2 = (H_{34})^2, & H_{53} &= \psi_X^4(\beta), & H_{61} &= H_{51}, \\
H_{62} &= \frac{1}{2} \int_0^1 \psi^2 \psi_X^2 dx - \int_0^1 \psi \psi_X \psi_{XX} \left(\int_x^1 \psi d\xi \right) dx, & H_{63} &= H_{52}, \\
H_{64} &= H_{42} - \psi(\beta) \int_0^\beta \psi \psi_X \psi_{XX} dx, & H_{65} &= \frac{1}{2} H_{53}, & H_{71} &= H_{62}, \\
x &= \frac{s}{L}, & \beta &= \frac{d}{L}, & \mu &= \frac{m}{\rho L}, & \lambda &= \frac{r}{L}, & j &= \frac{J}{\rho L r^2}. \tag{4.70}
\end{aligned}$$

The fourth derivative was approximated from the linear problem given by

$$\psi^{iv}(s) = \frac{\omega^2}{EI} [\rho + m\delta(s-d)]\psi(s). \tag{4.71}$$

The small dimensionless parameter ϵ was introduced to scale the nonlinear terms. Because one of the boundary conditions resulting from an integration by parts did not vanish for $d = L$, this analysis must be modified to treat the case when the concentrated mass is located at the tip.

We define a new time scale as

$$\tau = \theta t. \tag{4.72}$$

Hence, the time derivatives become

$$\frac{d}{dt} = \theta \frac{d}{d\tau} \quad \text{and} \quad \frac{d^2}{dt^2} = \theta^2 \frac{d^2}{d\tau^2}. \tag{4.73}$$

Equation (4.68) is thus transformed to

$$\begin{aligned}
 0 = & G_{\tau\tau} + 2\varepsilon\zeta G_{\tau} + [1 - \varepsilon f \cos(\phi\tau)]G + \varepsilon\alpha G^3 + \varepsilon\kappa_1 G G_{\tau}^2 \\
 & + \varepsilon\kappa_2 G^2 G_{\tau\tau} - 2\varepsilon\zeta\nu G^2 G_{\tau} , \quad (4.74)
 \end{aligned}$$

where

$$\zeta = \frac{\hat{\zeta}}{\theta}, \quad \alpha = \frac{\hat{\alpha}}{\theta}, \quad \text{and} \quad \phi = \frac{\Omega}{\theta} . \quad (4.75)$$

This equation contains cubic nonlinearities and nonlinear damping, and hence it does not lend itself to a closed-form solution. It must be analyzed by a perturbation or a numerical technique. Moreover, the coefficients are evaluated according to (4.69) and (4.70) and are dependent on $\psi(s)$. When the amplitude of vibration gets large, $\psi(s)$ may no longer approximate the mode shape, and consequently the coefficients of the time modulation equation have increasing error.

4.4 Scaling the Time Modulation Equation

In the previous section we derived the time modulation equation for the parametric response of a slender cantilever beam with a lumped mass, and introduced ε in what may seem to have been an arbitrary manner. In this section we will show the results of a sample calculation that were used to suggest the scaling introduced in (4.68).

Consider a beam-mass system with the following properties:

$$\begin{array}{lll} L = 125.4, & w = 11.11, & h = 0.368, \\ r = 125.4, & m = 14.70, & I = 4.626 \times 10^{-2}, \\ J = 600.9, & \mu = 3.690, & \rho = 0.0377, \\ d = 93.68, & \lambda = 1.00, & c = 1.469 \times 10^{-3}, \\ E = 0.20936 \times 10^6. & & \end{array} \quad (4.76)$$

The units chosen were Newton-gram-millimeter-second. The scaling factor r is typically chosen such that it represents a dimensional unit of the model displacement such as the radius of gyration of the beam, the thickness h , the width w , or the length L , depending on the anticipated response. The objective here is to scale the problem such that the normalized shape function $\psi(s)$ times the scaling factor r allows the time function $G(t)$ to be of order one. Since we observed rather large vibrations, we chose L as the scaling factor, realizing that peak amplitudes on the order of $L/4$ are anticipated. The above choices of parameters are the values from the second metallic beam. Similar values were used for the calculations required to plot Figures 4.3 and 4.4.

Performing the indicated integrations according to (4.70) using Simpson's Rule, we calculated the following values for the H_{ij}

$$\begin{array}{lll}
H_{11} = 0.977127, & H_{12} = 0.168365, & H_{13} = 0.687553, \\
H_{21} = 0.977127, & H_{31} = 0.977127, & H_{32} = 0.168365, \\
H_{33} = 0.153578, & H_{34} = 0.270738, & H_{41} = 0.325800, \\
H_{42} = 0.578800, & H_{43} = -0.319906, & H_{51} = 0.217654, \\
H_{52} = 0.732989, & H_{53} = 0.472729, & H_{61} = 0.217654, \\
H_{62} = 0.231875, & H_{63} = 0.732989, & H_{64} = 0.393123, \\
H_{65} = 0.236364, & H_{71} = 0.231875. &
\end{array}
\tag{4.77}$$

The first root of the characteristic equation was found numerically to be $k_1 = 1.60865806$. Using the computed values of the H_{ij} for $r = 2.00$, we compute the following coefficients for the time modulation equation (with the scaling parameter ϵ set equal to unity)

$$\begin{array}{ll}
\zeta = 0.1460 \times 10^{-2}, & g = 0.1123, \\
\alpha = 0.8090 \times 10^{-1}, & v = 0.2373, \\
\kappa_1 = 0.4090, & \kappa_2 = 0.1740, \\
\theta = 43.78. &
\end{array}
\tag{4.78}$$

The coefficients α , κ_1 , and κ_2 of the cubic terms are seen to be of nearly the same order, and although the excitation f is small, it is dependent on the amplitude r and frequency ω . The nonlinear damping term $-2\zeta v G^2 G_\tau$ is of higher order, and should actually be promoted to order ϵ^2 . However, if we only carry out a first-order expansion, the nonlinear damping term should be ordered at ϵ . This will allow its effect--however small--to be felt in the perturbation analysis.

A perturbation solution for (4.74) will be obtained in the next chapter. The features of this solution, including the amplitude

response and the frequency response, will be compared to experimental results obtained in the laboratory.

4.5 Chapter Summary

In this chapter we have derived the nonlinear partial differential equation that governs the motion of an elastic flexible prismatic beam which is attached to a moving support. A concentrated mass is located between the clamped support and the free end. The nonlinear terms arising from the curvature are retained to third order, and the nonlinear axial displacements caused by large transverse displacements are also retained to third order. Since the beam is relatively long, the Euler-Bernoulli theory was used. The resulting equation of motion subject to the prescribed boundary conditions was approximated by a second-order ordinary differential equation using Galerkin's method. The eigenfunction from the linear problem was used in the numerical computation of the coefficients of the time modulation equation. The resulting equation was scaled and put into non-dimensional form, ready for analysis by a perturbation technique.

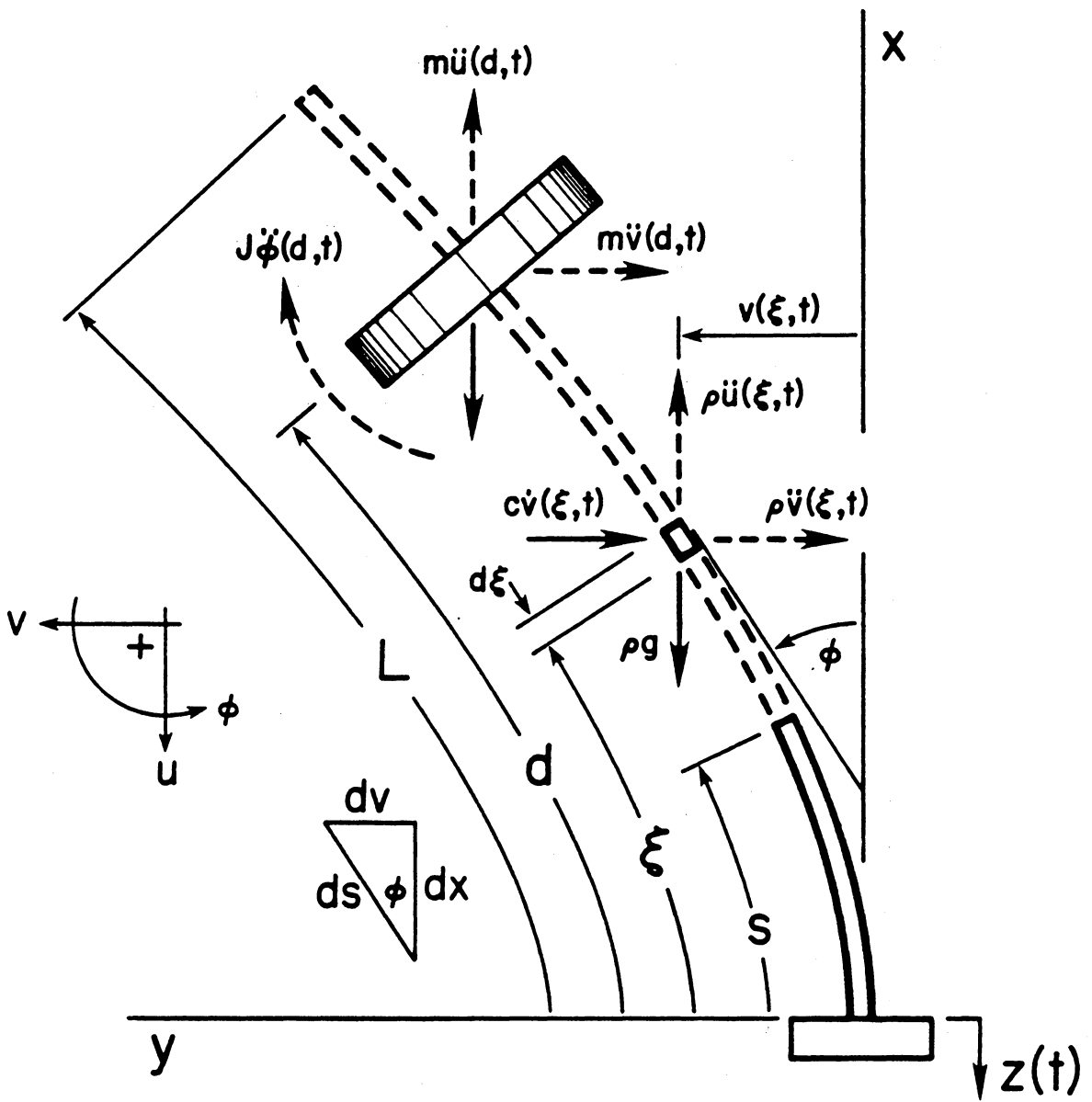


Figure 4.1 Cantilevered beam with a concentrated mass subjected to vertical base motion.

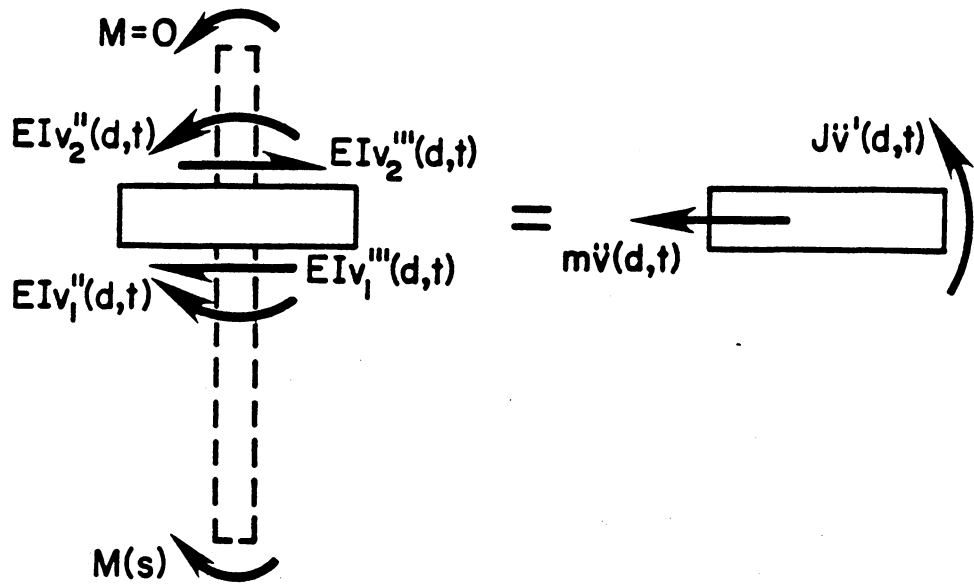


Figure 4.2 Free-body diagram of the concentrated mass showing shearing forces and bending moments which cause the resultant accelerations.

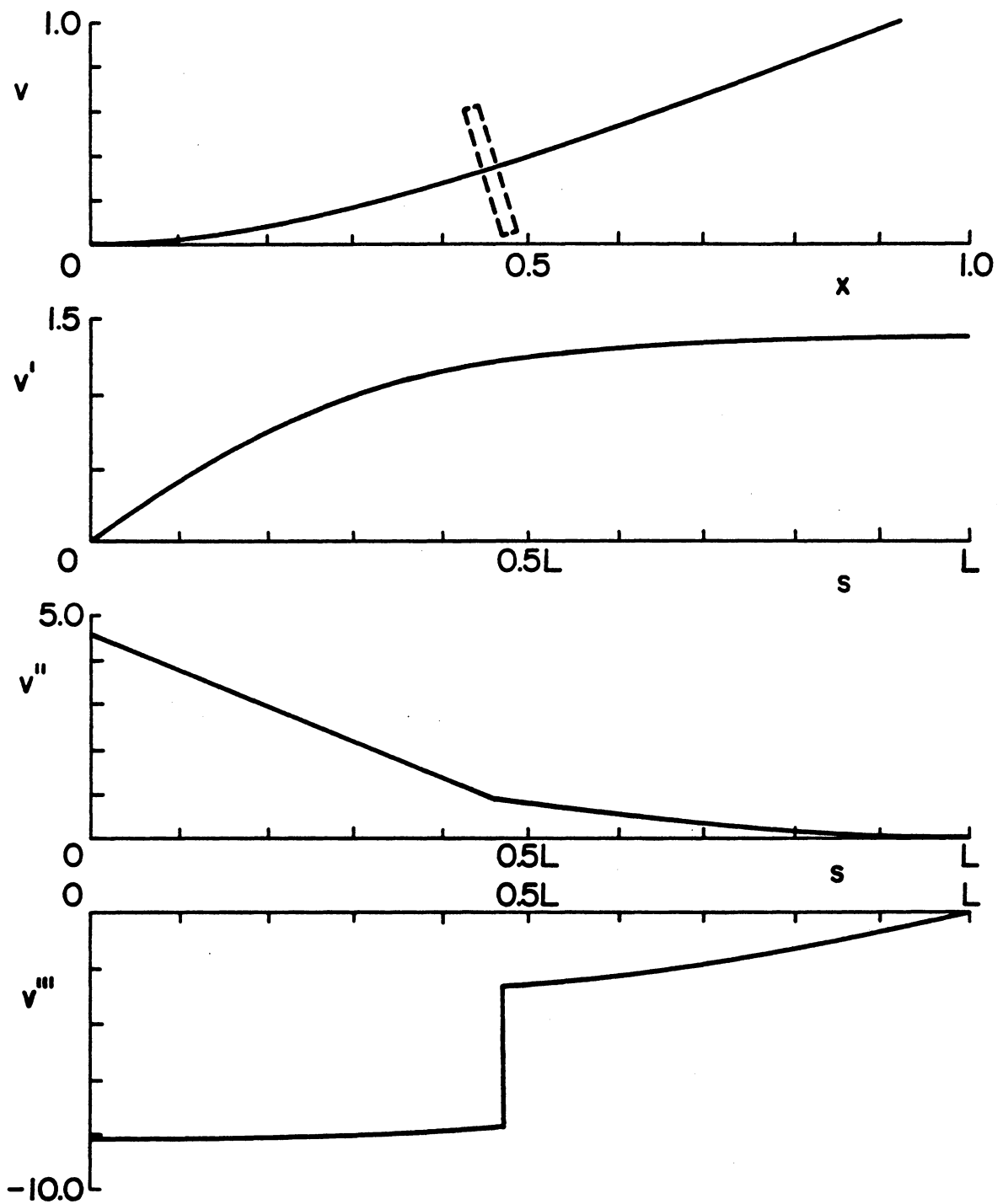


Figure 4.3 Shape function and derivatives for the first mode of the cantilevered beam shown in Figure 4.1. These curves represent the solution to the linearized free vibration problem.

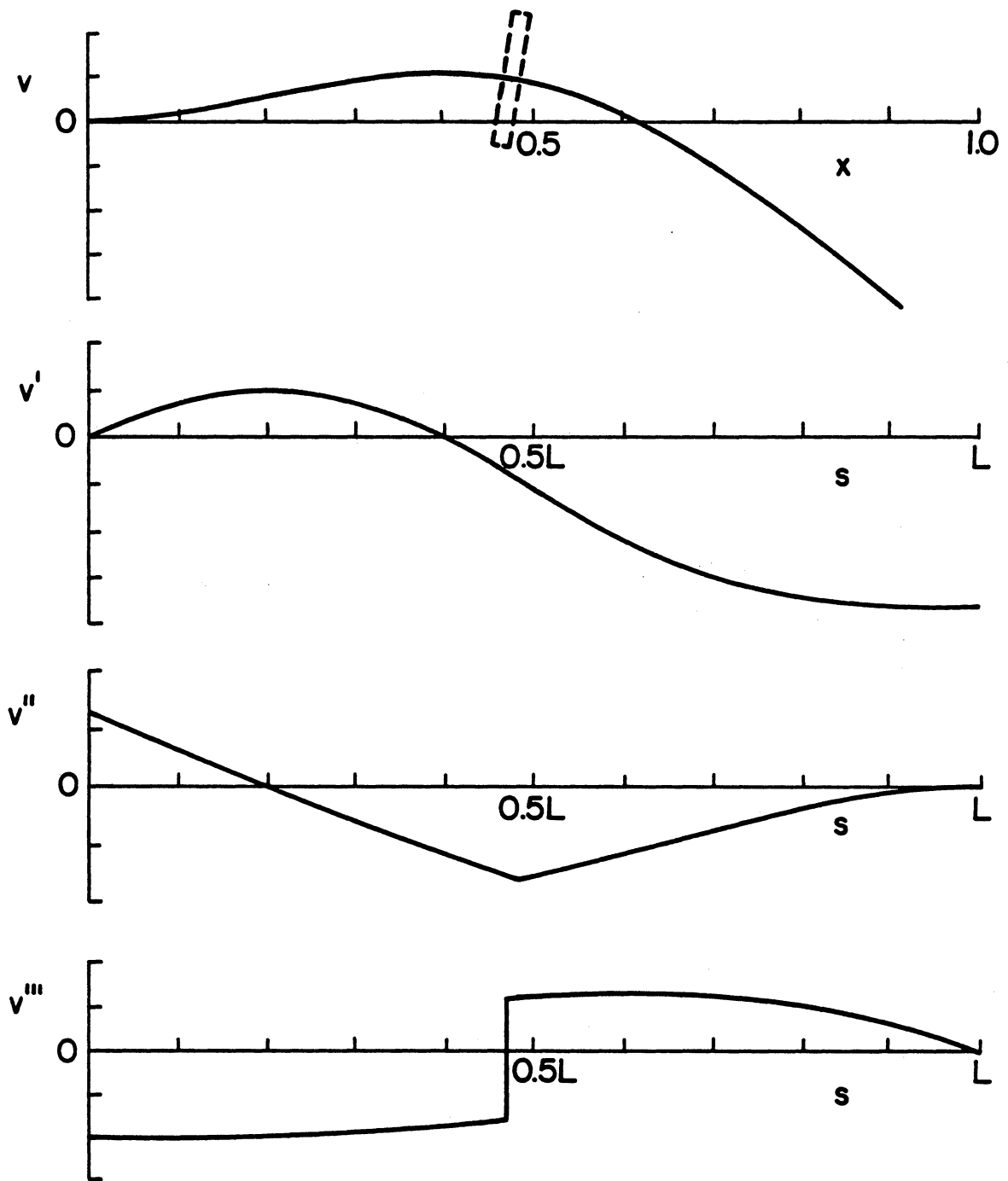


Figure 4.4 Shape function and derivatives for the second mode of the cantilevered beam shown in Figure 4.1. These curves represent the solution to the linearized free vibration problem.

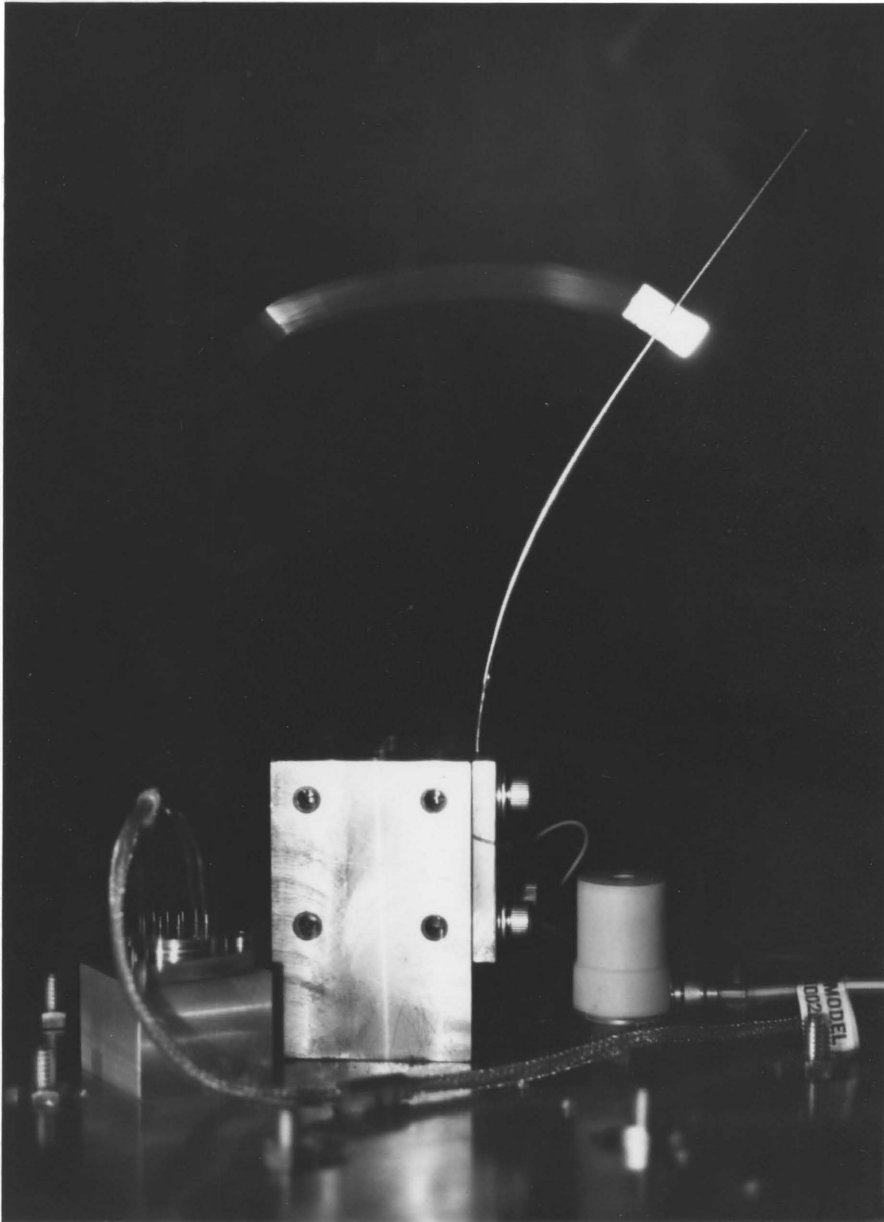


Figure 4.5 Stroboscopic photograph of a beam in the maximum deflected position when excited by a principal parametric resonance to the first mode.

CHAPTER V

PERTURBATION SOLUTION AND EXPERIMENTAL RESULTS OF A SLENDER BEAM CARRYING A LUMPED MASS SUBJECT TO A PARAMETRIC EXCITATION

In this chapter we examine the response of a slender beam carrying a lumped mass subject to a principal parametric excitation considered in Chapter IV. The time modulation is governed by

$$\begin{aligned} G_{\tau\tau} + 2\varepsilon\zeta G_{\tau} + [1 - \varepsilon f \cos(\phi\tau)]G + \varepsilon\alpha G^3 + \varepsilon\kappa_1 G G_{\tau}^2 \\ + \varepsilon\kappa_2 G^2 G_{\tau\tau} - 2\varepsilon\zeta\nu G^2 G_{\tau} = 0, \end{aligned} \quad (5.1)$$

where the subscript τ indicates differentiation with respect to the nondimensional time τ , ε is a small dimensionless parameter, and ζ , α , κ_1 , κ_2 , and ν are constants related to the physical properties of the beam; the excitation amplitude f and frequency ϕ are also constant. We seek an approximate solution to (5.1) using a perturbation technique. An experiment will be performed to determine the accuracy of (5.1) in predicting the response.

5.1 Multiple Scales Analysis

A first-order uniform solution of (5.1) is sought using the method of multiple scales in the form

$$G(\tau;\varepsilon) = u_0(T_0, T_1) + \varepsilon u_1(T_0, T_1) + \dots \quad (5.2)$$

where $T_0 = \tau$ is a fast scale associated with changes occurring at the frequency ϕ , and $T_1 = \varepsilon\tau$ is a slow scale associated with modulations in the amplitude and phase caused by the damping, resonance, and nonlinearity. In terms of the T_n , the time derivatives become

$$\begin{aligned}\frac{d}{dt} &= D_0 + \varepsilon D_1 + \dots, \\ \frac{d^2}{d\tau^2} &= D_0^2 + 2\varepsilon D_0 D_1 + \dots,\end{aligned}\tag{5.3}$$

where $D_n = \partial/\partial T_n$. Substituting (5.2) and (5.3) into (5.1) and equating coefficients of like powers of ε , we obtain

$$D_0^2 u_0 + \frac{1}{4} \phi^2 u_0 = 0,\tag{5.4}$$

$$\begin{aligned}D_0^2 u_1 + \frac{1}{4} \phi^2 u_1 &= -2D_0 D_1 u_0 - \sigma u_0 - 2\zeta D_0 u_0 - f u_0 \cos(\phi T_0) \\ &\quad - \alpha u_0^3 - \kappa_1 u_0 (D_0 u_0)^2 - \kappa_2 u_0^2 (D_0^2 u_0) \\ &\quad + 2\zeta u_0^2 D_0 u_0,\end{aligned}\tag{5.5}$$

where the detuning σ was introduced into the normalized natural frequency of the system as

$$1 = (\frac{1}{2}\phi)^2 + \varepsilon\sigma.\tag{5.6}$$

We are justified in doing this because the frequency of the response for a principal parametric resonance will be exactly one-half that of the excitation. In Chapters II and III we expressed the excitation frequency in terms of the natural frequency by introducing the detuning

later into the analysis as $\Omega = n\omega_0 + \varepsilon^m \sigma$, where $m, n = 1, 2$, and we obtained nonautonomous amplitude- and phase-modulation equations. This was done because we considered two different resonances. In the present analysis, we express the natural frequency in terms of the excitation frequency and introduce the detuning as in (5.6); this has the additional benefit of obtaining autonomous amplitude- and phase-modulation equations.

The solution of (5.4) can be expressed in complex form as

$$u_0 = A(T_1)e^{\frac{1}{2}i\phi T_0} + \bar{A}(T_1)e^{-\frac{1}{2}i\phi T_0}, \quad (5.7)$$

where \bar{A} is the complex conjugate of A . Then, (5.5) becomes

$$\begin{aligned} D_0^2 u_1 + \frac{1}{4} \phi^2 u_1 = & [-i\phi A' - i\phi \zeta A - \sigma A - 3\alpha A^2 \bar{A} - \frac{1}{4} \phi^2 \kappa_1 A^2 \bar{A} \\ & + \frac{3}{4} \phi^2 \kappa_2 A^2 \bar{A} - \frac{1}{2} f \bar{A} + i\phi \zeta \nu A^2 \bar{A}] e^{\frac{1}{2}i\phi T_0} \\ & + [-\frac{1}{2} f A - \alpha A^3 + \frac{1}{4} \phi^2 \kappa_1 A^3 + \frac{1}{4} \phi^2 \kappa_2 A^3 \\ & + i\phi \zeta \nu A^3] e^{3i\phi T_0/2} + cc, \end{aligned} \quad (5.8)$$

where the prime denotes differentiation with respect to T_1 . Any particular solution of (5.8) contains secular terms; hence we eliminate them by setting

$$A' = \left(\frac{i\sigma}{\phi} - \zeta\right)A + \frac{4i}{\phi} \alpha_e A^2 \bar{A} + \zeta \nu A^2 \bar{A} + \frac{if}{2\phi} \bar{A}, \quad (5.9)$$

where

$$\alpha_e = \frac{1}{4} \left(3\alpha + \frac{1}{4} \phi^2 \kappa_1 - \frac{3}{4} \phi^2 \kappa_2\right). \quad (5.10)$$

Consequently, the solution of (5.8) becomes

$$u_1 = \left\{ \frac{fA}{4\phi} + \left[\frac{\alpha}{2\phi} - \frac{1}{8} (\kappa_1 + \kappa_2) \right] A^3 - i \frac{\zeta\nu}{2\phi} A^3 \right\} e^{3i\phi T_0/2} + cc . \quad (5.11)$$

At this point it is convenient to express the complex function A in polar form as

$$A = \frac{1}{2} a e^{i\beta} . \quad (5.12)$$

Substituting (5.12) into (5.9), separating real and imaginary parts, and replacing T_1 with ϵt , we obtain

$$\dot{a} = -\epsilon\zeta \left(1 - \frac{1}{4} \nu a^2\right) a + \frac{\epsilon f a}{2\phi} \sin 2\beta , \quad (5.13)$$

$$a\dot{\beta} = \frac{\epsilon}{\phi} (\sigma + \alpha_e a^2) a + \frac{\epsilon f a}{2\phi} \cos 2\beta . \quad (5.14)$$

Substituting (5.12), (5.11), and (5.7) into (5.2), we obtain

$$G(\tau) = a \cos\left(\frac{1}{2}\phi\tau + \beta\right) + \epsilon a \left\{ \frac{f}{4\phi} + \frac{a^2}{32} \left(\frac{4\alpha}{\phi} - \kappa_1 - \kappa_2 \right) \cos\left[3\left(\frac{1}{2}\phi\tau + \beta\right)\right] + \frac{\zeta\nu}{8\phi} a^2 \sin\left[3\left(\frac{1}{2}\phi\tau + \beta\right)\right] \right\} + \dots , \quad (5.15)$$

where a and β are given by (5.13) and (5.14). It follows from (5.15) that, to the first approximation, the nonlinearity produces a third harmonic in the response.

Periodic solutions of (5.1) correspond to the fixed points (i.e., constant solutions) of the modulation equations (5.13) and (5.14), which

in turn correspond to $\dot{a} = 0$ and $\dot{\beta} = 0$. By squaring and summing the two equations, we obtain

$$a^2 = 0, \frac{1}{2q} [-r \pm \sqrt{r^2 - 4qs}] , \quad (5.16)$$

where

$$\begin{aligned} q &= \frac{1}{4} (1 - \varepsilon\sigma)\zeta^2 v^2 + \alpha_e^2 , \\ r &= 2\sigma(\alpha_e + \varepsilon\zeta^2 v) - 2v\zeta^2 , \\ s &= 4(1 - \varepsilon\sigma)\zeta^2 + \sigma^2 - \frac{1}{4} f^2 , \end{aligned} \quad (5.17)$$

where ϕ^2 was replaced with $4(1 - \varepsilon\sigma)$ from (5.6).

To determine the stability of the trivial fixed points, we investigate the solutions of the linearized form of (5.9); that is

$$\dot{A} = \varepsilon\left(\frac{i\sigma}{\phi} - \zeta\right)A + \frac{i\varepsilon}{2\phi} f \bar{A} . \quad (5.18)$$

Letting

$$A = B_r + iB_i \quad (5.19)$$

in (5.18) and separating real and imaginary parts, we obtain

$$\dot{B}_r = -\varepsilon\zeta B_r + \frac{\varepsilon}{\phi} \left(\frac{f}{2} - \sigma\right) B_i , \quad (5.20)$$

$$\dot{B}_i = \frac{\varepsilon}{\phi} \left(\frac{f}{2} + \sigma\right) B_r - \varepsilon\zeta B_i . \quad (5.21)$$

Equations (5.20) and (5.21) admit solutions of the form

$$(B_r, B_i) = (b_r, b_i) e^{\epsilon \lambda t} \quad (5.22)$$

provided that

$$\lambda = -\zeta \pm \frac{1}{2\phi} \sqrt{f^2 - 4\sigma^2} . \quad (5.23)$$

Consequently, a trivial fixed point is unstable if and only if

$$f > f_{\text{crit}} = 2\sqrt{\sigma^2 - \phi^2 \zeta^2} , \quad (5.24)$$

otherwise it is stable.

To determine the stability of the nontrivial fixed points, we let

$$a = a_0 + a_1(t), \quad \beta = \beta_0 + \beta_1(t) , \quad (5.25)$$

where a_0 and β_0 correspond to a stable nontrivial fixed point, and a_1 and β_1 are perturbations which are assumed to be small compared with a_0 and β_0 . Substituting (5.25) into (5.13) and (5.14) and linearizing the resulting equations, we obtain

$$\dot{a}_1 = \epsilon \left(-\zeta + \frac{3}{4} \zeta \nu a_0^2 + \frac{f}{2\phi} \sin 2\beta_0 \right) a_1 + \left(\frac{\epsilon f}{\phi} a_0 \cos 2\beta_0 \right) \beta_1 , \quad (5.26)$$

$$\dot{\beta}_1 = \left(\frac{2\epsilon \alpha e^{a_0}}{\phi} \right) a_1 + \left(\frac{-\epsilon f}{\phi} \sin 2\beta_0 \right) \beta_1 . \quad (5.27)$$

Consequently, a nontrivial fixed point is stable if and only if the real parts of both eigenvalues of the coefficient matrix in (5.26) and (5.27) are less than or equal to zero.

5.2 Numerical Results of Approximate Solution

Equation (5.15) gives a first-order perturbation solution to (5.1), where a and β are governed by (5.13) and (5.14). When the amplitude achieves a constant nontrivial value, a steady-state parametric vibration exists. Using (5.16), we can assess the influence of the amplitude of excitation f and the frequency detuning σ on the steady-state amplitude.

The frequency-response curve is shown in Figure 5.1 for system parameters corresponding to the second metallic beam used in the experiments. It shows a parametric resonance of the hardening type. There are three distinct regions: in I, where $\phi < \phi_1$, only the trivial solution is possible and it is stable; in II, where $\phi_1 < \phi < \phi_2$, there is one stable nontrivial solution and one unstable trivial solution; and in III, where $\phi > \phi_2$, two nontrivial solutions are possible with the larger one being stable, and a stable trivial solution. In the latter case, the initial conditions determine the response, whereas in regions I and II the final state is independent of the initial conditions. Although the two nontrivial branches do not terminate, we know in practice they must.

If we choose a frequency in regions II and III and plot the amplitude of the response as a function of the amplitude of the excitation, we obtain the results shown in Figures 5.2 and 5.3. Figure 5.2, which corresponds to region II, shows that parametric vibrations exist only when the excitation amplitude exceeds a threshold value. When the frequency of the excitation is increased to region III of

Figure 5.1, the frequency-response curve is multi-valued, resulting in a subcritical instability, as seen in Chapters I, II, and III. Because the nonlinearity is of the hardening type, the subcritical instability is only realized when the system is detuned in the positive direction. Had it been of the softening type, the system needs to be detuned in the negative direction.

If it was desirable to suppress or eliminate this parametric resonance, the dependence of the response on the other system parameters could be investigated. However, part of the nonlinearity is due to the large deflection (the other part is due to inertia) and cannot be "controlled" or "designed" away. If the damping could be increased, we may diminish or quench the response, but we have seen that a critical damping coefficient must be exceeded to suppress the response; otherwise increasing the damping coefficient may have modest effects on controlling the amplitude of the response.

If we extend the frequency axis of the response curve shown in Figure 5.1, the perturbation theory predicts that the two branches will close, as shown in Figure 5.4. This happens because the detuning is used to express the natural frequency in terms of the excitation frequency, and hence introduces some (but not all) second-order effects. When the detuning is used to express the excitation frequency in terms of the natural frequency (e.g., $\phi = 2 + \epsilon \hat{\sigma}$), the first order perturbation solution does not predict a jump down. This alternate solution is also shown in Figure 5.4. Interestingly, this alternate

solution more accurately predicts the steady-state amplitude obtained by numerical integration of equation (5.1).

5.3 Results of Preliminary Experiments on Test Models

The first experiments to parametrically excite flexible structures were also the first "tests" of the shaker system. Details of the experimental facility and procedures are given in the appendix, where we discuss the problems we encountered and the remedies we chose. We were quite surprised to see the very large displacements that the model experienced considering the relatively small amplitudes of the excitation. The strain gages cemented near the base of the cantilevered beam did not remain in place very long--the surface strains were too large. Subsequent beams had strain gages mounted much higher, and in some cases, just below the mass. This enabled us to measure much larger displacements.

During the frequency sweeps, we occasionally observed sudden changes in the response of the model. In one of the tests performed we chose an acceleration level, which was held constant by the computer feedback control system, and very slowly swept the frequency up and down through a resonance, noting the steady-state amplitude at each step. During one test, we noted an increase in the response amplitude as we decreased the excitation frequency--then suddenly we heard a clicking sound accompanied by a jump down in the steady-state amplitude. As we decreased the excitation frequency further, the response amplitude again increased and then suddenly jumped down. This scenario was repeated

several times; the results are shown in Figure 5.5. The natural frequency after the experiment had dropped significantly. After removing the beam from its clamped support, we discovered that a fatigue crack had developed and propagated across 70% of the width of the beam. We concluded then that each click and subsequent jump down in response amplitude was associated with the crack growth. A photograph of the beam showing the crack is shown in Figure 5.6.

The second beam was therefore polished in the region of high bending stress to delay the onset of crack initiation. The frequency response of this beam was very similar to that shown later (Figure 5.14), but it too failed in a similar fashion: sudden jumps down in the steady-state response accompanied by changes in the natural frequency. For the third beam, we used an alloy steel that could be easily hardened. The beam was precision ground to the dimensions shown in Figure 5.7 and then heat-treated and tempered to R_c45 . Additional properties and heat treatment procedures are given in the appendix. This design was chosen to gradually reduce the high bending stress at its base and to allow for its removal and replacement from the clamp support without any change in its length. Strain gages were attached to both sides and wired to provide a half-bridge connection to the bridge amplifier.

The modulus of elasticity was calculated to be $30 \times 366 \times 10^6$ psi (0.20942×10^{12} Pa) from the natural frequency of the beam, which was estimated using the procedure described in the appendix. The beam was in a horizontal position for this measurement. The lumped mass, also

shown in Figure 5.7, was machined so that a narrow ridge 0.005 inches wide made contact with the beam. In this way we approximated the boundary conditions at the mass that was used in the theory. Steel set screws were embedded in the mass so that the measured and predicted frequencies could be matched by a minor adjustment (less than two turns of the set screws). Equation (4.69) gives the natural frequency in a gravity field; however, in the horizontal position gravity does not affect the natural frequency and hence the gravity term was deleted. When the model was put into the upright position, the observed change of 0.120 Hz in the natural frequency was accurately predicted! This observation lent credibility to the theory. The damping coefficient was estimated by observing the free response, as described in the appendix. The difference between the damped and undamped natural frequencies is less than the resolution of our measurement, so no correction was necessary.

When the model began to vibrate at large amplitudes, we noted a minor subharmonic distortion to the table motion caused by the reaction moment at the base of the beam. The distortion was barely visible in the accelerometer mounted near the base of the beam, but was quite noticeable in the displacement transducer signal. The model was positioned on the table in such a way that any bending of the beam created a reaction moment on the table causing rotation that was detected by the displacement transducer. Since the displacement transducer was positioned on the side of the table (with a dynamically tuned counterbalance on the other side), any rotation of the table was

mechanically amplified, and hence readily detected (see photograph in Figure A.2). Representative time traces of the table accelerometer signal, table displacement signal, and strain gage signal are shown in Figure 5.8.

The distortion was minimized by adding the other two diagonal legs to the table (which were removed to minimize weight for higher frequency experiments) with four additional bearings, and adding four new bearings to the top of the table which required extending the guide rails. These can be seen in Figure A.2. Unfortunately, when the testing resumed, we observed a sudden drop in the response amplitude, and our suspicion of a fatigue crack was verified by measuring a much lower natural frequency.

5.4 Results and Discussion of the Composite Beam Experiments

A symmetrical $0^\circ - 90^\circ - 90^\circ - 0^\circ$ 4-ply graphite-epoxy composite plate 0.022 inches thick was fabricated and cut into strips one-half inch wide. Since this beam was much more flexible, a smaller mass was used. It was machined in a similar fashion; that is, it had a 0.005 inch ridge where it made contact with the beam. A photograph of this beam is shown in Figure 5.9.

The frequency-response curves of the composite beam for three levels of excitation amplitude are shown in Figure 5.10, and they show several interesting features. First, we observe that the general behavior is as predicted by the theory. As the excitation frequency is increased from a value well below 2.000, the response remains trivial until a critical value is exceeded. Increasing the excitation frequency

beyond this value causes the response amplitude to increase. There is, however, a maximum frequency at which point further increases in the frequency cause a jump down to the lower branch. This jump down appears to be a turning-point bifurcation, and is drawn as such in the figure.

Second, we note the appearance of chaotic behavior for the largest amplitude response; it was preceded by a modulation in the amplitude. Since this amplitude was extremely large (the beam was bending such that the mass was down to about the level of the beam support), we did not dwell at this amplitude because we were fearful the beam would fail before completing the amplitude sweeps. We did, however, use the strobe light to "slow down" the vibration for observation and noted that the chaotic behavior was accompanied by out-of-plane bending and torsion. The chaotic behavior was observed on the oscilloscope displaying the time trace and in the instantaneous power spectrum which contained a low-level, broad-band component. This behavior was not unexpected because we have seen it in experiments using longer beams and we saw it in Chapters II and III.

Third, we observe a penetration of a stable trivial solution into what is typically the unstable region of parametric resonance. These jump points (boundary between stable and unstable trivial solutions as the frequency is increased) were determined in the manner described in the appendix. Inside this "unstable" region small disturbances decayed and large disturbances grew, but as the region was penetrated, the disturbances that decayed became smaller and smaller until the trivial solution was not able to even keep trivial solutions.

Fourth, we note the lower branch lifting off the frequency axis as the frequency is decreased from above. Because it has a behavior similar to a turning-point bifurcation, this parametric resonance looks similar to an externally excited resonance (e.g., a Duffing oscillator) with a hardening nonlinearity. This behavior was not predicted and appears to be intensified due to the higher level and nonlinear nature of the damping present in the composite beam.

The nature of the parametric resonance for $\phi = 2.000$ and a table acceleration level of 1.00 g is shown in Figure 5.11(a). This figure shows the spectral time history of the beam displacement starting with the trivial response at time $t = 0$. Approximately 33 seconds are required before any vibration is visible, but once the motion starts, it grows very quickly and achieves its steady state with minimal transient modulation. We also see the presence of the third harmonic, but since the amplitude is plotted on a linear scale, it is barely visible. When the excitation frequency is increased to $\phi = 2.013$, we have two possible steady-state solutions as shown in Figure 5.10. When the model is released from rest, only 12 seconds elapse before a response is visible, and as shown in Figure 5.11(b), it is the lower branch that attracts the response. After the system achieved steady-state, it was disturbed, and we note that the disturbance was sufficient to cause the system to jump up to the large amplitude response. We also note that the system modulates and does not achieve a constant steady-state amplitude. Also present with the large amplitude response is the third harmonic, and barely visible are the second and fourth harmonics.

For the next experiment, we fixed the frequency and slowly increased and then decreased the amplitude of the excitation; the results are shown in Figure 5.12. When $\phi = 2.000$, the amplitude-response curve shows that a critical excitation amplitude must be exceeded before a principal parametric resonance can be excited. For values of $\phi < 2.000$, the curves are quite similar. When $\phi = 2.008$ the results in Figure 5.10 show that the response curve is multivalued and hence a subcritical instability is anticipated. The measurements plotted in the figure show that the multivaluedness shifts to the right beyond the critical value; hence we did not observe a "sub-critical" instability per-se. However, we observed a small response at an excitation level below the critical value (corresponding to the trivial response lifting off the axis prior to jumping up) whereas the theory predicts a trivial response. For reasons not yet understood, this behavior may be related to the shifting of the response curve to the right. Further increases in ϕ causes this curve to migrate to the right as shown.

As discussed in the procedures (appendix), we checked the calibration of the strain gage and damped natural frequency after each run. The calibration varied by less than 1%, but we noted that the natural frequency was slowly decreasing during the series of tests. This explains why repeated experiments did not yield identical results, as seen in the response amplitudes to identical excitation levels and frequencies in Figures 5.10 and 5.12. Being a composite beam, it suffered fiber damage during the test runs which made it difficult to

obtain good comparative results. However, it did not fail as did all the metallic beams, so it was useful in this regard. Since it was a very flexible beam, feedback distortion to the vibration table was also minimized.

During the large amplitude response, we observed the presence of harmonics in the strain gage signal, as seen in Figures 5.11 and shown in Figure 5.13 using a log scale. Initially, both signals were very clean for small amplitudes (on both upper and lower branches). When the amplitude and frequency of excitation were adjusted so that the response amplitude increased, the third harmonic appeared. As the response amplitude increased, so did the amplitude of the third harmonic. This was predicted by the perturbation solution. However, at even larger amplitudes the second harmonic appeared without an increase in the zero frequency (i.e., D.C.) component. This second harmonic was later accompanied by the fourth harmonic and neither was predicted by the theory. The second harmonic coincided exactly with the driving frequency and hence may be caused by the excitation acting as an external excitation due to very large deflections of the model or imperfections in either the model or the shaker table.

5.5 Results and Discussion of the Metallic Beam Experiments

Since the flexural stiffness of the composite beam did not remain constant, it was not possible to repeat an experiment and get identical results. The steel beam, in addition to failing by fatigue, was stiff enough to cause harmonic distortion of the shaker table. In view of

these, we fabricated a more flexible steel beam; it was precision ground to 0.015 inches thick and 0.4375 inches wide. It had a large radius fillet leading to a 0.125 inch thick base, as was done with the previous steel beam; it was also heat treated and tempered to a hardness of $R_C 45$. In addition, the root area of the beam was carefully polished to remove any surface scratches that might be nucleation sites for micro-cracks. The beam was instrumented and fitted with the smaller mass used previously on the composite beam. We limited the amplitude of vibration so we could map a complete family of curves related to the principal parametric resonance. Unfortunately, we were unable to complete all the tests because we heard the "all too familiar click" accompanied by a sudden drop in the amplitude. A check of the natural frequency revealed that it had also decreased, as expected. A photograph of this beam in Figure 5.14 shows a small crack which is barely visible.

The frequency response curve is shown in Figure 5.15. There are several interesting features to note. First, a comparison with the perturbation solution shown in Figure 5.1 shows remarkable agreement with few exceptions. We note that there exists a point where the large-amplitude response jumps down to the trivial branch. When we sweep the frequency down starting well above the jump down point, we again note the trivial solution lifting off the axis as it "anticipates" jumping up to the nontrivial solution. This behavior cannot be explained by the present theory.

Second, we again note a penetration of a stable trivial solution into the region predicted to be unstable by the theory. Although the

precision grinding, alignment, and balancing of the attached mass eliminated sources of external excitation that would be required to start the parametric resonance, we did observe a small region where finite disturbances decayed. This penetration phenomenon has been observed in nonstationary responses when the frequency is continuously swept. But in these experiments, the system was allowed to achieve a steady state, so the penetration is not attributed to the nonstationary behavior.

Third, we note a modulation in the large steady-state amplitude just before it jumps down. This behavior was also observed in the composite beam. We used this characteristic to warn us of a pending jump; consequently we used very small steps to determine, as accurately as possible, the jump down points. It is possible that, had we waited long enough, the response may have jumped down sooner. However, we were fearful of the specimen failing and waited just long enough for the modulation to achieve "steady-state". In some cases, by waiting long enough, the modulation disappeared.

The amplitude response for $\phi = 2.000$ is shown in Figure 5.16. We were planning to run sweeps for $\phi = 2.008$ and $\phi = 2.016$, but the model failed prematurely. These results also show remarkable agreement with the theory (see Figure 5.2).

5.6 Concluding Remarks and Chapter Summary

In this chapter we have developed a first-order perturbation solution to the time modulation equation (4.74) derived in the previous

chapter. We have also conducted a series of experiments on both metallic and composite beams and have seen good qualitative agreement between the perturbation solution and the results of the experiments. The discrepancies have been noted and plausible reasons offered. The experiments, including the analogue computer simulation in Chapters II and III, have provided several insights into understanding the nature of parametric resonances. First, all of the metallic specimens failed during the testing! Our objective here was non-destructive testing because of lengthy and costly specimen preparation. We purposely kept the vibration amplitudes small on the last metallic beam, yet it too failed. We conclude then that parametric excitations, when they produce a parametric resonance, can be dangerous or fatal to the structure because of the large deflections often associated with them.

Second, we discovered that the predicted unstable trivial region could be penetrated. The penetration was greater in the case of the metallic beam, which has a small equivalent viscous damping coefficient, compared to the case of the composite beam, which has higher damping. As the region was penetrated by increasing the frequency, the domain of attraction for the trivial solution decreased. Since the test specimens were precision ground and precisely aligned, and hence did not have any external excitation to start the motion, a small disturbance to the system was required to start a parametric response. However, this does not explain why small disturbances decayed inside this "unstable" region. What we saw was a diminishing domain of attraction for the trivial solution as the "unstable" region was penetrated. Since the

stability analysis was based on the linearized form of the reduced equation, it gave information regarding the behavior of small but finite vibration. But how small is small? We noted that if given a large enough disturbance, the amplitude would grow. Consequently, there appears to be some deficiency in the theory that does not predict the penetration into the "unstable" region.

Third, we observed that some attractors have such small domains of attraction, that particular routes must be used to attract them. For example, we could not attract the large amplitude response near the jump down point shown in Figure 5.15 by simply disturbing the trivial solution. Even using initial disturbance amplitudes that were larger than the steady-state amplitude was not sufficient. We had to decrease the frequency to enlarge the domain of attraction in order to latch onto the nontrivial attractor. Once a steady-state vibration was established, we could increase the frequency slowly and stay on the attractor. A similar procedure was required to realize some attractors on the analogue computer discussed in Chapters II and III. This behavior lends insight into possible problems associated with numerical integration of nonlinear equations.

The other discrepancy that cannot be explained by the present theory is the premature gradual departure from the trivial branch as the frequency is decreased. It is a small discrepancy and, in one sense, does not seem to be unreasonable. This is similar to the behavior of an external resonance and it may be that our familiarity with the external

resonance is tending to make us complacent when we see similar behavior in a parametric resonance.

In summary, we can say the theory does a good job in predicting the resonance, the mode shape of vibration, the influence of gravity on the frequency, and the qualitative nature of the response. Although not well documented here, we did observe chaotic responses. Since all of the metallic beams failed, we should be warned of the possible dangers associated with parametric resonances!

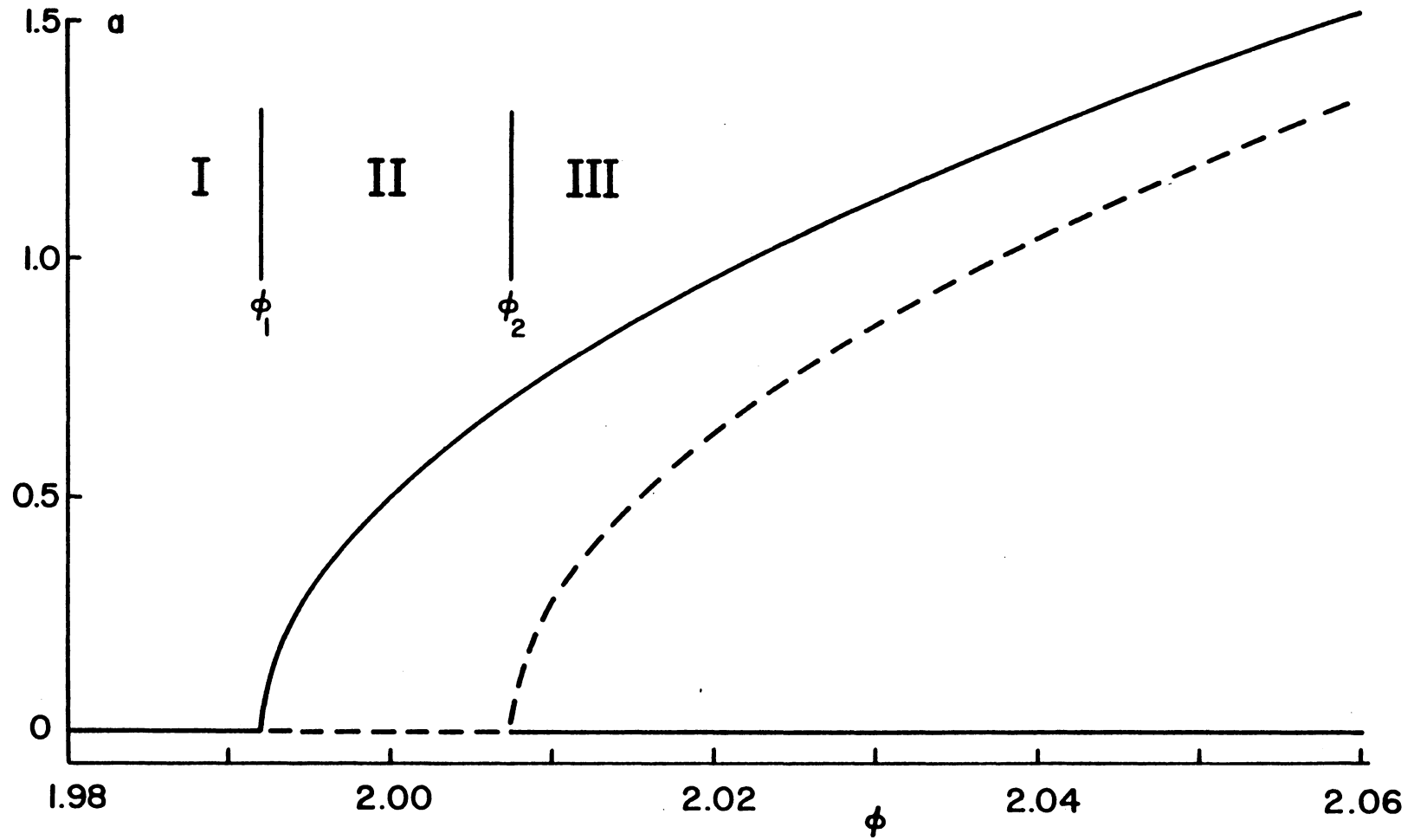


Figure 5.1 Variation of the steady-state amplitude a with the frequency of excitation ϕ : (—) stable, (---) unstable, $\alpha = 0.0808$, $\kappa_1 = 0.4163$, $\kappa_2 = 0.1716$, $\tau = 0.00147$, $\nu = 0.2577$, $f = 0.01653$, $\varepsilon = 1.00$.

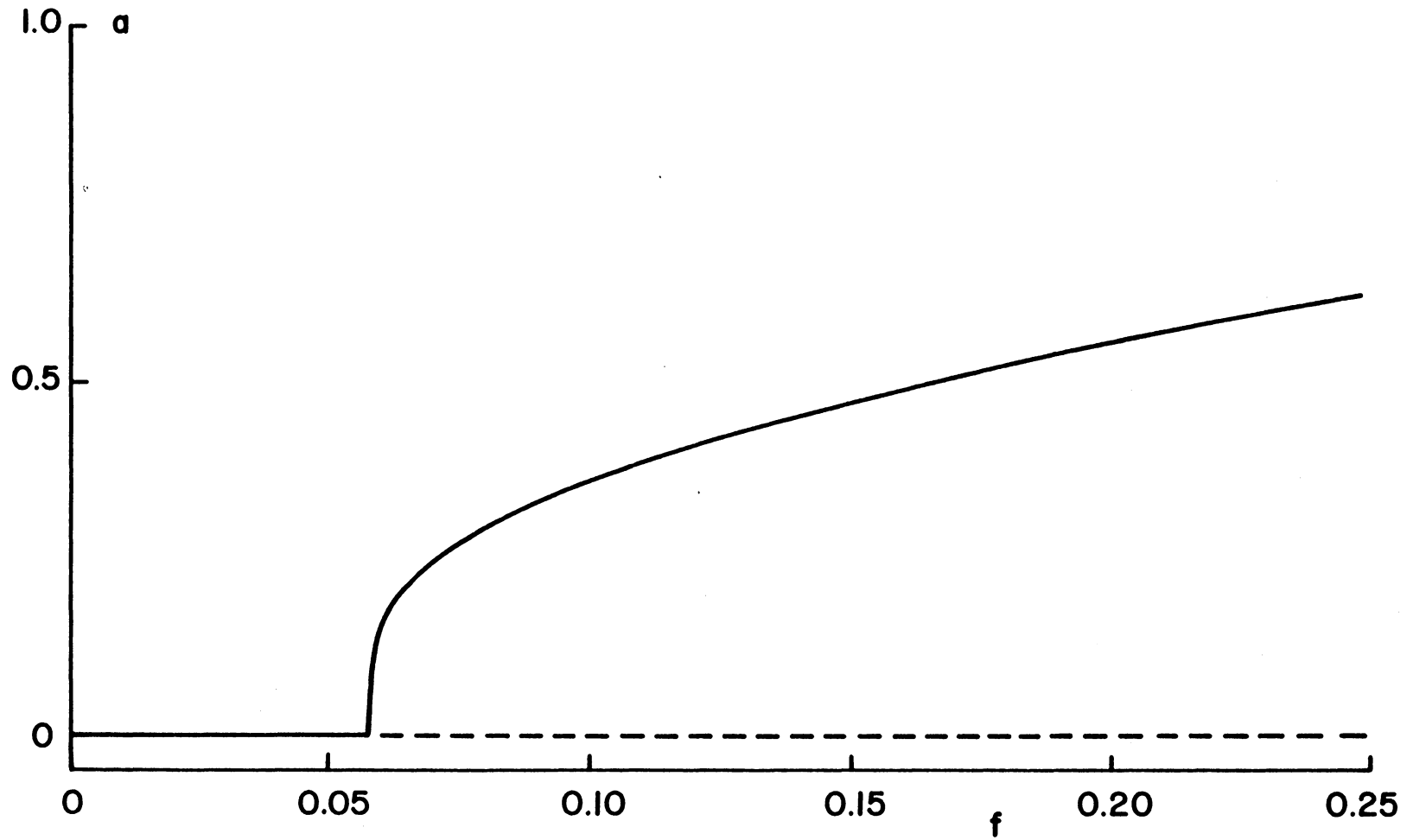


Figure 5.2 Variation of the steady-state amplitude a with the amplitude of excitation f in region II of Figure 5.1: (—) stable, (---) unstable, $\phi = 2.000$.

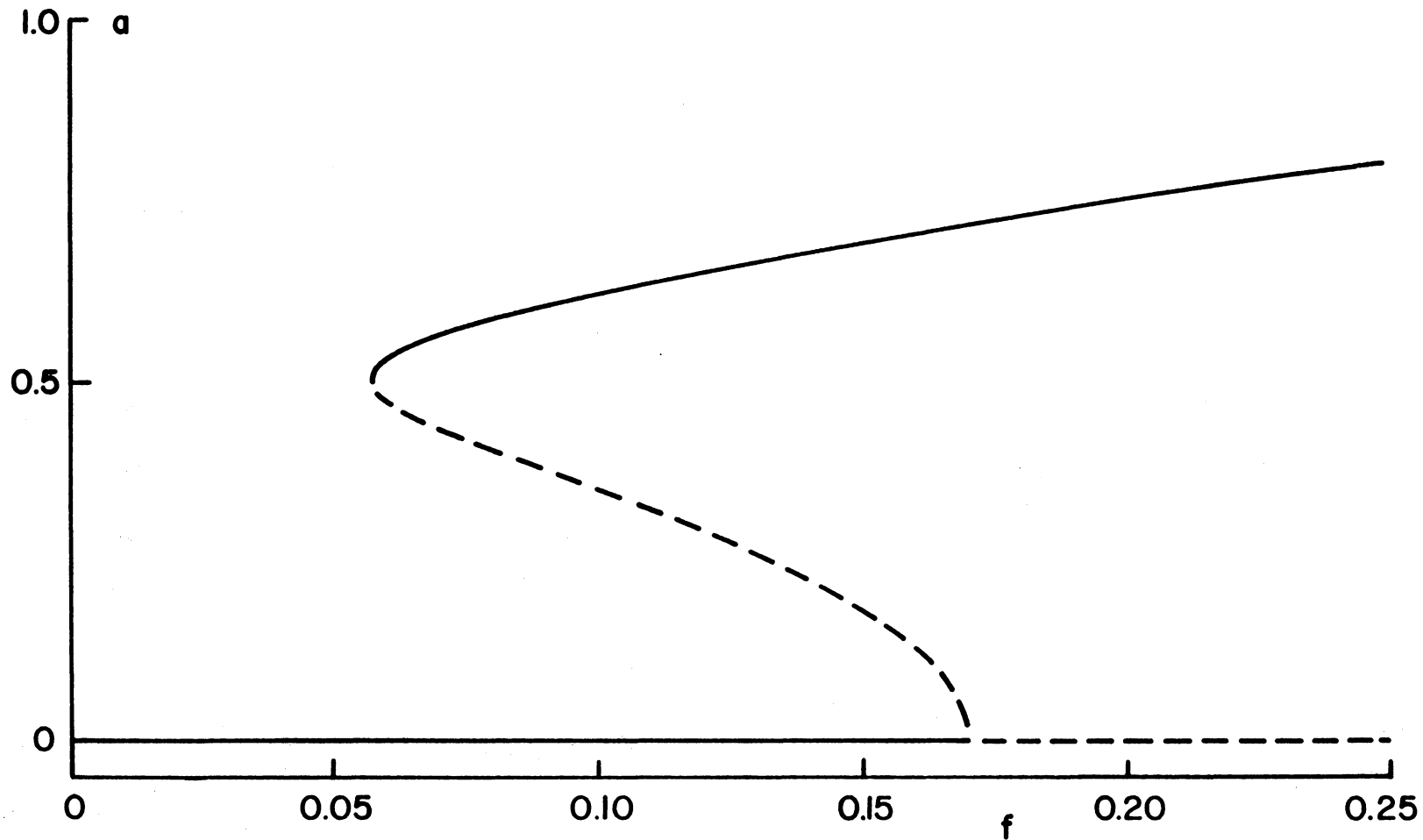


Figure 5.3 Variation of the steady-state amplitude a with the amplitude of excitation f in region III of Figure 5.1: (—) stable, (---) unstable.

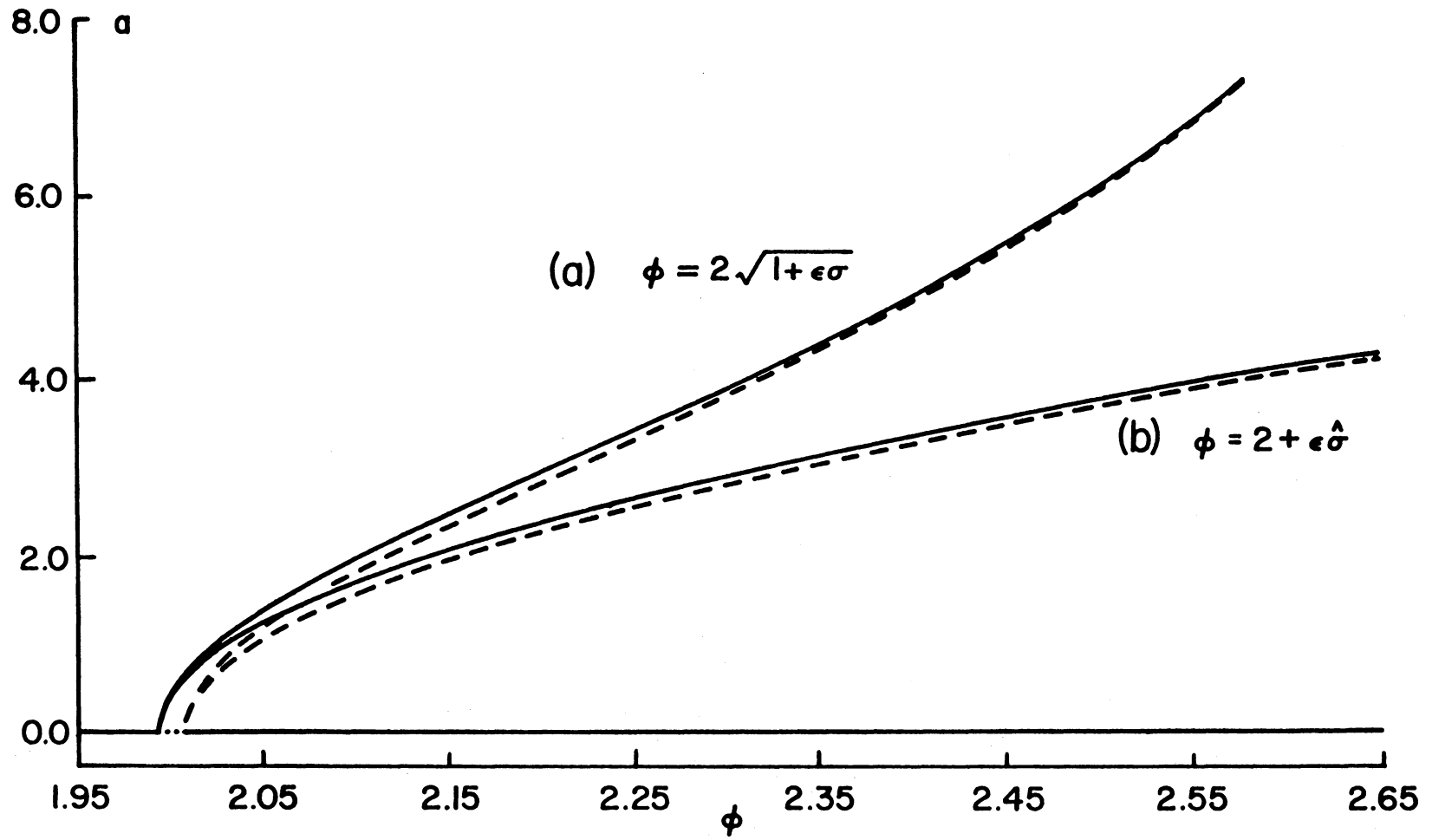


Figure 5.4 Comparison of the frequency response curves predicted by the perturbation theory when the frequency detuning is introduced (a) into the natural frequency as done in this analysis, and (b) into the excitation frequency.

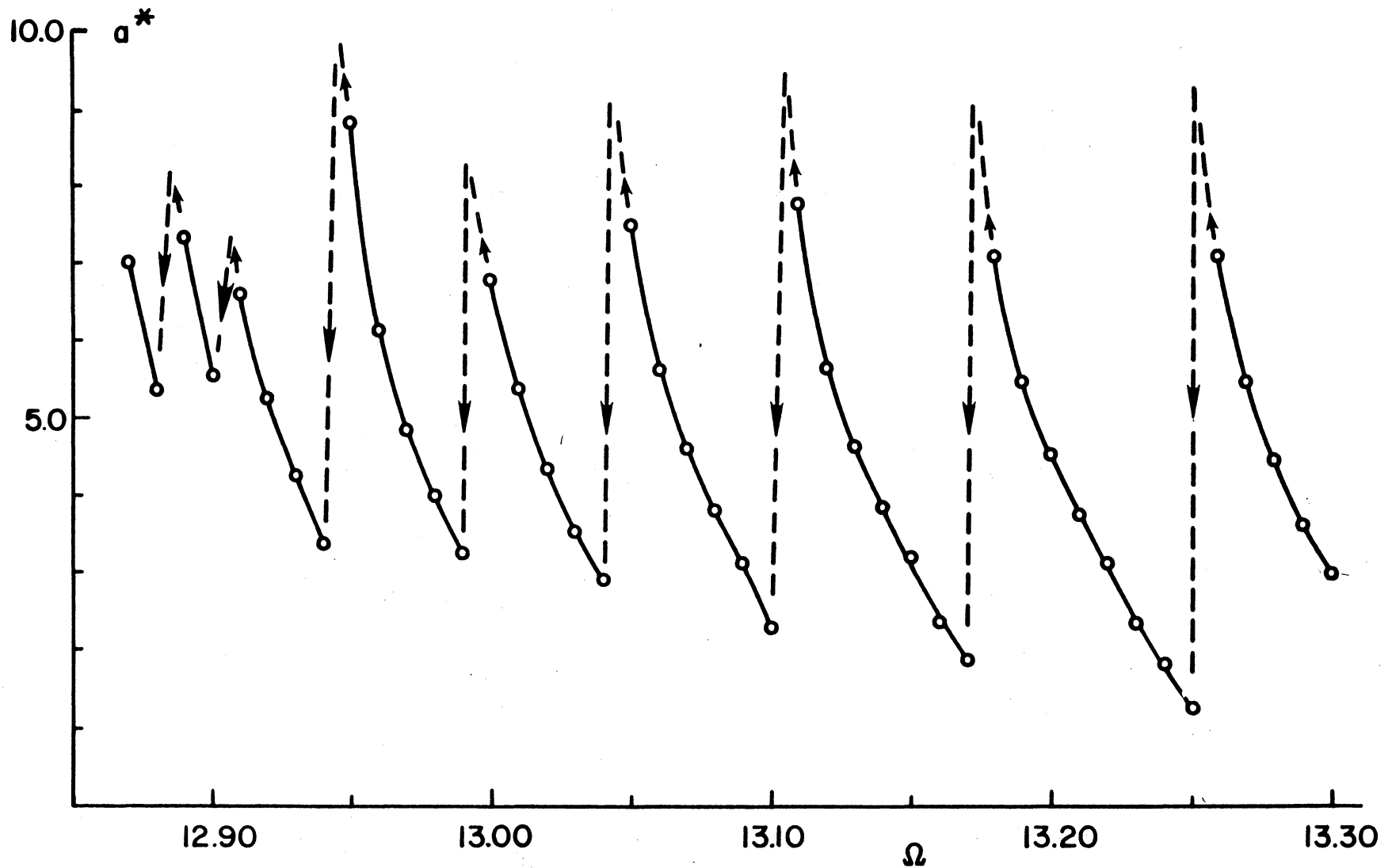


Figure 5.5

Variation of the steady-state amplitude a^* with the frequency of excitation Ω of a metallic beam that later had developed a fatigue crack (shown in Figure 5.6). Each jump down corresponds to a change in the natural frequency caused by crack growth. a^* represents the amplitude of displacement of the reference point on the beam.

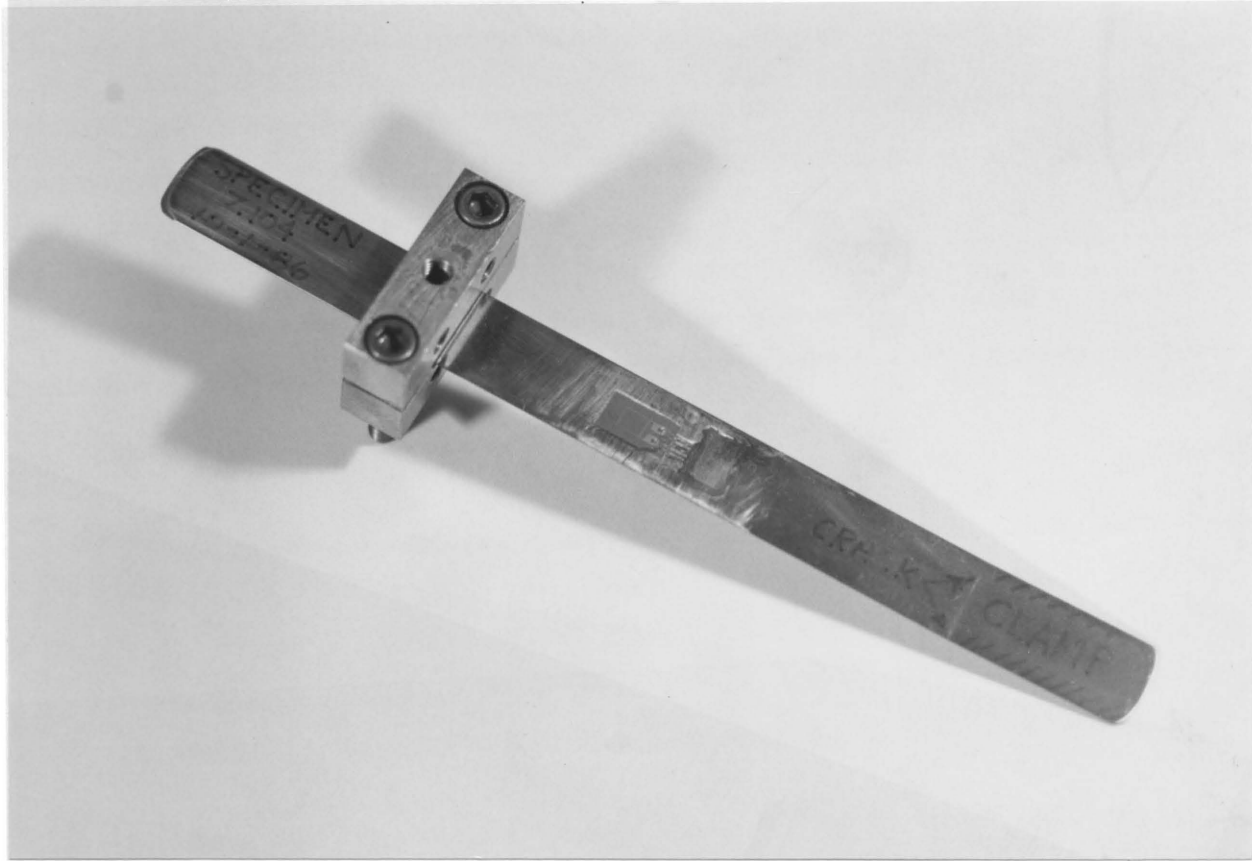


Figure 5.6 Photograph of the first metallic beam that failed by fatigue.

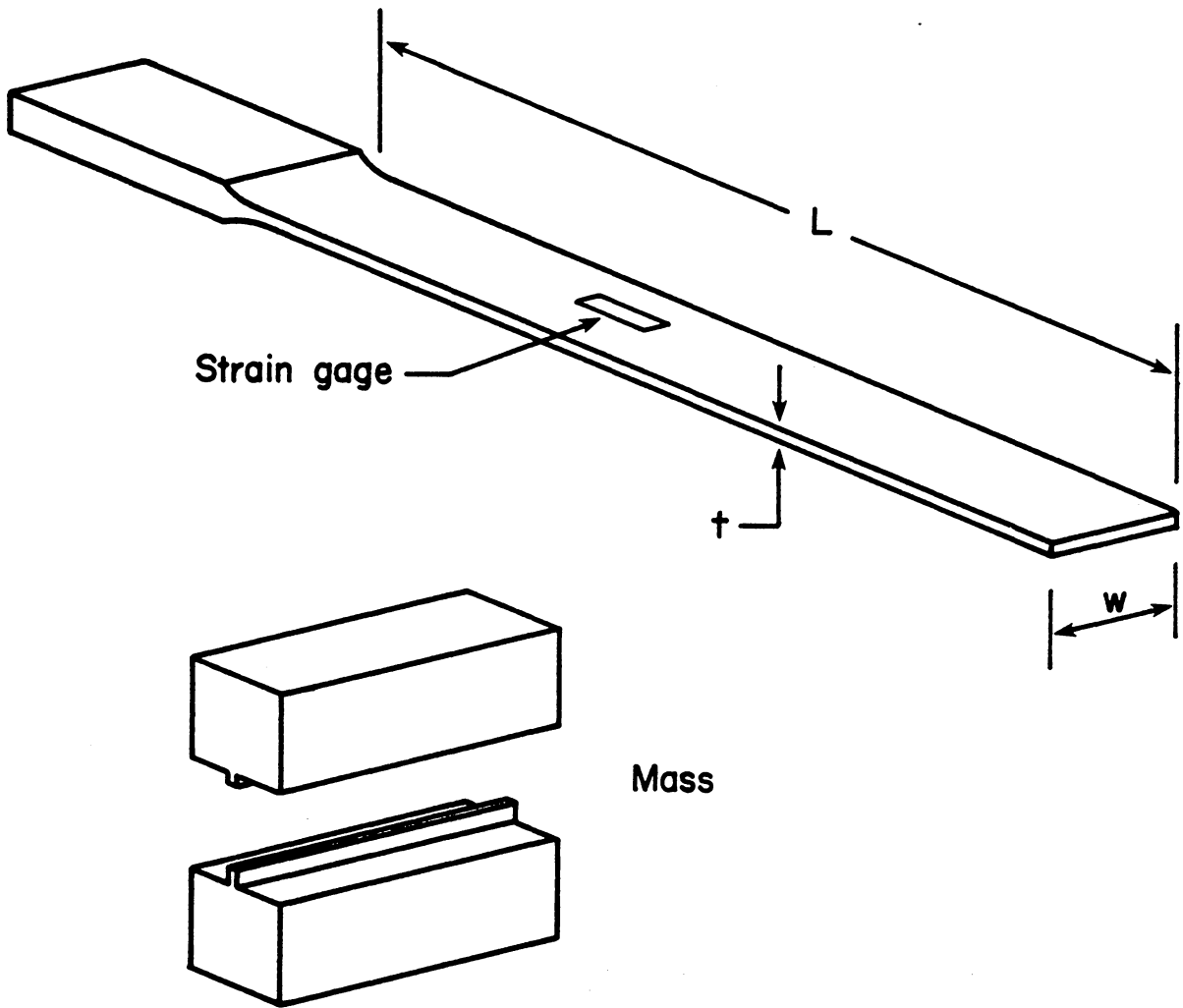


Figure 5.7 Metallic beam specimen made from alloy steel and ground to the dimensions shown.

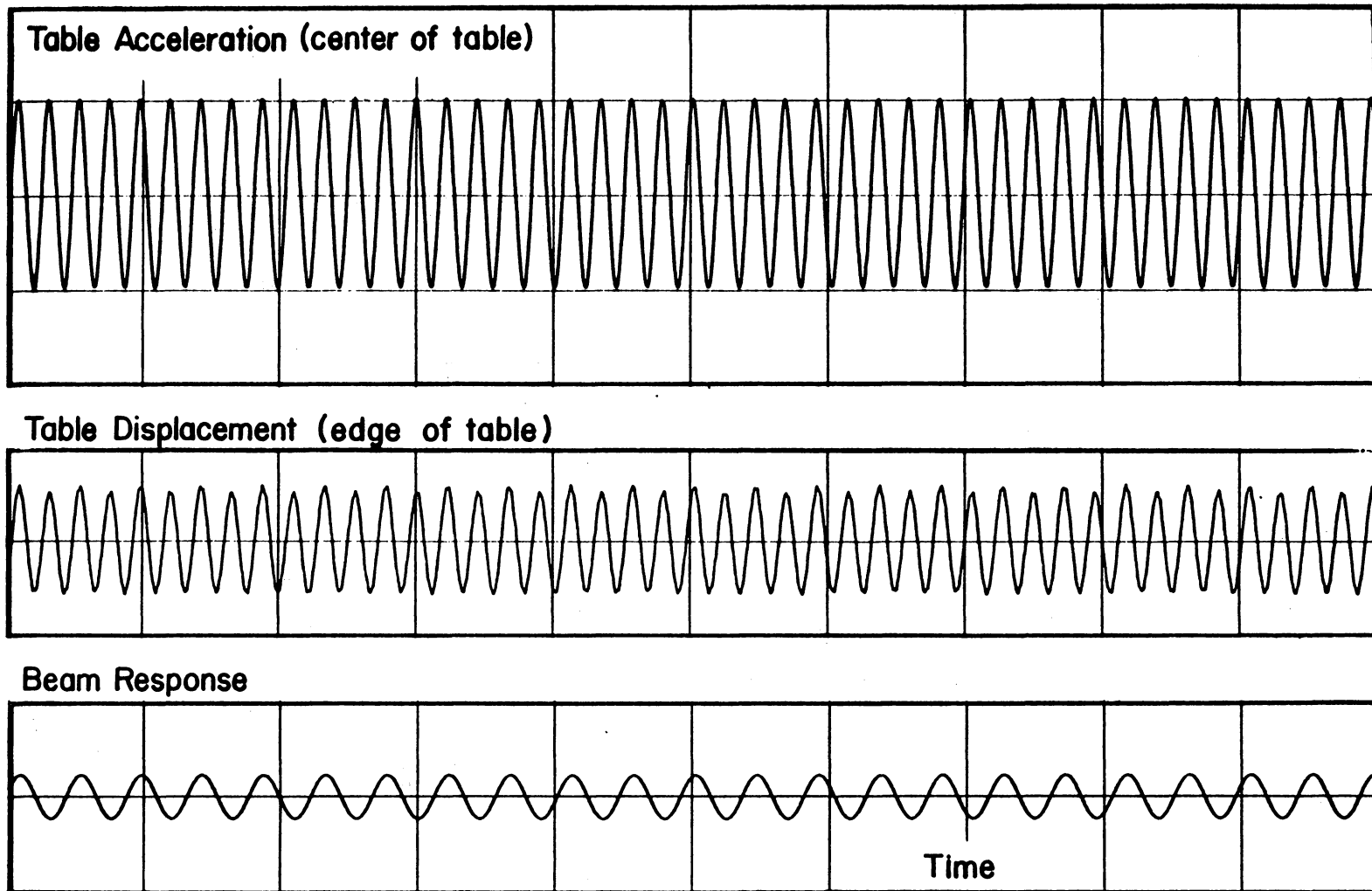


Figure 5.8 Time traces of (a) table acceleration, (b) table displacement, and (c) strain gage (beam displacement) showing the subharmonic distortion to the table motion caused by the large bending moment reaction from the beam; the central location of the accelerometer is immune to the distortion. Note that at the principal parametric resonance the frequency of response is exactly one-half that of the excitation.

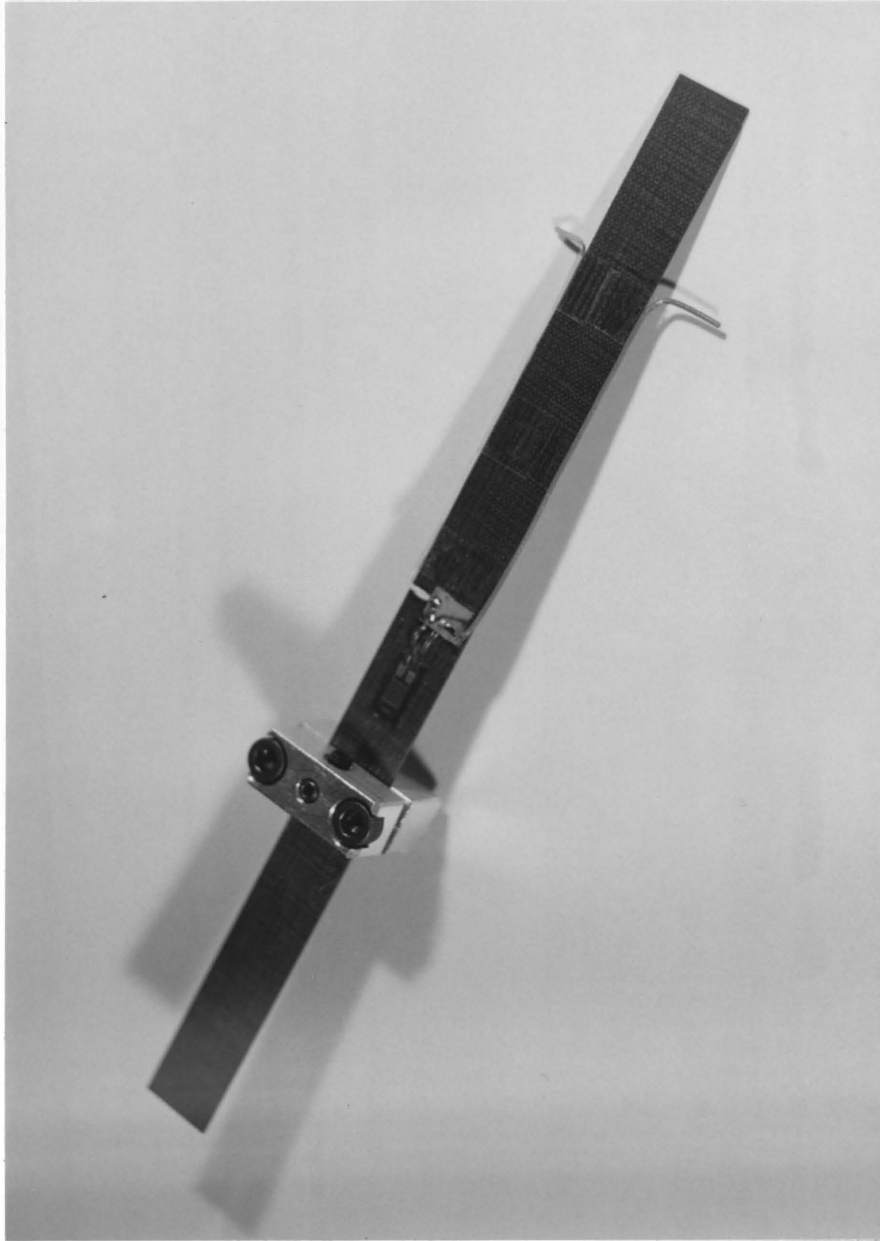


Figure 5.9 Photograph of the composite beam.

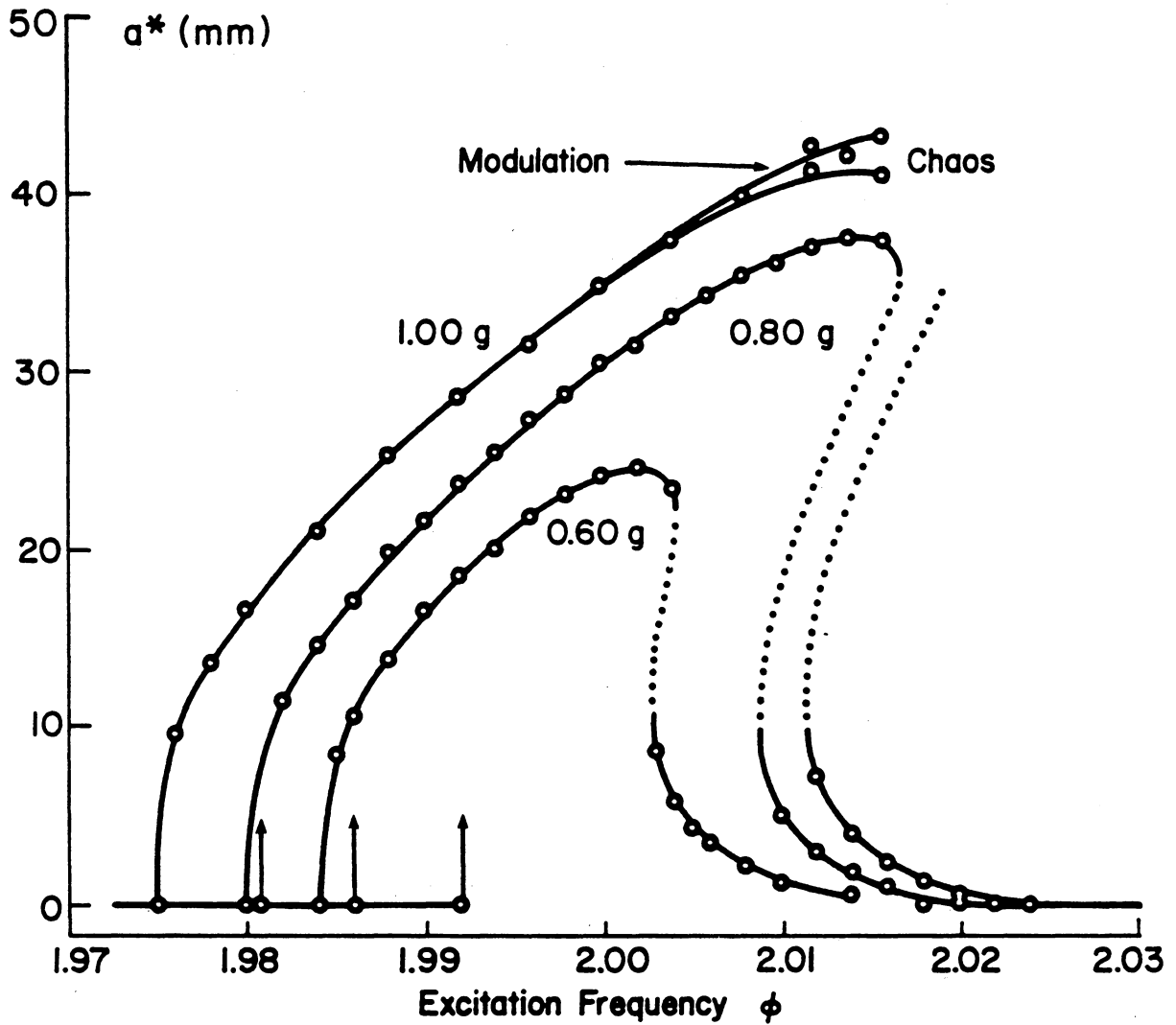


Figure 5.10 Variation of the response amplitude a^* with the frequency of excitation ϕ for three levels of excitation amplitude f of the composite beam. Note that chaotic behavior occurs at the largest amplitude of excitation.

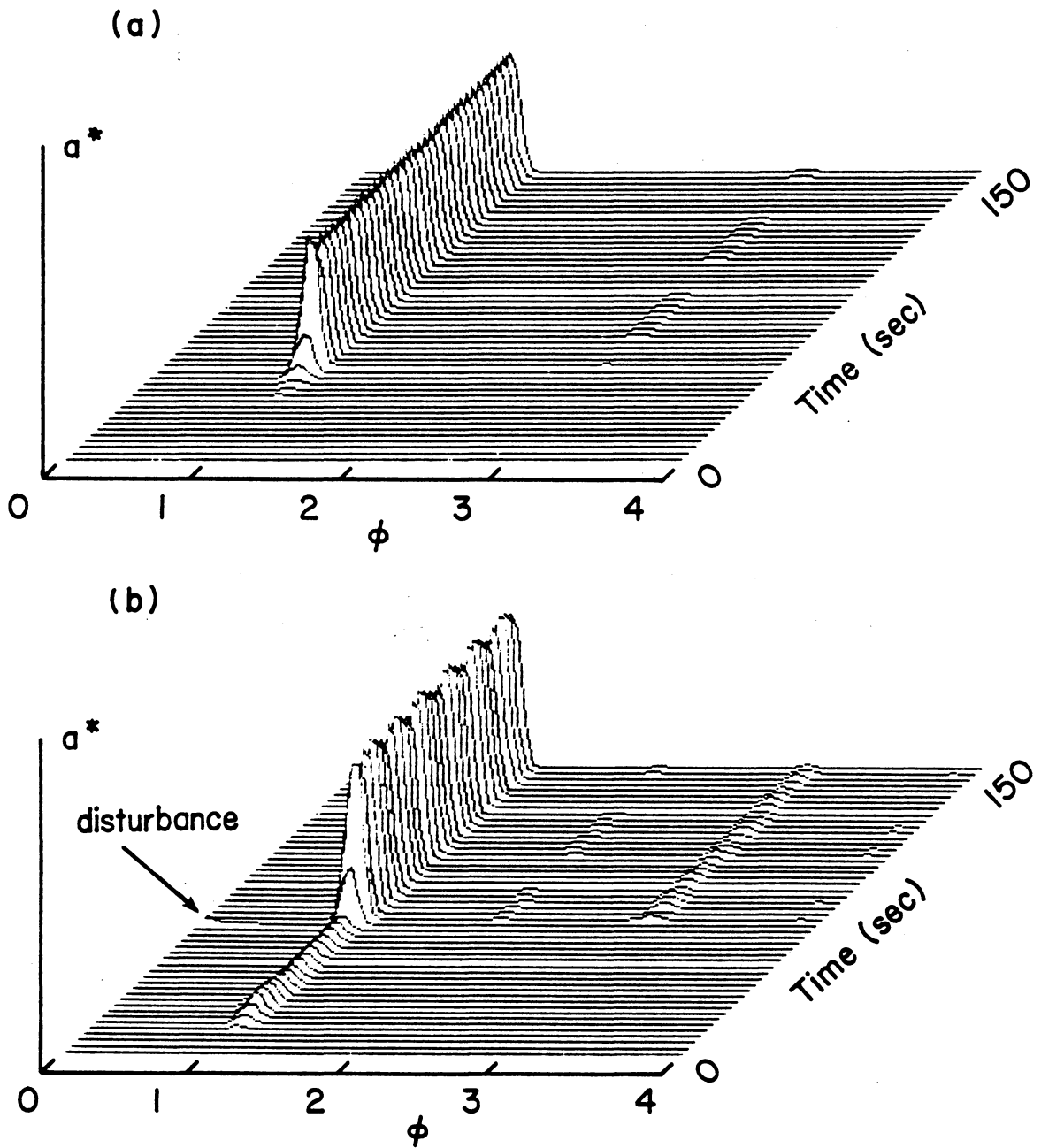


Figure 5.11 Spectral time history of the composite beam to a principal parametric excitation: (a) $\phi = 2.000$, (b) $\phi = 2.013$. Both responses start with the trivial solution. When $\phi = 2.013$ two solutions are possible.

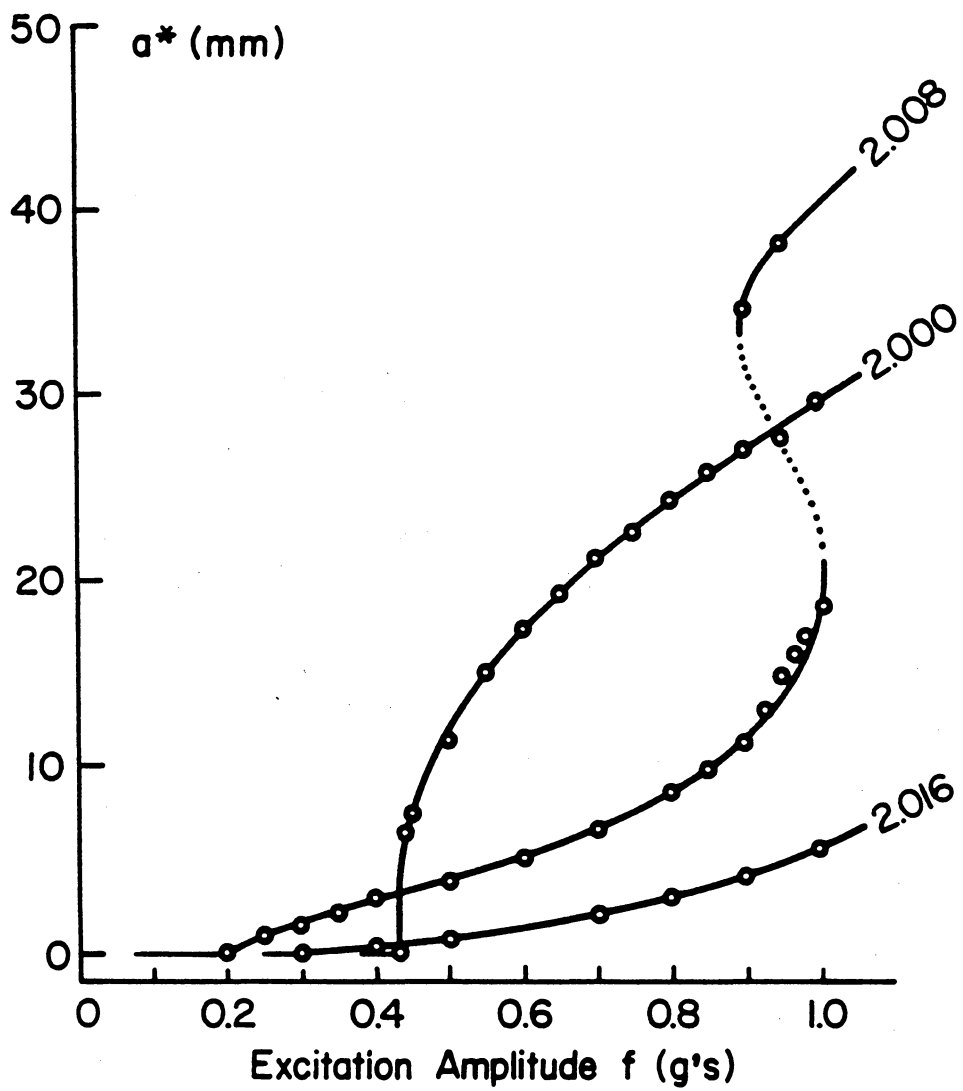


Figure 5.12 Variation of the steady-state amplitude a^* with the amplitude of excitation f of the composite beam for three frequencies of excitation.

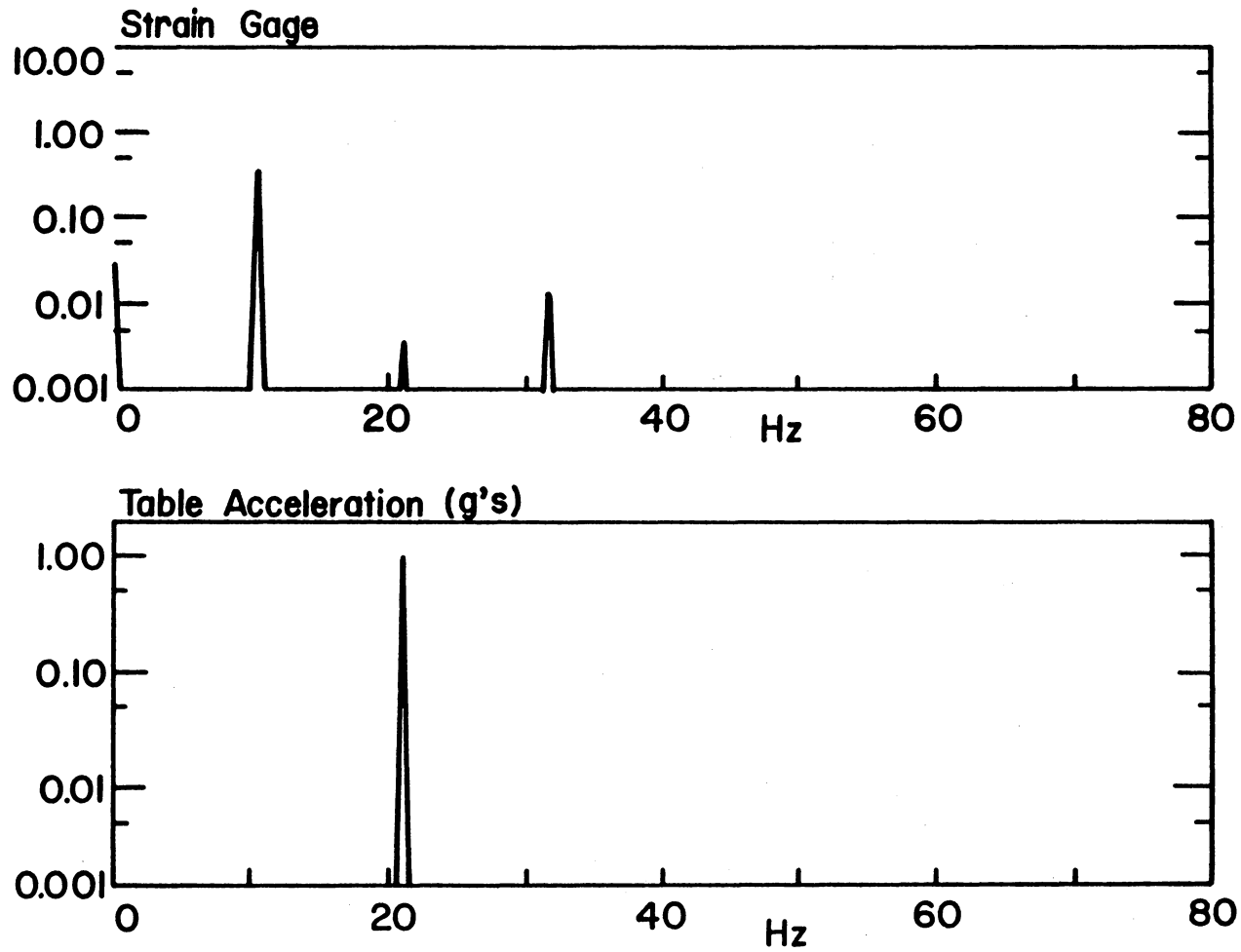


Figure 5.13 Power spectra of the table acceleration and strain gage signals for large amplitude motion of the composite beam. Note the harmonics present in the response.

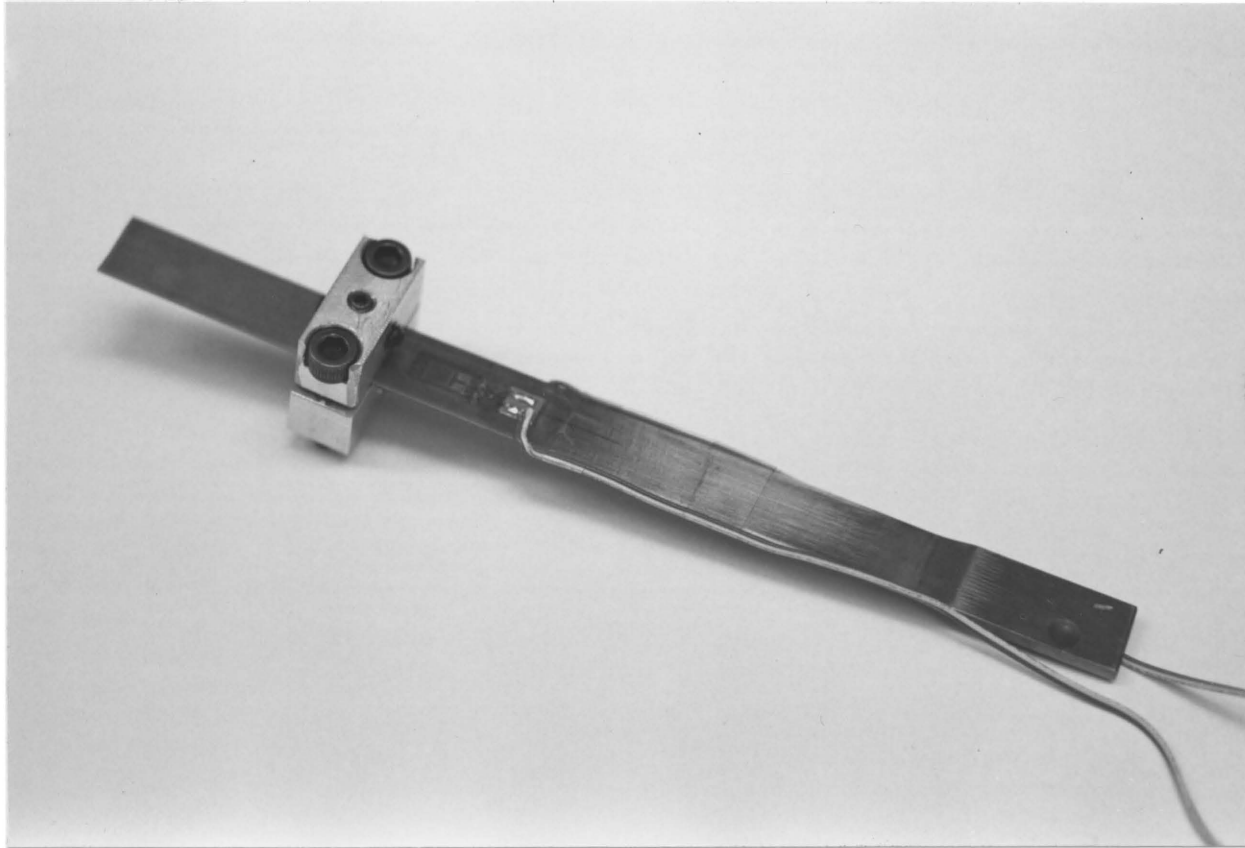


Figure 5.14 Photograph of the precision ground and polished beam after a fatigue crack rendered it useless for further research.

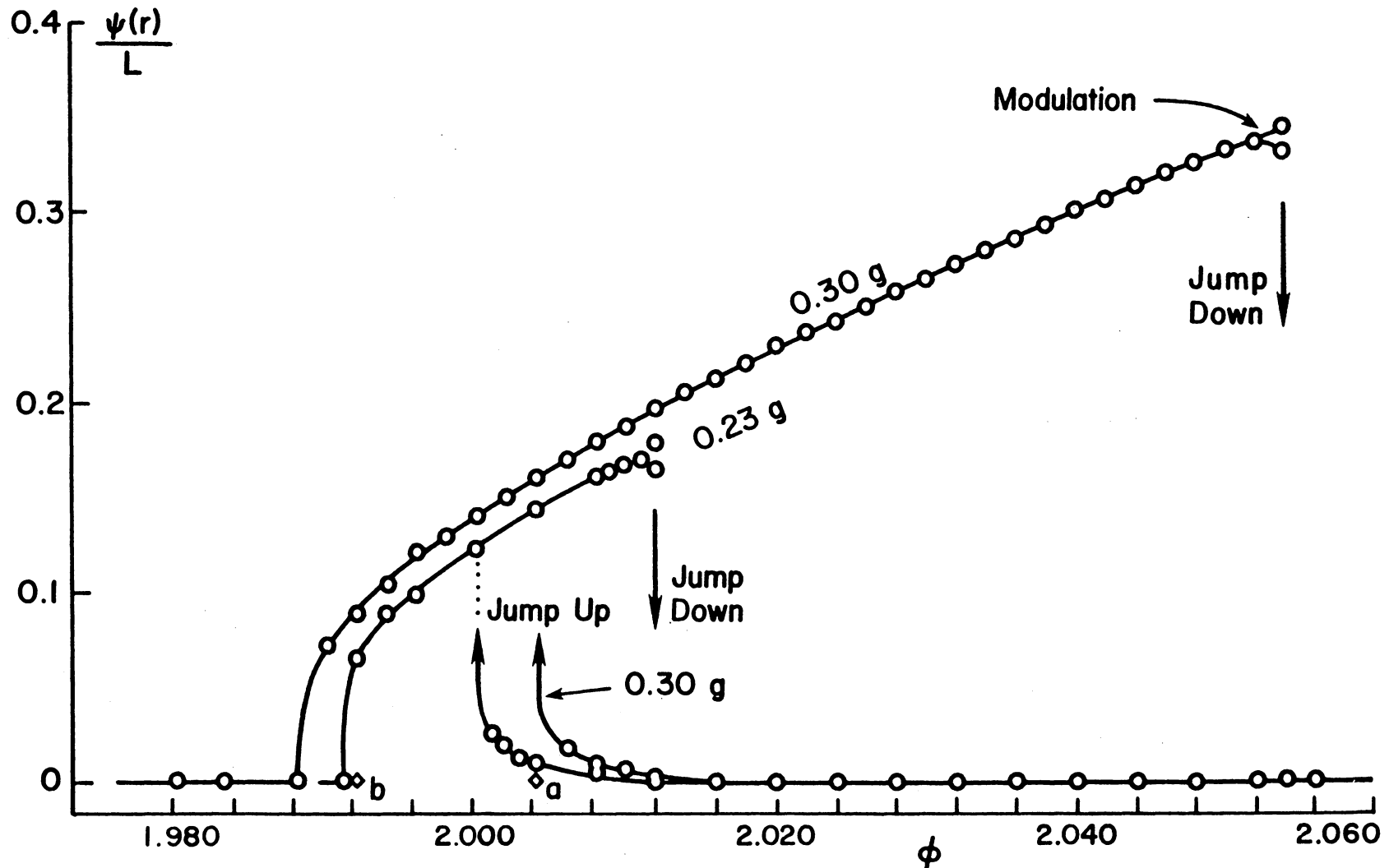


Figure 5.15 Variation of the steady-state amplitude a^* with the frequency of excitation ϕ of the metallic beam shown in Figure 5.13 for two acceleration levels. The diamond at a denotes the loss of stability of the trivial solution for the 0.300 g acceleration level, and the diamond at b for the 0.230 g acceleration level.

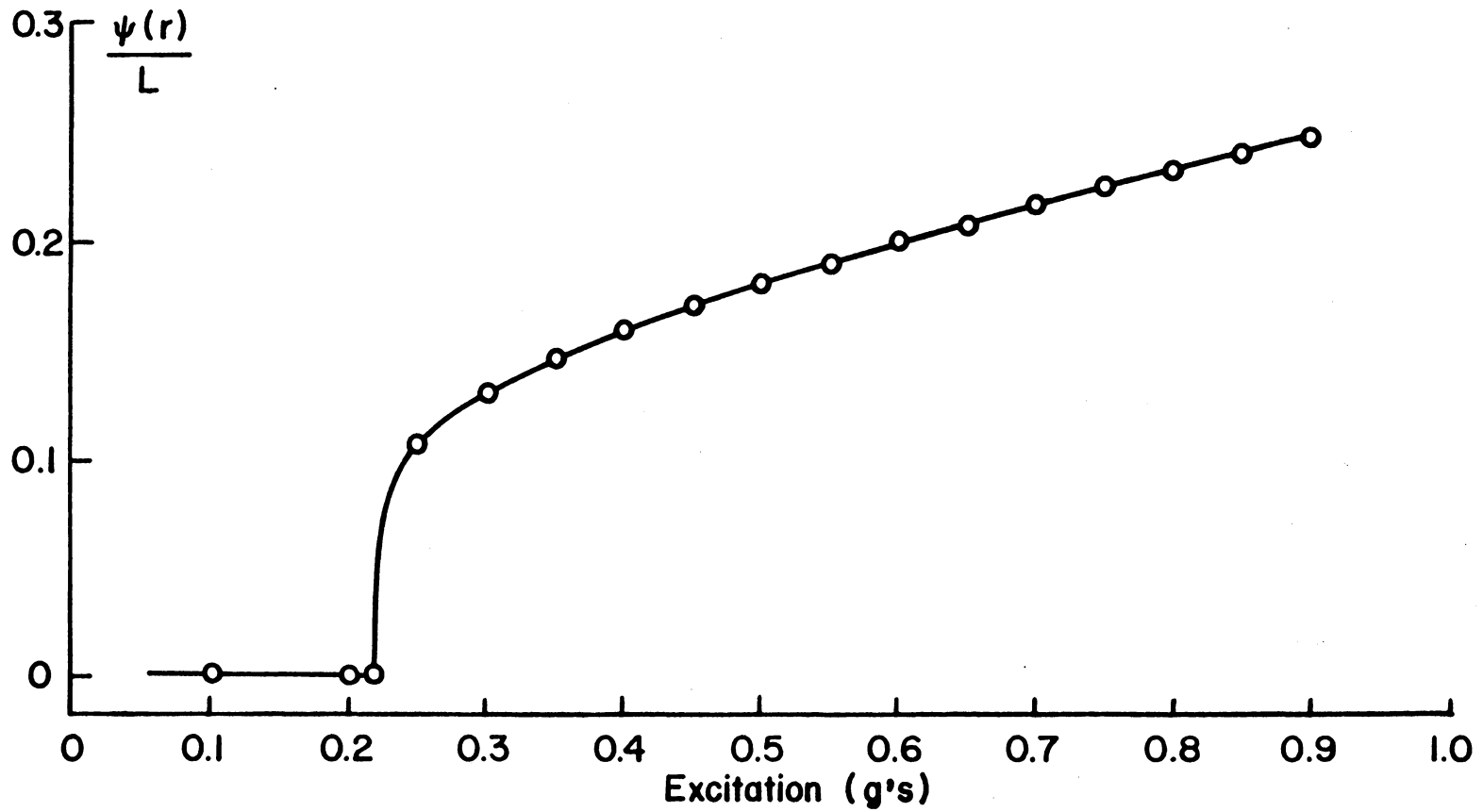


Figure 5.16 Variation of the amplitude a^* with the amplitude of excitation f of the beam shown in Figure 5.14 for $\phi = 2.000$.

CHAPTER VI

COMBINATION RESONANCES IN A TWO-DEGREE-OF-FREEDOM SYSTEM WITH INTERNAL RESONANCES AND QUADRATIC NONLINEARITIES

In the previous chapters we discussed parametric resonances in a SDOF system and introduced MDOF systems in Chapter I. In this chapter we will consider a MDOF system with quadratic nonlinearities. Nayfeh [1983b] investigated a similar internally resonant system and considered the two cases of principal parametric resonance to both modes (i.e., $\Omega \approx 2\omega_1$ and $\Omega \approx 2\omega_2$). Here we will consider 2DOF systems with quadratic nonlinearity and internally resonant subject to a combination resonance of the sum type governed by

$$\ddot{u}_1 + \omega_1^2 u_1 + \varepsilon [2\mu_1 \dot{u}_1 + \delta_1 u_1^2 + 2\delta_2 u_1 u_2 + \delta_3 u_2^2 + 2 \cos \Omega t (f_{11} u_1 + f_{12} u_2)] = 0, \quad (6.1)$$

$$\ddot{u}_2 + \omega_2^2 u_2 + \varepsilon [2\mu_2 \dot{u}_2 + \delta_2 u_1^2 + 2\mu_3 u_1 u_2 + \delta_4 u_2^2 + 2 \cos(\Omega t + \tau) (f_{21} u_1 + f_{22} u_2)] = 0, \quad (6.2)$$

where the ω_n , δ_n , f_{nm} , μ_n , Ω and τ are constants, and ε is a small dimensionless parameter. These equations, when the cubic terms are included, model arches, shells, plates and beams under static loading, and ship motion.

6.1 Multiple Scales Analysis

A first-order uniform solution of (6.1) and (6.2) is sought using the method of multiple scales in the form

$$u_n(t; \varepsilon) = u_{n0}(T_0, T_1) + \varepsilon u_{n1}(T_0, T_1) + \dots, \quad (6.3)$$

where $T_0 = t$ is a fast scale, which is associated with changes occurring at the frequencies ω_n and Ω , and $T_1 = \varepsilon t$ is a slow scale, which is associated with modulations in the amplitudes and the phases resulting from the nonlinearities and parametric resonances. In terms of T_0 and T_1 , the time derivatives become

$$\frac{d}{dt} = D_0 + \varepsilon D_1 + \dots, \quad \frac{d^2}{dt^2} = D_0^2 + 2\varepsilon D_0 D_1 + \dots, \quad (6.4)$$

where $D_n = \partial/\partial T_n$. Substituting (6.3) and (6.4) into (6.1) and (6.2) and equating coefficients of like powers of ε yields, to order ε ,

$$D_0^2 u_{10} + \omega_1^2 u_{10} = 0, \quad (6.5)$$

$$D_0^2 u_{20} + \omega_2^2 u_{20} = 0, \quad (6.6)$$

and to order ε ,

$$\begin{aligned} D_0^2 u_{11} + \omega_1^2 u_{11} = & -2D_0 D_1 u_{10} - 2\mu_1 D_0 D_1 u_{10} - \delta_1 u_{10}^2 - 2\delta_2 u_{10} u_{20} \\ & - \delta_3 u_{20}^2 - 2(f_{11} u_{10} + f_{12} u_{20}) \cos \Omega T_0, \end{aligned} \quad (6.7)$$

$$\begin{aligned} D_0^2 u_{21} + \omega_2^2 u_{21} = & -2D_0 D_1 u_{20} - 2\mu_2 D_0 D_1 u_{20} - \delta_2 u_{10}^2 - 2\delta_3 u_{10} u_{20} \\ & - \delta_4 u_{20}^2 - 2(f_{21} u_{10} + f_{22} u_{20}) \cos(\Omega T_0 + \tau). \end{aligned} \quad (6.8)$$

The general solution of (6.5) and (6.6) can be expressed as

$$u_{10} = A_1(T_1)\exp(i\omega_1 T_0) + \bar{A}_1(T_1)\exp(-i\omega_1 T_0) , \quad (6.9)$$

$$u_{20} = A_2(T_1)\exp(i\omega_2 T_0) + \bar{A}_2(T_1)\exp(-i\omega_2 T_0) , \quad (6.10)$$

where the overbar indicates the complex conjugate and the $A_n(T_1)$ are arbitrary functions of T_1 at this order of approximation; they are determined by imposing the solvability conditions at the next level of approximation.

Substituting (6.9) and (6.10) into (6.7) and (6.8) yields

$$\begin{aligned} D_0^2 u_{11} + \omega_1^2 u_{11} = & -2i\omega_1(A_1' + \mu_1 A_1)e^{i\omega_1 T_0} - \delta_1 A_1^2 e^{2i\omega_1 T_0} \\ & - \delta_3 A_2^2 e^{2i\omega_2 T_0} - 2\delta_2 A_2 A_1 e^{i(\omega_2 + \omega_1)T_0} \\ & - 2\delta_2 A_2 A_1 e^{-i(\omega_2 - \omega_1)T_0} - \delta_1 A_1 \bar{A}_1 - \delta_3 A_2 \bar{A}_2 \\ & - f_{11} A_1 e^{i(\Omega + \omega_1)T_0} - f_{11} A_1 e^{-i(\Omega - \omega_1)T_0} \\ & - f_{12} A_2 e^{i(\Omega + \omega_2)T_0} - f_{12} A_2 e^{-i(\Omega - \omega_2)T_0} + cc , \end{aligned} \quad (6.11)$$

$$\begin{aligned} D_0^2 u_{21} + \omega_2^2 u_{21} = & -2i\omega_2(A_2' + \mu_2 A_2)e^{i\omega_2 T_0} - \delta_2 A_1^2 e^{2i\omega_1 T_0} \\ & - \delta_4 A_2^2 e^{2i\omega_2 T_0} - 2\delta_3 A_2 A_1 e^{i(\omega_2 + \omega_1)T_0} \\ & - 2\delta_3 A_2 A_1 e^{-i(\omega_2 - \omega_1)T_0} - \delta_2 A_1 \bar{A}_1 - \delta_4 A_2 \bar{A}_2 \\ & - f_{21} A_1 e^{i[(\Omega + \omega_1)T_0 + \tau]} - f_{21} A_1 e^{-i[(\Omega - \omega_1)T_0 + \tau]} \\ & - f_{22} A_2 e^{i[(\Omega + \omega_2)T_0 + \tau]} - f_{22} A_2 e^{-i[(\Omega - \omega_2)T_0 + \tau]} + cc , \end{aligned} \quad (6.12)$$

where the cc stands for the complex conjugate of the preceding terms and the prime stands for the derivative with respect to T_1 . Any particular solution of (6.11) and (6.12) contains secular terms and may contain small divisor terms depending on the resonant combinations present.

These combinations are

$\omega_2 \approx 2\omega_1$ or $\omega_1 \approx 2\omega_2$:	two-to-one internal resonance
$\Omega \approx 2\omega_2$:	principal parametric resonance of the second mode
$\Omega \approx 2\omega_1$:	principal parametric resonance of the first mode
$\Omega \approx \omega_2 \pm \omega_1$:	combination parametric resonance of the sum and difference types

The case of simultaneous internal resonance and principal parametric resonance of either mode was investigated by Nayfeh [1983b]. In this chapter, the case of simultaneous internal resonance $\omega_2 \approx 2\omega_1$ and combination parametric resonance $\Omega \approx \omega_2 \pm \omega_1$ is considered. The case of combination resonance of the additive type is treated in detail. Then, the other case can be obtained by simply changing the sign of ω_1 .

To express quantitatively the nearness of these resonances, we introduce the detunings σ_1 and σ_2 according to

$$\omega_2 = 2\omega_1 + \varepsilon\sigma_1 \text{ and } \Omega = \omega_2 + \omega_1 + \varepsilon\sigma_2 \quad (6.13)$$

and write

$$(\omega_2 - \omega_1)T_0 = \omega_1T_0 + \sigma_1T_1, \quad 2\omega_1T_0 = \omega_2T_0 - \sigma_1T_1, \quad (6.14)$$

$$(\Omega - \omega_2)T_0 = \omega_1 T_0 + \sigma_2 T_1, \quad (\Omega - \omega_1)T_0 = \omega_2 T_0 + \sigma_2 T_1. \quad (6.15)$$

Using (6.14) and (6.15), we transform the small-divisor terms arising from $\exp(\pm 2i\omega_1 T_0)$, $\exp[\pm i(\omega_2 - \omega_1)T_0]$, $\exp[\pm i(\Omega - \omega_1)T_0]$ and $\exp[\pm i(\Omega - \omega_2)T_0]$ into terms that produce secular terms. Then, eliminating these secular terms yields the following equations:

$$2i\omega_1(A_1' + \mu_1 A_1) + 2\delta_2 A_2 \bar{A}_1 e^{-i\sigma_1 T_1} + f_{12} A_2 e^{-i\sigma_2 T_1} = 0, \quad (6.16)$$

$$2i\omega_2(A_2' + \mu_2 A_2) + \delta_2 A_1^2 e^{-i\sigma_1 T_1} + f_{21} A_1 e^{-i(\sigma_2 T_1 + \tau)} = 0. \quad (6.17)$$

To analyze the solutions of (6.16) and (6.17), we introduce the polar notation

$$A_n = \frac{1}{2} a_n \exp(i\beta_n), \quad (6.18)$$

separate the result into real and imaginary parts, and obtain

$$a_1' = -\mu_1 a_1 - \frac{\delta_2}{2\omega_1} a_1 a_2 \sin\gamma_1 - \frac{f_{12}}{2\omega_1} a_2 \sin\gamma_2, \quad (6.19)$$

$$a_1 \beta_1' = \frac{\delta_2}{2\omega_1} a_1 a_2 \cos\gamma_1 + \frac{f_{12}}{2\omega_1} a_2 \cos\gamma_2, \quad (6.20)$$

$$a_2' = -\mu_2 a_2 + \frac{\delta_2}{4\omega_2} a_1^2 \sin\gamma_1 - \frac{f_{21}}{2\omega_2} a_1 \sin(\gamma_2 + \tau), \quad (6.21)$$

$$a_2 \beta_2' = \frac{\delta_2}{4\omega_2} a_1^2 \cos\gamma_1 + \frac{f_{21}}{2\omega_2} a_1 \cos(\gamma_2 + \tau), \quad (6.22)$$

where

$$\gamma_1 = \beta_2 - 2\beta_1 + \sigma_1 T_1, \quad \gamma_2 = \sigma_2 T_1 - \beta_2 - \beta_1. \quad (6.23)$$

For steady-state solutions, a_1 and a_2 are constants. Then, it follows from (6.19) and (6.21) that γ_1 and γ_2 are constants. Hence, it follows from (6.23) that

$$\beta_1' = \frac{1}{3} (\sigma_1 + \sigma_2) \text{ and } \beta_2' = \frac{1}{3} (2\sigma_2 - \sigma_1) . \quad (6.24)$$

Consequently, steady-state solutions correspond to the solutions of

$$\mu_1 a_1 = -\frac{\delta_2}{2\omega_1} a_1 a_2 \sin\gamma_1 - \frac{f_{12}}{2\omega_1} a_2 \sin\gamma_2 , \quad (6.25)$$

$$\frac{1}{3} (\sigma_1 + \sigma_2) a_1 = \frac{\delta_2}{2\omega_1} a_1 a_2 \cos\gamma_1 + \frac{f_{12}}{2\omega_1} a_2 \cos\gamma_2 , \quad (6.26)$$

$$\mu_2 a_2 = \frac{\delta_2}{4\omega_2} a_1^2 \sin\gamma_1 - \frac{f_{21}}{2\omega_2} a_1 \sin(\gamma_2 + \tau) , \quad (6.27)$$

$$\frac{1}{3} (2\sigma_2 - \sigma_1) a_2 = \frac{\delta_2}{4\omega_2} a_1^2 \cos\gamma_1 + \frac{f_{21}}{2\omega_2} a_1 \cos(\gamma_2 + \tau) . \quad (6.28)$$

There are two possibilities. First, $a_1 = a_2 = 0$; second, a_1 and $a_2 \neq 0$ and (6.25)-(6.28) yield the following solution:

$$a_1 = \frac{2\omega_1}{\delta_2 \Gamma} \left[\left(\mu_1 + \frac{f_{12}}{2\omega_1} \Gamma \sin\gamma_2 \right)^2 + \left(\frac{1}{3} \sigma_2 + \frac{1}{3} \sigma_1 - \frac{f_{12}}{2\omega_1} \Gamma \cos\gamma_2 \right)^2 \right]^{\frac{1}{2}} , \quad (6.29)$$

$$a_2 = \Gamma a_1 , \quad (6.30)$$

where

$$\Gamma = [-b \pm (b^2 - c)^{\frac{1}{2}}]^{\frac{1}{2}} , \quad (6.31)$$

$$\sin\gamma_2 = d(c_{11}\Gamma^{-1} + c_{12}\Gamma), \quad \cos\gamma_2 = d(c_{21}\Gamma^{-1} + c_{22}\Gamma) , \quad (6.32)$$

$$b = \frac{2c_{11}c_{12}d^2 + 2c_{21}c_{22}d^2 - 1}{2d^2(c_{12}^2 + c_{22}^2)} , \quad c = \frac{c_{11}^2 + c_{21}^2}{c_{12}^2 + c_{22}^2} , \quad (6.33)$$

if $f_{12} \neq f_{21}$, and

$$\Gamma = (-c_{11}/c_{12})^{\frac{1}{2}} , \quad (6.34)$$

$$\gamma_2 = -\frac{1}{2} \tau - \arcsin[(\mu_1 \omega_1 + 2\mu_2 \omega_2 \Gamma^2)/2\Gamma f_{21} \cos \frac{1}{2} \tau] , \quad (6.35)$$

if $f_{12} = 2f_{21}$ provided that $\tau \neq \pm \pi$. When $f_{12} = 2f_{21}$ and $\tau = \pm \pi$, $a_1 = a_2 = 0$ is the only possible solution. The c_{mn} and d are defined as follows:

$$c_{11} = \mu_1 \omega_1 (2f_{21} \cos \tau - f_{12}) - \frac{2}{3} (\sigma_2 + \sigma_1) \omega_1 f_{21} \sin \tau , \quad (6.36)$$

$$c_{12} = 2\mu_2 \omega_2 (2f_{21} \cos \tau - f_{12}) + \frac{4}{3} (2\sigma_2 - \sigma_1) \omega_2 f_{21} \sin \tau , \quad (6.37)$$

$$c_{21} = \frac{1}{3} (\sigma_2 + \sigma_1) \omega_1 (f_{12} + 2f_{21} \cos \tau) + 2\mu_1 \omega_1 f_{21} \sin \tau , \quad (6.38)$$

$$c_{22} = -\frac{2}{3} (2\sigma_2 - \sigma_1) \omega_2 (f_{12} + 2f_{21} \cos \tau) + 4\mu_2 \omega_2 f_{21} \sin \tau , \quad (6.39)$$

$$d = 2(f_{12}^2 - 4f_{21}^2)^{-1} . \quad (6.40)$$

6.2 Stability of Steady-State Solutions

The problem of determining the stability of the trivial steady-state solution $a_1 = a_2 = 0$ is equivalent to the problem of determining the linearized solutions of (6.16) and (6.17); that is,

$$2i\omega_1 (A_1' + \mu_1 A_1) + f_{12} A_2 e^{-i\sigma_2 T_1} = 0 , \quad (6.41)$$

$$2i\omega_2 (A_2' + \mu_2 A_2) + f_{21} A_1 e^{-(\sigma_2 T_1 + \tau)} = 0 . \quad (6.42)$$

Equations (6.41) and (6.42) admit solutions of the form

$$A_1 = a_1 \exp(\lambda T_1 + i\sigma_2 T_1), \quad A_2 = a_2 \exp(\lambda T_1) , \quad (6.43)$$

provided that

$$\lambda^2 + (\mu_1 + \mu_2 + i\sigma_2)\lambda + \mu_1\mu_2 + i\sigma_2\mu_2 - \frac{1}{4}\Lambda e^{-i\tau} = 0 \quad (6.44)$$

or

$$\lambda = -\frac{1}{2}(\mu_1 + \mu_2 + i\sigma_2) \pm \frac{1}{2}[(\mu_2 - \mu_1)^2 - 2i\sigma_2(\mu_2 - \mu_1) - \sigma_2^2 + \Lambda e^{-i\tau}]^{\frac{1}{2}}, \quad (6.45)$$

where $\Lambda = f_{12}f_{21}/\omega_1\omega_2$. Thus, the trivial solution is stable if and only if the real parts of both values of λ are less than or equal to zero; that is, the trivial solution is stable if $(\mu_1 + \mu_2) \geq x$ and unstable if $(\mu_1 + \mu_2) < x$, where x is the real part of the radical in (6.45). The transition curves separating stable from unstable motions correspond to $(\mu_1 + \mu_2) = x$. In this case, the radical in (6.45) is $\mu_1 + \mu_2 + iy$. Hence,

$$\begin{aligned} (\mu_1 + \mu_2 + iy)^2 &= (\mu_2 - \mu_1)^2 - 2i\sigma_2(\mu_2 - \mu_1) - \sigma_2^2 \\ &\quad + \Lambda \cos\tau - i\Lambda \sin\tau. \end{aligned} \quad (6.46)$$

Equating real and imaginary parts in (6.46) yields

$$\begin{aligned} (\mu_1 + \mu_2)^2 - y^2 &= (\mu_2 - \mu_1)^2 - \sigma_2^2 + \Lambda \cos\tau, \\ 2(\mu_1 + \mu_2)y &= -2\sigma_2(\mu_2 - \mu_1) - \Lambda \sin\tau, \end{aligned} \quad (6.47)$$

which upon elimination of y , yields

$$(\mu_2 + \mu_1)^2 [4\mu_1\mu_2 + \sigma_2^2 - \Lambda \cos\tau] = [\sigma_2(\mu_2 - \mu_1) + \frac{1}{2}\Lambda \sin\tau]^2. \quad (6.48)$$

To determine the stability of the nontrivial solutions, we let

$$a_1 = a_{10} + a_{11}, \quad a_2 = a_{20} + a_{21}, \quad (6.49)$$

$$\gamma_1 = \gamma_{10} + \gamma_{11}, \quad \gamma_2 = \gamma_{20} + \gamma_{21}, \quad (6.50)$$

where the a_{n0} and γ_{n0} are solutions of (6.25)-(6.28). Substituting (6.49) and (6.50) into (6.19)-(6.23), using (6.25)-(6.28), and linearizing the resulting equations, we obtain

$$\begin{aligned} a'_{11} = & - \left(\mu_1 + \frac{\delta_2}{2\omega_1} a_{20} \sin \gamma_{10} \right) a_{11} - \frac{\delta_2}{2\omega_1} a_{10} a_{20} \cos \gamma_{10} \gamma_{11} \\ & - \left(\frac{\delta_2}{2\omega_1} a_{10} \sin \gamma_{10} + \frac{f_{12}}{2\omega_1} \sin \gamma_{20} \right) a_{21} - \frac{f_{12}}{2\omega_1} a_{20} \cos \gamma_{20} \gamma_{21}, \end{aligned} \quad (6.51)$$

$$\begin{aligned} \gamma'_{11} = & \left[\frac{\delta_2 a_{10}}{2\omega_2 a_{20}} \cos \gamma_{10} + \frac{f_{21}}{2\omega_2 a_{20}} \cos(\gamma_{20} + \tau) + \frac{f_{12} a_{20}}{\omega_1 a_{10}} \cos \gamma_{20} \right] a_{11} \\ & - \delta_2 \sin \gamma_{10} \left[\frac{a_{10}^2}{4\omega_2 a_{20}} - \frac{a_{20}}{\omega_1} \right] \gamma_{11} - \left[\frac{a_{10}^2}{4\omega_2 a_{20}} + \frac{1}{\omega_1} \right] \delta_2 \cos \gamma_{10} \\ & + \frac{f_{12}}{\omega_1 a_{10}} \cos \gamma_{20} + \frac{f_{21} a_{10}}{2\omega_2 a_{20}} \cos(\gamma_{20} + \tau) \Big] a_{21} \\ & - \left[\frac{f_{21} a_{10}}{2\omega_2 a_{20}} \sin(\gamma_{20} + \tau) - \frac{f_{12} a_{20}}{\omega_1 a_{10}} \sin \gamma_{20} \right] \gamma_{21}, \end{aligned} \quad (6.52)$$

$$\begin{aligned} a'_{21} = & \left[\frac{\delta_2}{2\omega_2} a_{10} \sin \gamma_{10} - \frac{f_{21}}{2\omega_2} \sin(\gamma_{20} + \tau) \right] a_{11} \\ & + \frac{\delta_2}{4\omega_2} a_{10}^2 \cos \gamma_{10} \gamma_{11} - \mu_2 a_{21} - \frac{f_{21}}{2\omega_2} a_{10} \cos(\gamma_{20} + \tau) \gamma_{21}, \end{aligned} \quad (6.53)$$

$$\begin{aligned}
\gamma'_{21} = & - \left[\frac{\delta_2 a_{10}}{2\omega_2 a_{20}} \cos\gamma_{10} + \frac{f_{21}}{2\omega_2 a_{20}} \cos(\gamma_{20} + \tau) - \frac{f_{12} a_{20}}{2\omega_1 a_{10}} \cos\gamma_{20} \right] a_{11} \\
& + \delta_2 \sin\gamma_{10} \left[\frac{a_{10}^2}{4\omega_2 a_{20}} + \frac{a_{20}}{2\omega_1} \right] \gamma_{11} + \left[\frac{\delta_2 a_{10}^2}{4\omega_2 a_{20}} \cos\gamma_{10} \right. \\
& + \frac{f_{21} a_{10}}{2\omega_2 a_{20}} \cos(\gamma_{20} + \tau) - \frac{\delta_2}{2\omega_1} \cos\gamma_{10} - \left. \frac{f_{12}}{2\omega_1 a_{10}} \cos\gamma_{20} \right] a_{21} \\
& + \left[\frac{f_{21} a_{10}}{2\omega_2 a_{20}} \sin(\gamma_{20} + \tau) + \frac{f_{12} a_{20}}{2\omega_1 a_{10}} \sin\gamma_{20} \right] \gamma_{21} . \tag{6.54}
\end{aligned}$$

Thus, the nontrivial solution is stable if and only if the real part of each of the eigenvalues of the coefficient matrix on the right-hand sides of (6.51)-(6.54) is less than or equal to zero.

6.3 Numerical Results and Discussion

Steady-state nontrivial solutions are given by (6.29)-(6.35). For nontrivial steady-state solutions to exist, r as defined in (6.31) must be real; this corresponds to non-negative values of the function $b^2 - c$. The nontrivial responses and their stability are computed and the stability of the trivial solutions are also computed. To verify the steady-state solutions, (6.19)-(6.23) were numerically integrated using a 5th and 6th order Runge-Kutta-Verner (RKV) algorithm. To verify the perturbation results, the governing equations (6.1) and (6.2) were numerically integrated. For all cases investigated, $\mu_1 = \mu_2 = 1$ and $\delta_1 = \delta_2 = \delta_3 = \delta_4 = 1$. The results show cases where there are only nontrivial steady-state solutions, only trivial solutions (quenching), only nonsteady-state solutions, and various combinations of the above. In addition, the results show the jump phenomenon (turning point

bifurcation), modal saturation, Hopf type bifurcation, period doubling bifurcations, and dependence on initial conditions.

6.3.1 Effects of Detuning Parameters σ_1 and σ_2

Figure 6.1 shows typical response curves as a function of the detuning σ_1 due to internal resonance. For the parameters chosen, the trivial solutions and the negative branch of (6.31) are stable. Stable nontrivial solutions exist only for relatively small values of σ_1 near the origin. When σ_1 is away from the region of stable finite-amplitude steady-state solutions, the response is quenched (no resonance) because the only stable solution is trivial. If $f_{21} = 7.00$ in the above example, the response curves are quite similar. However, the trivial response is unstable, so the motion for σ_1 away from the nontrivial steady-state region is a limit cycle solution of (6.19)-(6.23).

Figures 6.2 and 6.3 show typical response curves as a function of the detuning σ_2 due to parametric excitation. For values of τ greater than a critical value τ_c , stable nontrivial steady-state solutions exist only for values of σ_2 away from the origin. However, for small values of τ , the entire negative branch of the nontrivial solution can be stable. These curves and those of Figure 6.1 illustrate the jump phenomenon. It follows from Figure 6.3 that if we start with initial conditions such that the system response is trivial for $\sigma_2 = -10$ corresponding to point a, and then slowly increase the frequency ω by increasing σ_2 , we eventually reach b, the end of the stable region for the trivial solution. After this, the amplitude a_1 of the first mode

jumps up to the nontrivial steady-state value c (corresponding to a limit cycle for the system). Increasing σ_2 further causes both the amplitudes a_1 and a_2 to decrease until point d is reached. A further increase in σ_2 causes the response of the system to bifurcate to a torous (corresponding to limit cycles for a_1 and a_2) until point e is reached. The response of the system to the parametric resonance after point e is now quenched; the only stable steady-state response is trivial. Further increases beyond point f in σ_2 give two possible solutions for the a_n : trivial and nontrivial; if we are on the trivial response for a given σ_2 , disturbances to the system could knock it into a stable steady-state motion corresponding to the nontrivial branch g - h and vice versa. Likewise, if one starts at point h and decreases σ_2 , the response amplitude a_1 will jump from g to f , and follow f - e . After e , a bifurcation takes place and the a_n execute non-constant, nontrivial (nonstationary) motions of limit cycles (corresponding to a torous response of the system). Decreasing σ_2 beyond point d causes the response amplitudes to stabilize on the fixed point d and then follow the curve d - c . Further decreases in σ_2 would cause the system amplitudes to continue on the upper branch, unless a disturbance knocks them down to the trivial solution. It is also possible that disturbances could knock them to yet other stable solutions--limit cycles--if such solutions exist.

6.3.2 Effects of Phase τ

The phase τ is a significant parameter in this problem. Figure 6.4 shows a variation of the response curves with τ . For small values of τ , the steady-state solution given by the negative branch is the only stable response. As τ increases, the trivial solution becomes stable, and the nontrivial solution becomes unstable. Figure 6.4 shows a response curve where an overlap in stable solutions occurs. When this happens, τ_{crit} is given by the maximum value of τ for which stable nontrivial solutions exist. Then, for $\tau > \tau_{crit}$, the response of the system is quenched. Decreasing f_{21} causes the two separate branches to merge and form one closed curve, as shown in Figure 6.5. Since there is no overlapping region in this case, τ_{crit} is given by the trivial stability criterion, and is determined from (6.48). When there is an overlapping region of the stable responses, the jump phenomenon occurs when one reaches the end of the nontrivial stable region. In general, increasing τ stabilizes the trivial response. Depending on the other system parameters, one (but not both) of the nontrivial solutions may be stable also.

To verify the results in Figure 6.4, (6.19)-(6.23) were numerically integrated. In this case, $\tau = 2.0$ corresponds to a point on the stable nontrivial branch and unstable trivial branch, and $\tau = 3.0$ corresponds to a point on the stable trivial branch and unstable nontrivial branch. The results for a_1 in Figure 6.6 show that for the initial conditions used, a_1 and a_2 achieve steady-state nontrivial values when $\tau = 2.0$, and steady-state trivial values when $\tau = 3.0$. If a_2 is

plotted versus a_1 , these two steady-state conditions would appear as fixed points, the latter located at the origin. The governing differential equations (6.1) and (6.2) were numerically integrated for $\tau = 3.0$, when the response of the system is quenched. The results shown in Figure 6.7 verify the nature of the perturbation solution shown in Figures 6.4 and 6.6b. When $\tau = 2.0$, the time history of u_1 and u_2 is similar to Figure 6.8.

Figure 6.4 shows that there is only one stable nontrivial fixed-point solution when τ is small. By using different initial conditions (while fixing all other parameters), we see that (6.19)-(6.23) also admit a limit-cycle solution, as shown in Figure 6.9. This is easily seen by plotting a_2 versus a_1 , as shown in Figures 6.10 and 6.11. With appropriate initial conditions (6.1) and (6.2) yield a stable, non-constant torous response, whose time history is shown in Figure 6.12. This figure also shows the well known modal interaction (i.e., beating). Thus the fixed-point (or steady-state) solution of (6.19)-(6.23) corresponds to a limit-cycle solution of (6.1) and (6.2); the limit-cycle solution of (6.19)-(6.23) corresponds to a torous of (6.1) and (6.2). Figure 6.10, in addition to showing the nontrivial fixed-point and limit-cycle solutions of (6.19)-(6.23), also shows the separatrix dividing the basin of the fixed-point attractor from that of the limit-cycle attractor, for specific values of the initial phases $\gamma_1(0)$ and $\gamma_2(0)$ and phase angle τ . Figure 6.13 shows a trajectory of the system that is attracted to the nontrivial fixed point of Figure 6.9, and Figure 6.11 shows a trajectory of the system that is attracted

to the limit cycle also shown in Figure 6.9. These initial conditions are very close to each other, but on opposite sides of the separatrix. Although γ_1 and γ_2 are specified initially, they vary along the trajectory as governed by (6.19)-(6.23), so they do not remain constant. Figures 6.11 and 6.13 are actually projections of a four-dimensional space whose axes are a_1 , a_2 , γ_1 , γ_2 , with time t being a parameter along the curve, onto the two-dimensional space $a_2 - a_1$, where τ is held constant. This explains why excursions outside the domain of attraction are seen in these figures. When the system arrives at the fixed point, γ_1 and γ_2 become constant, but depending on the exact location within the domain of attraction where the trajectory begins, the values of γ_1 and γ_2 may be incremented by $2n\pi$ in the steady-state condition from those calculated from (6.25)-(6.28) and either (6.32) or (6.35). Figure 6.14 shows the trajectory of the system for $\tau = 3.0$, when the system is quenched; in this case the origin becomes the fixed-point attractor.

6.3.3 Effects of Amplitude of Second Excitation f_{21}

The addition of a second excitation having the amplitude f_{21} has a unique effect on the steady-state response. Figures 6.15-6.17 show typical responses of the system in the presence of moderate primary excitation having the amplitude f_{12} . These three figures combined show how the phase τ changes the nature of the steady-state response; increasing τ causes the two branches to collapse near the critical

point $f_{21} = 2f_{12}$, then break apart, with the left region eventually disappearing. The effects of τ on the trivial stability is minimal.

Figure 6.18 shows response curves, similar to Figure 6.16, for which the stability results were verified by numerically integrating (6.19)-(6.23). The time histories of a_1 for selected points are shown in Figure 6.19. The response a_2 , which is not shown, is proportional to a_1 because $a_2 = \Gamma a_1$. Figures 6.20 and 6.8 show the results of numerically integrating (6.1) and (6.2) with the system parameters corresponding to the two points e and f in Figures 6.18 and 6.19, again verifying the perturbation results.

Although this paper is primarily concerned with the fixed-point solutions of (6.19)-(6.23), limit-cycle solutions have been shown to coexist with the stable fixed-point solutions. Figure 6.21 shows the periodic trajectory corresponding to the solution of (6.19)-(6.23) for point c in Figures 6.18 and 6.19. This solution is a limit cycle whose trajectory is close to the upper fixed-point solution. As we move along the branch b-d in Figure 6.18, the fixed-point solution at b becomes marginally stable, because the real part of the eigenvalue has increased to zero. Increasing f_{21} causes the real part of the eigenvalue to become positive, thus causing the system to experience a Hopf type bifurcation. The amplitudes a_1 and a_2 begin to oscillate in a limit cycle near the fixed point of the upper previously stable steady-state solution, as shown in Figure 6.21. As f_{21} increases (i.e., as it moves away from the stable fixed point b), the trajectory enlarges; however, the trajectory stays near the upper (now unstable) steady-state

solution. As f_{21} approaches the stable fixed point near d , the trajectory size decreases, eventually collapsing to a point, which in this case is the fixed point where stability is again attained, just left of d .

Figures such as 6.3, 6.5 and 6.18 show that there are regions where no steady-state solutions exist. Unsteady solutions in the region between points x and y in Figure 6.18 have limit-cycle trajectories which experience a period doubling bifurcation. As f_{21} increases from x to y the period of the limit cycle slowly increases. However, at a critical value f_{21}^* of f_{21} , the trajectory requires two orbits to complete one period. This is barely seen in the amplitude-time curves in Figure 6.22. The bifurcated motion has every other peak slightly reduced and the little hump between peaks is distorted in every other valley. Thus, it takes two of the previous cycles to complete one cycle in the bifurcated response. The bifurcation is easily seen when plotted in the plane $a_2 - a_1$, as shown in Figure 6.23. As f_{21} increases to point y , the system bifurcates again because steady-state solutions exist, and one of them is stable.

Figure 6.24 shows typical response curves in the presence of a strong excitation of the first mode. There are no stable finite-amplitude steady-state solutions; the trivial solution is stable for only small values of f_{21} .

Figure 6.25 shows the unique phenomenon associated with the addition of an excitation having the amplitude f_{21} to the second mode. For small levels of excitation f_{12} of the first mode, the amplitude a_2

of the stable nontrivial response of the second mode reaches a constant value when $f_{21} \geq f_{\text{crit}}$, where f_{crit} is the threshold of existence of stable nontrivial solutions when varying f_{21} . Increasing f_{21} does not increase a_2 above this constant value; it has become saturated.

Instead, the energy exciting the second mode causes a large increase in a_1 to occur. This is known as the saturation phenomenon. If one were to perform an experiment in which f_{21} were slowly increased from zero, the jump phenomenon would occur at the end of the stable trivial response region. Both a_1 and a_2 would jump up to their respective steady-state values. Further increases in f_{21} would simply increase a_1 and not a_2 .

For values of $f_{12} \ll 1$ and $\tau = 2.094$, the two solutions (one stable and one unstable) for a_2 are so close to each other that they appear as one in Figure 6.26. The characteristics of the motion, however, remain the same.

To examine regions of nontrivial responses in general, (6.31)-(6.35) were solved for the transition curves separating existence and non-existence of nontrivial responses. Typical curves are shown in Figure 6.27. Comparing Figures 6.15-6.17 and 6.27, we can see where each curve (from Figures 6.15-6.17) would be positioned in Figure 6.27.

The accuracy of the perturbation solution for selected parameters is shown in Table 6.1. Since the perturbation solution is based on small values of ϵ , the improved accuracy with smaller ϵ is expected. The error decreases for small values of f_{21} . When $f_{12} = 7.00$ and $f_{21} = 1.04$, the perturbation results give $a_1 = 4.52$ and $a_2 = 3.62$. For

$\epsilon = 0.001$, numerical integration yields $a_1 = 4.59$ and $a_2 = 3.66$. These correspond to errors of 1.5% and 1.1% respectively.

6.4. Chapter Summary

The method of multiple scales was used to obtain a uniform first-order solution for the response of a two-degree-of-freedom system with quadratic nonlinearities to a combination parametric resonance in the presence of a two-to-one internal resonance. Steady-state solutions were obtained, and it was shown that the results qualitatively describe the system response for the parameters chosen.

The results show that detuning the internal resonance (increasing $|\sigma_1|$) eliminates nontrivial steady-state responses. In other words, steady-state responses exist only for a nearly perfectly tuned system. If the system parameters were such that the trivial response is stable, the response of the system is quenched for σ_1 outside the nontrivial response region.

Detuning the parametric resonance (increasing $|\sigma_2|$) has the opposite effect on the system because it yields both trivial and nontrivial stable steady-state solutions. The examples shown here illustrate that the response of the system can be quenched for appropriate system parameters.

The phase of second mode excitation τ , when increased, stabilizes the trivial response. Depending on the system parameters, it is shown that there may also be a nontrivial response that is stable. In the absence of a stable nontrivial solution, the response of the system can

be quenched when $\tau \geq \tau_{\text{crit}}$. These results can be used by design engineers to reduce or eliminate vibration of systems modelled by these equations. For example, if f_{21} is large enough, by simply detuning the two modes, the steady-state response could be quenched if a nonsteady-state solution does not exist (see Figure 6.1). Similarly, if the phase τ can be adjusted, we have seen (Figures 6.4 and 6.5) that an appropriate choice can also quench the steady-state response.

The amplitude f_{21} of the second excitation when increased, produces stable nontrivial steady-state solutions and simultaneously unstable trivial solutions. When f_{12} is small, increasing f_{21} causes the second mode to become saturated when $f_{21} \geq f_{\text{crit}}$, causing the first mode response to increase instead. This is another control that can be used to advantage by a designer. If the system is tuned sufficiently, the second mode will become saturated. This will limit the maximum amplitude of the second mode (at the expense of the first mode, of course), regardless of the magnitude of the excitation amplitude of the second mode. Hence, the first mode acts as a vibration absorber to the second mode.

In addition to the steady-state solutions, other periodic solutions are predicted and shown to exist by the amplitude-phase modulation equations (6.19) - (6.23). The motion experiences a Hopf bifurcation as transition from a stable fixed-point response to a limit cycle response occurs, if there exists an unstable fixed-point solution. This bifurcation occurs as the real part of both nontrivial eigenvalues become positive. In the region where no steady-state solutions are

shown to exist, the limit cycle itself is shown to experience a period doubling bifurcation. Some of these unsteady-state solutions have a smaller maximum amplitude. For example, Figure 6.9 shows that the maximum amplitude of the limit cycle is lower than the steady-state amplitude of the first mode and higher than the steady-state amplitude of the second mode. If the designer wants to reduce the first mode, he can adjust the initial conditions to achieve the limit cycle.

The perturbation solution was verified by numerically integrating the governing differential equations. Although the first-order perturbation solution characterizes the system response extremely well, it suffers in accurately predicting the magnitudes a_1 and a_2 of the steady-state response when either mode is strongly excited and when relatively large values of ε are used. When both the excitation and ε are small, the perturbation solution is within 1.5% of the numerically obtained results.

The accuracy of the perturbation solution to large excitations can be improved by developing a uniform second-order solution. We must then include the cubic nonlinear terms in the governing differential equations. This is also true if we wish to transform the initial conditions of the averaged equations $(a_1(0), a_2(0), \gamma_1(0), \gamma_2(0))$ into initial conditions for the original equations $(u_1(0), \dot{u}_1(0), u_2(0), \dot{u}_2(0))$.

The uniform first-order solution can be used to investigate the effects of the damping coefficients μ_1 and μ_2 and to extend the present analysis to the combined effects of several system parameters such as

small σ_1 and large σ_2 . The other stable limit-cycle solutions can be analyzed along with the domains of initial conditions that lead to the various solutions; this can be accomplished with projections of the phase spaces in various combinations of $a_1, a_2, \gamma_1, \gamma_2, u_1, \dot{u}_1, u_2$ and \dot{u}_2 . Figure 6.27 shows only the domains of existence of steady-state solutions, but it does not indicate the stability of such solutions. Of interest would be the domains of stable trivial and nontrivial solutions. However, the large number of system parameters certainly complicates the analysis and the concise presentation of the results.

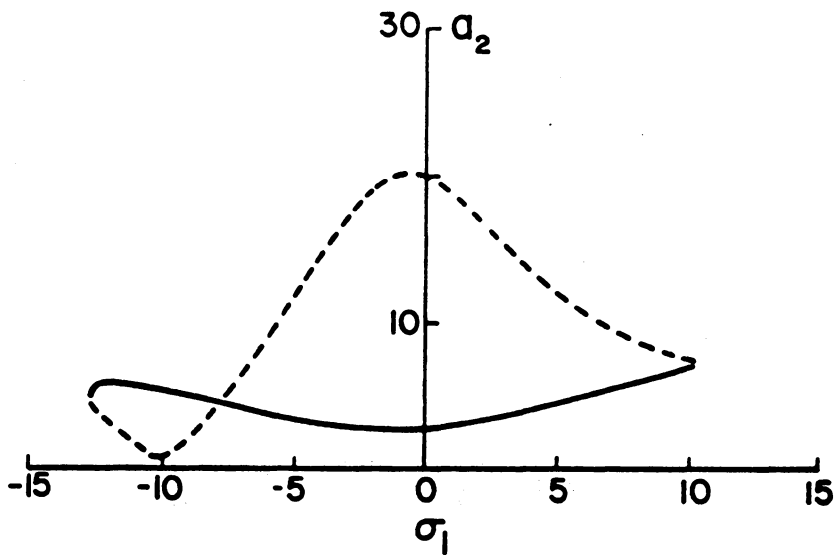
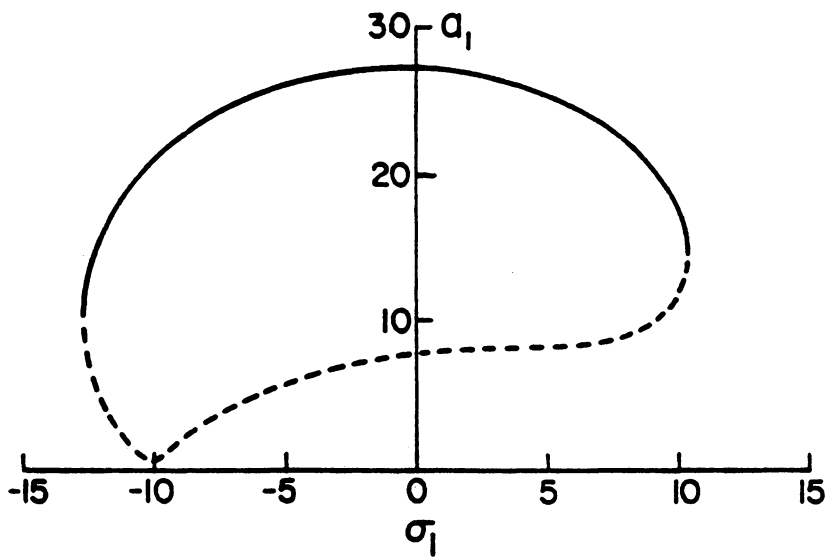


Figure 6.1

Variation of the steady-state response amplitudes a_1 and a_2 with the internal resonance detuning parameter σ_1 : (—) stable, (---) unstable, $\tau = 0.2618$ radians, $\sigma_2 = 0$, $f_{12} = 7.00$, $f_{21} = 14.00$. Note that for large values of σ_1 , the response of the system to parametric resonance is quenched. If $f_{21} = 7.00$, the response curves are similar, but the trivial response becomes unstable.

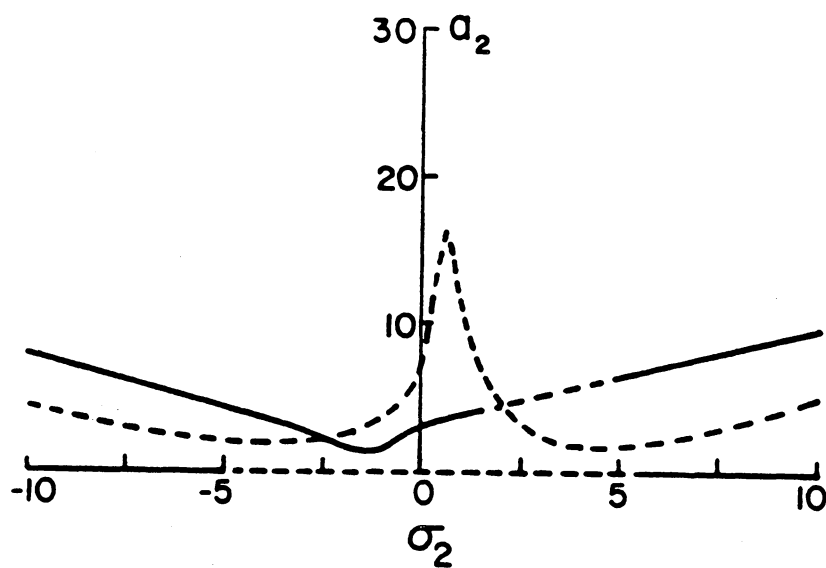
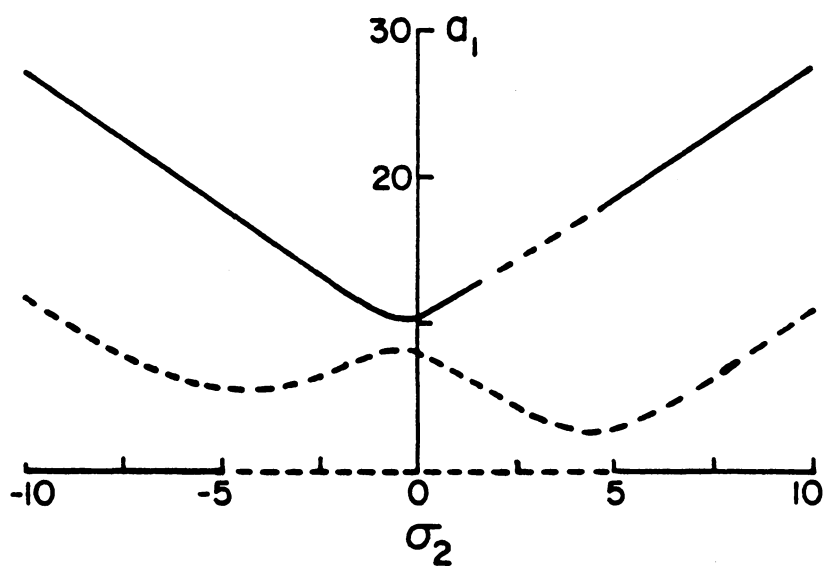


Figure 6.2 Steady-state response curves a_1 and a_2 vs. the detuning parameter σ_2 due to parametric resonance: (—) stable, (---) unstable, $\tau = 0.785$ radians, $\sigma_1 = 0$, $f_{12} = 7.00$, $f_{21} = 6.00$.

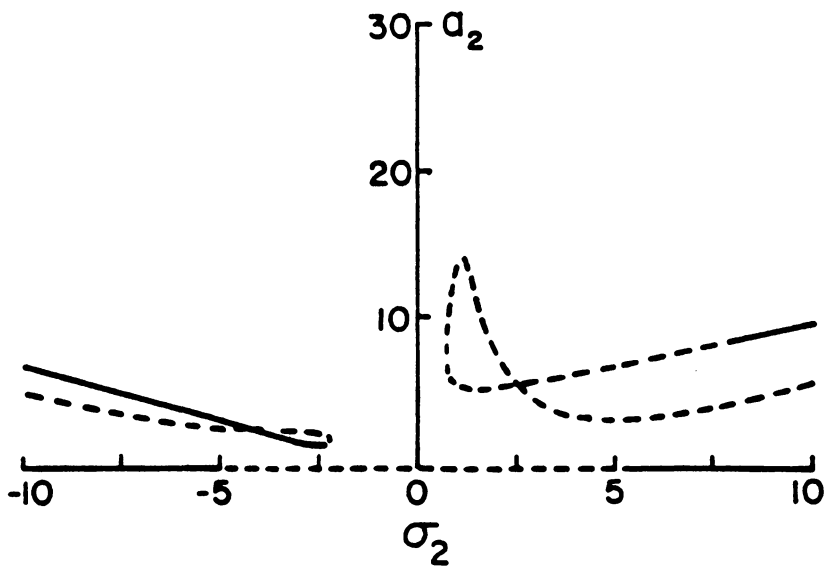
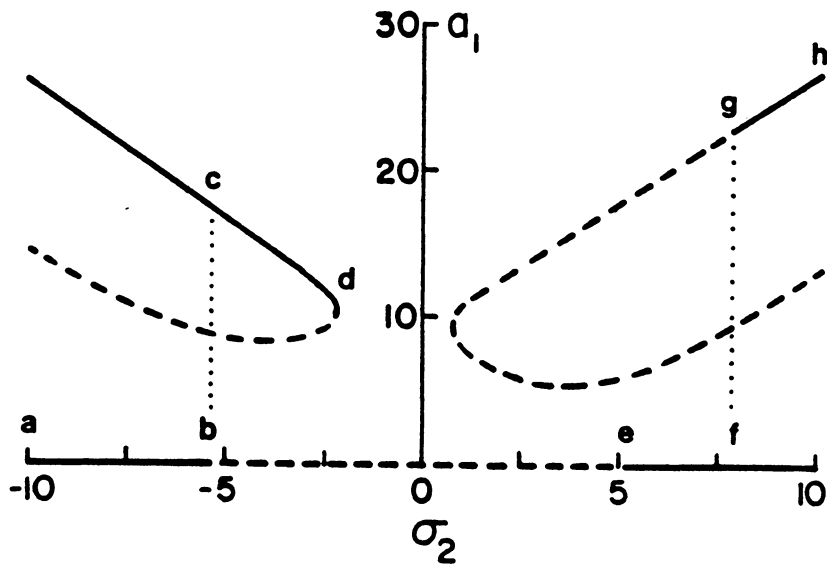


Figure 6.3 Steady-state response curves a_1 and a_2 vs. the detuning parameter σ_2 due to parametric resonance: (—) stable, (---) unstable, $\tau = 1.309$ radians, $\sigma_1 = 0.0$, $f_{12} = 7.00$, $f_{21} = 6.00$. Note that increasing τ causes the two continuous separate branches in Figure 6.2 to touch, and break apart, leaving a region where no steady-state solutions exist.

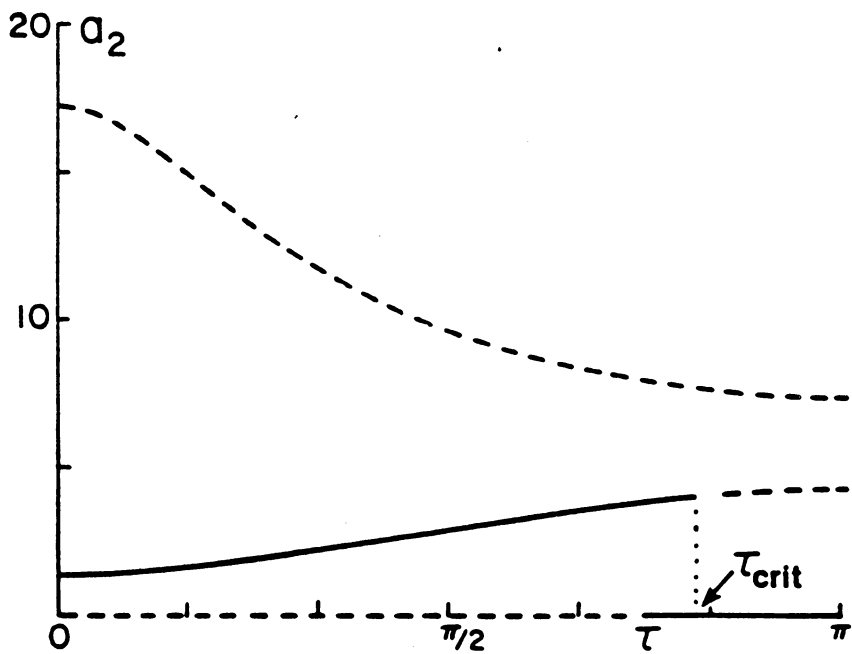
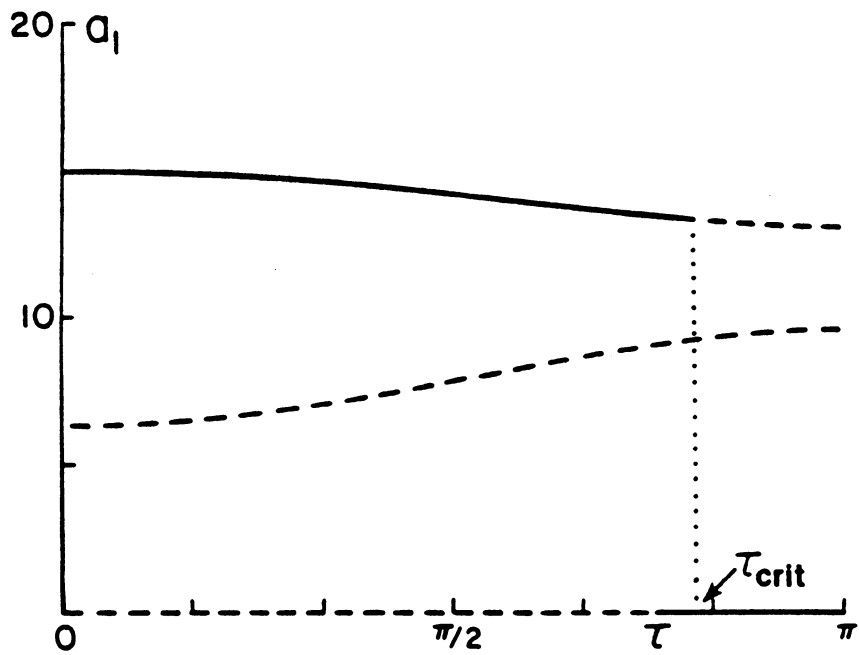


Figure 6.4

Variation of the steady-state response curves with the phase angle τ : (—) stable, (---) unstable, $\sigma_1 = \sigma_2 = 0$, $f_{12} = 7.00$, $f_{21} = 7.86$. For $\tau \geq \tau_{crit}$, only the trivial solution is stable; therefore the system is quenched.

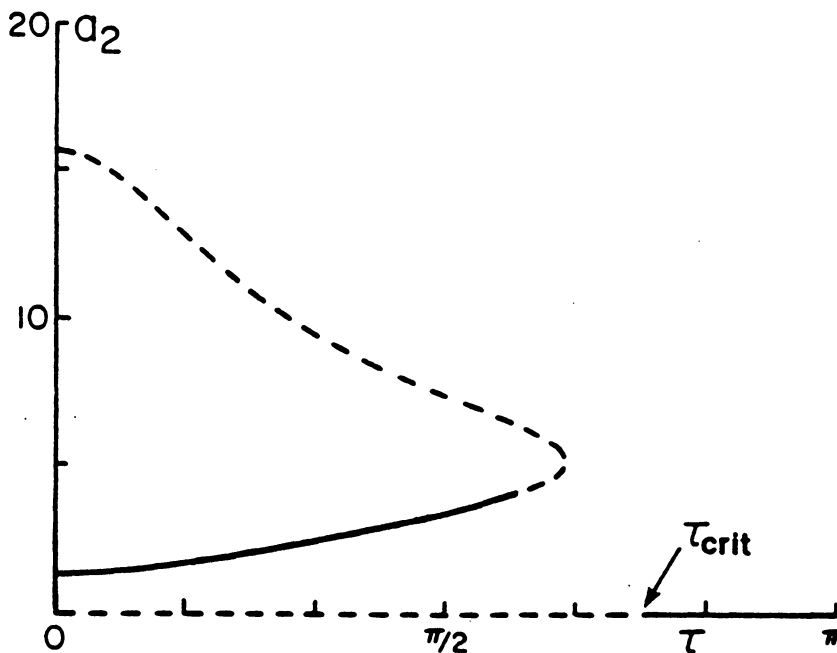
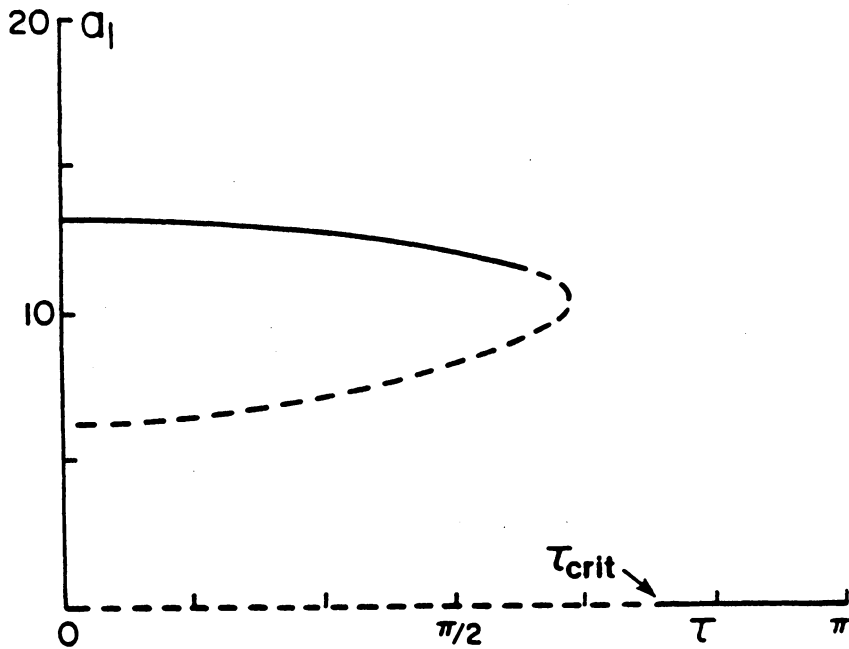


Figure 6.5 Variation of the steady-state response curves with the phase angle τ : (—) stable, (---) unstable, $\sigma_1 = \sigma_2 = 0.0$, $f_{12} = f_{21} = 7.00$. Note that for $\tau \geq \tau_{crit}$, the response of the system to the parametric resonance is quenched. Compare this figure with Figure 6.4 and note the effect of decreasing f_{21} .

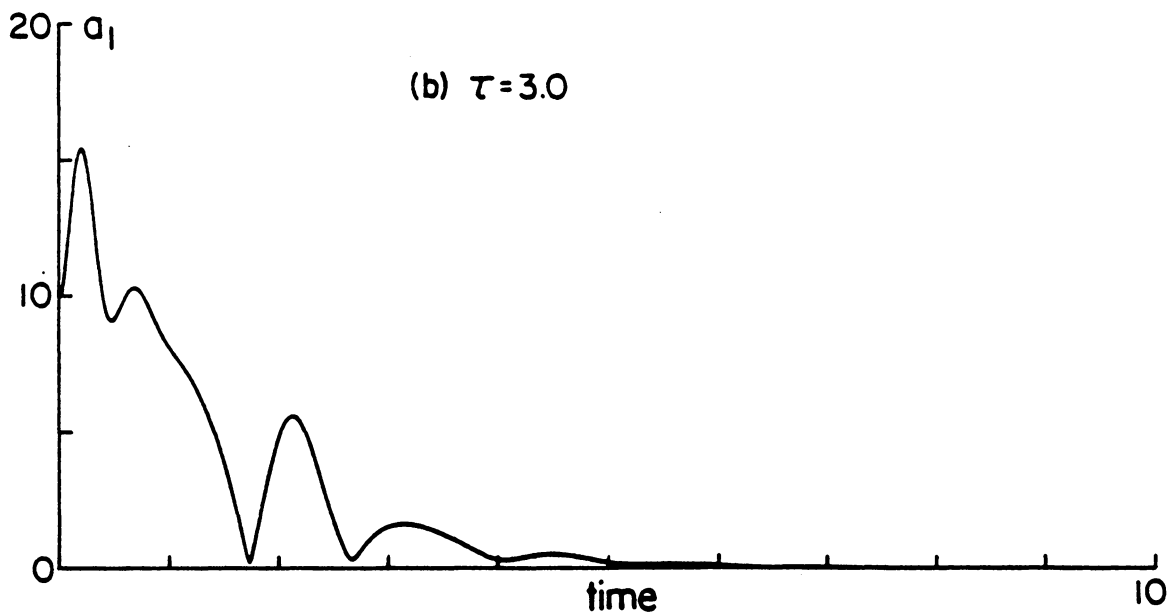
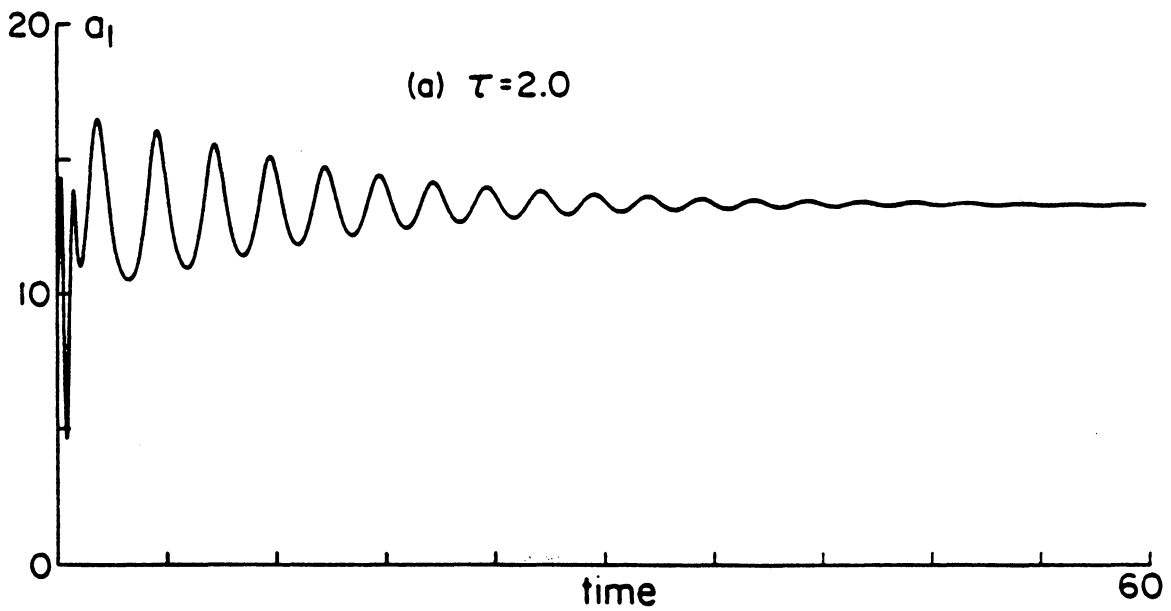


Figure 6.6 Time history of a_1 : $f_{12} = 7.00$, $f_{21} = 7.86$, $\sigma_1 = \sigma_2 = 0.0$. For $\tau = 2.0$ radians, the perturbation analysis gives a nontrivial steady-state stable response; for $\tau = 3.0$ the only stable response is trivial, and therefore the response is quenched. Compare these results with Figure 6.4. See Figure 6.9 for the limit cycle plot.

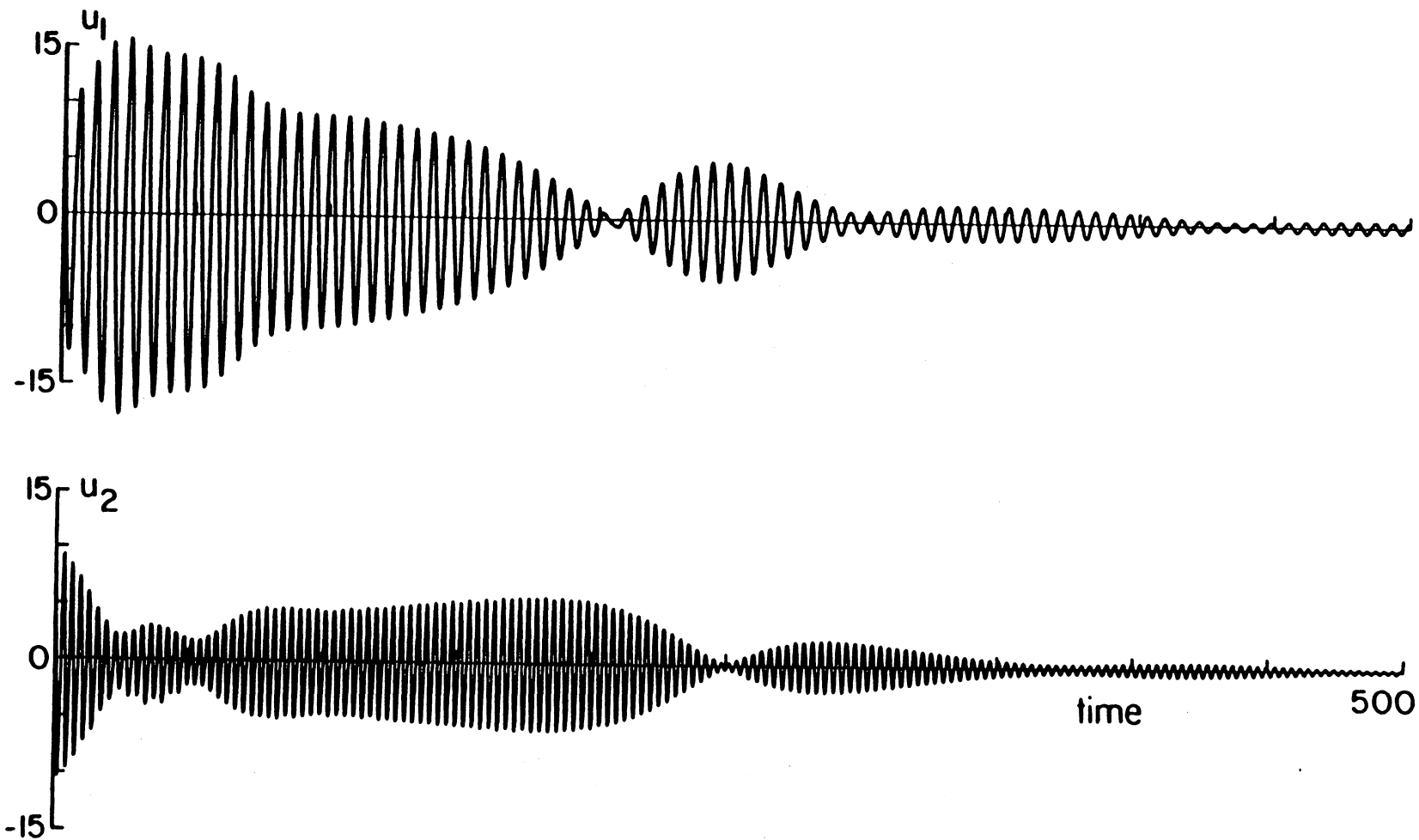


Figure 6.7 Time history of the response of the system corresponding to the parameters in Figures 6.4 and 6.6b as calculated by numerically integrating the governing differential Equations (6.1) and (6.2): $\tau = 3.0$ radians, $f_{12} = 7.00$, $f_{21} = 7.86$, $\sigma_1 = \sigma_2 = 0.0$. Note that the response of the system is quenched.

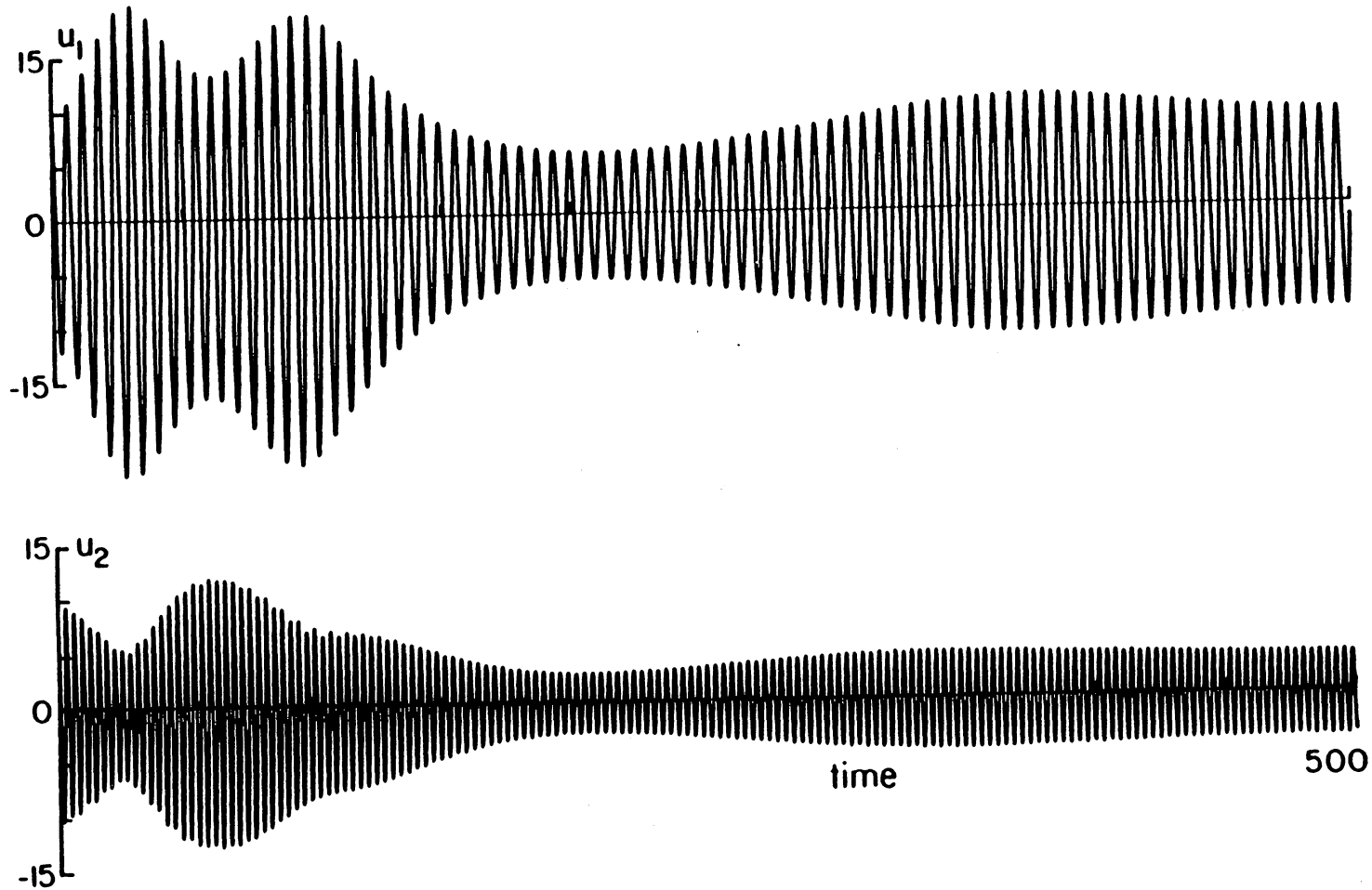


Figure 6.8 Variation of the u_n with time obtained by numerically integrating the governing differential equations: $\tau = 0.2618$ radians, $\sigma_1 = \sigma_2 = 0$, $f_{12} = 7.00$, $f_{21} = 5.04$, $\epsilon = 0.01$. Note that the modes of the system achieve constant steady-state amplitudes as predicted by the perturbation solution.

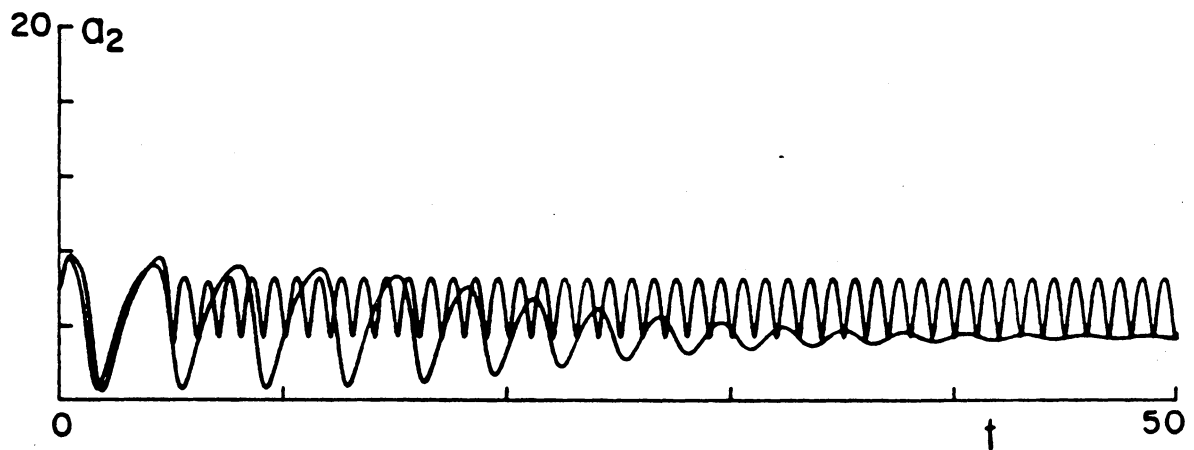
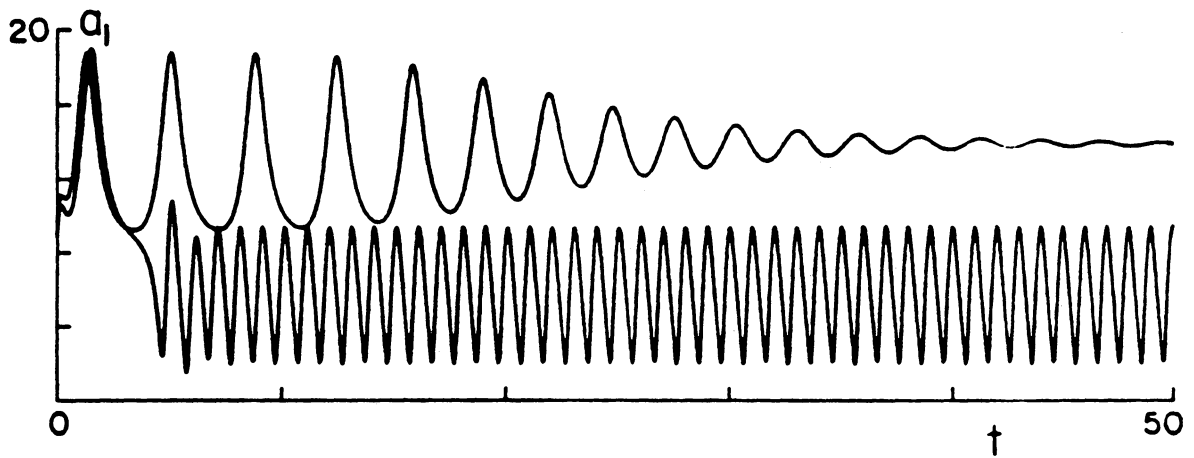


Figure 6.9 Modulation of the amplitudes of the modes of the system corresponding to the parameters in Figure 6.6(a) calculated by numerically integrating equations (6.19)-(6.23), showing both limit cycle and constant steady-state behavior: $\tau = 2.00$ radians, $f_{12} = 7.00$, $f_{21} = 7.86$, $\sigma_1 = \sigma_2 = 0.0$. The difference in the responses is caused by different initial conditions corresponding to the domains of the limit cycle and fixed point attractors, shown in Figure 6.10. Since the limit cycle is not a fixed point (i.e., steady-state solution where $\dot{a}_1 = \dot{a}_2 = 0.0$), it is not predicted by the steady-state perturbation solution. For the same parameters, Figures 6.11 and 6.13 show a_2 plotted vs. a_1 .

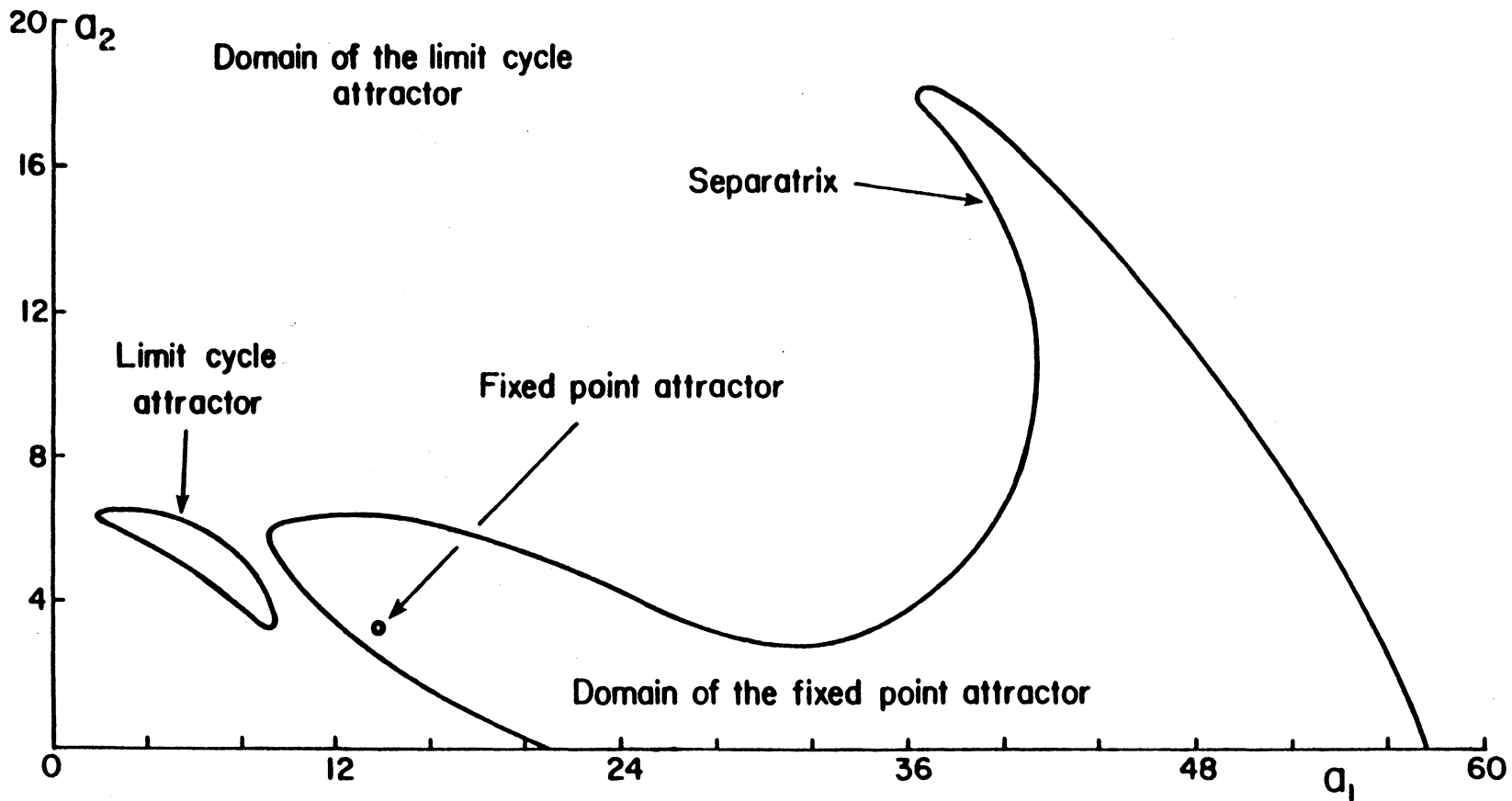


Figure 6.10 Separatrix dividing the $a_1(0)$ and $a_2(0)$ domain into the fixed point attractor basin and the limit-cycle attractor basin: $f_{12} = 7.00$, $f_{21} = 7.86$, $\sigma_1 = \sigma_2 = 0.0$, τ radians, $\gamma_1(0) = -1.00$ radians, $\gamma_2(0) = -3.00$ radians. The fixed point attractor corresponds to the constant steady-state solution shown in Figure 6.9, whereas the limit cycle attractor corresponds to the nonconstant steady-state solution also shown in Figure 6.9. The fixed point of a_1 and a_2 corresponds to a limit cycle in the original variables u_1 and u_2 , whereas the limit cycle corresponds to a torus.

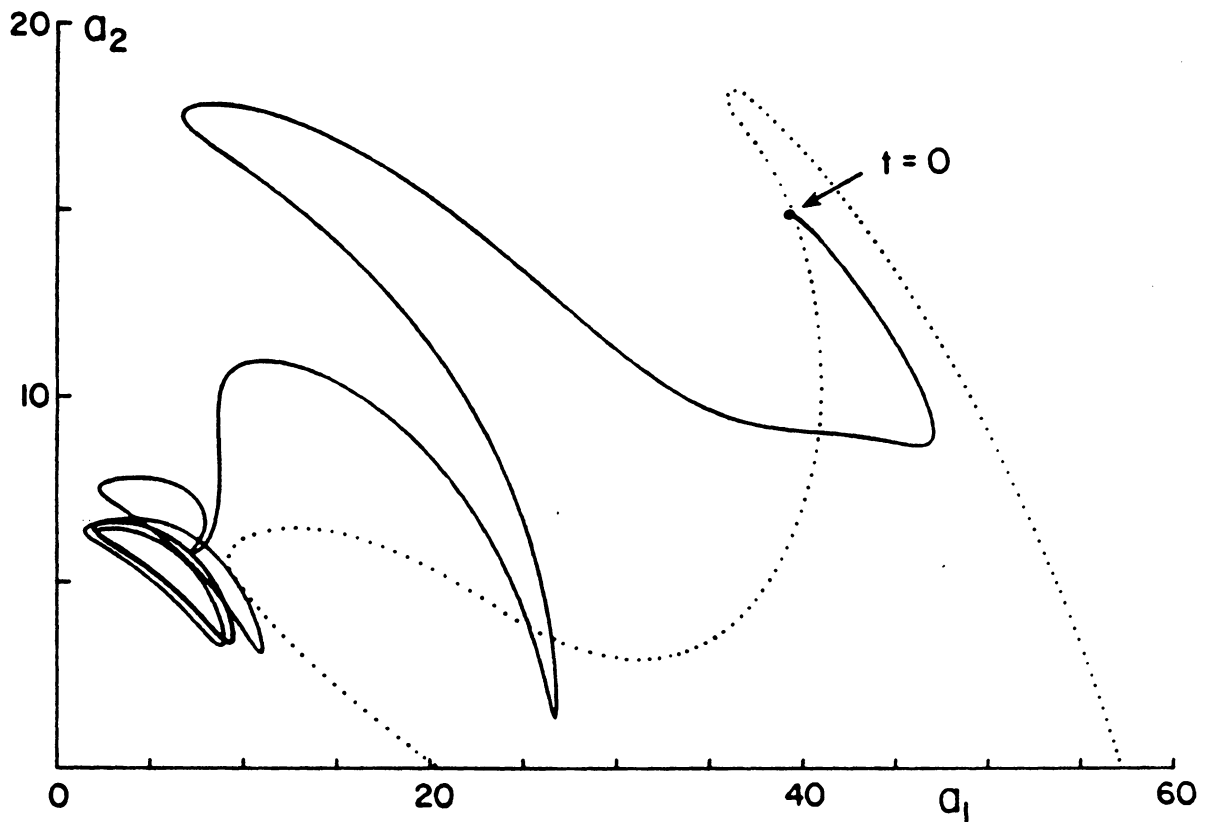


Figure 6.11 Initial values of a_1 and a_2 in the basin of the limit-cycle attractor of Figure 6.10: $f_{12} = 7.00$, $f_{21} = 7.86$, $\sigma_1 = \sigma_2 = 0.0$, $\tau = 2.0$ radians, $a_1(0) = 39.50$, $a_2(0) = 15.00$, $\gamma_1(0) = -0.0$ radians, $\gamma_2(0) = -3.0$ radians. Note that since this curve is a projection from the four dimensional hyperspace whose coordinate axes are a_1 , a_2 , γ_1 , γ_2 , the functions γ_1 and γ_2 are varying along this trajectory.

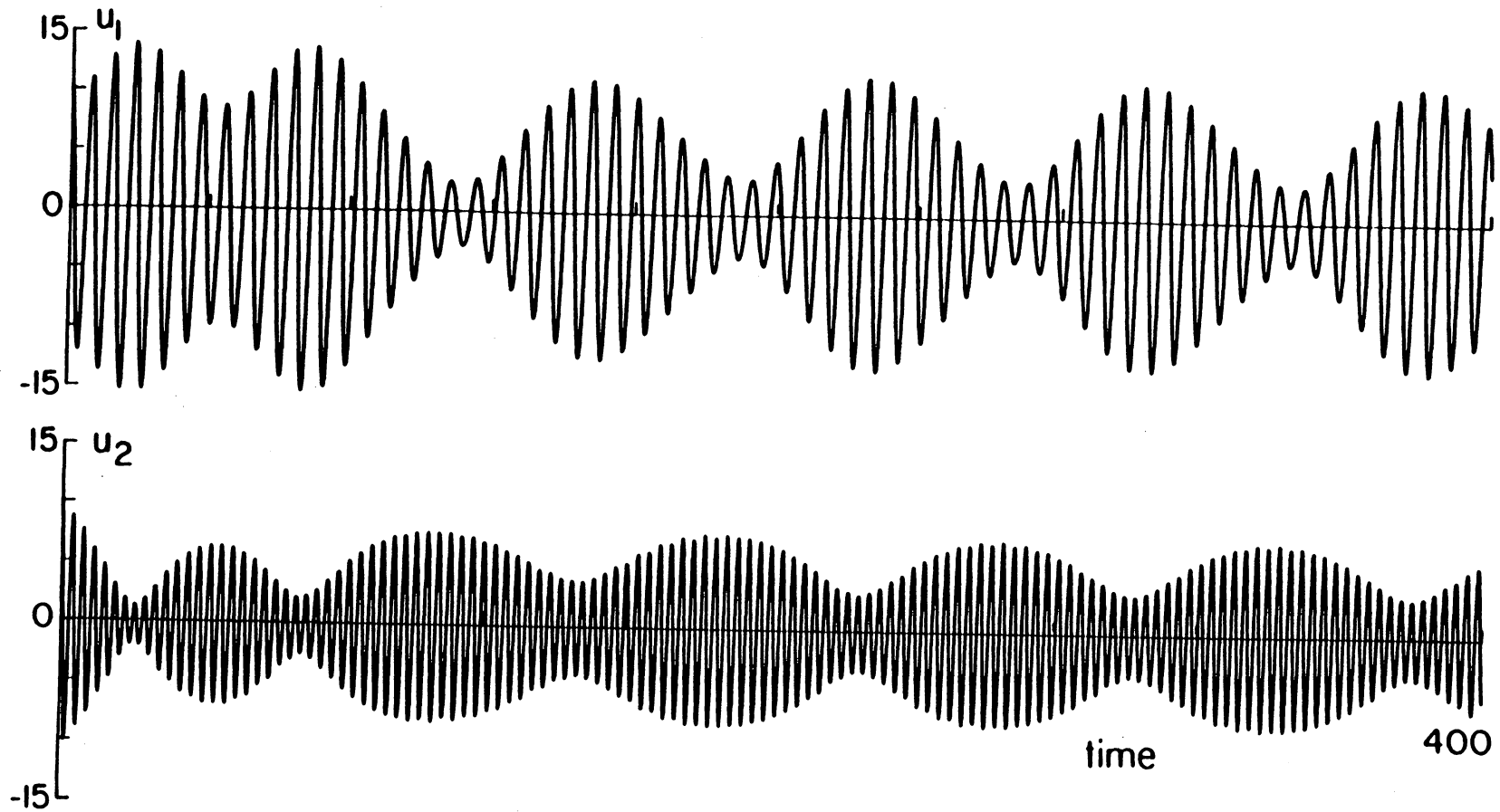


Figure 6.12

Response of the system corresponding to the parameters in Figure 6.9. It is calculated by numerically integrating the governing differential equations (6.1) and (6.2) with initial conditions such that the stable periodic response is not a limit cycle (constant amplitude), but a torus. The steady-state amplitudes a_1 and a_2 are limit cycles as shown in Figure 6.10.

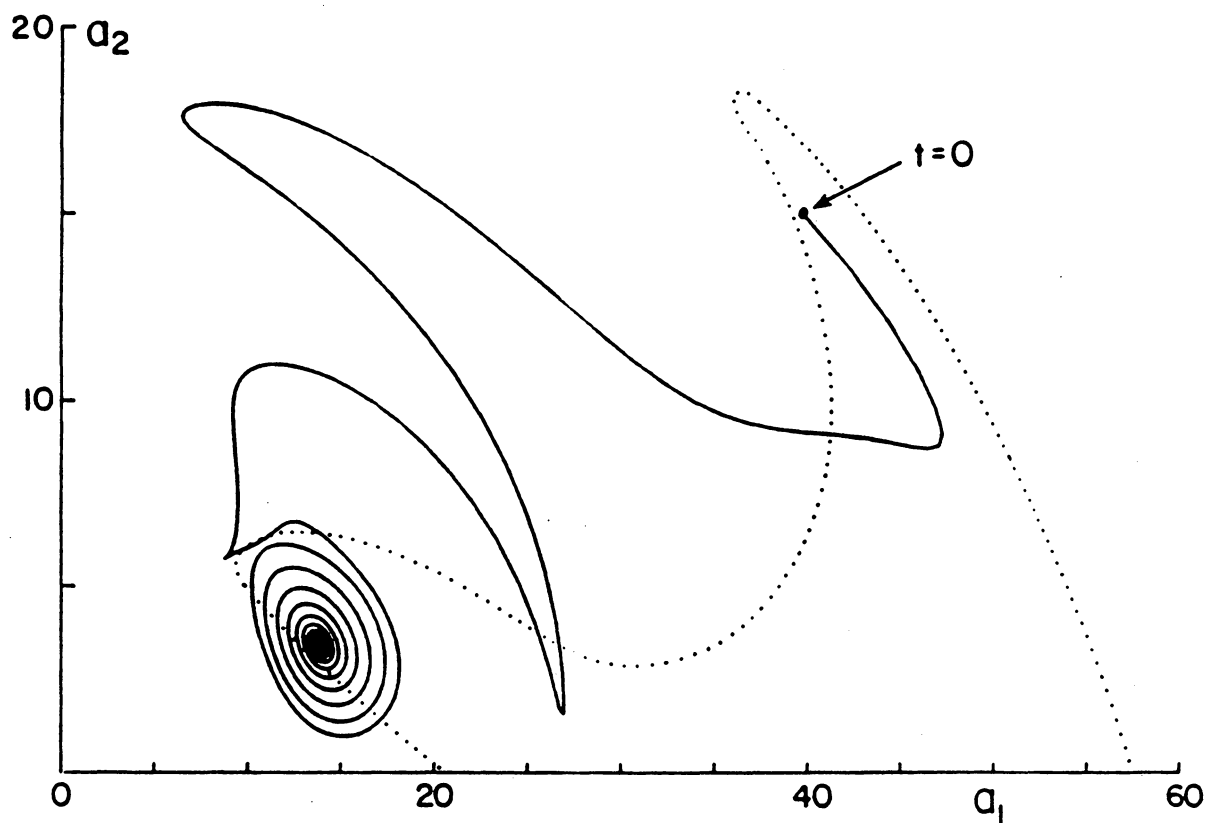


Figure 6.13 Projection of the trajectory in the $a_1 - a_2$ plane with initial values of a_1 and a_2 in the basin of the fixed point attractor of Figure 6.10. These system parameters are identical to those in Figure 6.11 except $a_1(0) = 39.75$ (0.6% difference).

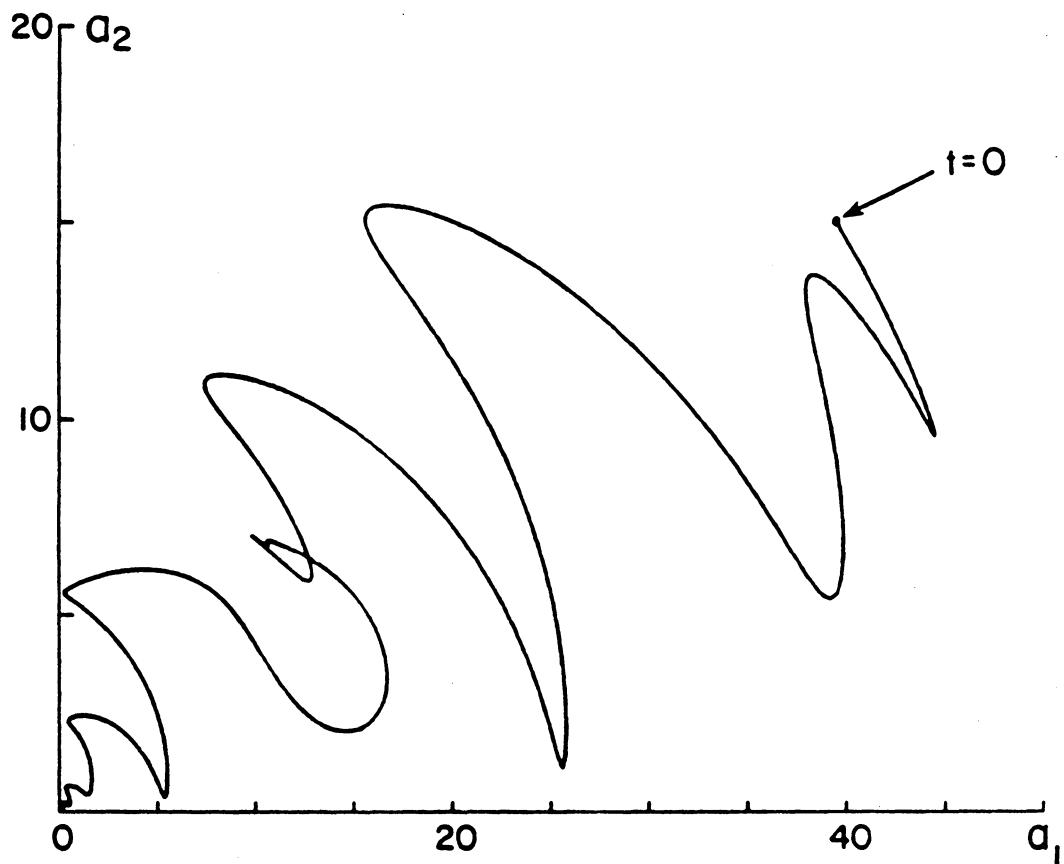


Figure 6.14 Projection of the trajectory onto the $a_1 - a_2$ plane for the case of a quenched response; the fixed point attractor is the origin: $f_{12} = 7.00$, $f_{21} = 7.86$, $\sigma_1 = \sigma_2 = 0.0$, $\tau = 3.0$ radians, $a_1(0) = 39.50$, $a_2(0) = 15.00$, $\gamma_1(0) = -1.0$ radians, $\gamma_2(0) = -3.0$ radians. See note in Figure 6.11.

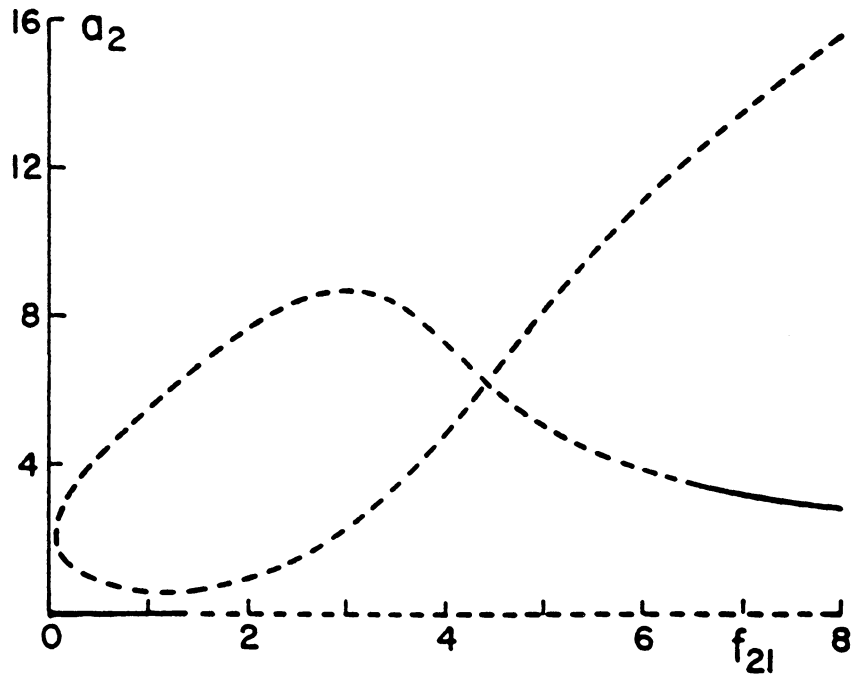
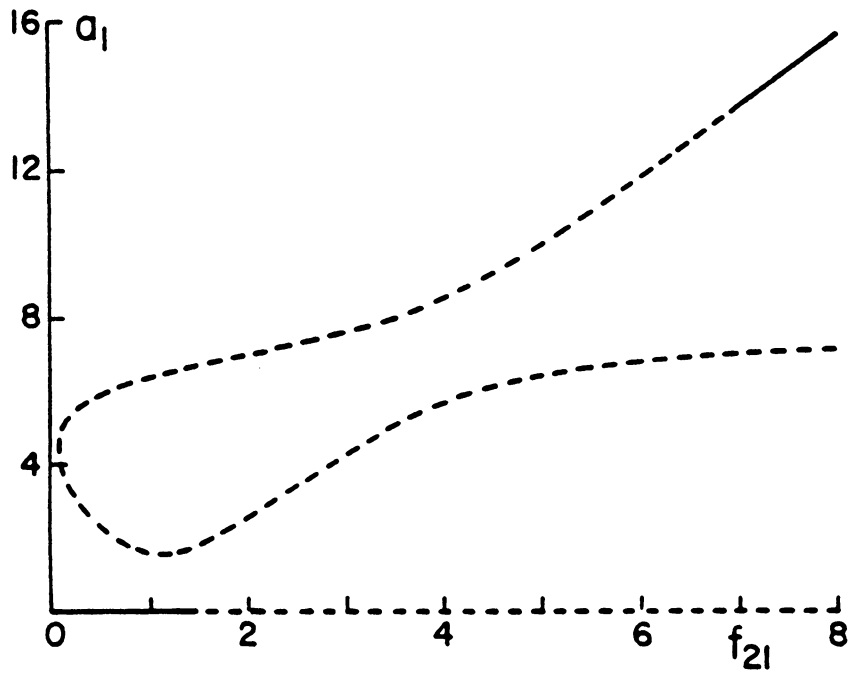


Figure 6.15 Variation of the steady-state response curves with the amplitude of the second excitation f_{21} : (—) stable, (---) unstable, $f_{12} = 8.0$, $\tau = 0.785$ radians, $\sigma_1 = 0$, $\sigma_2 = 1$.

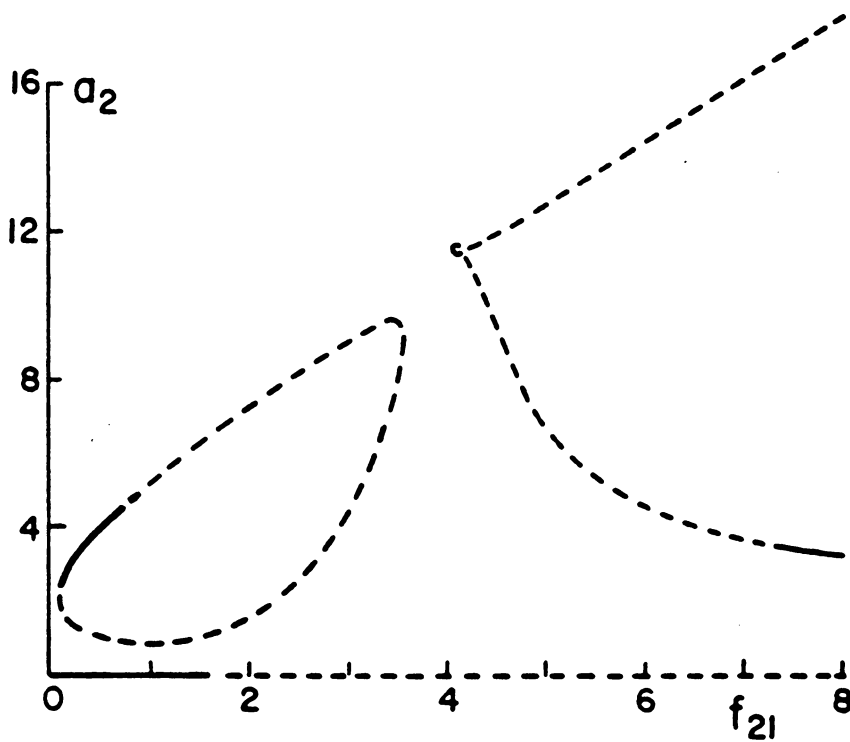
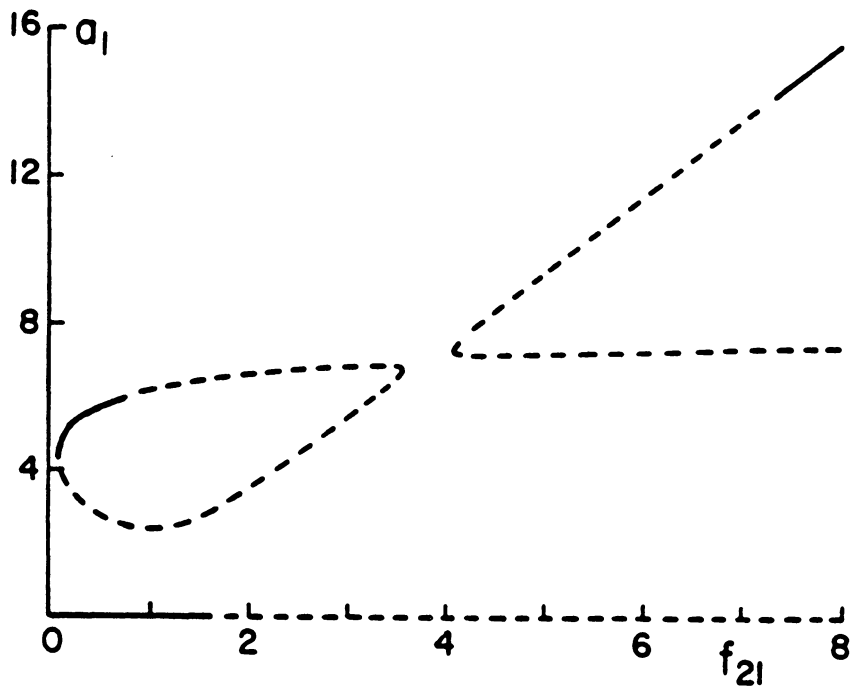


Figure 6.16 Variation of the steady-state response curves with f_{21} : (—) stable, (---) unstable, $f_{12} = 8.0$, $\tau = 1.047$ radians, $\sigma_1 = 0.0$, $\sigma_2 = 1$. Compare this figure with Figure 6.15 to note the effect of increasing τ on the nature of the response.

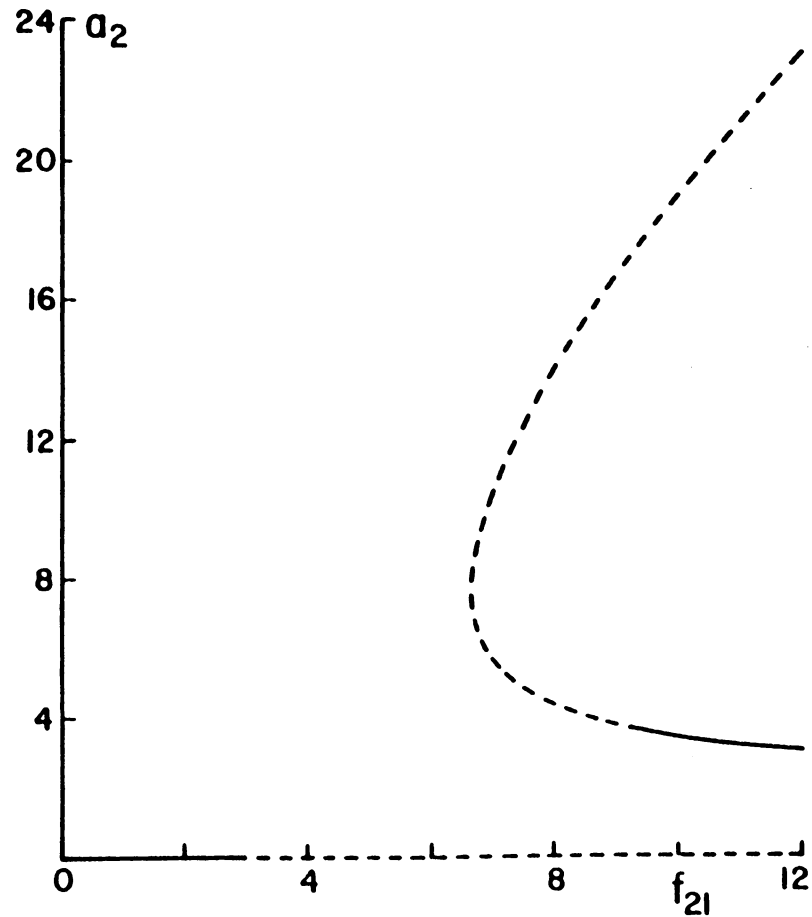
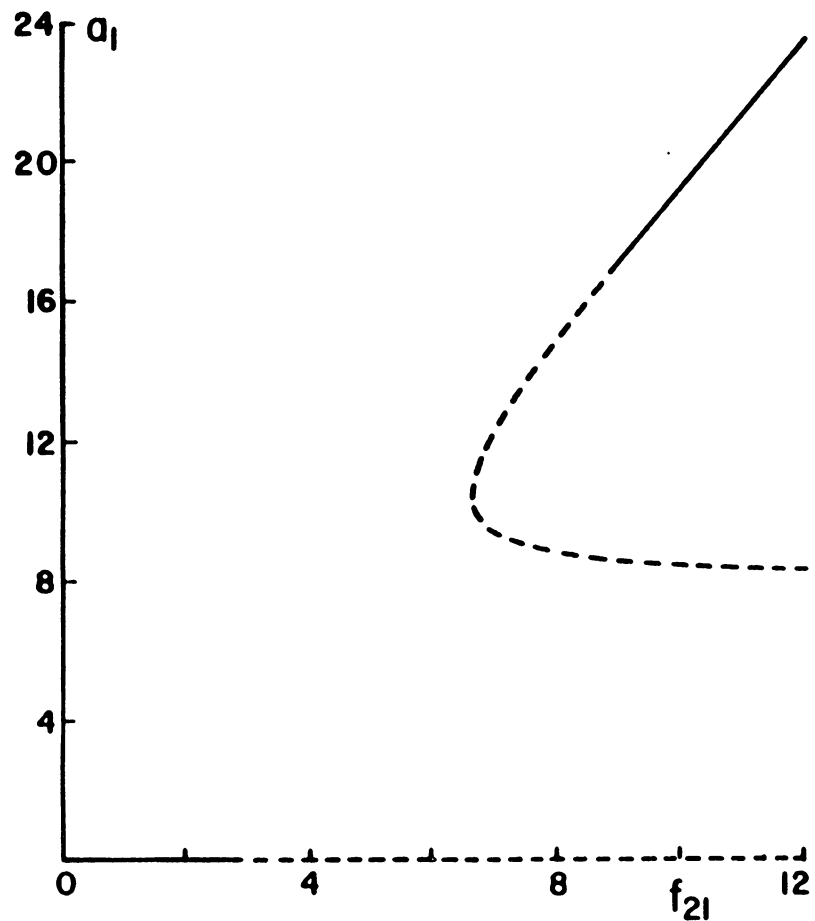


Figure 6.17 Variation of the steady-state response curves with f_{21} : (—) stable, (---) unstable, $f_{12} = 8.0$, $\tau = 1.833$ radians $\sigma_1 = 0.0$, $\sigma_2 = 1$. Compare this figure with Figures 6.15 and 6.16 to note the effect of increasing τ .

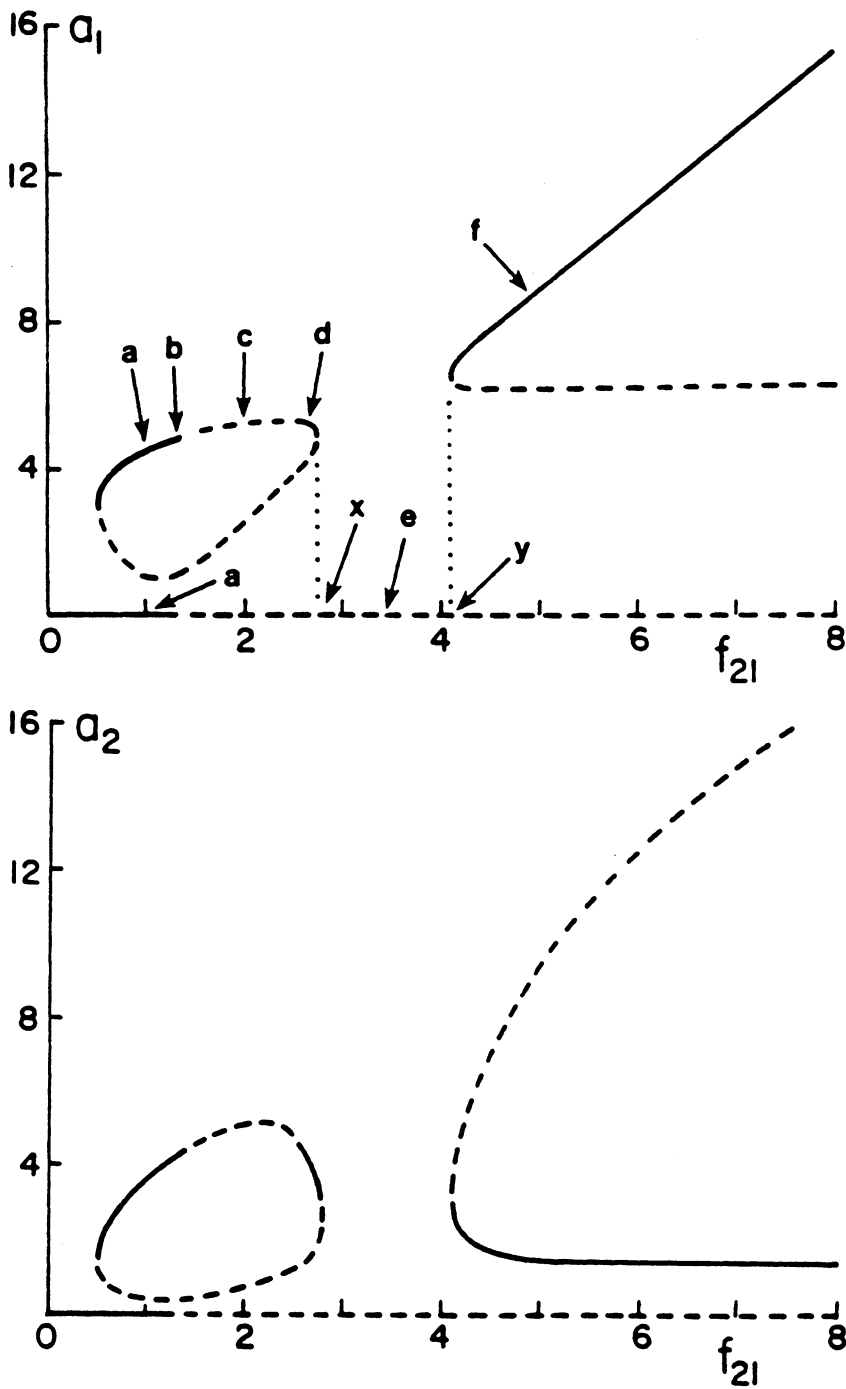


Figure 6.18 Variation of the steady-state response amplitudes a_1 and a_2 with f_{21} , showing three regions of stable nontrivial solutions: (—) stable, (---) unstable, $f_{12} = 7.0$, $\tau = 0.2618$ radians, $\sigma_1 = \sigma_2 = 0.0$. The system parameters at points (a)-(f) were used to integrate equations (6.19-6.23). The results are shown in Figure 6.19. Note also that a_2 is becoming saturated as f_{21} increases.

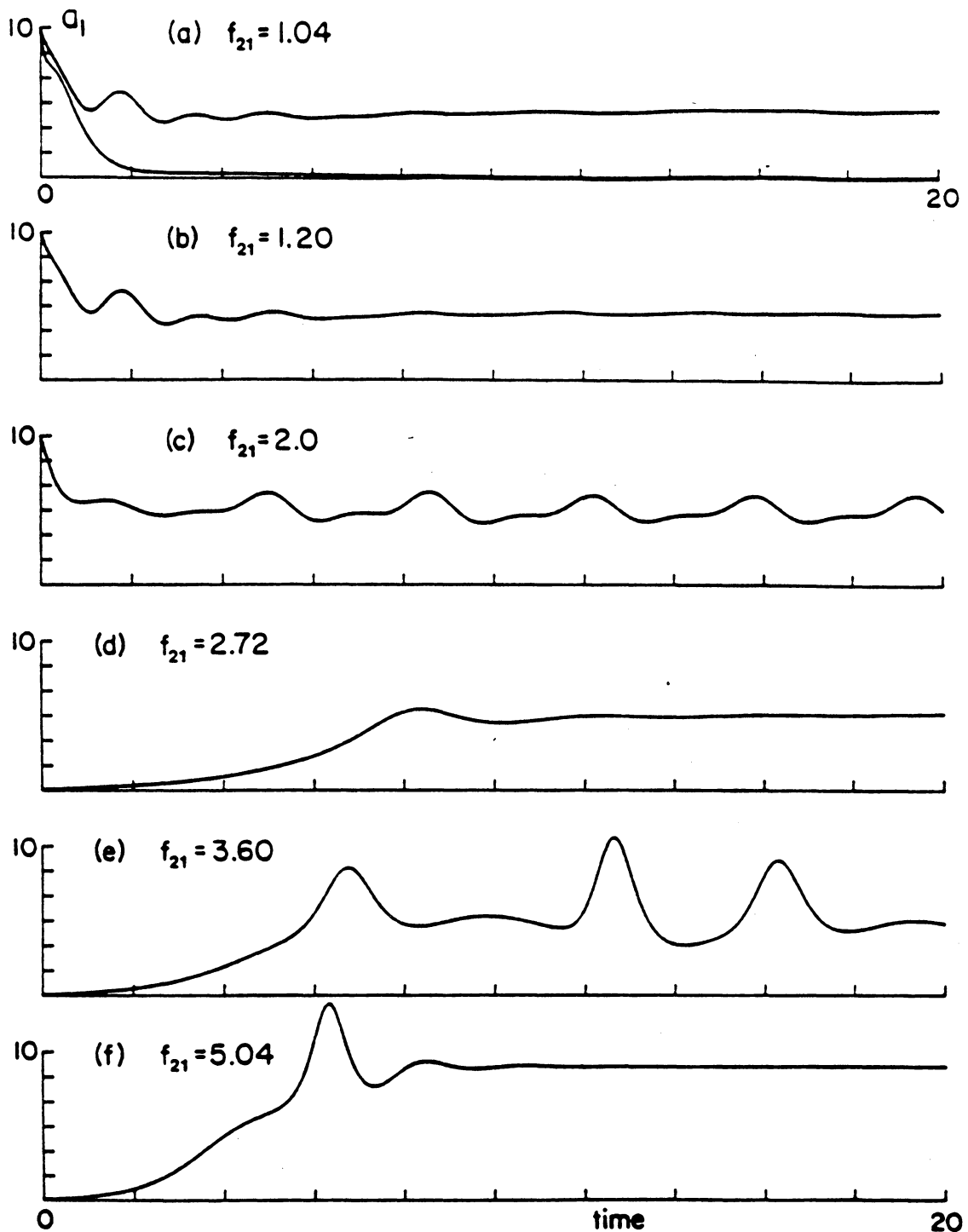


Figure 6.19 Time histories of a_1 for various points on the response curve in Figure 6.18 as predicted by the perturbation analysis: $f_{12} = 7.0$, $\tau = 0.2618$ radians, $\sigma_1 = \sigma_2 = 0.0$.

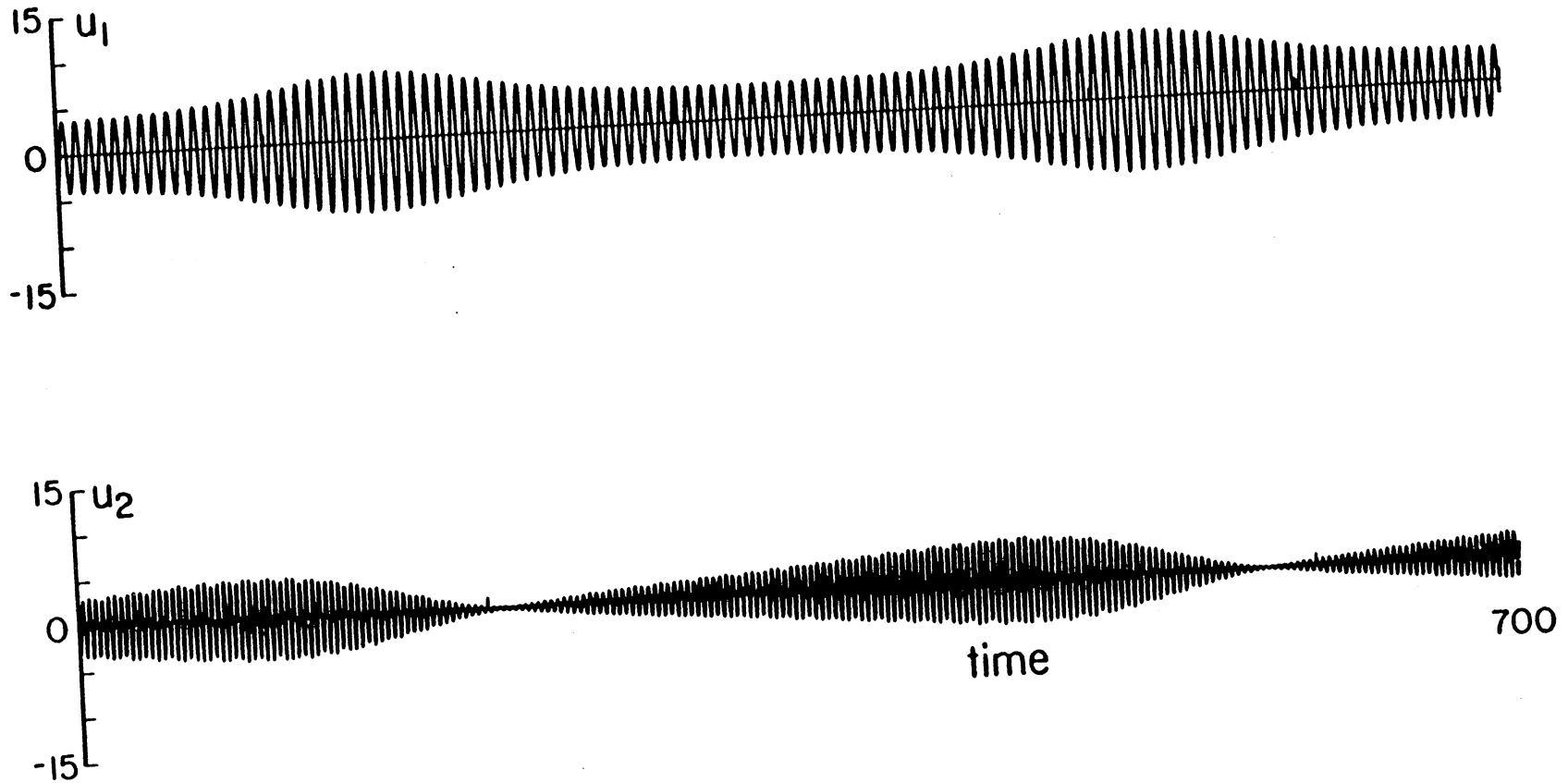


Figure 6.20 Time histories of the responses of u_1 and u_2 , as numerically integrated from the governing differential equations: $\tau = 0.2618$ radians, $\sigma_1 = \sigma_2 = 0$, $f_{12} = 7.0$, $f_{21} = 3.30$, $\epsilon = 0.01$. Note that the system does not achieve a constant steady-state amplitude in agreement with the perturbation solution.

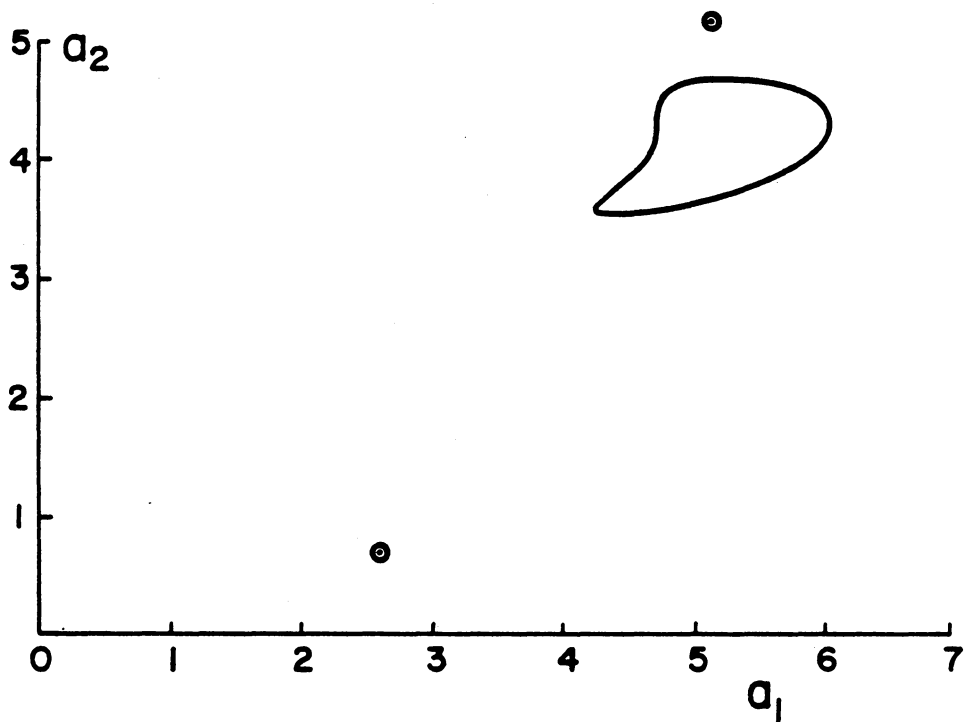


Figure 6.21 Periodic limit cycle corresponding to the parameters of Figures 6.18 and 6.19, point c: $f_{12} = 7.0$, $f_{21} = 2.0$, $\tau = 0.2618$ radians, $\sigma_1 = \sigma_2 = 0.0$. Note that the trajectory is close to the unstable fixed point that is on the same branch as the previously stable solution. The two points shown are the steady-state solutions from Figure 6.18.

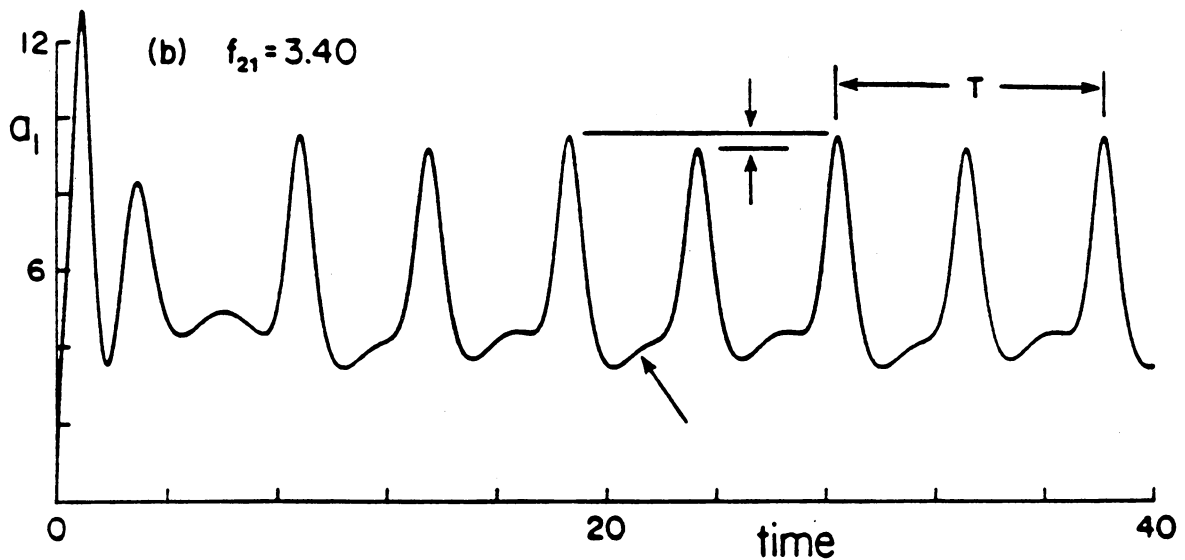
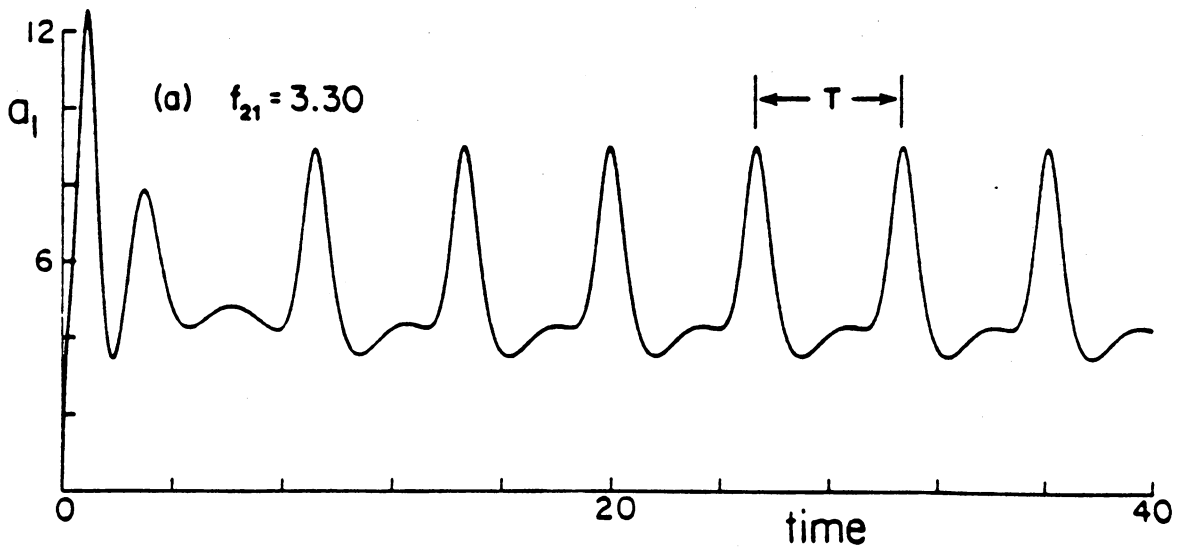


Figure 6.22 Time histories of a_1 , showing the limit cycle bifurcating in the region between points x and y in Figure 6.18. As f_{21} is increased from 3.30 to 3.40, the period essentially doubles. In the periodic region, every second peak is slightly lower and every second hump between peaks is distorted. This slight distortion is readily seen in the phase plane of Figure 6.23. Compare this figure with Figure 6.19(e) to see the effect of further increasing f_{21} .

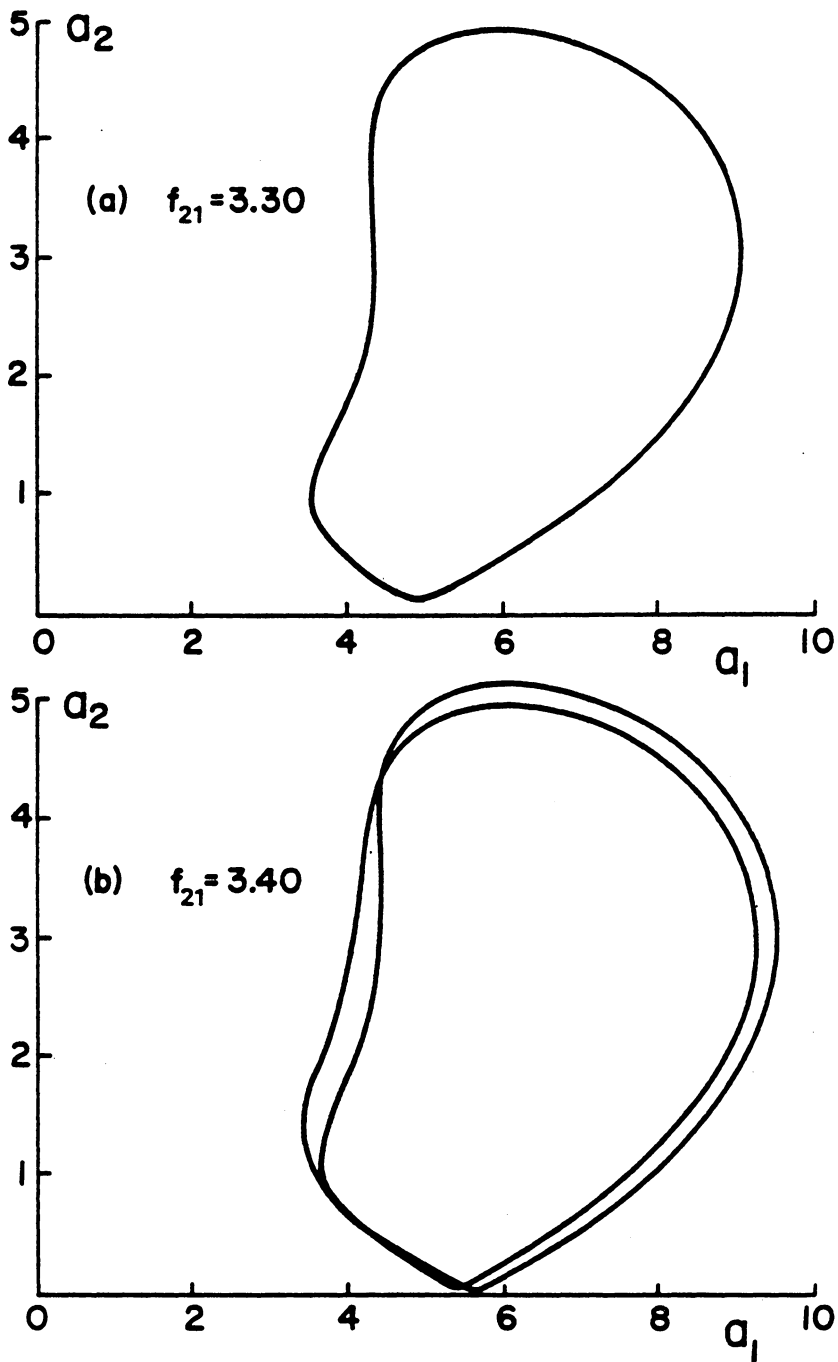


Figure 6.23 Projection of the limit cycle trajectory on the plane $a_1 - a_2$ corresponding to the parameters of Figures 6.18 and 6.22 between points x and y : $f_{12} = 7.0$, $\tau = 0.2618$, $\sigma_1 = \sigma_2 = 0.0$. Figure (a) shows the trajectory for $f_{21} = 3.30$ before it bifurcated, while (b) shows the trajectory for $f_{21} = 3.40$ after it bifurcated. The bifurcated trajectory requires two similar orbits to complete one period of the motion, and hence it is called period-doubling bifurcation.

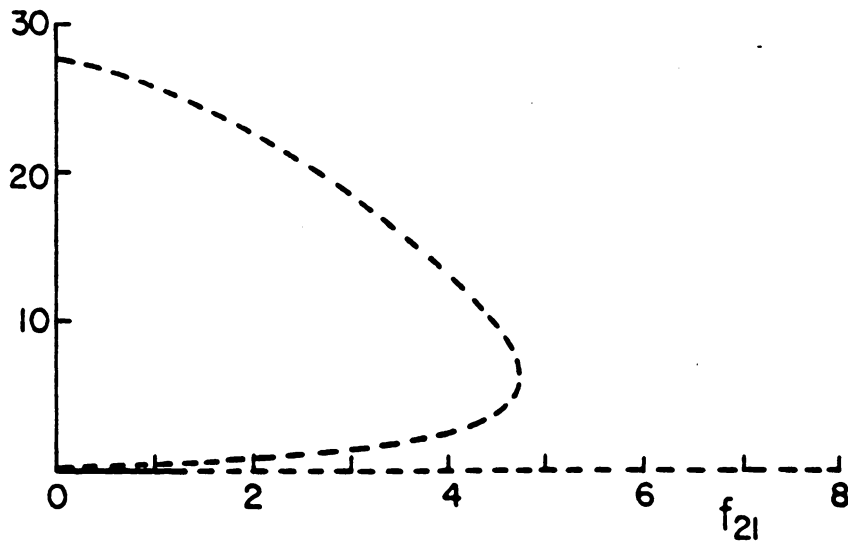
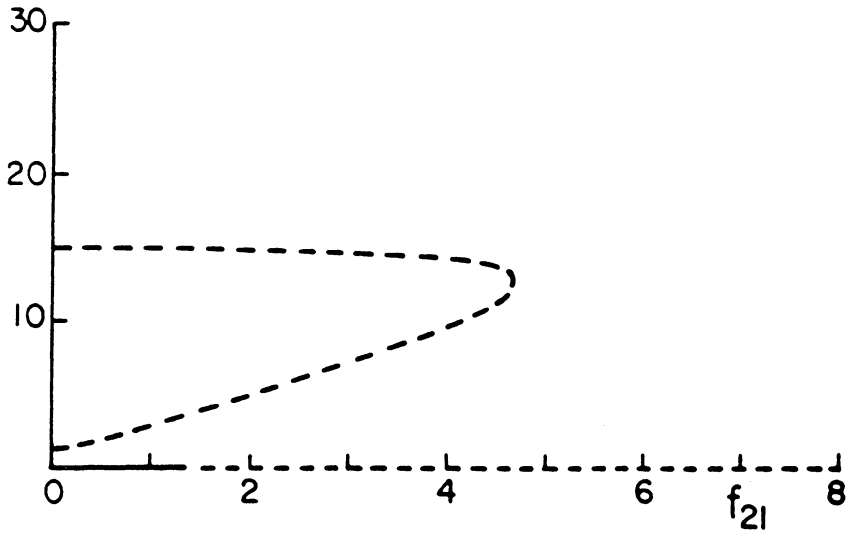


Figure 6.24 Variations of the amplitudes of the steady-state response with the amplitude f_{21} of the second mode in the presence of a strong excitation of the first mode: (—) stable, (---) unstable, $\tau = 1.883$ radians, $\sigma_1 = \sigma_2 = 0$, $f_{12} = 16.0$.

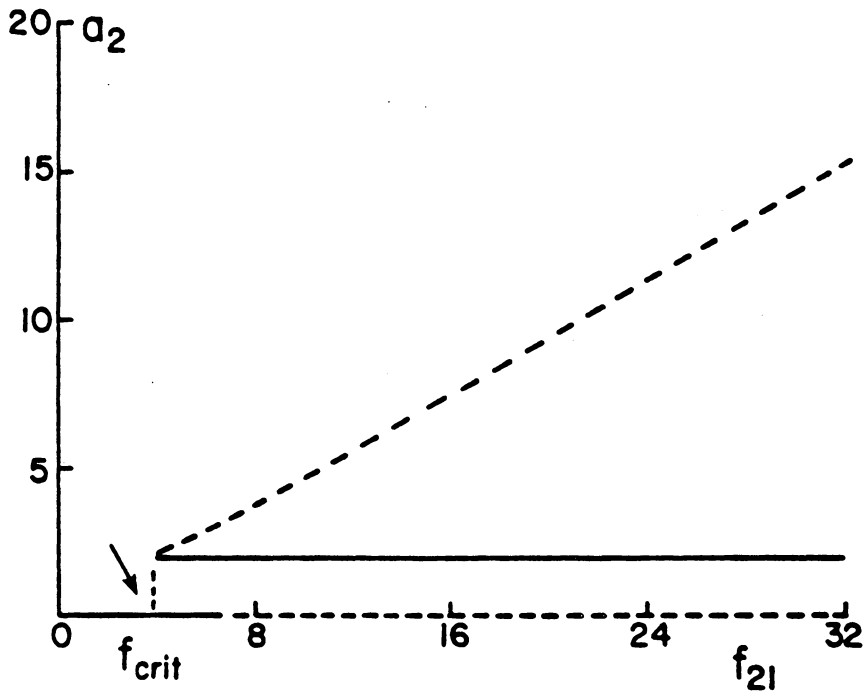
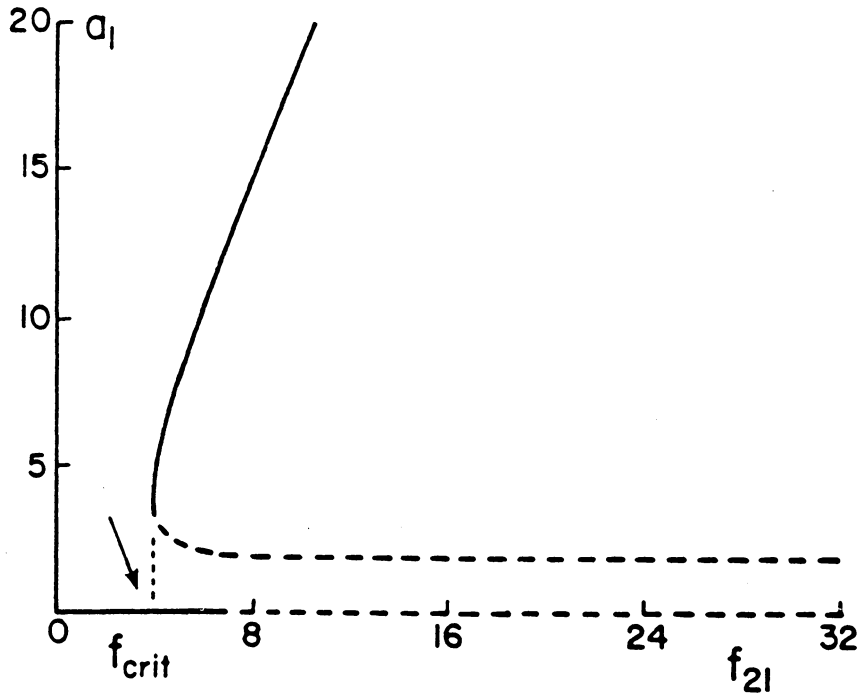


Figure 6.25 Variations of the amplitudes of the steady-state response with the second excitation amplitude f_{21} in the presence of a weak excitation of the first mode: $f_{12} = 2.00$, $\sigma_1 = \sigma_2 = 0$, $\tau = 1.047$ radians. Note that a_2 becomes saturated and a_1 increases with increasing f_{21} when $f_{21} \geq f_{crit}$.

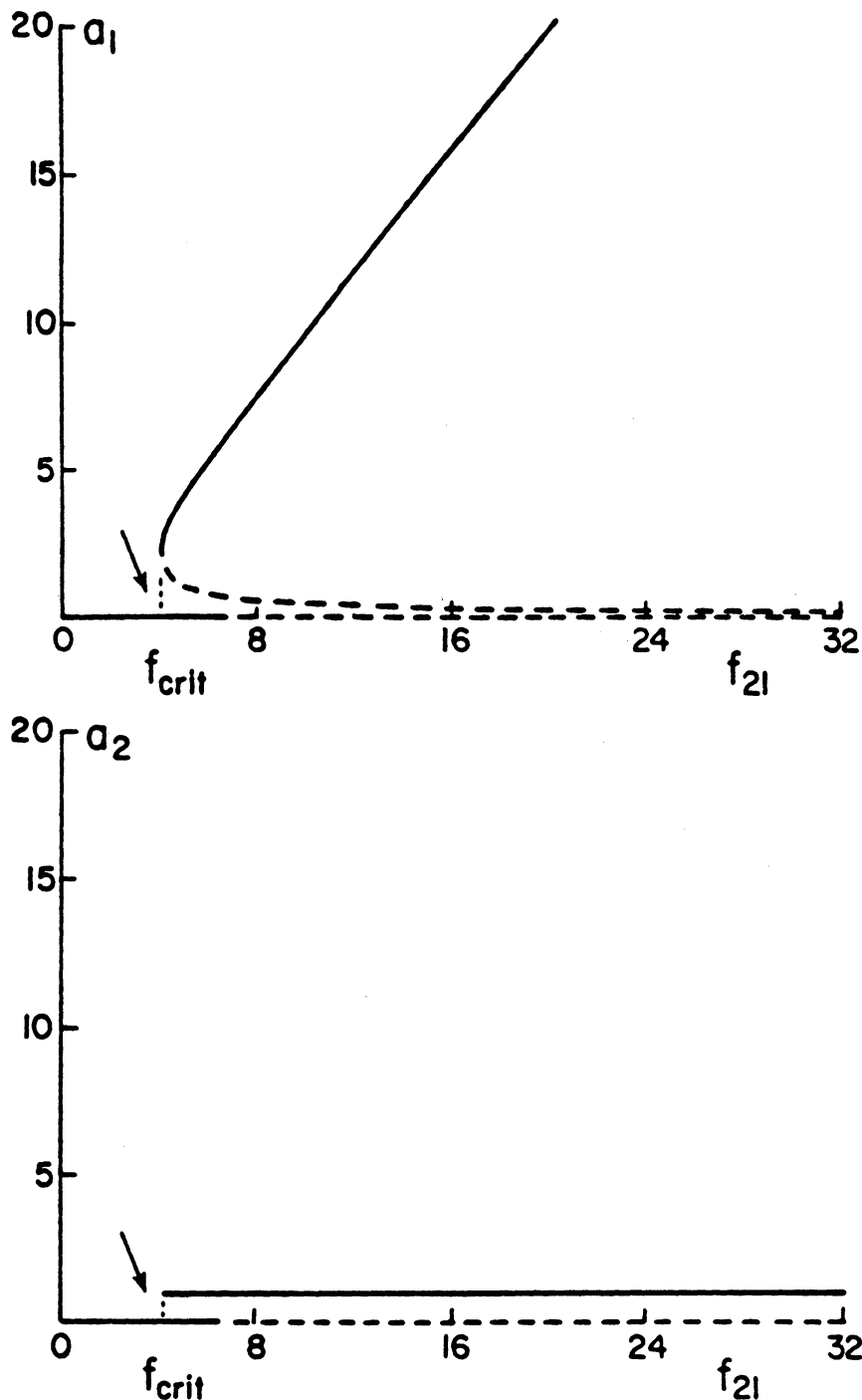


Figure 6.26 Variations of the amplitudes of the steady-state response with the second excitation amplitude f_{21} without first mode excitation: $f_{12} = 0.000001$, $\sigma_1 = \sigma_2 = 0$, $\tau = 2.094$ radians. Note that a_2 becomes saturated and a_1 increases with increasing f_{21} when $f_{21} \geq f_{crit}$. There are actually two solutions for a_2 (one stable and one unstable), but they are so close to each other, they appear as one in the figure.

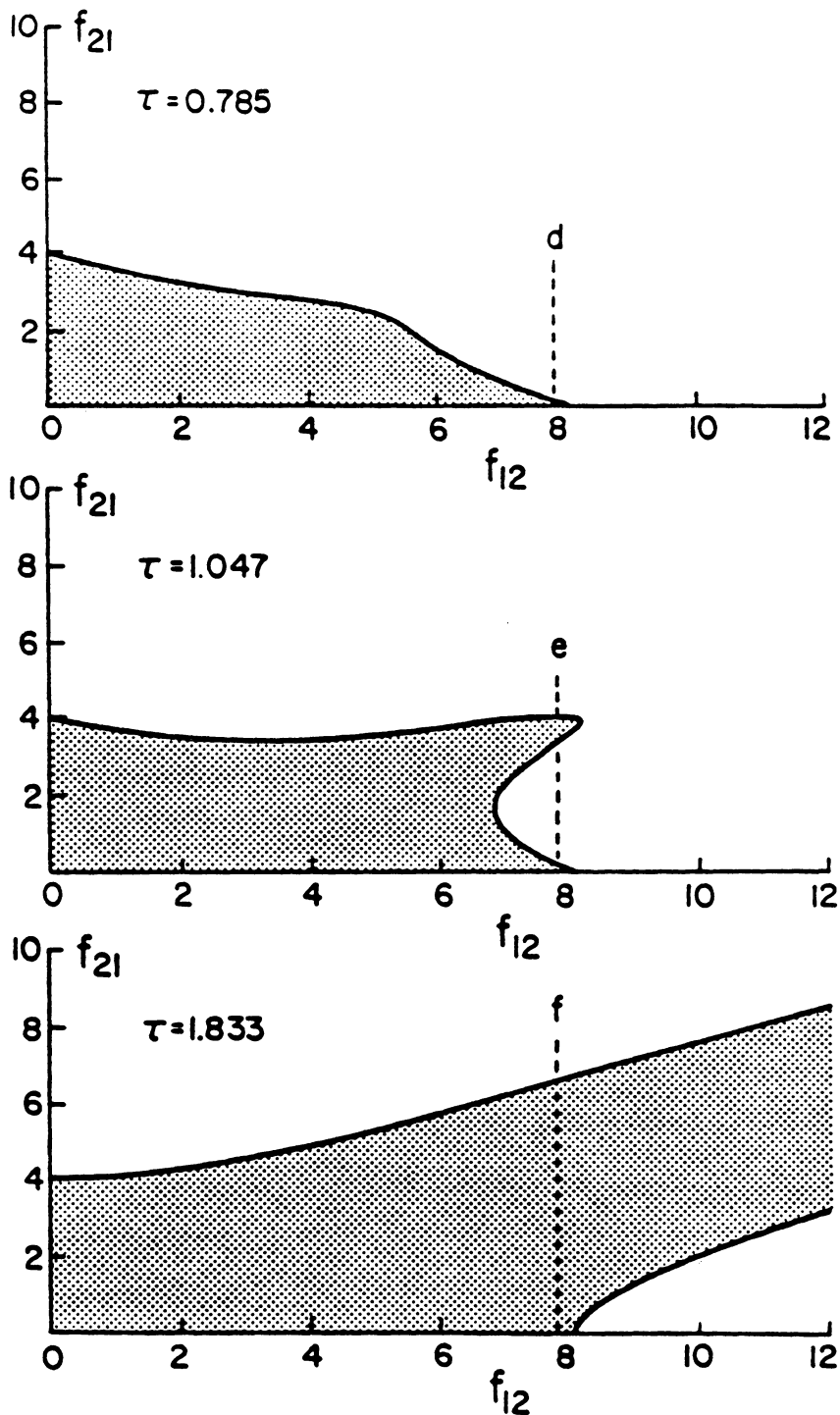


Figure 6.27 Transition curves separating regions of steady-state solutions from regions of nonsteady-state solutions: $\sigma_1 = 0.0$, $\sigma_2 = 1$. Planes d, e, and f correspond to Figures 6.15, 6.16 and 6.17, respectively. Shaded area denotes region where steady-state solutions do not exist. (a) $\tau = 0.275$ radians, (b) $\tau = 1.047$ radians, (c) $\tau = 1.833$ radians.

		$\epsilon = 0.01$		$\epsilon = 0.001$	
Amplitude	Perturbation	Numerical	% Error	Numerical	% Error
a_1	8.99	10.10	11	9.12	1.4
a_2	1.42	4.22	66	1.72	17

Table 6.1 Perturbation results for the steady-state nontrivial solution compared with the numerically obtained results: $f_{12} = 7.00$, $f_{21} = 5.04$, $\tau = 0.2618$, $\sigma_1 = \sigma_2 = 0$. The percent error decreases for decreasing f_{21} .

REFERENCES

1. Aggarwal, J. K. (1972). Notes on Nonlinear Systems, Van Nostrand Reinhold Co., New York.
2. Arnold, V. I. (1983). Geometrical Methods in the Theory of Ordinary Differential Equations, Springer-Verlag, New York.
3. Atherton, Derek P. (1981). Stability of Nonlinear Systems, Research Studies Press, England.
4. Bajaj, A. K., Sethna, P. R., and Lundgren, T. S. (1980). Hopf bifurcation phenomena in tubes carrying a fluid. SIAM Journal of Applied Mathematics, 39, 213-230.
5. Bajaj, A. K. and Sethna, P. R. (1982). Bifurcation in three-dimensional motions of articulated tubes, part 1: linear systems and symmetry. ASME Journal of Applied Mechanics, 49, 606-611.
6. Bajaj, A. K. and Sethna, P. R. (1982). Bifurcation in three-dimensional motions of articulated tubes, part 1: nonlinear analysis. Journal of Applied Mechanics, 49, 612-618.

7. Bajaj, A. K. (1984). Interactions between self and parametrically excited motions in articulated tubes. Journal of Applied Mechanics, 51, 423-429.
8. Bajaj, A. K. (1987). Bifurcations in a parametrically excited nonlinear oscillator. International Journal of Non-Linear Mechanics, 22, 47-59.
9. Bajkowski, J. and Szemplińska-Stupnicka, W. (1986). Internal resonances effects - simulation versus analytical methods results. Journal of Sound and Vibration, 104, 259-275.
10. Barr, Allan D. S. (1980). Some developments in parametric stability and nonlinear vibration. International Conference on Recent Advances in Structural Dynamics, July 7-11, Published by Institute of Sound and Vibration Research, Univ. of Southampton, England.
11. Beck, M. (1952). Die Knicklast des Einseitig Eigespannten, Tangential Gedruckten Stabes. Zeitschrift für angewandte Mathematik und Physik, 3, 225-228 and 476-477.
12. Benjamin, T. B. (1961). Dynamics of a system of articulated pipes conveying fluid: I. theory. Proceedings of the Royal Society of London, Series A, 261, 451-486.

13. Benjamin, T. B. (1961). Dynamics of a system of articulated pipes conveying fluid: II. experiment. Proceedings of the Royal Society of London, Series A, 261, 487-499.
14. Bohn, M. P. and Hermann, G. (1974). The dynamic behavior of articulated pipes conveying fluid with periodic flow rate. Journal of Applied Mechanics, 41, 55-62.
15. Bolotin, V. V. (1964). The Dynamic Stability of Elastic Systems, New York: Holden-Day, Inc.
16. Breitenberger, Ernst and Mueller, Robert D. (1981). The elastic pendulum: a nonlinear paradigm. Journal of Mathematical Physics, 22, 1196-1210.
17. Bux, S. L. and Roberts, J. W. (1986). Nonlinear vibratory interactions in systems of coupled beams. Journal of Sound and Vibration, 104, 497-520.
18. Carlson, Robert L. (1974). An experimental study of the parametric excitation of a tensioned sheet with a cracklike opening. Experimental Mechanics, 14, 452-458.

19. Chelomey, V. N. (1985). Paradoxes in mechanics caused by vibrations. Meceanica 20, 314-316.
20. Chopra, I. and Dugundji, J. (1979). Non-linear dynamic response of a wind turbine blade. Journal of Sound and Vibration, 63, 265-286.
21. Crespo da Silva, M. R. M. (1978). Harmonic nonlinear response of Beck's column to a lateral excitation. International Journal of Solids and Structures, 14, 987-997.
22. Crespo da Silva, M.R.M. (1980). Nonlinear resonances in a column subjected to a constant end force. Journal of Applied Mechanics, 47, 409-414.
23. Datta, P. K. (1978). An investigation of the buckling behavior and parametric resonance phenomenon of a tensioned sheet with a central opening. Journal of Sound and Vibration, 58, 527-534.
24. Datta, P. K. (1981). An analogue simulation of the nonlinear vibration of a plate with a central opening subjected to tension loading. Journal of Mechanical Engineering Science, 23,

25. Dokumaci, E. (1978). Pseudo-coupled bending-torsion vibrations of beams under lateral parametric excitation. Journal of Sound and Vibration, 58, 233-238.
26. Dugundji, J. and Mukhopadhyay, V. (1973). Lateral bending-torsion vibrations of a thin beam under parametric excitation. ASME Journal of Applied Mechanics, 40, 693-698, Paper No. 73-APM-13.
27. Elmaraghy, R. and Tabarrok, B. (1975). On the dynamic stability of an axially oscillating beam. Journal of the Franklin Institute, 300, 25-29.
28. Elsinger, K. and Merchant, H. C. (1979). Amplitude modulation of a forced system by parameter variation. Journal of Applied Mechanics, 46, 191-196.
29. Elsinger, K. and Merchant, H. C. (1979). Clamped beam parametric amplifier. Journal of Applied Mechanics, 46, 197-202.
30. Eshleman, R. L. and Eubanks, R. A. (1969). On the critical speeds of a continuous rotor. ASME Journal of Engineering for Industry, 91, 1180-1188.

31. Eshleman, R. L. (1967). On the stability of continuous rotors. Ph.D. Thesis, Illinois Institute of Technology.
32. Evan-Iwanowski (1976). Resonance Oscillations in Mechanical Systems, Elsevier Scientific Publishing Co., The Netherlands.
33. Floquet, G. (1883). Sur les équations différentielles linéaires. Ann. De L'école Normale Supérieure, 12, 47-88.
34. Forys, A and Nizioł, J. Internal Resonance in a Plane System of Rods. Journal of Sound and Vibration, 95, 361-374.
35. Forys, A. (1986). Periodic and non-periodic combination resonance in a nonlinear system of rods. Journal of Sound and Vibration, 105, 461-472.
36. Fu, F. C. L. and Nemat-Nasser, S. (1977). Coincidence problem and combination resonance. AIAA Journal, 15, 1785-1791.
37. Ginsberg, J. H. (1973). The dynamic stability of a pipe conveying a pulsatile flow. International Journal of Engineering Science, 11, 1013-1024.

38. Gregory, R. W. and Paidoussis, M. P. (1966). Unstable oscillation of tubular cantilevers conveying fluid: II. experiment. Proceedings of the Royal Society of London, Series A, 293, 528-542.
39. Guckenheimer, J. and Holmes, P. J. (1983). Nonlinear Oscillations, Dynamics Systems and Bifurcations of Vector Fields, Springer, Berlin.
40. Gürgöze, M. (1986). Parametric vibrations of a restrained beam with an end mass under displacement excitation. Journal of Sound and Vibration, 108, 73-84.
41. Haddow, A. G., HaQuang, N. and Mook, D. T., (1985). An experimental and analytical investigation of nonlinear resonances. ASME Design Engineering Division Conference and Exhibit on Mechanical Vibration and Noise, Cincinnati, OH, September 10-13, 85-DET-175.
42. Hagedorn, Peter (1978, English Translation 1981). Non-Linear Oscillations, Oxford University Press, Oxford.
43. Hale, Jack K. (1980). Topics in Dynamic Bifurcation Theory, The American Mathematical Society, Providence, Rhode Island.

44. Hansen, J. (1985). Stability diagrams for coupled Mathieu equations. Ingenieur-Archive, 55, 463-473.
45. HaQuang, N., Mook, D. T., and Plaut, R. H. A nonlinear analysis of the interactions between parametric and external excitations. Accepted for publication Journal of Sound and Vibration.
46. Hasegawa, Eiji and Kondoh, Nobukazu (1986). The prevention of wave motions in a liquid layer under a vertical periodic motion due to a superimposed thin viscous liquid layer. Bulletin of the JSME, 29, 3083-3089.
47. Hashimoto, Hiroyuki and Sudo, Seiichi (1984). Dynamic behavior of liquid free surface in a cylindrical container subject to vertical vibration. Bulletin of the JSME, 27, 923-930.
48. Hatwal, H. (1982). Notes on an autoparametric vibration absorber. Journal of Sound and Vibration, 83, 440-443.
49. Hatwal, H. and Mallik, A. K. and Ghosh, A. (1983). Forced nonlinear oscillations of an autoparametric system Part 1: periodic responses. Journal of Applied Mechanics, 50, 657-662.

50. Hatwal, H., Mallik, A. K. and Ghosh, A. (1983). Forced nonlinear oscillations of an autoparametric system Part 2: periodic responses. Journal of Applied Mechanics, 50, 663-668.
51. Hatwal, H., Mallik, A. K. and Ghosh, A. (1982). Non-linear vibrations of a harmonically excited autoparametric system. Journal of Applied Mechanics, 81, 153-164.
52. Haxton, R. S. and Barr, A. D. S. (1972). The autoparametric vibration absorber. Transactions of the ASME, Journal of Engineering for Industry, pp. 119-125.
53. Hayashi, Chihiro (1964). Nonlinear Oscillations in Physical Systems, McGraw-Hill Book Co., New York.
54. Holmes, P. J. (1977). Bifurcations to divergence and flutter in flow induced oscillations: a finite dimensional analysis. Journal of Sound and Vibration, 53, 471-503.
55. Holmes, C. A. and Rand, R. H. (1981). Coupled oscillations as a model for nonlinear parametric excitation. Mechanics Research Communications, 8, 263-268.

56. Hsieh, D. Y. (1980). On Mathieu equation with damping. Journal of Mathematics and Physics, 21, 722-725.
57. Hsu, C. S. (1965). Further results on parametric excitation of a dynamic system. Journal of Applied Mechanics, pp. 373-377.
58. Ibrahim, R. A. and Barr, A. D. S. (1975). Autoparametric resonance in a structure containing a liquid, Part 1: two mode interaction. Journal of Sound and Vibration, 42, 159-179.
59. Ibrahim, R. A. and Barr, A. D. S. (1975). Autoparametric resonance in a structure containing a liquid, Part 2: three mode interaction. Journal of Sound and Vibration, 42, 181-200.
60. Ibrahim, Raouf A. (1976). Multiple internal resonance in a structure-liquid system. ASME Journal of Engineering for Industry, No. 75-DET-133, 1092-1098.
61. Ishida, Y., Ikeda, T., Yamamoto, T. and Hiei, M. (1986). Effects of nonlinear spring characteristics on the dynamic unstable region of an unsymmetrical rotor. Bulletin of the JSME, 29, 200-207.

62. Khandelwal, R. S. and Nigam, N. C. (1981). Parametric instabilities of a liquid free surface in a flexible container under vertical periodic motion. Journal of Sound and Vibration, 74, 243-249.
63. Kojima, H., Nagaya, K., Shiraishi, H. and Yamashita, A. (1985). Nonlinear vibrations of a beam with a mass subjected to alternating electro-magnetic force. Bulletin of the JSME, 28, 468-474.
64. Kotera, Tadashi (1980). A new method of determining regions of instability of a system with parametric excitations. Bulletin of the JSME, 23, 419-424.
65. Kotera, Tadashi and Yano, Sumio (1985). Periodic solutions and the stability in a non-linear parametric excitation system. Bulletin of the JSME, 28, 1473-1480.
66. Leven, R. W., Pompe, C., Wilke, C. and Koch, B. P. (1985). Experiments on periodic and chaotic motions of a parametrically forced pendulum. Physica, 16D, 371-384.

67. Mallik, A. K., Kulkarni, S. B. and Ram, K. S. (1984). Parametric instability of a periodically supported pipe without and with vibration absorbers. Journal of Applied Mechanics, 51, 159-163.
68. McLaclan, N. W. (1964). Theory and Application of Mathieu Functions, Dover Publications, Inc., New York.
69. Merritt, R. G. and Willems, N. (1973). Parametric resonance of skew stiffened plates. ASME Journal of Applied Mechanics, 40, Paper No. 72-WA/APM-32, 439-444.
70. Mickens, Ronald E. (1981). An Introduction to Nonlinear Oscillations, Cambridge University Press, Cambridge.
71. Miles, John (1985). Parametric excitation of an internally resonant double pendulum. Journal of Applied Mathematics and Physics (ZAMP), 36, 337-345.
72. Month, L. A. and Rand, R. H. (1982). Bifurcation of 4:1 subharmonics in the nonlinear Mathieu equation. Mechanics Research Communications, 9, 233-240.

73. Mook, D. J., Nayfeh, A. H., and Mook, D. T. (1979). Resonant interactions of harmonic axial and transverse loads. Proceedings of the 16th Midwestern Mechanics Conference, Kansas State University, September 19-21, 145-147.
74. Mukhopadhyay, V. (1980). Combination resonance of parametrically excited coupled second order systems with nonlinear damping. Journal of Sound and Vibration, 69, 297-307.
75. Nakamura, T. and Tani, J. (1978). Parametric resonance of annular plates under pulsating uniform internal and external loads with different periods. Journal of Sound and Vibration, 60, 289-297.
76. Naslin, Pierre (1965). The Dynamics of Linear and Nonlinear Systems, Gordon and Breach, Science Publishers, Inc., New York.
77. Natanzon, M. S. (1962) (In Russian). Parametric vibrations of a tube excited by a pulsating dissociating fluid. Izv. Akad. Nauk SSR, Otd. Tekh. Nauk. Mekh. i Mash., 4, 42-46.
78. Nayfeh, A. H. (1973). Perturbation Methods, Wiley-Interscience, New York.

79. Nayfeh, A. H. and Mook, D. T. (1977). Parametric Excitations of Linear Systems Having Many Degrees of Freedom. Journal of the Acoustical Society of America, Vol. 62, No. 2, 375-381.
80. Nayfeh, A. H. and Mook, D. T. (1979). Nonlinear Oscillations, Wiley-Interscience, New York.
81. Nayfeh, A. H. (1981). Introduction to Perturbation Techniques, Wiley-Interscience, New York.
82. Nayfeh, A. H., (1983). Response of Two-Degree-of-Freedom Systems to Multifrequency Parametric Excitations. Journal of Sound and Vibration, Vol. 88, No. 1, 1-10.
83. Nayfeh, A. H., (1983). Response of Two-Degree-of-Freedom Systems with Quadratic Nonlinearities to a Parametric Excitation. Journal of Sound and Vibration, Vol. 88, No. 4, 547-557.
84. Nayfeh, A. H. (1983). The Response of Multidegree-of-Freedom Systems with Quadratic Nonlinearities to a Harmonic Parametric Excitation. Journal of Sound and Vibration, Vol. 90, No. 2, 237-244.

85. Nayfeh, A. H. (1984). Interaction of Fundamental Parametric Resonances with Subharmonic Resonances of Order One-Half. Journal of Sound and Vibration, Vol. 96, No. 3, 333-340.
86. Nayfeh, A. H. (1985). Problems in Perturbation, Wiley Interscience, 1985.
87. Nayfeh, A. H. and Zavodney, L. D. (1986). The Response of Two-Degree-of-Freedom Systems with Quadratic Non-Linearities to a Combination Parametric Resonance. Journal of Sound and Vibration, Vol. 107, No. 2, 329-350.
88. Nayfeh, A. H. and Jebril, Anwar E. S. (1987). The Response of Two-Degree-of-Freedom Systems with Quadratic and Cubic Nonlinearities to Multifrequency Parametric Excitations. Journal of Sound and Vibration, Vol. 115, No. 1, 83-101.
89. Nayfeh, A. H. (1987). Surface waves in closed basins under parametric and internal resonance. Physics of Fluids, 30, 2976-2983.
90. Ness, Douglas J. (1967). Small oscillations of a stabilized, inverted pendulum. American Journal of Physics. 35, 964-967.

91. Noah, S. T. and Hopkins, G. R. (1982). A generalized Hill's method for the stability analysis of parametrically excited dynamic systems. ASME Journal of Applied Mechanics, 49, 217-223.
92. Paidoussis, M. P. and Issid, T. N. (1974). Dynamic stability of pipes conveying fluid. Journal of Sound and Vibration, 33, 267-294.
93. Paidoussis, M. P. and Sundararajan, C. (1975). Parametric and combination resonances of a pipe conveying pulsatile fluid. Journal of Applied Mechanics, 42, 780-784.
94. Paidoussis, M. P., Issid, T. N. and Tsui, M. (1980). Parametric resonance oscillations of flexible slender cylinder in harmonically perturbed axial flows: Part 1 - theory. Transactions of the ASME, Journal of Applied Mechanics, 47, 709-714.
95. Paidoussis, M. P., Issid, N. T. and Tsui, M. (1980). Parametric resonance oscillations of flexible slender cylinder in harmonically perturbed axial flows: Part 2 - experiments. Transactions of the ASME, Journal of Applied Mechanics, 47, 715-719.

96. Papastavridis, J. G. (1982). Parametric excitation stability via Hamilton's action principle. Journal of Sound and Vibration, 82, 401-410.
97. Parlitz, U. and Lauterborn, W. (1985). Superstructure in the bifurcation set of the Duffing equation $\ddot{x} + d\dot{x} + x + x^3 = f\cos(\omega t)$. Physics Letters, 107A, 351-355.
98. Rousselt, J. and Herrmann, G. (1977). Flutter of articulated pipes at finite amplitude. Journal of Applied Mechanics, 44, 154-159.
99. Sato, K., Saito, H. and Otomi, K. (1978). The parametric response of a horizontal beam carrying a concentrated mass under gravity. Journal of Applied Mechanics, 45, 643-648.
100. Schmidt, B. A. (1980). Vibrated pendulum with a mass free to move radially. ASME Journal of Applied Mechanics, 47, 428-430.
101. Schmidt, B. A. (1981). Pendulum with a rotational vibration. ASME Journal of Applied Mechanics, 48, 200-203.

102. Schmidt, B. A. (1983). The radially flexible pendulum subjected a high-frequency excitation. ASME Journal of Applied Mechanics, 50, 443-448.
103. Schmidt, G. and Tondl, Ales (1986). Non-Linear Vibrations, Akademie-Verlag, Berlin.
104. Sevin, Eugene (1961). On the parametric excitation of pendulum-type vibration absorber. Journal of Applied Mechanics, 28, Series E, 330-334.
105. Singh, K. and Mallik, A. K. (1979). Parametric instabilities of a periodically supported pipe conveying fluid. Journal of Sound and Vibration, 62, 379-397.
106. Sinha, S. C., Chou, C. C., and Denman, H. H. (1979). Stability analysis of systems with periodic coefficients: an approximate approach. Journal of Sound and Vibration, 64, 515-527.
107. Stoker, J. J. (1950). Nonlinear Vibrations (in Mechanical and Electrical Systems), Interscience Publishers, Inc., New York.

108. Sueoka, A., Tamura, H., Kondou, T., Fujimoto, T., and Osaki, E. (1986). Nonlinear response of roller chain to combined forcing and parametric excitations. Bulletin of the JSME, 29, 178-186.
109. Sugiyama, Y., Iwatsubo T., and Ishihara, K. (1982). Parametric resonances of a cantilevered column under a periodic tangential force. Journal of Sound and Vibration, 84, 301-303.
110. Swift, J. W. and Wiesenfeld, K. (1984). Suppression of period doubling in symmetric systems. Physical Review Letters, 52, 705-708.
111. Szemplinska-Stupnicka, Wanda (1978). The generalized harmonic balance method for determining the combination resonance in the parametric dynamic systems. Journal of Sound and Vibration, 58, 347-361.
112. Tagata, G. (1983). A parametrically driven harmonic analysis of a nonlinear stretched string with time-varying length. Journal of Sound and Vibration, 87, 493-511.

113. Takahashi, K. (1981). An approach to investigate the instability of the multiple-degree-of-freedom parametric dynamic systems. Journal of Sound and Vibration, 78, 519-529.
114. Takahashi, K. (1982). Instability of parametric dynamic systems with non-uniform damping. Journal of Sound and Vibration, 85, 257-262.
115. Takahashi, Kazuo (1985). Nonlinear response of a rectangular plate subjected to inplane moment. 19th Midwestern Mechanics Conference.
116. Tani, J. and Nakamura, T. (1978). Parametric resonances of annular plates under pulsating uniform internal and external loads with different periods. Journal of Sound and Vibration, 60, 289-297.
117. Tezak, E. G., Mook, D. T., and Nayfeh, A. H. (1978). Nonlinear analysis of the lateral response of columns to periodic loads, Journal of Mechanical Design, 100, 651-659.
118. Tezak, E. G., Nayfeh, A. H., and Mook, D. T. (1982). Parametrically excited nonlinear multidegree-of-freedom systems with repeated natural frequencies. Journal of Sound and Vibration, 85, 459-472.

119. Thomson, W. T. (1965). Vibration Theory and Applications, Prentice-Hall, Inc., New Jersey.
120. Tondl, A. (1978). Monographs and Memoranda, No. 25, National Research Institute for Machine Design, Bechovice (Prague).
121. Unger, A. and Brull, M. A. (1981). Parametric instability of a rotating shaft due to pulsating torque. ASME Journal of Applied Mechanics, 48, 948-958.
122. Valeev, K. G. (1963). On the danger of combination resonances (translation of Prikladnaia Matematika i Mekhanika). Journal of Applied Mathematics and Mechanics, 27, 1745-1759.
123. Watanabe, Takeshi (1984). Forced vibration of nonlinear systems with symmetrical piecewise-linear characteristics. Bulletin of the JSME, 27, 1493-1498
124. Witt, A. and Gorelik, G. (1933). Z. Techn. Phys. Sowjetunion, 3 294 (in Russian).

125. Wu, W. Z. and Mote, C. D., Jr., (1986). Parametric excitation of an axially moving band by periodic edge loading. Journal of Sound and Vibration, 110, 27-39.
126. Yano, Sumio (1984a). Parametric excitation in the self-excited vibration system with dry friction (1st report, parametric resonance). Bulletin of the JSME, 27, 255-262.
127. Yano, Sumio (1984b). Parametric excitation in the self-excited vibration system with dry friction (2nd report, in the neighborhood of the region of parametric resonance). Bulletin of the JSME, 27, 263-270.
128. Yano, S. (1984c). Parametric excitation in a self-exciting system (1st report, behaviors in the region of subharmonic resonance of order 1/2). Bulletin of the JSME, 27, 2483-2491.
129. Yano, Sumio (1984d). Parametric excitation in a self-excited vibration system (3rd report, the influence of cubic non-linearity). Bulletin of the JSME, 27, 1264-1271.
130. Yano, Sumio (1985). Parametric excitation in a self-exciting system (2nd report, behaviors in the regions of resonances of orders 1/3 and 2). Bulletin of the JSME, 28, 483-491.

131. Yano, Sumio, Kotera, Tadashi, and Hiramatsu, Tsutomu (1986a). Parametric excitation with an asymmetric characteristic in a self-exciting system (1st report, behaviors of region of resonance of order 1/2). Bulletin of the JSME, 29, 902-907.
132. Yano, Sumio, Kotera, Tadashi, and Hiramatsu, T. (1986b). Periodic solutions and the stability in a nonlinear parametric excitation system (2nd report, consideration of solutions in the neighborhood of resonance of order 1). Bulletin of the JSME, 29, 3484-3490.
133. Yoshizawa, Masatsuya, Kawahara, Ikuo, and Tsujioka, Yasushi (1984). Flexural vibration of a simply supported beam under the action of a moving body with a pendulum. Bulletin of the JSME, 27, 779-785.
134. Zajaczkowski, J. and Lipinski, J. (1979). Instability of the motion of a beam of periodically varying length. Journal of Sound and Vibration, 63, 9-18.
135. Zajaczkowski, J. and Lipinski, J. (1979). Vibrations of parametrically excited systems. Journal of Sound and Vibration, 63, 1-7.

136. Zajaczkowski, J. and Yamada, G. (1980a). Further results on instability of the motion of a beam of periodically varying length. Journal of Sound and Vibration, 68, 173-180.
137. Zajaczkowski, J. and Yamada, G. (1980b). Instability of a periodically moving plate. Journal of Sound and Vibration, 68, 181-186.

APPENDIX A

DESCRIPTION OF LABORATORY FACILITY

The laboratory facility at VPI & SU is shown in Figure A.1 which shows the signal generation instrumentation, the shaker, the signal conditioning instrumentation, and the signal analysis instrumentation. A photograph of the shaker table and transducer locations is shown in Figure A.2, and the instrumentation schematic is shown in Figure A.3.

A.1 Signal Generation

Experiments on the models were conducted with sinusoidal signals generated by a two-channel, variable-phase wave synthesizer (Wavetek Model 650). It has a 0.0001 Hz resolution and an IEEE-488 (GPIB) interface that permits computer control of all functions. This feature was used to provide a closed-loop feedback controller for the amplitude of vibration. The 0.0001 Hz frequency resolution was required to map out in detail the frequency response of the test models. The harmonic distortion of the signal generator is less than -90 db.

A.2 Motion Actuator

The models tested in this dissertation were subject to a displacement excitation by attaching them to a moving platform. The platform (shaker table) was constrained to pure translation in the vertical direction as shown in Figure A.2. The reaction moments were minimized by adding additional bearings and mass. The shaker table was

actuated by a four-inch-stroke, 250-pound-force electrodynamic shaker (Unholtz-Dickie Model 4) driven by a 2,500 watt power amplifier. The shaker was securely bolted to the concrete ground-level floor. External suspension for the table was provided by elastic shock cord suspended from overhead. This was required because the shaker (a modal exciter) did not have any armature stiffness. The tension in the shock cord was adjusted to carry the static load of the shaker table and accessories attached to it such as the accelerometers, the displacement transducer, and the model.

A.3 Transducers and Signal Conditioning

The signals required to measure the excitation and the response of the flexible structure consisted of: (a) strain gages to measure the amplitude of response, (b) an accelerometer to measure table acceleration, and (c) a displacement transducer to measure table displacement.

Dynamic strain gages were bonded to the test specimens (as discussed in Chapter V) and wired to form a half-bridge for the bridge amplifier, which provided the other half-bridge to complete the circuit. A low-pass filter with pre- and post-gain amplifiers was used to boost the nominal 100 mv signal to a nominal one volt signal. The signal was monitored on an oscilloscope, the FFT analyzer, the AC rms voltage meter, and frequency counter. The amplitude of the response was measured by the rms meter and checked by the FFT analyzer. The

displacement of the beam was calibrated by a micrometer head that displaced the beam to one side, as shown in Figure A.4.

A piezo-electric accelerometer (PCB-308) was used to measure the table acceleration, which required a 27 volt DC supply. Since it was a piezo-electric transducer, it was not capable of measuring DC and low frequency acceleration levels. The accelerometer produced a voltage proportional to the instantaneous acceleration of the table. The sensitivity of the accelerometer was nominally 100 mv/g, so the signal was amplified ten times by the signal conditioner to produce a signal with a nominal sensitivity of 1.00 volt/g. This signal was very clean and required no filtering or further amplification. The waveform in the time and frequency domain was monitored during the entire test. The amplitude of the table acceleration was most conveniently measured by an rms voltage meter (B&K 2432), which also formed an integral part of the computer feedback control loop that was used to keep the table acceleration at the desired level. The amplitude of the acceleration was also monitored by the FFT analyzer.

For very small amplitude acceleration levels we used a servo accelerometer (Sundstrand Model 1400). A signal conditioner/amplifier was designed and built in the vibration laboratory since one was not available commercially. The accelerometer required a ± 15.0 volt supply and produced a current proportional to the total instantaneous acceleration level, including the static gravitational field. The DC component was removed with biasing, and using the appropriate load resistor, sensitivities of 5 to 10 volts/g before amplification were

achieved. Calibration was achieved by simply turning the accelerometer upside down.

The displacement transducer was attached to the side of the shaker table (see photo in Figure A.2) and served two purposes: it provided an independent check on the acceleration signal and it detected the presence of angular displacement (caused by model feedback) of the shaker table since it was located off to the side. This location amplified any rotation present in the table motion. Since the accelerometer was mounted near the center of the shaker table to minimize the dynamic moment of the transducer, it was not able to detect the additional acceleration associated with the rotation. Additionally, since the cross-axis sensitivity of the accelerometer was extremely low, any rotation of the accelerometer would generate a low-level signal that would be lost in the noise anyway. To offset the dynamic imbalance caused by the displacement transducer, a dynamically tuned counter-balance was attached to the opposite side of the shaker table such that its mass and moment were identical to that of the moving portion of the displacement transducer.

The instrumentation schematic in Figure A.3 shows a typical wiring diagram used for the experiments. Care was taken to minimize common mode currents in the signals by the instrumentation as seen by the absence of a 60 Hz peak in Figure 5.12.

Although the system worked extremely well and we were able to obtain good and reliable data, it required five years to develop and refine. The task was begun in 1982 with the purchase of the shaker,

which arrived in the Spring of 1984. The only shakers (in the force range of less than 1000 lbs.) with displacements greater than two inches were modal exciters. That Summer I designed and redesigned the shaker table and suspension system; it was fabricated in the Fall and modified in the Winter of 1985. The laboratory room was prepared and the signal generator and accelerometers were purchased next. An FFT analyzer for general purpose research was purchased.

Preliminary experiments with the system showed the test specimens (when resonating with large amplitude vibration) caused serious subharmonic distortion that was of the order of the excitation. This problem was resolved by adding mass to the shaker table. Since we added additional mass, we discovered we also had to add additional bearings. The masses were added in the Fall of 1986, and permanent masses, along with the additional bearings, were fabricated and installed in the Fall of 1987.

Some experiments required very low levels of acceleration, which created the need for measuring low levels of acceleration. A servo accelerometer was purchased and I began building a conditioner/amplifier in the Summer of 1985. It was completed one year later. The displacement transducer was installed during the Summer of 1987. Vibration voltmeters, frequency counters, digital storage scopes, and filters were also purchased for the lab.

During the preliminary experiments, I discovered the acceleration levels would slowly drift. This created a need for a closed-loop feedback controller to keep the table acceleration at a predetermined

level. An IBM-PC with a GPIB card was used to interface with the signal generator and voltmeter. A comprehensive menu-driven program was developed during the Summer of 1986 and a feedback controller was added in the Spring of 1987. With this software, frequency sweeps and amplitude sweeps were accomplished automatically.

In summary, the system is capable of performing a wide variety of vibration tests. Since the shaker table has a stroke of four inches, it is ideally suited for low-frequency research. The transducers, conditioners, and measuring instrumentation produce exceptionally clean signals. The table acceleration is exceptionally clean and free of harmonic distortion.

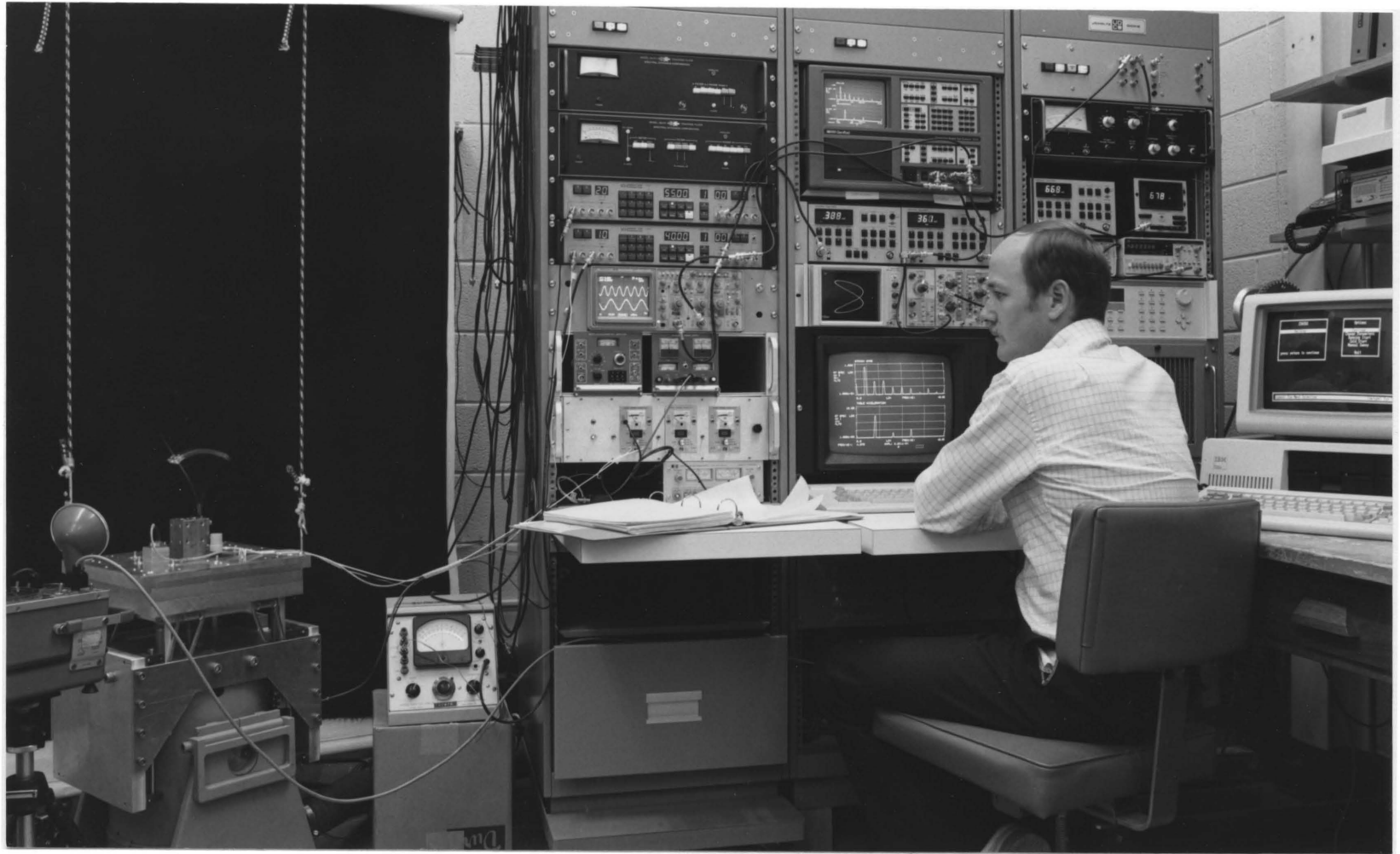


Figure A.1 Photograph of the vibration laboratory at VPI & SU.

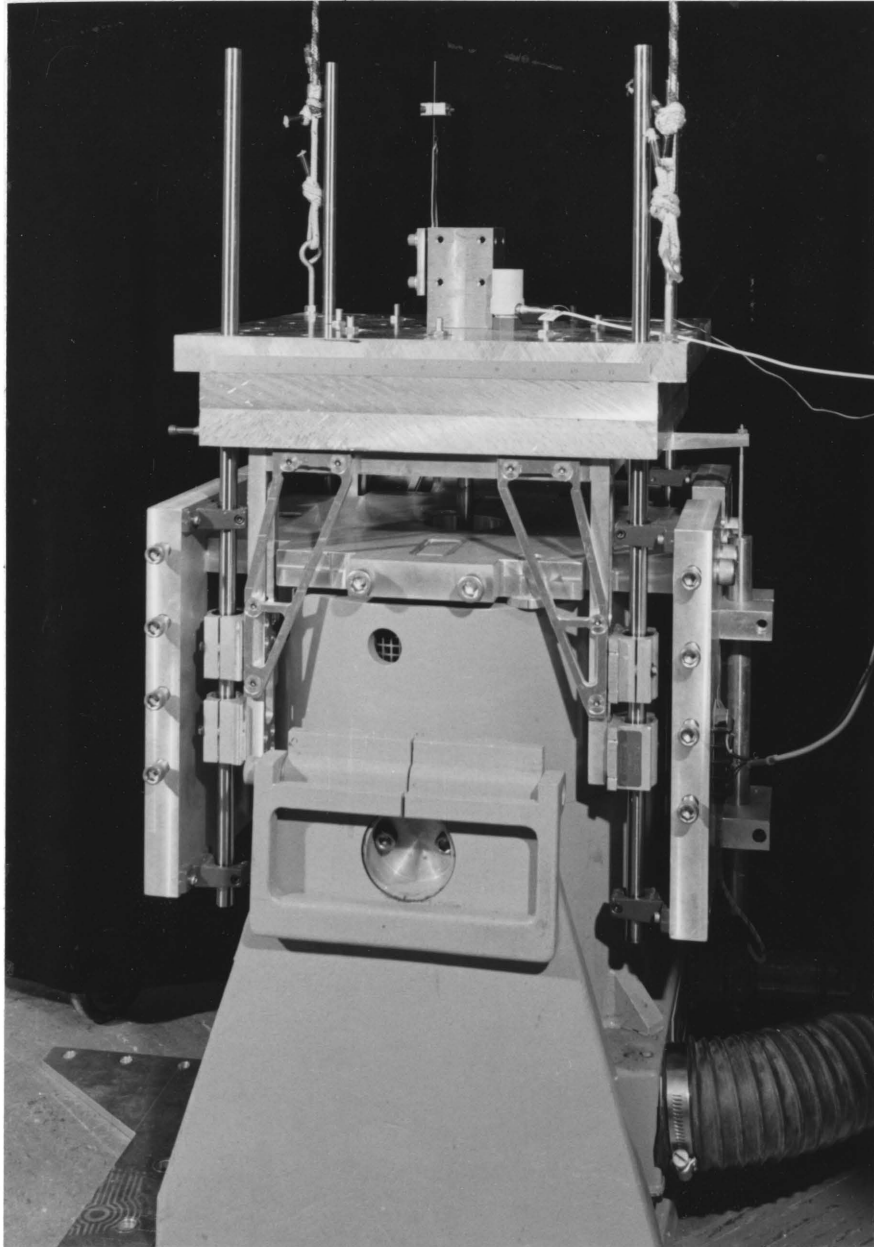


Figure A.2 Close-up photograph of the shaker showing head, bearings, displacement transducer, accelerometer, and flexible beam with lumped mass.

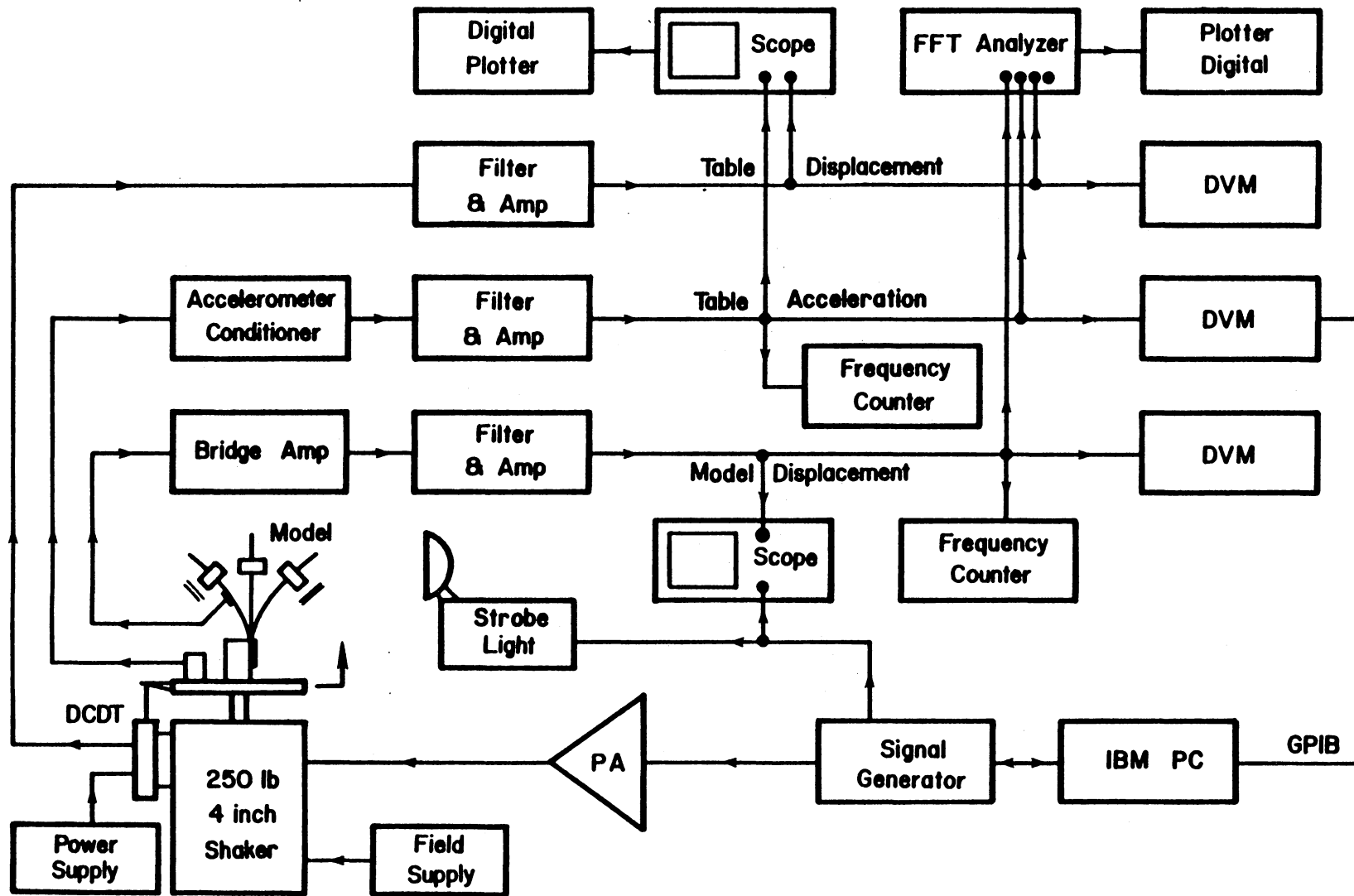


Figure A.3 Typical instrumentation schematic.

APPENDIX B

PROCEDURE TO MEASURE THE NATURAL FREQUENCY

The research in this dissertation required extremely accurate estimates of the natural frequency--accuracy on the order of five to six digits! Typically, experimental results may have 5%-10% error associated with them. Several conventional methods were used and proved unsatisfactory; they are discussed later. The procedure that is described below was one that I developed to perform the research in this dissertation.

Since we had a precise signal generator with a digital display of the frequency, it was used as a comparator to the free response signal of the beam. By displaying the output of the signal generator on the vertical axis of an X-Y oscilloscope, and the strain gage signal (measuring the response of the beam) on the horizontal axis, a Lissajous pattern was displayed. When the frequency of the signal generator exactly matched the damped natural frequency of the beam, a stationary ellipse appeared on the screen. When there was a mismatch of the frequencies, the ellipse rotated at a frequency equal to the difference in the two frequencies. Hence, I simply adjusted the frequency of the oscillator such that the ellipse was stationary. One problem with this procedure was that it was difficult to visualize rotation frequencies of 0.001 Hz associated with changes in the fifth and sixth digits during a decay envelope.

For this reason, I used a comparison frequency that was twice the damped natural frequency of the beam. This had the advantage of cutting any error in half, but more importantly, it produced a "figure eight" pattern that allowed immediate detection of any precession because the cross point would move from side to side at the "beat" frequency. This method worked so well, it was possible to observe the small change in the natural frequency as the amplitude of the response decayed to zero. Since we had a hardening type nonlinearity, the frequency decreased slowly as the amplitude decayed. When the frequency of the oscillator was set at the midpoint of the frequency drift range, we could see the "cross-point" drift initially as it came to a stationary point when the two frequencies were commensurable, and then reverse direction as the model decayed further to zero amplitude. This procedure typically required six to ten attempts at matching and refining, and it was accomplished in less than five minutes. The initial guess was obtained from the FFT analysis. This procedure had the additional advantage because we did not have to dismantle the beam to measure the natural frequency.

The other methods that were tried and found unsuitable are discussed below. One conventional method involves exciting the structure and noting the frequency of the maximum point on the frequency-response function (FRF). When this was done with a sinusoidal excitation, there was a range of frequencies where the peak response was flat and was accompanied on both sides by steps due to the discretization of the digital voltmeter. What was required to use this

method was some sort of quadratic curve fit through a number of data points at the resonance in order to determine the natural frequency. Alternatively, random excitation was used to obtain the FRF, which was searched for the maximum peak. Unfortunately, zoom acquisition was required to get 0.001 Hz resolution and the data acquisition took 45 minutes because of the low frequencies in the 5-15 Hz range. This procedure was further complicated because the beam had to be positioned horizontally on the shaker table to have an externally excited system. Modal-Plus software, donated to the lab by SDRC, was used for this procedure. By using an acoustic speaker to excite the beam, the beam could remain in its clamped support, but we were still plagued by the lengthy data acquisition time.

APPENDIX C

PROCEDURE TO MEASURE THE DAMPING COEFFICIENT

The damping coefficient was estimated from a free response using the log decrement method. A transient response was captured on the oscilloscope and a hard copy was obtained. An envelope curve was drawn through the peaks at what appeared to be an average value and was used to measure the amplitude at the selected peaks. Approximately 100 cycles were used to obtain an average value. We noted that the composite beam had what appeared to be a quadratic damping because it was highly nonlinear.

APPENDIX D

PROCEDURE TO CALIBRATE THE STRAIN GAGE

To obtain quantitative data from the experiments, it was necessary to know the displacement of a reference point on the beam. This was accomplished by displacing the beam a known distance by using a micrometer head and adjusting the gain of the bridge amplifier to a desired quantity. A reference point located just above the mass seemed to work the best. A photograph showing the apparatus is shown in Figure D.1. The head was moved in to slightly displace the beam. The voltage output was noted and the micrometer head was advanced approximately 0.400 inch. The output voltage was noted and then the micrometer head was returned to its original position and the voltage noted.

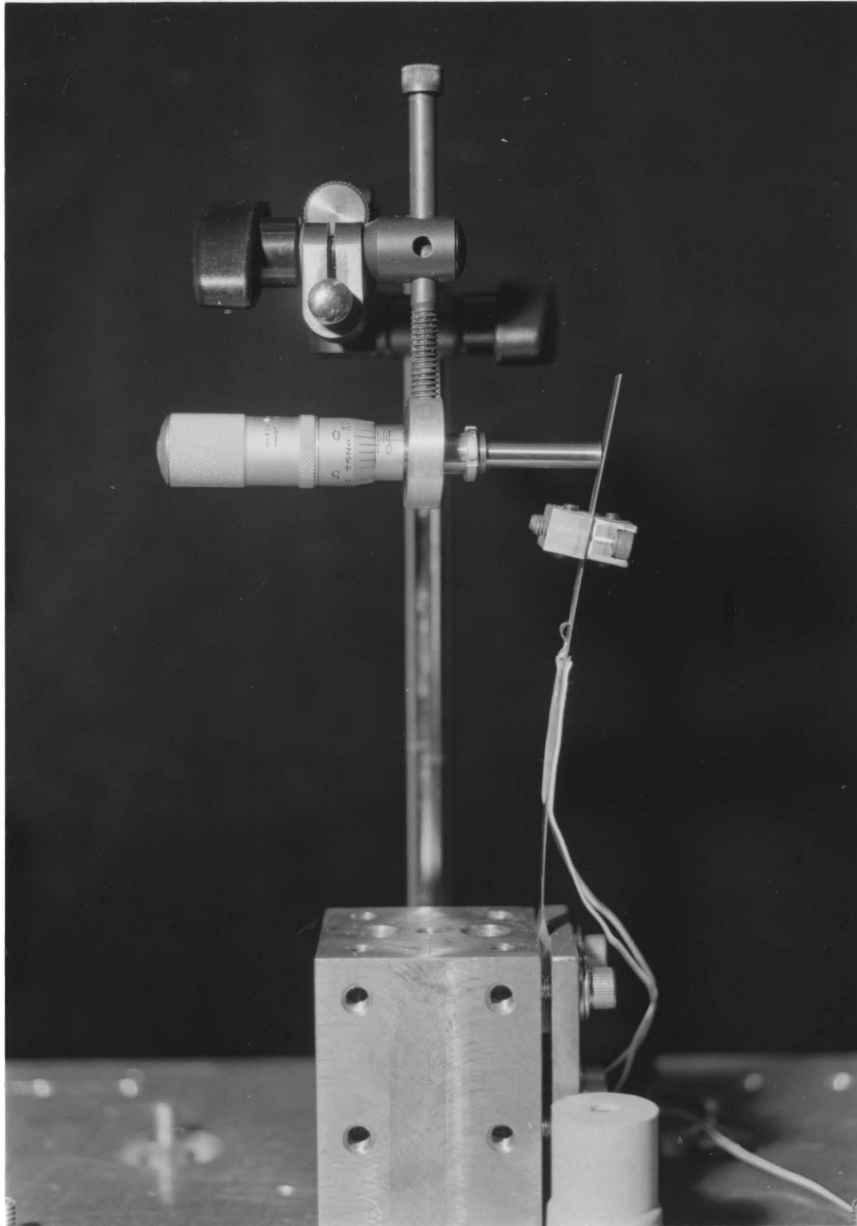


Figure D.1 Photograph of micrometer used to calibrate the strain gage that measured the beam displacement. The displacement of the reference point $\psi(r)$ is plotted as a^* .

APPENDIX E

PROCEDURE TO MEASURE THE FREQUENCY RESPONSE

The frequency response was obtained by varying the excitation frequency ω while keeping the magnitude of the table acceleration $|\omega^2 A|$ constant. The table acceleration was held constant by the computer-controlled feedback loop described in Appendix A. Once a steady-state vibration was achieved, the amplitude of vibration was noted and the frequency was changed in small increments (not exceeding step sizes of 0.0010 Hz) to the next step. This procedure was repeated throughout the region of resonance and included sweeping up and down.

The stability of the trivial solution was determined by observing the behavior of small disturbances--i.e., whether the small disturbances grew or decayed. Care was taken to insure that the small disturbances were properly phased so that if a critical amplitude were exceeded, the response would be attracted to the nontrivial response. This was accomplished by latching onto the nontrivial response and waiting until a steady state was achieved. Then the amplitude was slowly decreased by placing constraints on both sides of the beam and slowly moving them towards the beam. Eventually the beam made contact with the constraints. The constraints were slowly moved in to a predetermined position and then removed. The response was observed, and if it grew, the procedure was repeated with a smaller (disturbance) amplitude. If the trivial solution was stable, eventually an amplitude was reached where the disturbance would decay.

The strain gage calibration and the natural frequency were checked after each sweep.

APPENDIX F

PROCEDURE TO MEASURE THE AMPLITUDE RESPONSE

The amplitude response was obtained by varying the magnitude of the table acceleration $|\omega^2 A|$ while keeping the excitation frequency ω constant. This was done in very small steps so there would be very small disturbances to the system. The feedback-control system was used to hold the acceleration level constant while we waited for a steady-state response, and to step smoothly to the next level. Since there were several jump points for some of the responses, the amplitude was swept up and down.

The stability of the trivial solution was determined in the manner described in Appendix E. The strain gage calibration and the natural frequency were checked after each sweep.

APPENDIX G

DIMENSIONS AND PROPERTIES OF BEAM SPECIMENS

Beam	1st Metallic	Composite	2nd Metallic
Length (mm)	125.40	149.86	127.00
Width (mm)	15.85	12.59	11.11
Thickness (mm)	0.559	0.538	0.378
I (mm ⁴)	6.599x10 ⁻²	16.35x10 ⁻²	4.626x10 ⁻²
E (N/mm)	0.20936x10 ⁶	0.1300x10 ⁶	0.20936x10 ⁶
ρ (gm/mm)	7.762x10 ⁻³	1.794x10 ⁻³	3.177x10 ⁻²
ζ (sec ⁻¹)	1.469x10 ⁻³	0.948-2.51x10 ⁻³	1.469x10 ⁻³
Lumped Mass			
Length (mm)	31.75	22.86	22.86
Height (mm)	9.53	9.53	9.53
Width (mm)	9.05	19.05	19.05
Mass (gm)	25.40	14.70	14.70
J (gm-mm ²)	1969.0	600.9	600.9
d*(mm)	76.20	93.73	85.60
Natural Frequency (Hz)	15.038	10.519	7.845

* position on the beam measured from the clamped support

Alloy Steel composition of the metallic beams

Carbon	0.85 - 0.95
Silicon	0.15 - 0.35
Chromium	0.40 - 0.60
Vanadium	0.15 - 0.25
Tungsten	0.40 - 0.60
Manganese	1.00 - 1.25

Heat treatment procedure

1. Heat slowly to 1440-1490°F
2. Hold for one-half hour
3. Quench in oil at 100-125°F
4. Temper at 1015-1035°F for one-half hour

**The two page vita has been
removed from the scanned
document. Page 1 of 2**

**The two page vita has been
removed from the scanned
document. Page 2 of 2**

A THEORETICAL AND EXPERIMENTAL INVESTIGATION OF
PARAMETRICALLY EXCITED NONLINEAR MECHANICAL SYSTEMS

Lawrence D. Zavodney

(Abstract)

The response of one- and two-degree-of-freedom (SDOF and 2DOF) systems with quadratic and cubic nonlinearities to fundamental, principal, and combination harmonic parametric excitations is investigated theoretically and experimentally. The method of multiple scales (MMS) is used to determine the equations that describe to first and second order the amplitude- and phase-modulations with time. These equations are used to determine the fixed points and their stability. The perturbation results are verified by integrating the governing equations on a digital computer. The analytical results are in excellent agreement with the numerical solutions. In the SDOF systems with quadratic and cubic nonlinearities, the large responses that oscillate about three equilibrium positions are investigated on the digital and analogue computers. The analogue computer is used to generate a bifurcation diagram in the excitation amplitude versus excitation frequency domain. The digital computer is used to obtain Poincaré maps of strange attractors, to investigate larger amplitude responses, and to show the transition to a fractal basin of attraction. The system exhibits $2T$, $3T$, $4T$, $5T$, $6T$, $7T$, $8T$, $12T$, $16T$, and ∞T period-multiplying bifurcations.

The response of a flexible cantilever beam with a concentrated mass to principal parametric base excitation of the first bending mode is

analyzed theoretically. The model takes into account the geometric nonlinearities due to large displacements. Galerkin's method is used to reduce the fourth-order nonlinear PDE to a second-order ODE having periodic coefficients and cubic nonlinearities. The MMS is used to determine steady-state responses and their stability. Experiments are performed on metallic and composite beams; the results show good qualitative agreement with the theory. Chaotic responses are observed in the response of the composite beam.

The response of 2DOF systems with quadratic nonlinearities to a combination parametric resonance in the presence of 2:1 internal resonances is investigated using the MMS. The first-order perturbation solution predicts qualitatively the stable steady-state solutions and illustrates the quenching and saturation phenomena. The reduced equations also predict a transition from periodic to quasi-periodic responses (i.e., Hopf bifurcation). 359 pages, 110 figures.